

ELECTRON TRANSFER KINETICS AND LIGAND EXCHANGE MECHANISM OF
COPPER COMPLEXES USED IN DYE-SENSITIZED SOLAR CELLS

By

Yujue Wang

A DISSERTATION

Submitted to
Michigan State University
in partial fulfillment of the requirements
for the degree of

Chemistry—Doctor of Philosophy

2019

ABSTRACT

ELECTRON TRANSFER KINETICS AND LIGAND EXCHANGE MECHANISM OF COPPER COMPLEXES USED IN DYE-SENSITIZED SOLAR CELLS

By

Yujue Wang

To reduce the emission problem induced by using fossil fuels, solar energy has become one of the most promising clean energy resources. Different technologies have been developed to support efficient and affordable pathways for solar energy conversion. A dye-sensitized solar cell (DSSC) is considered as a type of promising device for this purpose. Due to complexity of the internal structure of DSSCs, the interaction between different materials influences drastically the performance of the cell. Copper coordination complexes in their lower oxidation state, such as Cu(I), have intense color and proper energy gap between their ground and excited states. And Cu(I/II) pair acts as a good redox couple in solution with relatively positive potential energy. Therefore, Cu(I) complexes are promising alternative photosensitizers for DSSCs to the expensive ruthenium complexes, and Cu(I/II) complex pairs are promising outer-sphere redox couples.

This dissertation discussed the usage of copper sensitizers in DSSCs and aimed to reveal the reasons for the low performance of the cells. A ligand exchange reaction between the common additive in DSSC electrolyte (*4-tert*-butylpyridine) and copper complexes was studied. The unique effect of this ligand exchange reaction improved the performance of the cell. Other electron-donating additives are explored, and the goal was to establish a design rule for DSSCs with copper complexes as one of the components.

Copyright by
YUJUE WANG
2019

ACKNOWLEDGEMENTS

Looking back at my six-year grad school life at Michigan State University, I have gained so much more than I have expected, knowledge of chemistry, academic accomplishments, social experiences and more importantly, friendships. There are many thanks I would like to express.

First is to my advisor, Professor Hamann. Thank you, Tom, for being a great advisor and provide me the guidance in my research. Without your guidance and persistent help, it would not have been possible for me to get my Ph.D. degree. Your attitude toward scientific research reminds me how a real scientist should behave.

I also want to thank my committee, especially my second reader, Professor Beaulac. Thank you, Remi, to read my entire dissertation very carefully and spent the time to discuss with me about how to improve it.

I would like to thank everyone else that I met and worked with in the Hamann lab. They are Dr. Yuling Xie, Dr. Yuan Gao, Dr. Faezeh Habib Zadeh, Parisa Shadabipour, Austin Raitzel, Dr. Tea-Yon Kim, Dr. Dhritabrata Mandal, Dr. Hamed Hajibabaei Najafabadi, Dr. Josh Baillargeo, Dr. Daniel Little, Dr. Qiong Wang, Dr. Geletu Qing, Dr. Omid Zandi, Dr. Arianna Savini, Dr. Kelley Hutchins, Dr. Jorge Rossero, Shane Jackowski, Eric Firestone, Ben Cecil and Hua-Kuang Lee. There are so many big brains among these people, and without the communication and learning from any single one of them, I could not achieve what I have today. I will not forget how many enlightening conversations we had about research during the past six years and how many joyful times we have spent together. Although the research can be tough sometimes, I didn't get lost because of all the help I received from you.

I would also like to express my gratitude to my families and my boyfriend for their support. Thank you, mom and dad, for making me feel relief and laugh without any stress every time after we talk. I have been abroad and wasn't able to be with you during the Chinese New Year for the past six years. And I still don't know when I can go back and live in a closer city to you. But I love you a lot!

I have grown up a lot during these years at graduate school, and I'm grateful for getting to know all of you that I've met, worked with and spent time with. Dr. Shuang Liang, Dr. Yiqing Yang, Dr. Ruiqiong Guo, Dr. Xiaoran Zhang, Dr. Chuanpeng Jiang, Dr. Ke Ma, Dr. Chenjia Mi, Dr. Dianyi Liu, Dr. Nan Du and so many others. You all had a significant impact on me. Thank you all!

TABLE OF CONTENTS

LIST OF TABLES	ix
LIST OF FIGURES	xii
LIST OF SCHEMES	xx
KEY TO ABBREVIATIONS	xxi
Chapter 1. Introduction	1
1.1 Motivations in solar energy.....	1
1.2 Historical development of DSSCs.....	3
1.2.1 Photoelectrochemistry and dye sensitization.....	3
1.2.2 Conversion of solar energy into electricity.....	4
1.2.3 The development of Dye-Sensitized Solar Cells.....	5
1.3 Different components in DSSCs.....	7
1.3.1 Sensitizers in DSSCs.....	7
1.3.2 DSSCs using copper(I) complexes as sensitizers.....	12
1.3.3 Redox couples in DSSCs.....	15
1.3.4 DSSCs using copper(II/I) redox couples.....	18
1.3.5 Solid-state DSSCs using copper(II/I) redox couples and whole copper DSSCs.....	26
1.4 Motivation for studying the electron transfer processes of copper complexes.....	26
REFERENCES	28
Chapter 2. Electron transfer processes of DSSCs using copper sensitizers	34
2.1 Introduction.....	34
2.2 The problems with using copper(I) sensitizers in DSSCs.....	37
2.3 Experimental details.....	38
2.3.1 Synthesis of the Chemicals.....	38
2.3.2 Photophysical and Electrochemical Measurement.....	44
2.3.3 DSSC preparation and characterization.....	45
2.3.4 General methods for the characterization of DSSCs.....	48
2.4 Result and discussion.....	50
2.4.1 Structure of the copper dye.....	50
2.4.2 Electrochemical and photophysical measurement.....	51
2.4.3 DSSCs with triiodide/iodide redox couple.....	54
2.5 Research summary.....	61
APPENDIX	62
REFERENCES	70
Chapter 3. Ligand exchange between 4-<i>tert</i>-butylpyridine and [Cu(dmbpy)₂]²⁺	73
3.1 Introduction.....	73
3.2 Experimental methods.....	75
3.2.1 Synthetic methods.....	75

3.2.2 Electrochemical methods.....	79
3.2.3 Other spectroscopic methods.....	80
3.3 Result and discussion.....	84
3.3.1 The structural difference between [Cu(dmbpy) ₂]OTf and [Cu(dmbpy) ₂ H ₂ O]OTf ₂	84
3.3.2 The electrochemical properties of [Cu(dmbpy) ₂]OTf and [Cu(dmbpy) ₂ H ₂ O]OTf ₂ and the effect of TBP.....	85
3.3.3 Monitoring the ligand exchange of dmbpy by TBP.....	92
3.3.4 Reversibility, kinetics and equilibrium of the ligand exchange reaction.....	98
3.4 Conclusion.....	105
APPENDIX.....	107
REFERENCES.....	120

Chapter 4 The effect of the *in-situ* ligand exchange reaction between [Cu(dmbpy)]^{2+/+} redox couple and TBP, on the DSSC performance..... 122

4.1 Introduction.....	122
4.2 Experimental methods.....	125
4.2.1 Solar cell assembly.....	125
4.2.2 Cell characterization methods.....	127
4.2.3 Three-electrode setup.....	128
4.3 Result and discussion.....	128
4.3.1 The effect of the addition TBP on the solution potential of the electrolyte.....	128
4.3.2 The effect of TBP on solar cell performance.....	130
4.3.3 Reduced recombination by the <i>in-situ</i> ligand exchange.....	133
4.3.4 Reorganization energy of electron recombination reaction to [Cu(dmbpy) ₂] ²⁺	135
4.3.5 The discussion about the origin of the electron recombination.....	138
4.4 Conclusion.....	141
APPENDIX.....	143
REFERENCES.....	158

Chapter 5 Searching for bases other than TBP to be used as an additive in copper DSSCs..... 161

5.1 Introduction.....	161
5.2 Experimental methods.....	162
5.3 Results and discussion.....	166
5.3.1 Ligand exchange of [Cu(dmbpy) ₂] ²⁺ in solution with different bases.....	166
5.3.2 Ligand exchange induced electrochemical changes of the redox species with different bases.....	171
5.3.3 The effect of different bases on overpotentials and charge transfer kinetics at the counter electrode.....	173
5.3.4 The effect of different bases on mass transport in electrolyte.....	176
5.3.5 The effect of different bases on the charge recombination.....	176
5.4 Conclusion and remaining questions.....	179
APPENDIX.....	180
REFERENCES.....	189

Chapter 6 Future directions for copper redox couples for DSSCs..... 191

6.1 Summary of results.....	191
-----------------------------	-----

6.2 Future directions.....	195
6.2.1 Studying the kinetics and equilibrium of the ligand exchange between $[\text{Cu}(\text{dmbpy})_2]^{2+}$ and TBP	195
6.2.2 The effect of halogens in the coordinating sphere of copper complexes	195
6.2.3 Constructing a “single component” copper DSSC	197
6.2.4 Solid-state DSSCs with copper redox couples	197
APPENDIX.....	199
REFERENCES.....	204

LIST OF TABLES

Table 1.1	Copper complexes that were used as redox couples in DSSCs.....	22
Table 2.1	Bond lengths in Å for Cu(dmdcbpy) ₂ Cl.....	64
Table 2.2	Bond angles in ° for Cu(dmdcbpy) ₂ Cl.....	64
Table 3.1	The detailed sample information for the kinetic study by NMR.....	83
Table 3.2	Bond lengths in Å for [Cu(dmbpy) ₂]OTf.....	108
Table 3.3	Bond angles in ° for [Cu(dmbpy) ₂]OTf.....	108
Table 3.4	Bond lengths in Å for [Cu(dmbpy) ₂ H ₂ O]OTf ₂	109
Table 3.5	Bond angles in ° for [Cu(dmbpy) ₂ H ₂ O]OTf ₂	109
Table 3.6	Hydrogen bond information for [Cu(dmbpy) ₂ H ₂ O]OTf ₂	109
Table 3.7	The linewidths of solvent peak at 1.94 ppm at different [Cu(dmbpy) ₂] ²⁺ concentrations.....	115
Table 3.8	Fitting results for EPR spectra Mix1, Mix2, Mix3.....	118
Table 3.9	Concentrations of species in the Mix samples for EPR measurement.....	119
Table 4.1	Solution potentials of the electrolyte with different concentrations of TBP. The solution potential was measured on Pt, glassy carbon and PEDOT electrodes, versus Ag/AgNO ₃ (Fc ⁺⁰ is 0.09 V vs Ag/AgNO ₃). Electrolyte contains 0.2 M [Cu(dmbpy) ₂]OTf, 0.02 M [Cu(dmbpy) ₂ H ₂ O]OTf ₂ , 0.1 M LiOTf and different concentrations TBP in acetonitrile.....	130
Table 4.2	Summary of the reorganization energies and the electron transfer rate constants calculated for [Cu(dmbpy) ₂] ^{2+/+} redox couple in acetonitrile. -ΔG is the free energy change of the electron recombination from the conduction band of TiO ₂ to [Cu(dmbpy) ₂] ²⁺ in the electrolyte.....	137
Table 4.3	The parameters in the DX-Bisqurt#3 model.....	145
Table 4.4	Parameters extracted from fitting dark EIS data of cobalt DSSC with Y123 dye. Electrolyte contains 0.1 M LiOTf, 0.2 M [Co(bpy) ₃] ³⁺ , 0.02 M [Co(bpy) ₃] ²⁺ and 0.5 M TBP.....	147
Table 4.5	Parameters extracted from fitting dark EIS data of cobalt DSSC with Y123 dye. Electrolyte contains 0.1 M LiOTf, 0.2 M [Co(bpy) ₃] ³⁺ and 0.02 M [Co(bpy) ₃] ²⁺	148

Table 4.6	Parameters extracted from fitting dark EIS data of copper DSSC with Y123 dye. Electrolyte contains 0.1 M LiOTf, 0.2 M [Cu(dmbpy) ₂] ⁺ and 0.02 M [Cu(dmbpy) ₂] ²⁺	150
Table 4.7	Parameters extracted from fitting dark EIS data of copper DSSC with Y123 dye. Electrolyte contains 0.1 M LiOTf, 0.2 M [Cu(dmbpy) ₂] ⁺ , 0.02 M [Cu(dmbpy) ₂] ²⁺ and 0.1 M TBP.	151
Table 4.8	Parameters extracted from fitting dark EIS data of copper DSSC with Y123 dye. Electrolyte contains 0.1 M LiOTf, 0.2 M [Cu(dmbpy) ₂] ⁺ , 0.02 M [Cu(dmbpy) ₂] ²⁺ and 0.2 M TBP.	152
Table 4.9	Parameters extracted from fitting dark EIS data of copper DSSC with Y123 dye. Electrolyte contains 0.1 M LiOTf, 0.2 M [Cu(dmbpy) ₂] ⁺ , 0.02 M [Cu(dmbpy) ₂] ²⁺ and 0.3 M TBP.	153
Table 4.10	Parameters extracted from fitting dark EIS data of copper DSSC with Y123 dye. Electrolyte contains 0.1 M LiOTf, 0.2 M [Cu(dmbpy) ₂] ⁺ , 0.02 M [Cu(dmbpy) ₂] ²⁺ and 0.4 M TBP.	154
Table 4.11	Parameters extracted from fitting dark EIS data of copper DSSC with Y123 dye. Electrolyte contains 0.1 M LiOTf, 0.2 M [Cu(dmbpy) ₂] ⁺ , 0.02 M [Cu(dmbpy) ₂] ²⁺ and 0.5 M TBP.	155
Table 4.12	Parameters extracted from fitting dark EIS data of three electrode cell system. Electrolyte contains 0.1 M LiOTf, 0.2 M [Cu(dmbpy) ₂] ⁺ , 0.02 M [Cu(dmbpy) ₂] ²⁺ and 0.5 M TBP. Working electrode was Y123 dye sensitized TiO ₂ nanoparticle film on FTO. Counter electrode was Pt mesh. Reference was Ag/AgNO ₃ . The solution was stirred during the measurement.	156
Table 5.1	A list of bases used in this chapter and their pKa value in water.	162
Table 5.2	Electrolyte composition ^a and the corresponding charge transfer resistance, <i>R</i> _{CT} , on the counter electrode.	175
Table 5.3	Parameters extracted from fitting dark EIS data of symmetrical PEDOT cells at 0 V applied potential. Electrolyte contains 0.1 M LiOTf, 0.2 M [Cu(dmbpy) ₂] ⁺ and 0.04 M [Cu(dmbpy) ₂] ²⁺ and different basic additives. The active area of the cell was 0.36 cm ²	182
Table 5.4	Parameters extracted from fitting dark EIS data of copper DSSC with Y123 dye. Electrolyte contains 0.1 M LiOTf, 0.2 M [Cu(dmbpy) ₂] ⁺ , 0.04 M [Cu(dmbpy) ₂] ²⁺ and 0.3 M TBP.	184
Table 5.5	Parameters extracted from fitting dark EIS data of copper DSSC with Y123 dye. Electrolyte contains 0.1 M LiOTf, 0.2 M [Cu(dmbpy) ₂] ⁺ , 0.04 M [Cu(dmbpy) ₂] ²⁺ and 0.5 M TBP.	184

Table 5.6	Parameters extracted from fitting dark EIS data of copper DSSC with Y123 dye. Electrolyte contains 0.1 M LiOTf, 0.2 M [Cu(dmbpy) ₂] ⁺ , 0.04 M [Cu(dmbpy) ₂] ²⁺ and 0.3 M Im.....	185
Table 5.7	Parameters extracted from fitting dark EIS data of copper DSSC with Y123 dye. Electrolyte contains 0.1 M LiOTf, 0.2 M [Cu(dmbpy) ₂] ⁺ , 0.04 M [Cu(dmbpy) ₂] ²⁺ and 0.5 M Im.....	185
Table 5.8	Parameters extracted from fitting dark EIS data of copper DSSC with Y123 dye. Electrolyte contains 0.1 M LiOTf, 0.2 M [Cu(dmbpy) ₂] ⁺ , 0.04 M [Cu(dmbpy) ₂] ²⁺ and 0.1 M MBIm.....	186
Table 5.9	Parameters extracted from fitting dark EIS data of copper DSSC with Y123 dye. Electrolyte contains 0.1 M LiOTf, 0.2 M [Cu(dmbpy) ₂] ⁺ , 0.04 M [Cu(dmbpy) ₂] ²⁺ and 0.3 M MBIm.....	186
Table 5.10	Parameters extracted from fitting dark EIS data of copper DSSC with Y123 dye. Electrolyte contains 0.1 M LiOTf, 0.2 M [Cu(dmbpy) ₂] ⁺ , 0.04 M [Cu(dmbpy) ₂] ²⁺ and 0.5 M MBIm.....	187
Table 5.11	Parameters extracted from fitting dark EIS data of copper DSSC with Y123 dye. Electrolyte contains 0.1 M LiOTf, 0.2 M [Cu(dmbpy) ₂] ⁺ , 0.04 M [Cu(dmbpy) ₂] ²⁺ and 0.1 M DMAP.....	187
Table 5.12	Parameters extracted from fitting dark EIS data of copper DSSC with Y123 dye. Electrolyte contains 0.1 M LiOTf, 0.2 M [Cu(dmbpy) ₂] ⁺ , 0.04 M [Cu(dmbpy) ₂] ²⁺ and 0.3 M DMAP.....	188
Table 6.1	Bond length in Å for blue crystal.....	201
Table 6.2	Bond angles in ° for blue crystal.....	201
Table 6.3	Bond length in Å for Cu(DMAP) ₂ OTf ₂	202
Table 6.4	Bond angles in ° for Cu(DMAP) ₂ OTf ₂	202
Table 6.5	Bond length in Å for Cu(tmbpy) ₂ TFSI ₂	203
Table 6.6	Bond angles in ° for Cu(tmbpy) ₂ TFSI ₂	203

LIST OF FIGURES

- Figure 1.1** AM 1.5 Solar spectrum (the ASTM G173 spectra) represents the terrestrial solar spectral irradiance on a surface of specified orientation under a set of the specified atmospheric condition. 8
- Figure 1.2** Different designs of copper dyes used in DSSCs. Details are described in the content. a. ref 40; b. and c. ref 42; d. ref 41; e. ref 54. All copper centers are Cu^+ 13
- Figure 2.1** A diagram showing the operating system of DSSC. Green arrows show the direction of electron transfer. Red arrows show the unwanted back electron transfer. FTO is fluorine-doped tin oxide. CB is the conduction band of TiO_2 . *Red* and *Ox* are the reduced and oxidized forms of the redox couple, respectively. $E_{1/2, \text{redox}}$ is the redox potential of the redox couple. 36
- Figure 2.2** Crystal structure of $\text{Cu}(\text{dmdebpy})_2\text{Cl}$ solved by single-crystal X-ray diffraction. Oxygen (red), carbon (gray), hydrogen (white), nitrogen (blue), and copper (center red) atoms are shown (see Appendix Table 2.1-2.2 and the notes for the detailed crystallography data). 50
- Figure 2.3** Black curve is the CV plot of $\text{Cu}(\text{dmdebpy})_2\text{PF}_6$ and ferrocene in DCM on a glassy carbon working electrode. Ferrocene was used as an internal potential reference. The red curve is the CV plot of $\text{Cu}(\text{dmdebpy})_2\text{Cl}$ sensitized ITO film in AcN. The electrolyte has 0.1 M TBAPF₆ as supporting electrolyte. Both scans are taken under an inert atmosphere using dry solvents. The scan rate was 200 mV/s. 51
- Figure 2.4** The absorption spectra of dyes in solution. The black curve is the absorption spectrum of N3 dye. The red curve is the absorption spectrum of $\text{Cu}(\text{dmdebpy})_2\text{Cl}$. Both are measured in dry methanol under an inert atmosphere with 1 cm path length cuvette. 53
- Figure 2.5** *JV* curves of DSSCs with different dyes. The red curve is the averaged *JV* curve of cells with N3 sensitizer. The black curve is the averaged *JV* curve of cells with $\text{Cu}(\text{dmdebpy})_2\text{Cl}$ sensitizer. Error bars are from the standard deviation between samples (more than 3 samples for each condition). DSSCs have anodes with a 7 μm transparent layer and 5 μm scattering layer TiO_2 . Electrolyte contains 0.6 M LiI, 0.03 M I_2 and 0.5 M TBP in acetonitrile. The counter electrode is Pt coated FTO glass. 15 μm thick Surlyn film is used between anode and cathode as spacer. Cells were measured under 1 sun condition with AM 1.5 spectrum. 54
- Figure 2.6** **a)** $IPCE_\lambda$ **b)** LHE_λ and **c)** $APCE_\lambda$ curves of cells. Red curves are for cells with N3 sensitizer. Black curves are for cells with $\text{Cu}(\text{dmdebpy})_2\text{Cl}$ sensitizer. Error bars are from the standard deviation between samples. Electrolyte contains 0.6 M LiI, 0.03 M I_2 and 0.5 M TBP in acetonitrile. The counter electrode is Pt coated FTO glass. 25 μm thick Surlyn film is used between anode and cathode as a spacer. 56

Figure 2.7	Electron lifetime plot under different applied voltage between photoanode and counter electrode of DSSCs. The red curve is the representative electron lifetime curve of DSSCs with N3 sensitizer. The black curve is the representative electron lifetime curve of DSSCs with Cu(dmdbcby) ₂ Cl sensitizer. Electrolyte contains 0.6 M LiI, 0.03 M I ₂ and 0.5 M TBP in acetonitrile. The counter electrode is Pt coated FTO glass. 25 μm thick Surlyn film is used between anode and cathode as a spacer.	59
Figure 2.8	CV of Cu(dmdbcby) ₂ Cl on ITO film measured in DCM. The concentrations of TBP in the electrolyte are indicated in the graph.	60
Figure 2.9	The home-made reference electrode.	63
Figure 2.10	Crystal structure of Cu(dmdbcby) ₂ Cl.	64
Figure 2.11	CV of 4 mM N3 dye in AcN. Working electrode was glassy carbon disk. Reference electrode was Ag/AgNO ₃ (0.01 M in AcN). Counter electrode was Pt mesh. Supporting electrolyte was 0.1 M TBAPF ₆ . Scan rate was 0.1 V/s. E _{1/2} for two pairs of waves are 0.49 and 0.81 V vs Fc ⁺⁰	65
Figure 2.12	CV of Cu(dmdbcby) ₂ Cl on ITO film in DCM. Working electrode was Cu(dmdbcby) ₂ Cl sensitized ITO nanoporous fim. Reference electrode was Ag/AgNO ₃ (0.01 M in AcN). Counter electrode was Pt mesh. Supporting electrolyte was 0.1 M TBAPF ₆ . Scan rate was 0.1 V/s.	65
Figure 2.13	CV of N3 on ITO film in DCM. Working electrode was N3 sensitized ITO nanoporous fim. Reference electrode was Ag/AgNO ₃ (0.01 M in AcN). Counter electrode was Pt mesh. Supporting electrolyte was 0.1 M TBAPF ₆ . Scan rate was 0.1 V/s.	66
Figure 2.14	UV-vis of Cu(dmdbcby) ₂ Cl in MeOH/DCM 1:1 v/v mixture (green), MeOH (blue) and water (black).	66
Figure 2.15	Extinction coefficient of Cu(dmdbcby) ₂ Cl (black) and N3 (red) in 10 mM NaOH water solution. Errors are from the standard deviation between different samples of the same dye.	68
Figure 2.16	Absorption spectrum of desorbed dye in 10 mM NaOH water solution, 10 mM NaOH in water (green), Cu(dmdbcby) ₂ Cl (black) and N3 (red). Errors are from the standard deviation between different samples of the same dye.	68
Figure 3.1	a) Molecular drawing of [Cu(dmbpy) ₂]OTf. b) Red crystal of [Cu(dmbpy) ₂]OTf, formed by diethyl ether diffusion method into acetonitrile. c) The molecular structure measured by single-crystal XRD (see Appendix for more detailed crystallography information). d) ¹ H NMR spectrum of [Cu(dmbpy) ₂]OTf in CD ₃ CN.	76
Figure 3.2	a) Molecular drawing of [Cu(dmbpy) ₂ H ₂ O]OTf ₂ . b) Green crystal of [Cu(dmbpy) ₂ H ₂ O]OTf ₂ , formed by diethyl ether diffusion method into dichloromethane. c) The	

- molecular structure measured by single-crystal XRD. (see Appendix for more detailed crystallography information) **d**) ^1H NMR spectrum of $[\text{Cu}(\text{dmbpy})_2\text{H}_2\text{O}]\text{OTf}_2$ in CD_3CN 78
- Figure 3.3** **a)** Molecular drawing of $[\text{Cu}(\text{TBP})_4]\text{OTf}_2$. **b)** Purple crystal of $[\text{Cu}(\text{TBP})_4]\text{OTf}_2$, formed by diethyl ether diffusion method into acetonitrile. **c)** The molecular structure measured by single-crystal XRD. (see Appendix for more detailed crystallography information) **d)** ^1H NMR spectrum of $\text{Cu}(\text{TBP})_4\text{OTf}_2$ in CD_3CN . Peaks with stars are from diethyl ether. 79
- Figure 3.4** A simplified diagram of stopped-flow instrument. Solution A was $[\text{Cu}(\text{dmbpy})_2]^{2+}$ and solution B was TBP, in acetonitrile. 0.1 M LiOTf was used as supporting electrolyte and to control the ionic strength. Stop syringe was set to 0.35 mL..... 81
- Figure 3.5** The geometry difference between $[\text{Cu}(\text{dmbpy})_2]\text{OTf}$ and $[\text{Cu}(\text{dmbpy})_2\text{H}_2\text{O}]\text{OTf}_2$. The dihedral angles are 83.2° and 71.7° , respectively (counter ions are not shown because they are not in the coordination sphere). 84
- Figure 3.6** CV scans of 4mM **a)** $[\text{Cu}(\text{dmbpy})_2]^+$ and **b)** $[\text{Cu}(\text{dmbpy})_2]^{2+}$ in acetonitrile. Colors from light to dark represent scan rates from 0.005 to 0.5 V/s. A peak current versus square root of scan rate (i_p vs. $v^{1/2}$) is plotted in the insert. The linear behavior and the ratio between the cathodic and anodic peak current indicates the good electrochemical reversibility of the redox couple. 86
- Figure 3.7** **a)** Proton NMR spectrums measured by 500 MHz NMR spectrometer (Max T. Rogers NMR Facility of MSU) in deuterated acetonitrile (purchased from Sigma Aldrich) under room temperature. Solutions contained different concentrations of $[\text{Cu}(\text{dmbpy})_2]^{2+}$. The dashed rectangular indicates the methyl proton peaks of the dmbpy ligand in $[\text{Cu}(\text{dmbpy})_2]^+$. **b)** Fitted peaks around 2.2 ppm, indicated by the dashed rectangular in a). All the fittings were done by Mnova software, and the FWHM of each peak was calculated. **c)** Dependence of k_{obs} on the concentration of $[\text{Cu}(\text{dmbpy})_2]^{2+}$. Samples were prepared under N_2 atmosphere with dry solvents. The measurements were done under air-free condition and room temperature. 89
- Figure 3.8** Electrochemical behavior of $[\text{Cu}(\text{dmbpy})_2]^{2+}$ in acetonitrile with the presence of TBP. 4 mM $[\text{Cu}(\text{dmbpy})_2]^{2+}$ with the addition of 0, 3, 13 and 25 equivalents of TBP to the copper complex (**a** to **d**). The scan rate was 0.1 V/s. Glassy carbon disk was used as a working electrode, and the same peak shape was also observed on a Pt disk electrode. 91
- Figure 3.9** **a)** Plots of the absorption spectra of $[\text{Cu}(\text{dmbpy})_2]^+$ (red), $[\text{Cu}(\text{dmbpy})_2]^{2+}$ (green) and $[\text{Cu}(\text{TBP})_4]^{2+}$ (blue) in acetonitrile. **b)** Absorption spectra corresponding to the titration of $[\text{Cu}(\text{dmbpy})_2]^{2+}$ with aliquots of TBP in acetonitrile. The concentration of $[\text{Cu}(\text{dmbpy})_2]^{2+}$ was 4 mM, with 0, 3, 6, 13 and 25 equivalents TBP introduced to the solution. 93
- Figure 3.10** Absorption spectra corresponding to the titration of $[\text{Cu}(\text{TBP})_4]^{2+}$ with aliquots of dmbpy in acetonitrile. The concentration of $[\text{Cu}(\text{TBP})_4]^{2+}$ was 8 mM, with 0, 0.53,

- 1.1, 1.5, 2.4, 4.0, 5.2, 6.5 and 13 equivalents of dmbpy (from bottom to top) introduced to the solution. 94
- Figure 3.11** Partial ^1H NMR titration spectra of $[\text{Cu}(\text{dmbpy})_2]^{2+}$ with TBP in AcN-d_3 at room temperature. The concentration of $[\text{Cu}(\text{dmbpy})_2]^{2+}$ was 39 mM. The concentration of TBP added is listed on the left of the figure. The internal standard was dichloromethane which is non-coordinating. The concentration of dichloromethane was 26 mM. The signal of the proton in dichloromethane was integrated and used to calibrate the concentration of other protons. Signals of **a)** aromatic protons in dmbpy in $[\text{Cu}(\text{dmbpy})_2]^{2+}$ complex, **b)** aromatic protons in free dmbpy ligand, **c)** protons in dichloromethane, **d)** methyl protons in free dmbpy ligand and **e)** methyl protons in TBP. The samples were prepared with dry solvent under the air-free condition and measured under air-free condition using J. Young NMR tube. 96
- Figure 3.12** Titration results obtained by NMR. The ratio between the detected free dmbpy ligand and the total Cu^{2+} species is plotted versus the aliquots of TBP in the solution. The concentration of dmbpy was determined based on the integration of aromatic proton peaks. A controlled amount of DCM was added as an internal standard for the quantitative calculation. 98
- Figure 3.13** Plots of CV spectra (left) and absorption spectra (right) for solutions containing: a, b) 4 mM $[\text{Cu}(\text{TBP})_4]^{2+}$ and 0.1 M LiOTf (blue lines) in acetonitrile; c, d) 4 mM $[\text{Cu}(\text{TBP})_4]^{2+}$, 0.1 M LiOTf and 8 mM dmbpy in acetonitrile (green lines); e, f) 4 mM $[\text{Cu}(\text{TBP})_4]^{2+}$ 0.1 M LiOTf and 8 mM dmbpy in acetonitrile after bulk electrolysis at -0.37 V vs. $\text{Fc}^{+/0}$ which resulted in passing 1.7 C of charge cathodically (red lines). The absorption spectrum of the 10-fold diluted spectrum is shown in yellow line of plot f). The working electrode was a Pt disk, and the scan rate was 0.1 V/s. 99
- Figure 3.14** **a)** Plot of absorbance at 730 nm vs. time, corresponding to decay of the $[\text{Cu}(\text{dmbpy})_2]^{2+}$ species (red dot) and the resulting fit (black line) for the ligand displacement of $[\text{Cu}(\text{dmbpy})_2]^{2+}$ by TBP. The resulted $[\text{Cu}(\text{TBP})_4]^{2+}$ absorbs less under this wavelength. **b)** The resulting observed pseudo-first-order rate constants, k_{obs} , versus the excess concentration of reactant for the reactions between $[\text{Cu}(\text{dmbpy})_2]^{2+}$ and TBP. The measurement was done under room temperature with dry solvent. Efforts were made to get the data under air-free condition by using a dry and air-free solvent to rinse the instrument before measuring. But there should still be residual water and oxygen. 0.1 M of LiOTf was added to maintain the ionic strength for the samples with concentration lower than 0.1 M. 101
- Figure 3.15** EPR spectra of different copper complexes in solution. **a)** Spectra that are fitted and used to generate other spectra. **b)** Steady state spectra of mixing different complexes which are used to calculate K_2 . All samples were prepared in the gloved box with dry acetonitrile. Measurements were done at room temperature. 103
- Figure 3.16** The electrochemical cell configuration used for CV measurement. 110

Figure 3.17	The home-made counter electrode for bulk electrolysis.	111
Figure 3.18	The electrochemical cell configuration used for bulk electrolysis.....	111
Figure 3.19	The method used for transferring stopped-flow air sensitive samples.....	112
Figure 3.20	The stopped-flow raw data. Black are the raw data and red are the fitted curve. Concentrations of TBP and the R^2 of the fitting are shown in each plot.	112
Figure 3.21	Electrochemical behavior of $[\text{Cu}(\text{dmbpy})_2]^+$ in acetonitrile with the presence of TBP. 4 mM $[\text{Cu}(\text{dmbpy})_2]^+$ with the addition of 0, 3, 13 and 25 equivalents of TBP to the copper complex (a to d). The scan rate was 0.1 V/s. Glassy carbon disk was used as a working electrode, and the same peak shape was also observed on a Pt disk electrode.	113
Figure 3.22	CV scans of 1 mM ferrocene (red) and 0.5 M TBP (blue) in acetonitrile on glassy carbon working electrode. Supporting electrolyte was 0.1 M TBAPF ₆ . Scan rate was 0.1 V/s. Black dashed curve is the blank scan.....	114
Figure 3.23	Differential pulse voltammogram of different redox solutions in acetonitrile on glassy carbon working electrode. 0.5 mM ferrocene (black dashed); 1 mM $[\text{Cu}(\text{dmbpy})_2]^+$ and 2.5 mM TBP (red); 1 mM $[\text{Cu}(\text{dmbpy})_2]^+$, 0.1 mM $[\text{Cu}(\text{dmbpy})_2]^{2+}$ and 2.5 mM TBP (green); 1 mM $[\text{Cu}(\text{dmbpy})_2]^+$, 0.1 mM $[\text{Cu}(\text{TBP})_4]^{2+}$ and 2.5 mM TBP (blue dashed).....	114
Figure 3.24	¹ H NMR of dmbpy ligand from 1 mM to 70 mM. 20 mM DCM was used as a standard.	115
Figure 3.25	The absorption spectra of 0.014 mM $[\text{Cu}(\text{dmbpy})_2]^+$ adding 4, 8, 12,16, 20, 24, 28, 32, 36 and 40 equivalents TBP in DCM.	115
Figure 3.26	¹ H NMR spectra of $[\text{Cu}(\text{dmbpy})_2]\text{OTf}$ with the addition of TBP measured under room temperature in CD ₃ CN with dichloromethane as the internal standard. Spectra of 12.5 mM $[\text{Cu}(\text{dmbpy})_2]\text{OTf}$ and different concentrations of TBP (from bottom to top, 12.5 to 320 mM) are shown. The * labeled peaks are from TBP. The green line labeled peaks are from water.....	116
Figure 3.27	¹ H NMR spectra of $[\text{Cu}(\text{TBP})_4]\text{OTf}_2$ with the addition of TBP measured under room temperature in CD ₃ CN. The * labeled peaks are from the internal standard, 20 mM MTBE. Pure TBP spectrum is shown in red. Spectra of 16.7 mM $[\text{Cu}(\text{TBP})_4]\text{OTf}_2$ with different concentrations of TBP (from bottom to top, 0 to 80 mM) are shown in blue.	116
Figure 3.28	The fitted spectra: Spec1, Spec2, Spec3, Mix2, Mix3, Mix4.	117
Figure 4.1	Energy diagram of a DSSC showing the relevant kinetic processes involving $[\text{Cu}(\text{dmbpy})_2]^{2+/+}$ redox couple. In the diagram, dye regeneration by the redox couple,	

electron recombination to the Cu(II) species in the electrolyte, and electron injection to the conduction band of TiO₂ are shown by k_{reg} , k_{rec} , and k_{inj} respectively. 123

- Figure 4.2** Equivalent circuit used to fit the EIS data measured for sandwich cells under dark condition. R_S is the series resistance of the cell. R_T is the charge transport resistance inside TiO₂ nanoporous structure. R_{CT} is the charge transfer resistance between TiO₂ and liquid electrolyte interface. C_μ is the chemical capacitance of TiO₂. R_{Pt} and C_{Pt} are the resistance and capacitance on the counter electrode/electrolyte interface.¹⁶ (Figure 4.8 in the Appendix shows the elements used in Zview software for this equivalent circuit.)..... 127
- Figure 4.3** Plots of J-V curves for DSSCs employing different concentrations of TBP to the electrolyte. Plots are color-coded according to concentrations of TBP in the electrolyte: 0 M (black), 0.1 M (gray), 0.2 M (green), 0.3 M (dark yellow), 0.4 M (orange) and 0.5 M (red). 132
- Figure 4.4** Chemical capacitance measured (C_μ) by EIS of DSSCs applying [Co(bpy)₃]^{3+/2+} electrolyte. Black: 0.2 M [Co(bpy)₃]²⁺ and 0.02 M [Co(bpy)₃]³⁺, 0.1 M LiOTf. Red: 0.2 M [Co(bpy)₃]²⁺ and 0.02 M [Co(bpy)₃]³⁺, 0.1 M LiOTf and 0.5 M TBP. 133
- Figure 4.5** EIS measurement on DSSCs with [Cu(dmbpy)₂]^{2+/+} redox couple. Plots of the charge transfer resistance (R_{CT}) vs the chemical capacitance (C_μ) of DSSCs to show the effect of TBP on recombination kinetics. Plots are color-coded according to concentrations of TBP in the electrolyte: 0 M (black), 0.1 M (gray), 0.2 M (green), 0.3 M (dark yellow), 0.4 M (orange) and 0.5 M (red)..... 134
- Figure 4.6** **a)** Cyclic voltammogram done in a three-electrode cell setup for a TiO₂ nanoporous electrode in contact with electrolyte by 0.1 V/s scan rate. The electrolyte composed of 0.1 M LiOTf in acetonitrile. **b)** Chemical capacitance, C_μ , measured by EIS using the same setup, plotted on the ln scale versus the potential energy. The electrolyte composed of 0.1 M LiOTf, 0.5 M TBP, 0.02 M [Cu(dmbpy)₂]²⁺ in acetonitrile.. 139
- Figure 4.7** Electron lifetime of DSSCs measured in the dark with different amounts of TBP (concentration labeled in the plot). The electrolyte contains 0.2 M [Cu(dmbpy)₂]⁺, 0.02 M [Cu(dmbpy)₂]²⁺, 0.1 M LiOTf and TBP. Arrow a and b indicate two local minimums on the lifetime curve, indicates the different recombination pathways. The applied voltage on the two-electrode DSSCs is converted to the energy of the electrons by applying a correction for the equilibrium potential on the counter electrode use values in Table 4.1. 140
- Figure 4.8** Equivalent circuit in Z-view software. **a)** The circuit built by using the elements provided in Z-view. R is resistance, CPE is constant phase element, DX is a complex module and W is the Warburg element. **b)** The equivalent circuit of DX module used in a). X1, X2, X3 are each a parallel resistor and constant phase element combination. 144
- Figure 4.9** Nyquist plot of a DSSC at a fixed applied potential and the information that can be extracted from it. Each raw data point is collected with a different frequency of the

potential perturbation which follows a sine wave. From high to low frequency region, the main information that can be obtained from the plot are charge transfer on the counter electrode, charge transfer on the anode/electrolyte interface and the diffusion of charge carrier in the electrolyte..... 146

Figure 4.10 Nyquist plots of DSSCs with Y123 dye. Electrolyte contains 0.1 M LiOTf, 0.2 M $[\text{Co}(\text{bpy})_3]^{2+}$, 0.02 M $[\text{Co}(\text{bpy})_3]^{3+}$ and 0 M TBP (no TBP) or 0.5 M TBP (with TBP). The EIS was done in the dark. The plots shown are at the V_{OC} of each cell (-0.5 V for “no TBP” and -0.8 V for “with TBP”). Scattered plots are raw EIS data. Red curves are the fitted curves. 146

Figure 4.11 Nyquist plots of DSSCs with Y123 dye. Electrolyte contains 0.1 M LiOTf, 0.2 M $[\text{Cu}(\text{dmbpy})_2]^+$, 0.02 M $[\text{Cu}(\text{dmbpy})_2]^{2+}$ and different concentrations of TBP. The EIS was done in the dark. The plots shown are at the V_{OC} of each cell. Scattered plots are raw EIS data. Blue curves are the fitted curves..... 149

Figure 5.1 Equivalent circuit to fit the impedance data of the symmetric cells a) with only one semicircle and b) with two semicircles. R_s is the series resistance. R_{CT} is the charge transfer resistance of reduction of Cu(II) species on the PEDOT electrode. Z_w is the Warburg impedance. The constant phase element (CPE) represents the chemical capacitance of the electron transfer reaction on the PEDOT electrode. Since the PEDOT is a rough surface, the capacitance is not an ideal model, CPE has the correction factor to account for the imperfection..... 164

Figure 5.2 a) to e) Absorption spectra corresponding to the titration of 4 mM $[\text{Cu}(\text{dmbpy})_2]^{2+}$ with aliquots of different bases in acetonitrile. The experiment was done under an inert atmosphere. 166

Figure 5.3 Absorption spectra of 0.3 mM $[\text{Cu}(\text{dmbpy})_2]^+$ in acetonitrile with DMAP. From top to bottom, the added amount of DMAP is 0 to 8 equivalents. 169

Figure 5.4 Titration results obtained by NMR. The ratio between the detected free dmbpy ligand and the total Cu^{2+} species is plotted versus the aliquots of bases in the solution. The concentration of dmbpy was determined based on the integration of aromatic proton peaks. A controlled amount of DCM was added as an internal standard for the quantitative calculation. The curve for TBP has been shown in Chapter 3, and here it's shown for comparison. 170

Figure 5.5 Cyclic voltammetry scans of $[\text{Cu}(\text{dmbpy})_2]^+$ (d and e) and $[\text{Cu}(\text{dmbpy})_2]^{2+}$ (a-c and f) in acetonitrile with different amount of bases added. The initial scan without any base is shaded purple for $[\text{Cu}(\text{dmbpy})_2]^+$, and gray for $[\text{Cu}(\text{dmbpy})_2]^{2+}$. The shade is to help observe the changes in the shape..... 172

Figure 5.6 CV curves of symmetrical cells with PEDOT electrodes. Different bases are added to the electrolyte. Other than the basic additive, the electrolyte contains: 0.1 M LiOTf, 0.2 M $[\text{Cu}(\text{dmbpy})_2]^+$ 0.04 M $[\text{Cu}(\text{dmbpy})_2]^{2+}$ in acetonitrile. Measurement was done in the dark. The scan rate was 0.01 V/s..... 174

Figure 5.7	<i>JV</i> plots and R_{CT} vs. C_{μ} plots for DSSCs with different bases. <i>JV</i> curves were measured under 1 sun condition. R_{CT} and C_{μ} were obtained from EIS data measured in the dark.	178
Figure 5.8	Nyquist plots of symmetrical cells with PEDOT electrodes, measured at 0 V applied potential. Electrolyte contains 0.1 M LiOTf, 0.2 M $[\text{Cu}(\text{dmbpy})_2]^+$, 0.04 M $[\text{Cu}(\text{dmbpy})_2]^{2+}$ and different concentrations of base additives. a) cells with no base. b) cells with TBP. c) cells with Im. d) cells with MBIm. e/f) cells with DMAP. The EIS was done in the dark. Scattered plots are raw EIS data. Red/black lines are the fitted curves.	181
Figure 5.9	Nyquist plots of DSSCs with Y123 dye. Electrolyte contains 0.1 M LiOTf, 0.2 M $[\text{Cu}(\text{dmbpy})_2]^+$, 0.04 M $[\text{Cu}(\text{dmbpy})_2]^{2+}$ and different concentrations of base additives. a) DSSCs with TBP. b) DSSCs with Im. c) DSSCs with MBIm. d) DSSCs with DMAP. The EIS was done in the dark. The plots shown are at the V_{OC} of each cell. Scattered plots are raw EIS data. Red/black lines are the fitted curves.....	183
Figure 6.1	The CV curve of 4 mM $[\text{Cu}(\text{dmbpy})_2\text{Cl}]^+$ on glassy carbon measured in acetonitrile. The scan rate was 0.1 V/s.....	196
Figure 6.2	The picture of solid electrolyte under microscope.	201
Figure 6.3	Crystal structure of blue crystal.	201
Figure 6.4	Crystal structure of $\text{Cu}(\text{DMAP})_2\text{OTf}_2$	202
Figure 6.5	Crystal structure of $\text{Cu}(\text{tmbpy})_2\text{TFSI}_2$	203

LIST OF SCHEMES

Scheme 2.1 The synthetic route for 6,6'-dimethyl-2,2'-bipyridine-4,4'-dicarboxylic acid. 39

KEY TO ABBREVIATIONS

$^1\text{H NMR}$	Proton Nuclear Magnetic Resonance
<i>Abs / A</i>	Absorption
AcN	Acetonitrile
<i>APCE</i>	Absorbed Photon-to-Current conversion Efficiency
bpy	2,2-bipyridine
<i>C</i>	Capacitance
CB	Conduction Band
CD_3CN	Deuterated acetonitrile
CE	Counter Electrode
CT	Current Transient
CV	Cyclic Voltammetry
<i>d</i>	Length
<i>D</i>	Diffusion coefficient
D35cpdt	3-{6-{4-[bis(2',4'-dibutyloxybiphenyl-4-yl)amino-]phenyl}-4,4-dihexyl-cyclopenta-[2,1-b:3,4-b']dithiophene-2-yl}-2-cyanoacrylic acid
DCM	Dichloromethane
DMAP	4-(Dimethylamino)pyridine
DSSC	Dye-Sensitized Solar Cell
dmbpy	6,6'-dimethyl-2,2'-bipyridine
dmp	2,9-dimethyl-1,10-phenanthroline
DPV	Differential Pulse Voltammetry
dsbtmp	2,9-disec-butyl-3,4,7,8-tetramethyl-1,10-phenanthroline

dye^*	Excited state dye
dye^+	Oxidized dye
$E_{1/2}$	Half-wave Potential
E_F	Fermi Level
EIS	Electrochemical Impedance Spectroscopy
EPR	Electron Paramagnetic Resonance
eq	Equivalent
$Fc^{+/0}$	Ferrocenium/Ferrocene
FF	Fill Factor
FTO	Fluorine doped Tin Oxide
GS and ES	Ground State and Excited State
I	Ionic strength / Current
Im	Imidazole
IPA	Isopropyl Alcohol
$IPCE$	Incident Photon-to-Current conversion Efficiency
ITO	Indium Tin Oxide
J_{SC}	Short Circuit current density
K	Equilibrium constant
k	Rate constant
LHE	Light Harvesting Efficiency
MBIm	1-Methylbenzimidazole
MeIm	1-Methylimidazole
MLCT	Metal-to-Ligand Charge Transfer

MTBE	Methyl tert-butyl ether
N3	Cis-bis(isothiocyanato)bis(2,2'-bipyridyl-4,4'-dicarboxylato) ruthenium(II)
OCVD	Open Circuit Voltage Decay
OTf ⁻ / triflate	Trifluoromethanesulfonate
<i>Ox</i>	Oxidant in the electrolyte
PEDOT	Poly(3,4-ethylenedioxythiophene)
ppm	Part Per Million
py	Pyridine
<i>R</i>	Resistance
RE	Reference Electrode
<i>Red</i>	Reductant in the electrolyte
<i>T%</i> and <i>R%</i>	Percent Transmittance and percent Reflectance
TBAPF ₆	Tetrabutylammonium hexafluorophosphate
TBP	4-tert-butylpyridine
TCO	Transparent Conducting Oxide
TFMP	4-(Trifluoromethyl)pyridine
TFSI ⁻	Bis(trifluoromethane)sulfonimide
THF	Tetrahydrofuran
tmbpy	4,4',6,6'-tetramethyl-2,2'-bipyridine
UV	Ultraviolet
Vis	Visible
<i>V</i> _{oc}	Open Circuit Voltage
WE	Working Electrode

Y123	3-{6-{4-[bis(2',4'-dihexyloxybiphenyl-4-yl)amino-]phenyl}-4,4-dihexyl-cyclopenta-[2,1-b:3,4-b']dithiophene-2-yl}-2-cyanoacrylic acid
Z	Impedance
α	Absorption coefficient
ΔG	Free energy change
ε	Extinction coefficient
η	Efficiency
λ	Wavelength, Reorganization energy
σ	Absorption cross section

Chapter 1. Introduction

1.1 Motivations in solar energy

Energy is the fundamental of modern society. Energy consumption worldwide had a growth of 2.3% in the year 2018, and it reached nearly twice the average growth rate since the year of 2010. The annual change in solar global energy demand in 2018 was 328 Mtoe.¹ This fast pace growth is required by the robust global economy and is also driven by the demand in the cooling or heating in some parts of the world. The demand for all types of fuel sources has increased. The biggest gain was from the “fuel of choice” in 2018, natural gas, which accounted for 45% of the increase of the total energy demand and the fossil fuels meets nearly 70% of the growth.¹ From a chemistry perspective, any combustion reaction of the carbon hydride will produce carbon dioxide. As a result of the higher energy demand, and the fact that fossil fuels are still the leading energy sources, the global energy-related carbon dioxide emission (from fuel combustion, which is >80% of the CO₂ emission) increased by 1.7% to a historically high 33.1 Gt and had set a new record for the growing pace since 2013.¹ Although renewable and nuclear energy account for 32% of the increased energy demand and the change of the energy structure has made the emissions growing 25% slower than the energy demand, the low-carbon options are still not scaling fast enough to meet the rise in demand. The pre-industrial level of CO₂ concentration in the atmosphere is reported to be 180 to 280 ppm. However, as of 2018, the number is as high as 407.4 ppm, which is 2.4 ppm higher than in 2017, and it is predicted to keep increasing.² The impact of fossil fuel consumption on the global temperature increase is evaluated by the International Energy Agency (IEA) this year.³ Coal is shown to be the single largest source of the global temperature increase by the evaluation, and it should be responsible for over 0.3°C increase in the global average annual surface temperature comparing the pre-industrial levels, with the total increase of the surface

temperature being 1°C.³ It has been noticed from the statistical analyses that CO₂ emission rate needs to be reduced so that we are not boosting the global CO₂ level which causes the increasingly severe global warming.

On the other hand, the use of carbon-free energy sources is the strategy to reduce the CO₂ emission rate and generate cleaner power. Scientists and policymakers are working together on changing world energy structures. According to the data from 2018, the use of solar and wind power grew at a double-digit pace, and solar energy alone increased by 31%.⁴ Although that was not fast enough to meet higher electricity demand around the world, which also drove up coal use, a significant energy transition is underway.

Many factors contribute and will change the shape of the global energy future. The recent Paris Agreement on climate change is one example of how the government is trying on their perspective to regulate and reduce the emission of greenhouse gas.⁵ All parties are required to put forward their best effort through nationally determined contributions, and the whole purpose is to set the world on a course towards sustainable development.⁶ Another aspect is to develop a more efficient and variety of ways to use renewable energy. Solar energy is a very accessible and abundant type of renewable energy source. The amount of solar energy from sunlight striking on the surface of the earth each day is many times greater than the total energy demand on the earth each day. If we can use 4% of the world's desert areas to collect the sunlight and convert it into electricity, the electrical power it generates could supply the equivalent of all the world's electricity use.⁷ The energy of the sunlight from the sun is carried and transported to the earth in the form of photons. Photovoltaic (PV) devices can be treated as the bridge connecting between the intangible sunlight and the electricity that people can use. PVs generate electricity directly from sunlight by photon capturing, chemical and electronic processes to transfer the energy to electrons. The movement

(flow) of electrons generated, what we call current, will further power machines that can be used in people's daily activities. The PV installations are seen world widely nowadays and the global PV market has been continuously increased. The most recent forecast, according to global business information provider IHS Markit, predicts a 25% growth of the market in 2019. This growth will result in reaching 129 gigawatts of solar installations worldwide.⁸ The PV devices exceeded 2% share of the global total electricity generation and remained to be the fourth among all the renewable energy sources for electricity generation. So far, the development of PV is still on track to meet the requirement of the Sustainable Development Scenario (SDS), which requires an average of 16% annual growth from 2018 to 2030.⁹ Based on the current situation, it is reasonable to expect a robust PV growth with the help of the greater cost-competitiveness and continuous policy support.

From a chemist perspective, developing cost-competitive PV devices and exploring various ways of solar energy capturing has been the emergence in the field of renewable energy research. Under this historical circumstance, the Dye-Sensitized Solar Cell (DSSCs) came into play as a type of new generation of the thin-film solar cell, which utilizes low-cost semiconductor materials and constructs systems, which can be of various color and to be used in different environments.

1.2 Historical development of DSSCs

1.2.1 Photoelectrochemistry and dye sensitization

The achievement of functioning DSSCs is mainly dependent on the development of the theory of photoelectrochemistry, of which field the studies concern about the interaction between light and electrochemical systems. Photoelectrochemistry was first discovered by Becquerel in 1839 and were intensively studied when people realized that fossil fuels are non-renewable and it is necessary to develop ways to use clean energy sources, such as solar energy. Artificial

photosynthesis, electrochemistry water splitting and solar to electricity conversion are all means of solar energy utilization base such theory.¹⁰ Semiconductors are materials that have bandgaps that can absorb photons that are suitable in energy. At the same time, they can generate a hole and electron pair which can be separated in the semiconductor and doing redox reaction on different surfaces. Adopting this idea and inspired by Vogel's discovery in 1873 of dye sensitization that dye molecules had on the silver halide emulsions, the first photosensitization effect was discovered in 1887 by Morse when he painted the red dye on the silver halide electrode. Later the electron injection behavior of the excited dye molecule on large bandgap semiconductor was explained by Gerischer in 1968¹¹. The sensitization effect was examined, and photocurrent was observed at different semiconductor surfaces with organic dye molecules using electrochemical methods.

1.2.2 Conversion of solar energy into electricity

After the recognition that photocurrent can be achieved when exposing some materials under sunlight, researchers have been working on solar energy to electricity conversion. Such systems were designed to capture solar energy through electron transfer processes. Photogalvanic cells were proposed firstly by Rabinowich in 1940.^{12, 13} In the study, the light was used to drive the redox reaction in the electrolyte solution, a thionine-iron system, and further generate a potential difference on the electrodes that have contact with the electrolyte. Since the electrodes used in early photogalvanic cells were metals, they were fully conductive and would not direct the electron flow to the desired external circuit. Also, due to the bulk property of the dye solution, most of the captured photons were not used to promote redox reduction before self-quenched by other ground state dye molecules.

The photovoltaic cells utilize semiconductor electrodes, and some have a thin layer of the liquid to form a junction with the solid electrodes. Dye-sensitized solar cell belongs to the families of

photovoltaic cells. According to Green, photovoltaic cells can be grouped into different categories, based on the cost of the materials and the power conversion efficiencies.¹⁴ The first-generation photovoltaic cells apply the highest purity of materials (such as single crystal silicon wafer) with the least concentration of the defects. The second-generation photovoltaic cells occurred under the background of the development of modern thin-film preparation techniques and it lowers the cost during the material preparation and device fabrication. But due to the high concentration of the defects, their maximum power conversion efficiency is low. Up till now, the first-generation photovoltaic cells are among the most efficient PV devices on the market.¹⁵ But their highest power conversion efficiency is intrinsically limited by the Shockley and Queisser limit (SQ limit) of around 30%.¹⁶ On the contrary, the third-generation photovoltaic cells are potentially not limited by the SQ limit. The idea is to use multijunction of materials to achieve the ultra-high conversion efficiency at low cost.¹⁷ By the end of 2018, the confirmed efficiency of terrestrial cells under AM1.5 at 25°C is 29.1% (GaAs¹⁸) for the single-junction cells and 38.8% (5 junction cell¹⁹) for the multi-junction cells.

1.2.3 The development of Dye-Sensitized Solar Cells.

Although DSSCs are not among the most efficient PV cells at present, their structure of liquid electrolyte-semiconductor electrode junction promoted a tremendous amount of research done in the related field. Such researches include the work done by Dung, that the interfacial electron-transfer was observed by using aqueous colloidal suspensions of TiO₂ particles to make contact with redox reagents in the liquid electrolyte.²⁰ After a better understanding was developed, the theory of interfacial electron transfer in non-aqueous solution was widely extended into the study of DSSCs²¹. Dye sensitization of bulk semiconductor electrodes promoted the development of DSSCs from another perspective. Tributsch did some pioneer works in the area.²² In his study,

large band gap inorganic semiconductor, like zinc oxide (3.2 eV), could capture the electrons from the excited dye molecules, like chlorophyll, in the electrolyte. This system showed similar behavior of chlorophyll in the photosynthetic reaction centers and was able to convert electronic excitation to electric energy.

Earlier attempts of dye-sensitized photoelectrochemical cells were performed by using flat semiconductor electrodes.^{23, 24, 25} Although the system generated low photocurrent, people realized the main problem was the low light harvest efficiency which was limited by utilizing the monolayer dye as photon absorber on the flat electrode surface. To enhance the light absorption, the light absorption property needed to be improved. The following studies also concluded that the insufficient sensitization could be attributed to the reduction reaction of electron transfer from semiconductor to the oxidized dye molecules.²⁶

In 1985, Desilvestro presented results on efficient sensitization of high surface colloidal anatase particles and polycrystalline electrodes with tris(2,2'-bipyridyl-4,4-dicarboxylate) ruthenium (II) dichloride.²⁷ And the significant improvement of the power conversion efficiency of DSSCs was reported in 1991 by O'Regan and Grätzel²⁸ using mesoporous semiconductor electrode. This new type of thin-film solar cell has drawn researchers' attention ever since.

The standard structure of DSSCs is adopted from what was reported in 1991. The photoanode of the cell contains high-molar extinction photosensitizer adsorbed on the high-surface-area nanoporous semiconductor film. Redox couples are dissolved in the liquid electrolyte, which acts as the electronic bridge between anode and cathode. The counter electrode is a catalytic thin film which can facilitate the regeneration of the redox species.

1.3 Different components in DSSCs

The complexity of the operating system of DSSCs provides a wide choice for different components. Many wide bandgap semiconductors have been examined and TiO_2 turned out to be the most versatile. Different redox couples have been tested, and the iodide/triiodide couple is among the best. The family of transition metal outersphere complexes provides a vast library for the choice of redox couples. There are also numerous studies on dye molecules and counter electrode materials. In this thesis, discussions about sensitizers and redox couples will be focused.

1.3.1 Sensitizers in DSSCs

The sensitizers of DSSCs are dye molecules that can sensitize the large-bandgap semiconductors and absorb photons with sub-bandgap energies. In order to maximize the use of the photons in the sunlight, dyes with the absorption in the visible and near IR region of the solar spectrum are preferred. The solar spectrum is shown in Figure 1.1.²⁹ In addition, the dye molecules must have functional groups to be attached to the semiconductor surface. Carboxylate or phosphonate groups are the most employed ones. On the energetic perspective, the excited state energy level of the dye molecules must be well-matched but still more negative than the conduction band of the semiconductor, to minimize the energy loss and ensure efficient electron injection. And the redox potential of the dye molecules in their ground state must be sufficiently positive to be regenerated through reduction by the reductant in the electrolyte. Therefore, the gap between the ground state and the excited state of the dye molecules should be small enough to absorb a considerable portion of the solar spectrum, and meanwhile, be large enough to maximize the potential output of the solar cell.

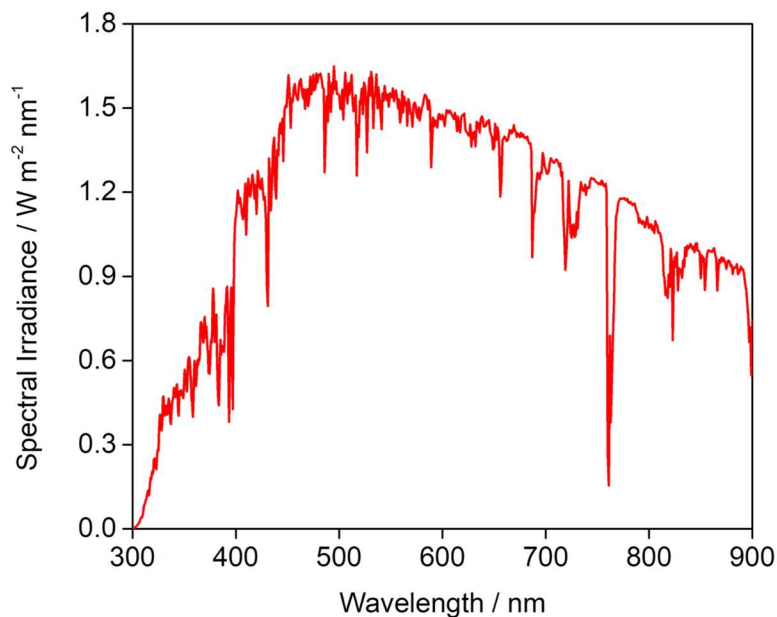


Figure 1.1 AM 1.5 Solar spectrum (the ASTM G173 spectra) represents the terrestrial solar spectral irradiance on a surface of specified orientation under a set of the specified atmospheric condition.

On the kinetic perspective, due to the chance of electron recombination between the electrons injected into the conduction band of the semiconductor and the oxidized dye molecules in their ground state, it is required that the oxidized dye molecules be efficiently regenerated in a shorter time scale compared to the recombination reaction. Besides the above, relative photo- and thermal-stabilities are also required to achieve long term application.

Given these requirements, inorganic metal complexes have been studied widely as promising candidates for sensitizers in DSSCs. Ru(II) polypyridyl complexes are the most well studied and the champion sensitizers in the early stage of the DSSC research. For ruthenium(II) complexes, the metal center has six electrons in the d-orbitals in the ground state. The light absorption of the ruthenium coordination complexes normally promotes the electron transfer from their metal-centered d-orbital to an empty π^* orbital of the ligand.^{30, 31} The metal-to-ligand charge transfer (MLCT) band of ruthenium(II) complexes provides them with the opportunity to sensitize large-

bandgap semiconductors. They have the extinction coefficients on the order of $10^4 \text{ M}^{-1}\text{cm}^{-1}$. Although they are less absorptive than organic dyes (over $10^5 \text{ M}^{-1}\text{cm}^{-1}$), by using a thicker semiconductor nanocrystalline film (6-10 μm) to adsorb more dye molecules, the shortcomings in the light-harvesting can be compensated. Compared to organic dyes the advantage of using inorganic metal complexes is their better photophysical and electrochemical tunability. By ligand design, their ground state redox potential, absorption property and the MLCT band energetics can all be tuned. The energy level of the excited state of ruthenium dye ($E_{(\text{Ru}^{\text{III}*})}^\circ$) is calculated by the Equation 1.1:

$$E_{(\text{Ru}^{\text{III}*})}^\circ = E_{(\text{Ru}^{\text{III}})}^\circ - \Delta G_{\text{ES}} \quad (1.1)$$

In Equation 1.1, $E_{(\text{Ru}^{\text{III}})}^\circ$ is the redox potential of ruthenium dye. ΔG_{ES} is the energy gap between dye ground state and excited state, which is equal to the energy of the zero-zero transition. Besides all the advantages, the biggest drawback of using ruthenium dyes is the low abundance of the metal. Although ruthenium has been widely used in the electrochemical industry, it is very scarce in earth crust. It is mined each year and the world-reserve is estimated to be only 5,000 tons.³² The demand for ruthenium metal in industry in 2018 is around 33.6 tons which the demand can be well supplied with the producer.³³ But unlike the catalytic materials that can be well recycled, using ruthenium metal as precursors for sensitizers may force the demand to the bottleneck if we are looking for the development of a big market of DSSCs. A rough calculation for DSSCs using N3 dye (ruthenium(II) cis-Bis(isothiocyanato)bis(2,2'-bipyridyl-4,4'-dicarboxylato)) can be made: with the normal dye coverage on the photoanode being 10^{-7} mol/cm^2 and assuming they have 10% solar to electricity conversion efficiency, the usage of the ruthenium metal would be about 1 mg per watt under AM 1.5. On a larger scale, it is 1000 tons per TW. The world energy demand in 2018

was 166320 TWh (18.99 TW in power) and will increase. So, we need to search for alternative metal to carry on this energy conversion task. Because of the aforementioned abundance issue, copper-centered complexes have recently been considered a promising alternative. Copper is 10^4 times more abundant than ruthenium.³² In the late 1970s, McMillin and coworkers studied the photoinduced redox properties of copper(I) bisphenanthroline, $\text{Cu}(\text{phen})_2^+$, in solution.³⁴ By doing a quench study with cobalt (III) cis-bis(iminodiacetato), $\text{cis-Co}(\text{IDA})^-$, they found that the electrons promoted onto the MLCT band of $\text{Cu}(\text{phen})_2^+$ could reduce $\text{cis-Co}(\text{IDA})^-$. This observation was very similar to the mechanistic schemes that had been developed for the ruthenium(II) tris-(2,2'-bipyridine) complex. The ground state reduction potentials of $\text{Cu}(\text{phen})_2^+$ and $\text{cis-Co}(\text{IDA})^-$ were measured to be 0.63 V and 0.40 V vs SHE respectively. And the reduction of Co(III) indicated that the excited state of $\text{Cu}(\text{phen})_2^+$ was more reductive in nature and the photoinduced redox behavior was proved to exist for such complex.³⁵ The photoluminescence of such copper(I) complexes were also looked at in McMillin's later work, and the nature of the emissive state was claimed to be the excited MLCT state.³⁶

All these features, such as the high extinction coefficient of the MLCT band and the proper redox potential of both the ground state and excited state, opened ways for using copper(I) complexes to convert photon energy to other types of energies. On the other hand, an interesting feature inherent to copper coordinated complexes is the structural difference between copper(I) and copper(II) centered complexes. The d^{10} copper(I) prefers 4-coordinate tetrahedral geometry, while d^9 copper(II) prefers penta- or hexa-coordination due to the Jahn-Teller distortion. The consequences of such distortion between copper(I) and copper(II) should be considered in two aspects, thermodynamic and kinetic. The thermodynamic consequences of the distortion within the inner-coordination sphere of copper(II) have been examined by Patterson and Sakaguchi.^{37,38} In their

works, they have confirmed that by using ligand that sterically destabilizes copper(II) or stabilizes copper(I), the redox potential of $\text{Cu}^{2+/+}$ can be tuned to more positive. The most commonly used ligands are 6,6'-dimethyl bipyridine or 2,9-dimethyl phenanthroline, and their derivatives, to make the reduction potential of copper(I) complex in a reasonable range to be used as a photosensitizer. Therefore, the thermodynamic consequence of the distortion paves the way to tune the formal potential of copper(I) sensitizers easily. While the kinetic consequence of the structure distortion, however, introduces problems to some extent. According to the Marcus theory of electron transfer, rapid electron transfer is promoted by rigidity in the inner-coordination sphere in the way of lowering the reorganization energy between the reactant and product. The structural distortion between copper(I) and copper(II) complexes makes the electron transfer rates between those species lower than that of the rigid ruthenium(II/III) complexes. On the photophysical standpoint, blocking pathways for fast relaxation of excited-state electrons to ground state is one requirement of sensitizers for large bandgap semiconductors. Under photoexcitation, copper center in the complex is Cu^{2+} in nature. The distortion therefore can induce a D_{2d} (nearly tetrahedral) to D_2 (flattened tetrahedral) symmetry change upon photoexcitation of the complexes, due to the increase of the oxidation state of copper center. Any Lewis basic species (i.e. counterions and solvent molecules) will have access to the newly opened 5th coordination site and lower the energy of the excited state. The mechanism of this process was recognized as "exciplex quenching" by McMillin.³⁹ This quenching is responsible for the decrease of the excited state lifetime of copper(I) complexes, and the extent of quenching depends on the nucleophilicity of the incoming ligand.

The functional groups on the 6, 6'- positions of bipyridines and 2, 9- positions of phenanthrolines can be used to hinder the exciplex quenching pathways.

1.3.2 DSSCs using copper(I) complexes as sensitizers

The first report of copper(I) complex acting as a photosensitizer was published in 1994.⁴⁰ The ligand had a 2,9-substitution on the phenanthroline ligand by two phenyl groups (Figure 1.2a). On the para position of the phenyl group, bulky alkyl groups used to increase the rigidity of the structure. The structural distortion of the sensitizer upon photoexcitation and oxidation was therefore hampered. COO⁻ functional groups were used to attach the complex to the TiO₂ surface. Although the photocurrent density of the constructed cell was only 0.6 mAcm⁻² with triiodide/iodide containing propylene carbonate electrolyte, the photovoltage achieved was close to the difference between the Fermi level of the semiconductor and the redox potential of the electron donor. This study was also the first example of using copper(I) sensitizer in regenerative photoelectrochemical solar cells. In 2002, a tetramethyl substituted bipyridine copper(I) dye (Figure 1.2d) with carboxylic functional groups was used as dyes in a similar system.⁴¹ The electrolyte was triiodide/iodide containing propylene carbonate and acetonitrile mixture (11:1, v/v). 4-*tert*-butylpyridine (TBP) was used and for the first time they reveal that the addition of 1 M TBP improved both the photocurrent (1.98 mAcm⁻² to 2.9 mAcm⁻²) and the photovoltage (430 mV to 640 mV). The reason for the improvement by adding TBP was associated with the effect TBP might have on blocking the electron recombination to copper(II) centers.

In 2008, Bessho et al. reported DSSCs using bipyridyl ligand coordinated copper(I) complexes as dyes (Figure 1.2b and c).⁴² The device employed triiodide/iodide redox couple in valeronitrile and acetonitrile mixture (15:85, v/v). 0.5 M TBP was added in the electrolyte to compare the performance with the benchmark ruthenium dye cell system with N719 dye. And the photocurrent

was improved to 5.9 mAcm^{-2} by the dye with the extended conjugation. The reason for the better performance from the dye with the extended conjugation was attributed to the red-shifted absorption spectrum and higher extinction coefficient of the dye. And after these successful examples of utilizing copper(I) sensitizers in DSSCs, researchers started to recognize the potential of replacing ruthenium complexes with the much cheaper copper complexes.⁴³

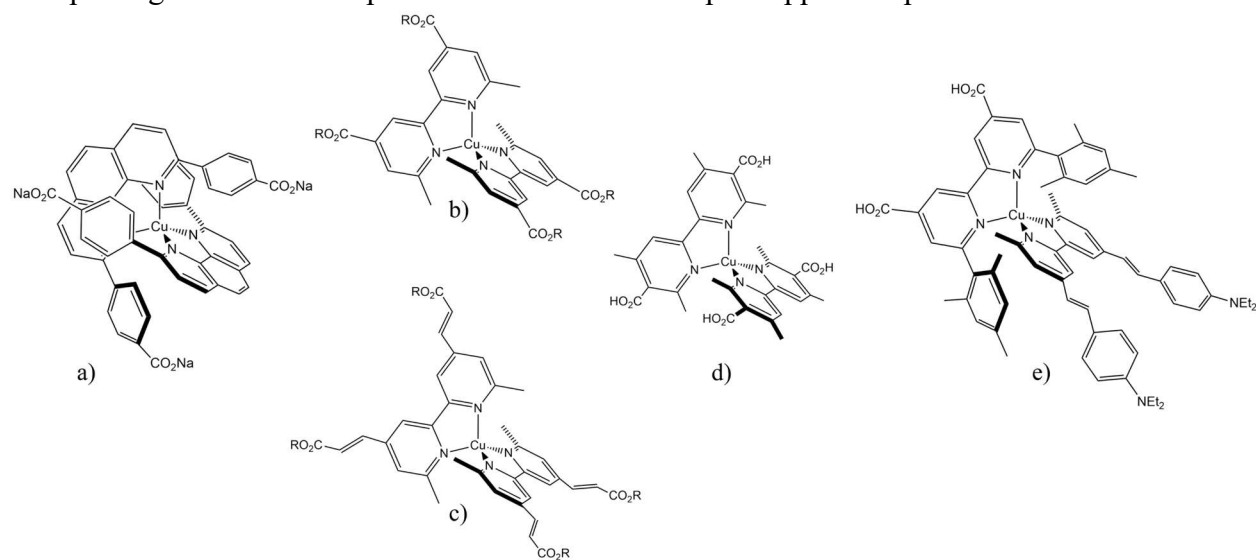


Figure 1.2 Different designs of copper dyes used in DSSCs. Details are described in the content. a. ref 40; b. and c. ref 42; d. ref 41; e. ref 54. All copper centers are Cu^+ .

In order to further increase the overall efficiency, different strategies were proposed by different research groups. Increasing the absorptivity of the sensitizer was a straightforward way to increase the photon to current conversion efficiency of the cells. Manipulation of the ligands was the most studied as this may tune the light-harvesting properties of the dye molecules the most.^{44, 45, 46, 47, 48, 49, 50, 51, 52, 53, 54, 55} The best efficiency so far is reported to be 4.66%, achieved by Sandroni et al. in 2014 using a heteroleptic copper sensitizer with a light-harvesting efficiency (*LHE*) near unity at 550 nm and bluer.⁵⁴ The sensitizer they used had an anchoring ligand to form interactions with TiO_2 film and an ancillary ligand to maintain desired photophysical and redox properties (Figure 1.2e). In this specific copper complex, the anchoring ligand was a 4,4'-dicarboxylic acid-6,6'-dimesityl-2,2'-bipyridine and the ancillary ligand was 4,4'-bis(N,N diethylaminestyryl)-6,6'

dimethyl-2,2'-bipyridine. This exciting improvement showed some potential to replace ruthenium sensitizers by copper sensitizers.

Despite the improvement in the overall efficiency, copper(I) sensitizers are still unable to compete with ruthenium(II) sensitizers based device which achieved over 11%. From literature published so far, there are intense studies about how to improve the light harvesting efficiency (*LHE*) of the dyes but not much analysis on the property of electron transfer processes on the copper-based dye cells. Therefore, there are minimal understandings about why cells with copper dyes are incapable of achieving comparable efficiencies as with ruthenium dyes, even though they already have the competitive *LHE* over the visible spectrum. At first glance, an apparent reason would be that the conditions for ruthenium-based devices have been optimized, as opposed to those with copper dyes (triiodide/iodide as the redox couple, acetonitrile as the solvent and TBP as the additive). The iodide/triiodide couple especially may not be a good match in the case of applying copper dyes, since halogen can easily bind with the copper(II) center and may therefore quench the excited state by forming an exciplex. The halogen ion can even bridge the electron recombination from the conduction band to the oxidized dye molecules. There are studies when people tested different electrolyte conditions and trying to improve the efficiencies for copper dye-sensitized solar cells.^{56,}

⁵¹ The best functioning electrolyte is still triiodide/iodide based solution with TBP, even though based on the knowledge about the liability of copper coordination complex, both the redox couple and the additive should not be the ideal ones. However, there is not yet a systematic study to

determine which process in an operating copper sensitizer based solar cell limits the efficiency the most.

1.3.3 Redox couples in DSSCs

DSSCs belong to the family of regenerative solar cells. One of the critical components in DSSCs to help maintain the regeneration ability is the redox couple. Most DSSCs so far have liquid electrolyte, in which both the reduced and oxidized form of the redox couple dissolve to preserve the conductivity between the photoanode and the counter electrode. The reduced form of the redox couple should have relative negative reduction potential than the dyes in their ground state. After injecting an electron to the semiconductor, the dye molecule will be oxidized. The reduced species of the redox couple acts like an electron donor, and it regenerates the oxidized dye to set it ready for the next incoming photon. So, the rate of regeneration process of the dye by the electron donor is essential, and it highly limits amplitude of the photocurrent. After the electron donor gives off one of its electrons, it becomes the oxidized form of the redox couple. The concentration of the oxidized form of the redox couple is higher close to photoanode, where the dye regeneration process happens. By diffusion in the liquid electrolyte, the oxidized species will move to the counter electrode and being reduced there, by accepting the electron from a catalyst surface. Just like the importance of the rate of the dye regeneration, the rate of the electron transfer on the counter electrode is as critical and controls the electron flux throughout the solar cell.

Besides the kinetic consideration, the redox potential of each component in DSSCs also determines the photovoltage output. The open-circuit voltage (V_{OC}) is the difference between the energy level of the photoanode and the counter electrode of the cell. The energy level of the anode can be defined by the Fermi level of TiO_2 (E_F), and the redox potential of the redox couple in the electrolyte controls the energy level of the counter electrode. The upper limit of the energy level

on the photoanode can be changed by dye molecules and the semiconductor materials. On the other hand, the lower limit of the energy level on the counter electrode can be changed with different redox couples. By using different redox couples, $E_{1/2, \text{redox}}$ can vary in a large range and V_{OC} can be tuned.

Different redox couple can also influence the effective Fermi level of TiO_2 (E_F) that determines the energetics of the electrons on the conduction band of the photoanode.

$$E_F = E_C - \frac{k_B T}{e} \ln \frac{n_C}{N_C} \quad (\text{V}) \quad (1.2)$$

In Equation 1.2, k_B is the Boltzmann constant in JK^{-1} and T is temperature in K; e is 1.602×10^{-19} C which is the elementary charge. n_C is the density of conduction band electrons, and N_C is the effective density of states in the conduction band. N_C is on the order of 10^{20} cm^{-3} for TiO_2 anatase at room temperature.⁵⁷ E_F is about 0.1 V more positive than E_C at 1 sun, and the value of E_F depends on n_C , and thus depends on both the flux of the injection electrons from the dye to the semiconductor and the rate of the electron recombination.⁵⁸ Methods are developed to modify the surface of the semiconductor to change the E_C . Additives like TBP is thought to adsorb on the TiO_2 surface and move the E_C to more negative.⁵⁹ The change on the V_{OC} that different anode materials can introduce is less than the influence from using different electrolyte components, especially by using different redox couples with different redox potentials and different electron transfer abilities.

On the counter electrode, the equilibrium potential of the liquid electrolyte on the counter electrode defines the energy level of the cathode. A redox couple with more positive redox potential gives rise to the V_{OC} of the cell. The positive limit of electronic energy is the ground state of the dye. In

order to have a fast electron transfer in the dye regeneration process, some driving force for electron transfer is required, and that part of the energy will be lost. At the same time, the existence of the electron acceptor (oxidized form of the redox couple) in the electrolyte in a more positive potential than the E_F , will also open the way for electron recombination from the conduction band. Due to Marcus theory, the rate of the electron transfer is faster with a larger driving force when the reaction happens in the Marcus normal region. Redox couples with fast electron transfer ability and more positive potential usually suffer from the electron recombination and thus lowers the generated electron flux under equilibrium. Therefore, manipulating the redox property of the redox couple is critical in improving the performance of the solar cell.

Original works of DSSCs focus on the use of triiodide/iodide redox couple, which is shown to have very satisfactory electron transfer kinetics and can assist in achieving high photocurrent output of the cells. Boschloo has studied the mechanism of the triiodide/iodide redox couple.⁶⁰ The electron-donating species, iodide ion, regenerates the dye molecule and produces the diiodide radical. The radical undergoes fast disproportionation to form triiodide and iodide. The reduction potential of triiodide is more positive therefore the electron recombination from the conduction band has been eliminated to some extent. This property of triiodide/iodide redox couple helps to maintain a high current output of the cell at the cost of a large energy loss. The electron transfer processes of triiodide/iodide redox couple are hard to understand because there are multiple electrons involved in the process and the evidence of each intermediate is hard to collect. Other redox couples are studied as well, in order to minimize the energy loss and help improve the V_{OC} while still maintaining the large J_{SC} . Transition metal redox couples undergo outersphere electron transfer therefore have simpler mechanisms compare to iodide/triiodide redox couple. Especially cobalt(III/II) redox couples which have been studied for years. Cobalt(III/II) tri(2,2'-bipyridine)

couple ($\text{Co}(\text{bpy})_3^{3+/2+}$) are the most widely used. Their reduction potential is 0.56 V vs. NHE in acetonitrile and the best-performing cells with $\text{Co}(\text{bpy})_3^{3+/2+}$ couple have V_{OC} around 0.9 V which is reaching the limit of the energy difference between the E_{CB} of TiO_2 and the redox potential of the redox couple.⁶¹ Cobalt complexes have a low self-exchange rate constants compared to iron or ruthenium complexes, due to the change of cobalt's spin state during redox reaction. Therefore, the dye regeneration by cobalt complexes still requires a quite large driving force (around 300 mV) to keep up with the rate of electron generation by the dye and preserve a large J_{SC} . To further improve the performance of the solar cells, minimizing energy loss is the emergence.

1.3.4 DSSCs using copper(II/I) redox couples

Copper(II/I) redox couple has drawn a lot attention recently. By few years of research on the copper redox couple, the efficiency of solar cells which have copper(II/I) complex as the redox couple, have reached out to one of the best.⁶² What is more exciting is that the V_{OC} of those cells with copper redox couples, are over 1 V. These redox couples have relatively more positive redox potential compare to cobalt complexes and they have a higher self-exchange rate constant. Some examples of copper redox couples are listed in table 1.1.

Historically, copper complexes have been studied for their electron transfer processes in biological and inorganic reactions. Early researches about the copper coordination complex are motivated by the desire to understand the copper active site in metalloproteins. The metabolic roles of copper metalloenzymes involve many reactions like transferring electrons from a substrate molecule to molecular oxygen and participation in electron-transfer reactions.⁶³ Due to the large size of real proteins and their low symmetry, studies on the protein site are of low resolution and cause more problems. Small molecule analogs of copper-containing protein have been used in the later works to mimic the environment of copper centers in the protein for direct spectroscopic and

electrochemical studies. These researches triggered the synthesis of copper(II) coordination complexes and the studies about their redox chemistry. The Type I, “blue-copper”, protein has drawn inorganic chemists’ attention due to their markedly positive reduction potentials than other copper complexes. The higher reduction potential and the fast electron transfer property make the complex more stable in the copper(I) state and act as an efficient mediator in many natural electron transport systems.⁶⁴ Both properties of copper complexes also match with the requirements for redox couples in solar energy conversion. Therefore, the adoption of the complex to the field of solar energy conversion occurred accordingly.

The very first example of using the copper complex as redox couple in DSSCs was showed up in 2005 by Hattori.⁶⁵ Three pairs of copper redox couples with different ligand environments were used in the study and paired with N719 dye. The ligands have different bulkiness and rigidity, therefore could force the copper complex to be in a different geometry. One of the complexes was [(-)-sparteine-N,N'](maleonitriledithiolato-S,S')copper(II/I) ($[\text{Cu}(\text{SP})(\text{mmt})]^{0/-}$), which was also a blue-copper protein model complex. The ligand was used to mimic the protein environment around the copper center in nature and the spectral and redox behavior of the complex was similar to the blue-copper protein.⁶⁶ The use of this complex was aimed at taking advantage of the distorted tetragonal geometry, to achieve fast electron transfer kinetics. The other complexes used in that study was a symmetric complex, bis(2,9-dimethyl-1,10-phenanthroline) copper ($[\text{Cu}(\text{dmp})_2](\text{CF}_3\text{SO}_3)_2$). With methyl groups on the 2,9-position of the phenanthroline, the steric hindrance was thought to prevent the structural distortion during the redox reaction. And the third complex was phenanthroline coordinated copper complex without any functional groups on the phenanthroline. The structure of the third couple was more labile and the complex was expected to undergo structural distortion during redox process. The solar cells with these three different

redox couples obtained different efficiency. $[\text{Cu}(\text{SP})(\text{mmt})]^{0/-}$ and $[\text{Cu}(\text{dmp})_2]^{2+/+}$ were better redox couples compare to $[\text{Cu}(\text{phen})_2]^{2+/+}$ due to their faster electron transfer ability, which agreed with the kinetic data they obtained for the self-exchange rate constant. Although all three copper complexes were not able to compete with the high efficiency of triiodide/iodide cells when pairing with N719 dye in this case, this very first attempt build some basic understanding and encouraged people to study more on the possibility of using copper redox couples. Followed by this work, other copper complexes with ligands having functional groups to obtain steric hindrance were developed and used in DSSCs as redox couples. The improvement was made by Bai in 2011. Comparing to the previous work, the same copper redox couple, $[\text{Cu}(\text{dmp})_2]^{2+/+}$, was used but paired with an organic dye C218. The efficiency of the DSSCs was improved from 1.4% (in 2005) to 7.0%, which is higher than the efficiency of triiodide/iodide system under the same condition.⁶⁷ The redox potential of C218 dye was reported to be 0.3 V⁶⁸ and the redox potential of N719 was 0.33 V⁶⁹ (all converted vs. $\text{Fc}^{+/0}$) which didn't make much difference in the driving force of the dye regeneration. However, both the V_{OC} and J_{SC} of the two systems are quite different. The voltage output of DSSCs with N719 dye and C218 dye were 0.79 V and 0.93 V and the photocurrent was 3.2 mAcm^{-2} and 11.29 mAcm^{-2} respectively. The only major difference between these two systems was the preparation methods of the redox couple. In Bai's work, the oxidized form of the redox couple is not simply just the copper(II) version of $[\text{Cu}(\text{dmp})_2]^+$. Instead, the synthesized complex was $[\text{Cu}(\text{dmp})_2\text{Cl}]^+$ with the one chlorine anion in its coordination sphere. Due to the lack of reported cyclic voltammetry data in the report, it was not known how much this coordinated chlorine would affect the electrochemical property of the electrolyte. Therefore, the reason for the improvement in both V_{OC} and J_{SC} was unrevealed. It could be either a better dye regeneration kinetics between $[\text{Cu}(\text{dmp})_2]^{2+/+}$ and C218, or the better electrolyte composition by introducing the

chlorine coordinated species, or both. After these pioneer works, other researchers had been working on making a better performing DSSCs with the copper redox couple.

Most people were trying to find a dye that can match with the copper redox couples better. Colombo used a redox pair of bulky asymmetric phenanthroline copper(II/I) complexes as redox couple to pair with four distinct photosensitizers for DSSCs.⁷⁰ The couple had a redox potential of -0.02 V vs Fc⁺⁰ and the actual oxidized form in the electrolyte should be recognized more carefully in this work since the copper(II) complexes were not isolated in the form of powder, instead, NOBF₄ was used to oxidize the copper(I) complex, [Cu(2-mesityl-4,7-dimethyl-1,10-phenanthroline)₂]PF₆, in-situ. It is highly possible that the reaction may introduce NO coordinated copper(II) species.⁷¹ Moreover, TBP was not added into the electrolyte when fabricating DSSCs. Therefore, the resulted cells did not reach as high efficiency as Bai has reported, even they used similar ruthenium dyes and the same [Cu(dmp)₂]^{2+/+} redox couple.

Table 1.1 Copper complexes that were used as redox couples in DSSCs.

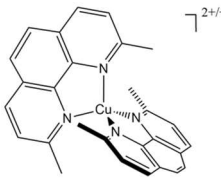
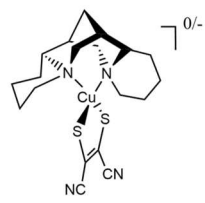
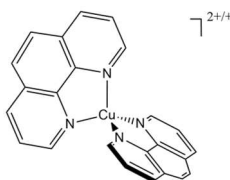
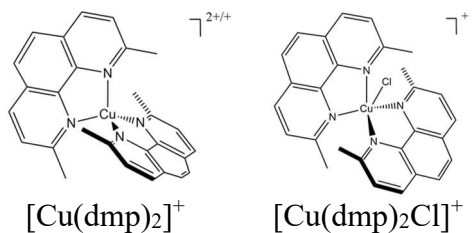
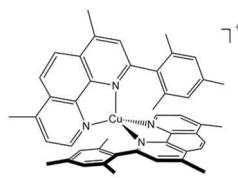
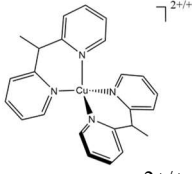
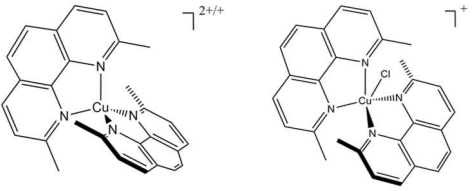
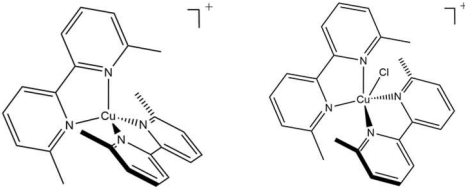
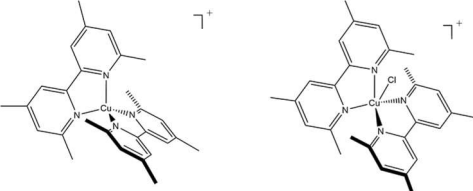
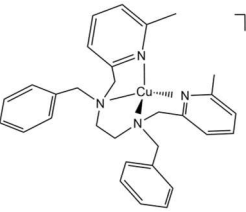
Redox couple (names used as in corresponding reference papers)	$E_{1/2}$ V vs. $\text{Fc}^{+/0}$	Electrolyte	Ref.
 $[\text{Cu}(\text{dmp})_2]^{2+/-}$	0.26		65
 $[\text{Cu}(\text{SP})(\text{mmt})]^{0/-}$	-0.11	0.2 M total Cu(I) and Cu(II) [Cu(II)]/[total Cu]=0.04 0.5 M TBP 0.5 M LiClO_4 in anhydrous methoxyacetonitrile.	65
 $[\text{Cu}(\text{phen})_2]^{2+/-}$	-0.50		65
 $[\text{Cu}(\text{dmp})_2]^+$ $[\text{Cu}(\text{dmp})_2\text{Cl}]^+$	0.08	0.2 M $[\text{Cu}(\text{dmp})_2]^+$ 0.05 M $[\text{Cu}(\text{dmp})_2\text{Cl}]^+$ 0.5 M TBP 0.1 M LiTFSI in acetonitrile	67
 Complex 3	-0.02	0.1 M total Cu(I) and Cu(II) [Cu(II)]/[total Cu]=0.05 by NOBF_4 0.1 M LiClO_4 in acetonitrile	70

Table 1.1 (cont'd)

Redox couple (names used as in corresponding reference papers)	$E_{1/2}$ V vs. $\text{Fc}^{+/0}$	Electrolyte	Ref.
 $[\text{Cu}(\text{bpye})_2]^{2+/+}$	-0.05	0.22 M $[\text{Cu}(\text{bpye})_2]^+$ 0.05 M $[\text{Cu}(\text{bpye})_2]^{2+}$ 0.2 M TBP 0.1 M LiClO_4 in acetonitrile	72
 $[\text{Cu}(\text{dmp})_2]^+$ $[\text{Cu}(\text{dmp})_2\text{Cl}]^+$	0.30	0.2 M $[\text{Cu}(\text{dmp})_2]^+$ 0.05 M $[\text{Cu}(\text{dmp})_2\text{Cl}]^+$ 0.5 M TBP 0.1 M LiTFSI in acetonitrile	73
 $[\text{Cu}(\text{dmpy})_2]^+$ $[\text{Cu}(\text{dmpy})_2\text{Cl}]^+$	0.33	0.2 M $\text{Cu}(\text{I})$ 0.04 M $\text{Cu}(\text{II})$ 0.6 M TBP 0.1 M LiTFSI in acetonitrile.	75
 $[\text{Cu}(\text{tmpy})_2]^+$ $[\text{Cu}(\text{tmpy})_2\text{Cl}]^+$	0.23		
 $[\text{Cu}(\text{L2})]^{2+/+}$	-0.03	0.25 M $\text{Cu}(\text{I})$ 0.065 M $\text{Cu}(\text{II})$ 0.6 M TBP 0.1 M Li-TFSI in acetonitrile	77

In the year 2016, there were many high efficient DSSC systems reported to achieve better efficiencies using copper redox couples.^{72,73,74,75} Cong reported the use of copper(II/I) 1,1-bis(2-pyridyl)ethane, $[\text{Cu}(\text{bpye})_2]^{2+/+}$, as the redox couple to pair with LEG4 dye and achieved 9% efficiency.⁷² The method reported for making $[\text{Cu}(\text{bpye})_2]^{2+}$ was neat. $\text{Cu}(\text{ClO}_4)_2$ was used as the copper(II) precursor to react with the bpye ligand and followed by the counter ion exchange in water with NH_4PF_6 . The resulted complex was free of any other coordinating species such as chlorine or water shown in the single crystal structure in the solid state (although there might still be a change of the coordinating sphere of $[\text{Cu}(\text{bpye})_2]^{2+}$ in the liquid electrolyte by taking up the solvent molecule⁷⁶). The redox potential of $[\text{Cu}(\text{bpye})_2]^{2+/+}$ was 0.59 V vs. NHE (-0.04 V vs. Fc) and the V_{OC} achieved from the DSSCs was around 0.9 V. This voltage output was high and more importantly, matched with the energy difference between the E_{CB} and $E_{1/2}$ of the redox couple. The only energy loss in this system was the large energy difference (over 400 mV) between the dye (1.04 V vs NHE, 0.40 V vs Fc) and the redox couple (0.59 V vs. NHE). On the other hand, Freitag paired $[\text{Cu}(\text{dmp})_2]^{2+/+}$ (chlorine coordinated copper(II) species, 0.30 V vs. Fc⁺⁰) with the same dye, LEG4, and achieved 8.3% efficiency, outcompete with the $\text{Co}(\text{bpy})_3^{3+/2+}$ standard.⁷³ Surprisingly, the driving force for the dye regeneration was only 100 mV and the regeneration efficiency was reported to be very close to 100%. However, the V_{OC} of 1.0 V was the most questionable. Comparing to Cong's work, the redox potential of $[\text{Cu}(\text{dmp})_2]^{2+/+}$ was 350 mV more negative than $[\text{Cu}(\text{bpye})_2]^{2+/+}$, but the V_{OC} was improved by only 100 mV. If the missing 200 mV can be fully understood, the cells with copper redox couples can achieve even higher voltage output and overall efficiency.

The best performing copper redox systems were first published also in 2016. This progress on using copper redox couples were made by Saygili.⁷⁵ Copper bipyridyl redox couples, copper(II/I)

6,6'-dimethyl-2,2'-bipyridine (0.97 V vs SHE, $[\text{Cu}(\text{dmpy})_2]^{2+/+}$) and copper(II/I) 4,4',6,6'-tetramethyl-2,2'-bipyridine (0.87 V vs SHE, $[\text{Cu}(\text{tmpy})_2]^{2+/+}$), were used to pair with Y123 dye. Both $[\text{Cu}(\text{dmpy})_2]^{2+/+}$ and $[\text{Cu}(\text{tmpy})_2]^{2+/+}$, even the “standard” $[\text{Cu}(\text{dmp})_2]^{2+/+}$ achieved over 10% efficiency. However, questions can be drawn from two main aspects. 1) From the synthetic route used for the bipyridyl complexes, chlorine should still be in the coordination sphere of the copper(II) species. Based on their reported CV curves, the coordinated chlorine did introduce a second redox wave in a more negative potential. The role of the chlorine remained unrevealed. 2) The V_{OC} of all the DSSCs reported in the study were around 1 V, which neither depended on the redox potential of the different redox couples used nor matched with the energy difference between the E_{CB} of TiO_2 and the redox potential of the couples. The source of the 400 mV potential loss needs to be identified.

A stable tetradentate copper(II/I) redox couple was synthesized by Hu in 2018.⁷⁷ The complex denoted as $[\text{Cu}(\text{L2})]^{2+/+}$ in the paper, where L2 refers to N, N'-dibenzyl-N, N'-bis(6-methylpyridin-2-ylmethyl)ethylenediamine), had a redox potential of 0.61 V vs NHE. When pairing with Y123 dye, the voltage output could reach 0.87 V and the overall efficiency was 9.2%. It is worth emphasizing that this newly synthesized copper redox couple had identical ligand regardless of the oxidation states, and no coordinating species like chlorine was introduced in the synthetic route. This could eliminate the complexity in identifying functional species in the electrolyte to some extent and result in stable DSSCs.

Up till now, the $[\text{Cu}(\text{tmpy})_2]^{2+/+}$ with Y123 is still the best performing system for DSSCs, but there is an emergence gaining the fundamental understanding of the electron transfer processes of such redox couples to help understand the dye regeneration and electron recombination kinetics.

1.3.5 Solid-state DSSCs using copper(II/I) redox couples and whole copper DSSCs.

Another promising use of copper redox couples is in solid-state DSSCs. A blend of $[\text{Cu}(\text{tmpy})_2]^{2+/+}$ was reported to act as a hole transporting material to facilitate hole hopping infiltrated into mesoporous TiO_2 film and manifested good conductivity. A record of 11% was achieved by the stable solid-state DSSCs.⁷⁸ The normal DSSCs with copper redox couples in the electrolyte were let air dry slowly to evaporate any volatile solvent, and the resulted “zombie cells” were found to have good photo to current conversion efficiencies. This surprising phenomenon was first observed by Freitag in 2015 when some of the tested DSSCs were accidentally dried and be measured to achieve improved photocurrent than the liquid cells.⁷⁹ This opens up an exciting direction of research on using copper redox couples as a hole transporting material for solid-state DSSCs.

As mentioned above, copper complexes can function as both sensitizers and redox couples. As a result, the energy levels can be well matched if a whole copper DSSC can be developed. Dragonetti in 2018 has tested the possibility of this “full-copper” DSSC and was succeeded.⁸⁰ Despite the low efficiencies achieved, this work was a proof-of-concept.

1.4 Motivation for studying the electron transfer processes of copper complexes.

Because of the multiple usages of copper complexes in the field of DSSCs and the already achieved excellent performance of using both copper dyes and copper redox couples, the need for a better understanding of the electron transfer mechanism of copper complexes is brought under the spotlight. Taking the copper redox couples as an example, although being applied in the solar cell devices for many years, fundamental understandings are lack. Understanding why they can regenerate the dye efficiently, why they don't suffer from fast electron recombination and why the voltage output is not as large as 1.5 V could be essential and could help develop better performing DSSC systems.

Copper coordination complexes have different geometry depend on their oxidation state, as mentioned already in section 1.3.1. This structural change will affect the electron transfer kinetics of copper redox couples dramatically. Moreover, during the redox reaction, this potential structural change will make copper redox couples very sensitive to their ligand and solvent environment. One example was the proposed ligand exchange phenomena by Hoffedit in 2016.⁸¹ In this study, 1,8-bis(2'-pyridyl)-3,6-dithiaoctane (PDTO) was used as a tetradentate ligand for copper. PDTO can form stable complexes with both copper(I) and copper(II) centers. However, during the operating condition where the redox couple dissolves in the electrolyte containing TBP, $[\text{Cu}(\text{PDTO})]^{2+}$ was proved to change its coordination sphere from a mono PDTO ligand to a tetra-TBP coordinate species, because the multiple TBP ligands could help copper(II) complex having a more favored square pyramidal geometry than the PDTO ligand which was more rigid. This ligand exchange introduced changes in both the spectroscopic and the electrochemical properties. If we look back at the short history of using copper redox couples in DSSCs, TBP was a common additive in the electrolyte. The concentrations of the added TBP ranged from 0.4 to 0.6 M, which was in large excess compare to the concentrations of copper(II) species (from 0.02 to 0.06 M). Therefore, we should cast doubt on all the previous systems and ask whether the copper coordination spheres remain the same or have changed under in the TBP rich environment? If the exchange does exist, should we prevent it or try to use it? How should we control this ligand exchange? There is a need for fundamental researches on copper redox couples to solve these mysteries.

REFERENCES

REFERENCES

- (1) IEA. *Global Energy & CO₂ Status Report The latest trends in energy and emissions in 2018*; **2019**.
- (2) Lindsey, R.; Dlugokencky, E. *Climate Change: Atmospheric Carbon Dioxide*; <https://www.climate.gov/news-features/understanding-climate/climate-change-atmospheric-carbon-dioxide>
- (3) IEA. *Historically High Energy Consumption & CO₂ Emissions in 2018*; **2019**.
- (4) ExxonMobile. *2019 Outlook for Energy: A perspective to 2040*; **2019**.
- (5) United Nations. *The Paris Agreement*; <https://unfccc.int/process-and-meetings/the-paris-agreement/the-paris-agreement>
- (6) United Nations. *Nationally Determined Contributions*; <https://unfccc.int/process-and-meetings/the-paris-agreement/nationally-determined-contributions-ndcs>
- (7) EIA. *Where Solar Is Found*; https://www.eia.gov/energyexplained/index.cfm?page=solar_where
- (8) IHS Markit. *Global Solar PV Market Returns to Double-Digit Growth in 2019*; **2019**.
- (9) IEA. *Solar PV: Tracking Clean Energy Progress*; <https://www.iea.org/tcep/power/renewables/solarpv/>
- (10) Lewis, N. S. *Science* **2007**, *315*, 798
- (11) Gerischer, H.; Michel-Beyerle, M. E.; Rebentrost, F.; Tributsch, H. *Electrochim. Acta.* **1968**, *13*, 1509
- (12) Rabinowitch, E. *J. Chem. Phys.* **1940**, *8*, 551
- (13) Rabinowitch, E. *J. Chem. Phys.* **1940**, *8*, 560
- (14) Green, M. A. *Prog. Photovoltaics Res. Appl.* **2001**, *9*, 123
- (15) Green, M. A.; Hishikawa, Y.; Dunlop, E. D.; Levi, D. H.; Hohl-Ebinger, J.; Yoshita, M.; Ho-Baillie, A. W. Y. *Prog. Photovoltaics Res. Appl.* **2019**, *27*, 3
- (16) Shockley, W.; Queisser, H. J. *J. Appl. Phys.* **1961**, *32*, 510
- (17) Green, M. A. *Prog. Photovoltaics Res. Appl.* **2001**, *9*, 123
- (18) Kayes, B. M.; Nie, H.; Twist, R.; Spruytte, S. G.; Reinhardt, F.; Kizilyalli, I. C.; Higashi, G. S. In *2011 37th IEEE Photovoltaic Specialists Conference*; IEEE, **2011**; pp 000004–

000008

- (19) Chiu, P. T.; Law, D. .; Woo, R. L.; Singer, S. B.; Bhusari, D.; Hong, W. D.; Zakaria, A.; Boisvert, J.; Mesropian, S.; King, R. R.; Karam, N. H. In *2014 IEEE 40th Photovoltaic Specialist Conference (PVSC)*; IEEE, **2014**; pp 0011–0013
- (20) Dung, D.; Ramsden, J.; Graetzel, M. *J. Am. Chem. Soc.* **1982**, *104*, 2977
- (21) Watson, D. F.; Meyer, G. J. *Annu. Rev. Phys. Chem.* **2005**, *56*, 119
- (22) TRIBUTSCH, H.; CALVIN, M. *Photochem. Photobiol.* **1971**, *14*, 95
- (23) Spitler, M.; Calvin, M. *J. Chem. Phys.* **1977**, *67*, 5193
- (24) Gerischer, H. *Solar photoelectrolysis with semiconductor electrodes* **1979**; pp 115–172
- (25) Kalyanasundaram, K.; Vlachopoulos, N.; Krishnan, V.; Monnier, A.; Gratzel, M. *J. Phys. Chem.* **1987**, *91*, 2342
- (26) Matsumura, M.; Nomura, Y.; Tsubomura, H. *Bull. Chem. Soc. Jpn.* **1977**, *50*, 2533
- (27) Desilvestro, J.; Graetzel, M.; Kavan, L.; Moser, J.; Augustynski, J. *J. Am. Chem. Soc.* **1985**, *107*, 2988
- (28) O'Regan, B.; Grätzel, M. *Nature* **1991**, *353*, 737
- (29) ASTM. Reference Solar Spectral Irradiance: Air Mass 1.5
<https://rredc.nrel.gov/solar/spectra/am1.5/>
- (30) Paris, J. P.; Brandt, W. W. *J. Am. Chem. Soc.* **1959**, *81*, 5001
- (31) Lytle, F. E.; Hercules, D. M. *J. Am. Chem. Soc.* **1969**, *91*, 253
- (32) Emsley, J. *Nature's building blocks : an A-Z guide to the elements* **2003**.
- (33) Bloxham, L.; Cowley, A.; Han, L.; Shao, E. *JM Pgm Market Report*; **2019**.
- (34) McMillin, D. R.; Buckner, M. T.; Ahn, B. T. *Inorg. Chem.* **1977**, *16*, 943
- (35) Ahn, B.; McMillin, D. R. *Inorg. Chem.* **1978**, *17*, 2253
- (36) Buckner, M. T.; McMillin, D. R. *J. Chem. Soc. Chem. Commun.* **1978**, *17*, 759
- (37) Patterson, G. S.; Holm, R. H. *Bioinorg. Chem.* **1975**, *4*, 257
- (38) Sakaguchi, U.; Addison, A. W. *J. Chem. Soc. Dalt. Trans.* **1979**, *4*, 600
- (39) McMillin, D. R.; Kirchhoff, J. R.; Goodwin, K. V. *Coord. Chem. Rev.* **1985**, *64*, 83

- (40) Alonso-Vante, N.; Nierengarten, J.-F.; Sauvage, J.-P. *J. Chem. Soc. Dalton Trans.* **1994**, *11*, 1649
- (41) Sakaki, S.; Kuroki, T.; Hamada, T. *J. Chem. Soc. Dalton Trans.* **2002**, *6*, 840
- (42) Bessho, T.; Constable, E. C.; Graetzel, M.; Hernandez Redondo, A.; Housecroft, C. E.; Kylberg, W.; Nazeeruddin, M. K.; Neuburger, M.; Schaffner, S. *Chem. Commun.* **2008**, *32*, 3717
- (43) Hernandez Redondo, A.; Constable, E. C.; Housecroft, C. E. *Chimia* **2009**, *63*, 205
- (44) Constable, E. C.; Hernandez Redondo, A.; Housecroft, C. E.; Neuburger, M.; Schaffner, S. *Dalton Trans.* **2009**, *33*, 6634
- (45) Linfoot, C. L.; Richardson, P.; Hewat, T. E.; Moudam, O.; Forde, M. M.; Collins, A.; White, F.; Robertson, N. *Dalt. Trans.* **2010**, *39*, 8945
- (46) Kim, Y.; Jeong, J. H.; Kang, M. *Inorganica Chim. Acta* **2011**, *365*, 400
- (47) Yuan, Y.-J.; Yu, Z.-T.; Zhang, J.-Y.; Zou, Z.-G. *Dalt. Trans.* **2012**, *41*, 9594
- (48) Colombo, A.; Dragonetti, C.; Roberto, D.; Valore, A.; Biagini, P.; Melchiorre, F. *Inorganica Chim. Acta* **2013**, *407*, 204
- (49) Baldenebro-Lopez, J.; Flores-Holguin, N.; Castorena-Gonzalez, J.; Glossman-Mitnik, D. *J. Photochem. Photobiol. A Chem.* **2013**, *267*, 1
- (50) Wills, K. a.; Mandujano-Ramírez, H. J.; Merino, G.; Mattia, D.; Hewat, T.; Robertson, N.; Oskam, G.; Jones, M. D.; Lewis, S. E.; Cameron, P. J. *RSC Adv.* **2013**, *3*, 23361
- (51) Ashbrook, L. N.; Elliott, C. M. *J. Phys. Chem. C* **2013**, *117*, 3853
- (52) Bozic-Weber, B.; Brauchli, S. Y.; Constable, E. C.; Fürer, S. O.; Housecroft, C. E.; Wright, I. A. *Phys. Chem. Chem. Phys.* **2013**, *15*, 4500
- (53) Sandroni, M.; Kayanuma, M.; Planchat, A.; Szuwarski, N.; Blart, E.; Pellegrin, Y.; Daniel, C.; Boujtita, M.; Odobel, F. *Dalton Trans.* **2013**, *42*, 10818
- (54) Sandroni, M.; Favereau, L.; Planchat, A.; Akdas-Kilig, H.; Szuwarski, N.; Pellegrin, Y.; Blart, E.; Le Bozec, H.; Boujtita, M.; Odobel, F. *J. Mater. Chem. A* **2014**, *2*, 9944
- (55) Hewat, T. E.; Yellowlees, L. J.; Robertson, N. *Dalt. Trans.* **2014**, *43*, 4127
- (56) Colombo, A.; Dragonetti, C.; Fagnani, F.; Roberto, D.; Melchiorre, F.; Biagini, P. *Dalt. Trans.* **2019**, *48*, 9818
- (57) Ondersma, J. W.; Hamann, T. W. *Energy Environ. Sci.* **2012**, *4*, 370
- (58) Boschloo, G. *Front. Chem.* **2019**, *7*, Article 77

- (59) Boschloo, G.; Häggman, L.; Hagfeldt, A. *J. Phys. Chem. B* **2006**, *110*, 13144
- (60) Boschloo, G.; Hagfeldt, A. *Acc. Chem. Res.* **2009**, *42*, 1819
- (61) Mathew, S.; Yella, A.; Gao, P.; Humphry-Baker, R.; Curchod, B. F. E.; Ashari-Astani, N.; Tavernelli, I.; Rothlisberger, U.; Nazeeruddin, M. K.; Grätzel, M. *Nat. Chem.* **2014**, *6*, 242
- (62) Cao, Y.; Liu, Y.; Zakeeruddin, S. M.; Hagfeldt, A.; Grätzel, M. *Joule* **2018**, *2*, 1108
- (63) Beinert, H. *Coord. Chem. Rev.* **1980**, *33*, 55
- (64) Randall, D. W.; Gamelin, D. R.; LaCroix, L. B.; Solomon, E. I. *JBIC J. Biol. Inorg. Chem.* **2000**, *5*, 16
- (65) Hattori, S.; Wada, Y.; Yanagida, S.; Fukuzumi, S. *J. Am. Chem. Soc.* **2005**, *127*, 9648
- (66) Kim, Y.-J.; Kim, S.-O.; Kim, Y.-I.; Choi, S.-N. *Inorg. Chem.* **2001**, *40*, 4481
- (67) Bai, Y.; Yu, Q.; Cai, N.; Wang, Y.; Zhang, M.; Wang, P. *Chem. Commun.* **2011**, *47*, 4376
- (68) Li, R.; Liu, J.; Cai, N.; Zhang, M.; Wang, P. *J. Phys. Chem. B* **2010**, *114*, 4461
- (69) Nazeeruddin, M. K.; Zakeeruddin, S. M.; Humphry-Baker, R.; Jirousek, M.; Liska, P.; Vlachopoulos, N.; Shklover, V.; Fischer, C.-H.; Grätzel, M. *Inorg. Chem.* **1999**, *38*, 6298
- (70) Colombo, A.; Dragonetti, C.; Magni, M.; Roberto, D.; Demartin, F.; Caramori, S.; Bignozzi, C. A. *ACS Appl. Mater. Interfaces* **2014**, *6*, 13945
- (71) Connelly, N. G.; Geiger, W. E. *Chem. Rev.* **1996**, *96*, 877
- (72) Cong, J.; Kinschel, D.; Daniel, Q.; Safdari, M.; Gabrielsson, E.; Chen, H.; Svensson, P. H.; Sun, L.; Kloo, L. *J. Mater. Chem. A* **2016**, *4*, 14550
- (73) Freitag, M.; Giordano, F.; Yang, W.; Pazoki, M.; Hao, Y.; Zietz, B.; Grätzel, M.; Hagfeldt, A.; Boschloo, G. *J. Phys. Chem. C* **2016**, *120*, 9595
- (74) Magni, M.; Giannuzzi, R.; Colombo, A.; Cipolla, M. P.; Dragonetti, C.; Caramori, S.; Carli, S.; Grisorio, R.; Suranna, G. P.; Bignozzi, C. A.; Roberto, D.; Manca, M. *Inorg. Chem.* **2016**, *55*, 5245
- (75) Saygili, Y.; Söderberg, M.; Pellet, N.; Giordano, F.; Cao, Y.; Muñoz-García, A. B.; Zakeeruddin, S. M.; Vlachopoulos, N.; Pavone, M.; Boschloo, G.; Kavan, L.; Moser, J.-E.; Grätzel, M.; Hagfeldt, A.; Freitag, M. *J. Am. Chem. Soc.* **2016**, *138*, 15087
- (76) Doine, H.; Yano, Y.; Swaddle, T. W. *Inorg. Chem.* **1989**, *28*, 2319
- (77) Hu, M.; Shen, J.; Yu, Z.; Liao, R.-Z.; Gurzadyan, G. G.; Yang, X.; Hagfeldt, A.; Wang, M.; Sun, L. *ACS Appl. Mater. Interfaces* **2018**, *10*, 30409

- (78) Cao, Y.; Saygili, Y.; Ummadisingu, A.; Teuscher, J.; Luo, J.; Pellet, N.; Giordano, F.; Zakeeruddin, S. M.; Moser, J.-E.; Freitag, M.; Hagfeldt, A.; Grätzel, M. *Nat. Commun.* **2017**, *8*, 15390
- (79) Freitag, M.; Daniel, Q.; Pazoki, M.; Sveinbjörnsson, K.; Zhang, J.; Sun, L.; Hagfeldt, A.; Boschloo, G. *Energy Environ. Sci.* **2015**, *8*, 2634
- (80) Dragonetti, C.; Magni, M.; Colombo, A.; Melchiorre, F.; Biagini, P.; Roberto, D. *ACS Appl. Energy Mater.* **2018**, *1*, 751
- (81) Hoffeditz, W. L.; Katz, M. J.; Deria, P.; Cutsail III, G. E.; Pellin, M. J.; Farha, O. K.; Hupp, J. T. *J. Phys. Chem. C* **2016**, *120*, 3731

Chapter 2. Electron transfer processes of DSSCs using copper sensitizers

2.1 Introduction

The global energy consumption rate in 2018 has increased to nearly twice that in 2010 and will keep increasing based on the current status and estimation. Accompanied by it would be the increasing worldwide carbon emission rate. Controlling the CO₂ emission is part of the mission of the Paris Agreement.¹ In order to fulfill the goal of reducing the emission rate of the CO₂ without slowing down the energy consumption rate, the future energy structure needs to be switched to lower or no carbon intensity. Developing technologies for improving the usage of renewable energy is urgent. The technical potential for solar energy is the highest among all renewable energy resources.² The abundance and cleanness of solar power have motivated many researchers to develop cheaper and more efficient solar to electricity conversion devices.

Since the dye-sensitized solar cell (DSSC) with a 7% energy conversion efficiency was reported by Gratzel and O'Regan, this breakthrough for this low-cost type of device opened an exciting research field for solar energy capturing and conversion.³ Not only the low cost in manufacturing makes DSSCs promising for everyday use, but also the complexity in chemistry and material science inspired a lot of research interest.

The working system of a DSSC can be graphically expressed in Figure 2.1. The photoanode of the cell is a layer (few microns) of a wide band-gap nanoporous semiconductor, onto which are adsorbed dye molecules. Photoexcitation of dyes occurs upon illumination. Inorganic chromophores are of the most studied group of dyes. Their strong absorption in the visible region is a result of the excitation of a metal-to-ligand charge transfer (MLCT) band. The metal center of the dye will thus be oxidized to a higher oxidation state in its excited state (dye*). The excited electrons will be higher in energy level and can be further injected into the empty states of the

semiconductor. After injecting electron to the semiconductor, the dye molecule will be left in its oxidized form, dye^+ . The optical absorption gap of the semiconductor, such as anatase TiO_2 , is too large (3.2 eV) to absorb the visible photons directly.⁴ The electron injection from the excited state of the metal chromophore to the conduction band of TiO_2 is recognized as the photosensitization of large bandgap semiconductors. Dye^+ molecules can be regenerated by accepting electrons from the donor (reduced form of the redox couple, *Red*) in the liquid electrolyte. The injected electrons will transport through the nanoparticles layer of the semiconductor. And some portions of the injected electrons can be collected at the conductive substrate, which is the transparent conductive oxide layer (such as fluorine-doped tin oxide, FTO). There are other portions of the injected electron that undergo recombination rather than being collected on FTO. One of the recombination pathways is by reacting with dye^+ molecules, and another pathway is by reacting with the electron acceptor (oxidized form of the redox couple, *Ox*) in the liquid electrolyte. The electrons being collected on the transparent conductive oxides (TCO) will pass the outside load and do work. Finally, they will come back to the counter electrode at a lower energy level. Those electrons will react with the *Ox* in the electrolyte on the electrolyte-counter electrode interface and complete the circuit. Facilitated by the fast diffusion in the liquid electrolyte, *Red* can reduce the dye molecules on the photoanode, and the produced *Ox* can be regenerated on the counter electrode to achieve the reversibility of the chemistry. This type of regenerative solar cell requires energy matching between different materials (semiconductor, dye, and redox couple) and a kinetic corporation between interfacial electron transfer reactions.

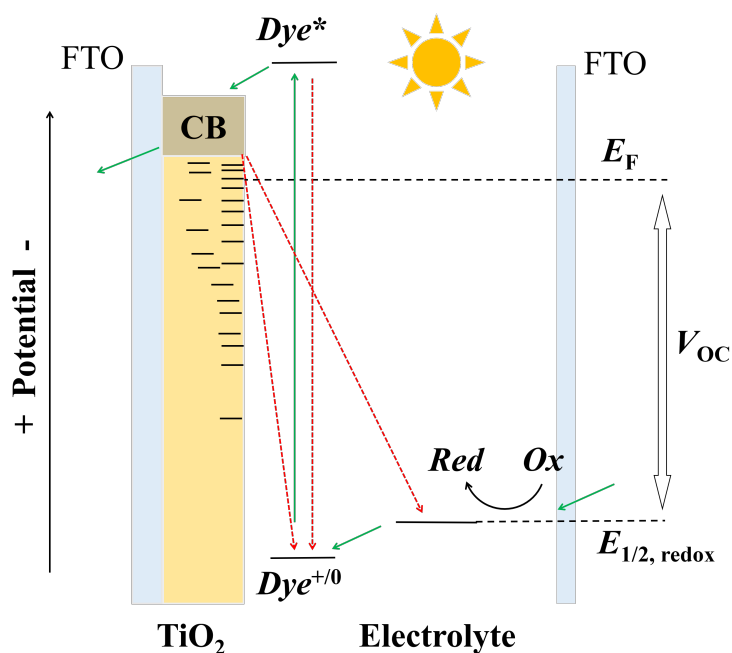


Figure 2.1 A diagram showing the operating system of DSSC. Green arrows show the direction of electron transfer. Red arrows show the unwanted back electron transfer. FTO is fluorine-doped tin oxide. CB is the conduction band of TiO_2 . *Red* and *Ox* are the reduced and oxidized forms of the redox couple, respectively. $E_{1/2, \text{redox}}$ is the redox potential of the redox couple.

The operation of DSSCs is essentially based on the charge separation and transport between different materials. Improving the charge transfer rate at a lower energy cost is the key to improve the efficiency of DSSCs. There are interactions between different components (semiconductor, dye and redox couple) in DSSCs. If one of them got changed, the interaction between all the related components should be studied.

Copper polypyridyl complexes have been studied as a cheaper alternative to replace ruthenium polypyridyl complexes as discussed in Chapter 1.^{5, 6, 7, 8, 9} Copper is much abundance compared to ruthenium in the earth crust, and copper(I) complexes also have good absorption ability in the visible region of the solar spectrum from their metal-to-ligand charge transfer (MLCT) bands. The energy gaps between their ground state (GS) and excited state (ES) are similar in size compared to that of ruthenium(II) complexes, which makes them a proper photosensitizer for large bandgap

semiconductors. Therefore, these features make copper(I) a suitable replacement for ruthenium(II) and can be used in DSSCs to reduce the cost. Although the electrolyte components to pair with ruthenium sensitizers in DSSCs have been well developed,¹⁰ studies are still needed for optimized conditions for copper complexes.

2.2 The problems with using copper(I) sensitizers in DSSCs.

The history of using copper complexes as a photosensitizer for DSSCs has been introduced in chapter 1. After being successfully used as the sensitizer in DSSCs in 1994,¹¹ many different copper(I) complexes have been synthesized for this use.^{12, 6, 8} Most of the designs of molecules aimed at improving the absorptivity of the dye molecules and to help the excited electron being localized more on the side of the molecule closer to the semiconductor, to facilitate a more efficient electron injection.^{13, 14, 15, 16} So far, the best performing copper dye for DSSC was designed under this principle.¹⁷ Despite this significant improvement in the overall efficiency, copper(I) sensitizers are still unable to generate as high power conversion efficiency as ruthenium(II) sensitizers. From ligand designs and the development of technics for making heteroleptic copper(I) sensitizers, the light-harvesting efficiency (*LHE*) of copper DSSCs can be comparable to that of ruthenium(II) complex sensitized ones. But the overall power conversion efficiency was not improved as much. Most of the copper(I) sensitizers are used in combination with triiodide/iodide redox couple, who can facilitate proper dye regeneration with ruthenium(II) sensitizers. But according to the photoinduced intrinsic structural difference between copper(I) sensitizers and their oxidized form, it is worth pointing out that the use of triiodide/iodide redox couple may not be a wise choice due to the chance of forming a stable copper(II)-iodide interaction.^{18, 19, 20} The possible reaction between photoexcited copper sensitizers and coordinating species in the electrolyte may prevent successful reduction of copper(II) centers and also quench their excited state. Although the

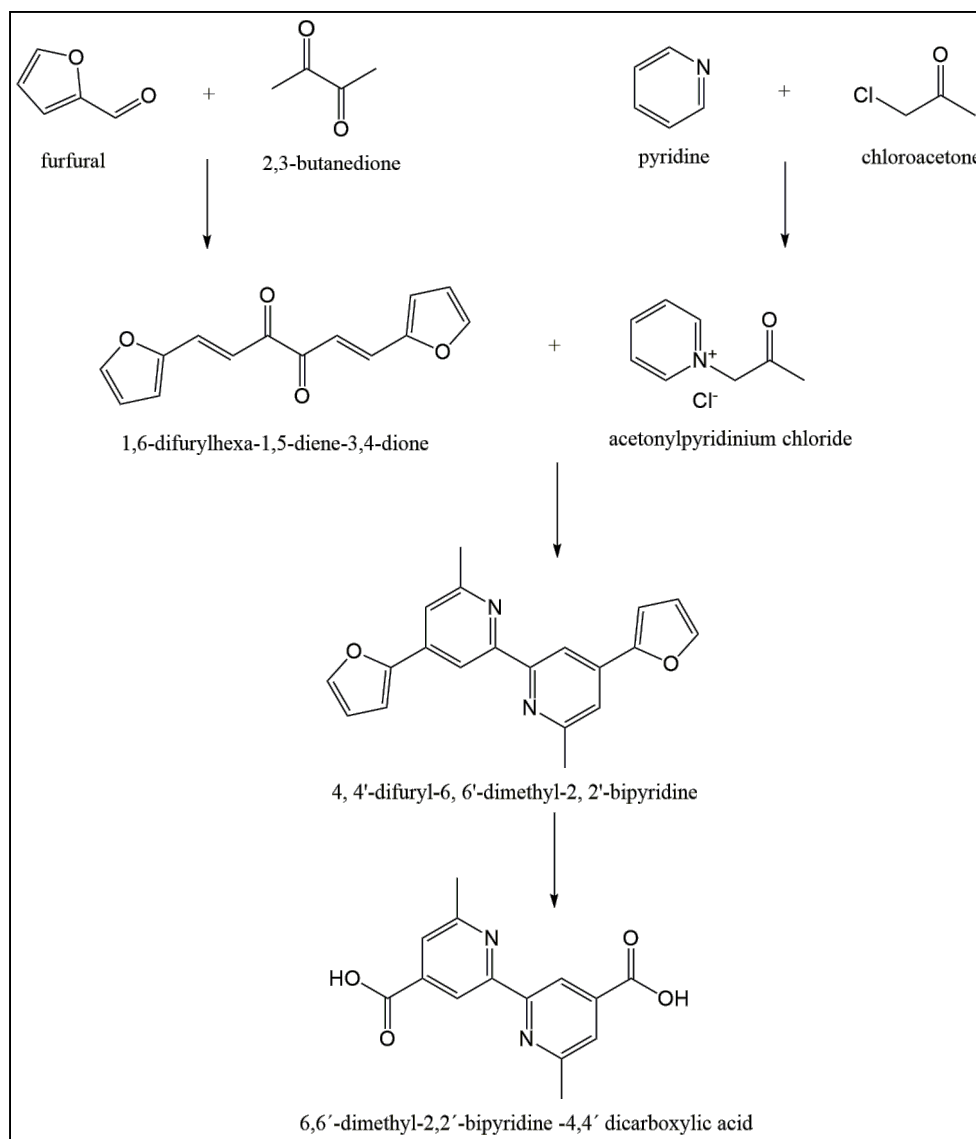
importance of switching from the conventional triiodide/iodide redox couple for copper(I) sensitizer systems has been pointed out,²⁰ and the electrolyte conditions have been manipulated,⁹ fundamental understanding of copper(I) sensitizing system is still scarce. The most important will be determining what electron transfer processes in an operating copper DSSC limit their power conversion efficiency.

In this chapter, copper(I) bis(6,6'-dimethyl-2,2'-bipyridine-4,4'-dicarboxylic) salt is used as a model complex to study the general behavior of copper(I) sensitizers. Experimental results will be presented for both solution-based study and complete dye cell systems. By testing the fundamental parameters, like electron transfer efficiencies, some determinations of the origin of the low efficiency of copper-based devices were explored, and it will be discussed how we may further improve the cell efficiency.

2.3 Experimental details

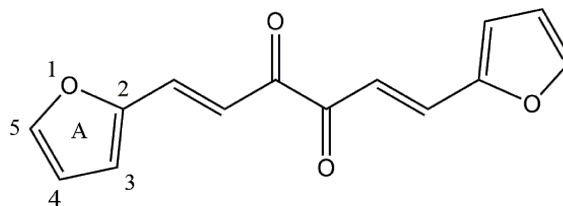
2.3.1 Synthesis of the Chemicals

By Kröhnke pyridine synthesis, acetonilpyridinium chloride and 1,6-difurylhexa-1,5-diene-3,4-dione will react to produce 4,4'-difuryl-6,6'-dimethyl-2,2'-bipyridine, dmdfbpy. The two furyl groups on dmdfbpy were oxidized into dicarboxylic groups by KMnO_4 to produce 6,6'-dimethyl-2,2'-bipyridine -4,4' dicarboxylic acid, dmddbpy. The dmddbpy can be further converted into its ester form. The general synthetic scheme is shown in Scheme 2.1. Detailed methods are also described.



Scheme 2.1 The synthetic route for 6,6'-dimethyl-2,2'-bipyridine-4,4'-dicarboxylic acid.

2.3.1.1 Preparation of 1,6-difurylhexa-1,5-diene-3,4-dione.²¹



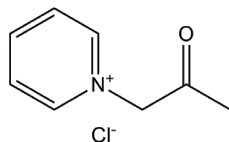
(1*E*,5*E*)-1,6-di(furan-2-yl)hexa-1,5-diene-3,4-dione

Piperidine (3 mmol) and glacial acetic acid (3 mmol) were added sequentially to a solution containing furfural (60 mmol) and 2,3-butanedione (15 mmol) in methanol (MeOH) (20 mL). The reaction mixture was heated to 70 °C and refluxed for 6.5 h. MeOH was removed by rotavap. Then

the resulting mixture was cooled to 0 °C with ice bath. Precipitates were formed at this low temperature. The mixture was filtered through a fine grade glass frit. The collected powder was washed with ice-cold MeOH. 1,6-difurylhexa-1,5-diene-3,4-dione was obtained as a brown powder in 31% yield.

¹H NMR (CDCl₃, 500 MHz): δ/ppm 7.62 (d, *J* = 15.5 Hz, 2H; H^{CH=CH-CO}), 7.58 (d, *J* = 1 Hz, 2H; H^{5A}), 7.33 (d, *J* = 16 Hz, 2H; H^{HC=CH-CO}), 6.81 (d, *J* = 3.5 Hz, 2H; H^{3A}), 6.54 (dd, *J* = 1.5 Hz, 3.5 Hz, 2H; H^{4A}).

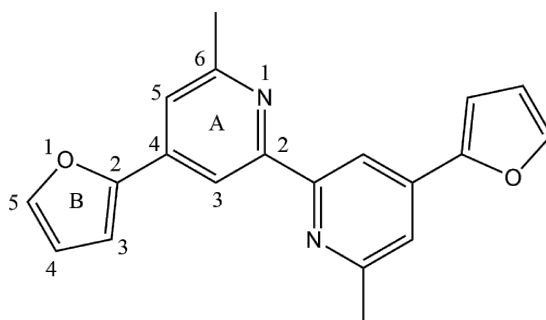
2.3.1.2 Preparation of acetylpyridinium chloride.²²



acetylpyridinium chloride

Equal amounts of chloroacetone and pyridine (46.8 mmol) were added into 30 mL tetrahydrofuran (THF). The reaction mixture was heated to 70 °C and refluxed for 4 h under nitrogen. Precipitates were formed during the fluxing. Acetylpyridinium chloride was collected as white powder in 61% yield.

2.3.1.3 Preparation of 4, 4'-difuryl-6, 6'-dimethyl-2, 2'-bipyridine.²³



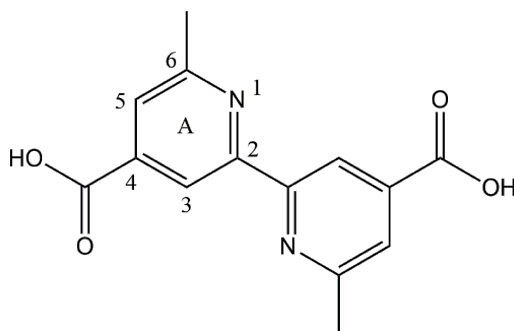
4, 4'-difuryl-6, 6'-dimethyl-2, 2'-bipyridine

1,6-difurylhexa-1,5-diene-3,4-dione (2.06 mmol) was dissolved in MeOH (10 mL). Acetylpyridinium chloride (4.06 mmol) and ammonium acetate (16.5 – 20.6 mmol) in MeOH

(10 mL) was added. The reaction mixture was heated to 70 °C and refluxed for 12 h, and then it was cooled to 4 °C in the fridge for 3h. Precipitate was formed in the low temperature and was filtered and washed by ice-cold MeOH. 4, 4'-difuryl-6, 6'-dimethyl-2, 2'-bipyridine was obtained as light brown powder in 42% yield.

^1H NMR (CDCl_3 , 500 MHz): δ /ppm 8.45 (d, $J = 1.5$ Hz, 2H; $\text{H}^{3\text{A}}$), 7.57 (d, $J = 1$ Hz, 2H; $\text{H}^{5\text{B}}$), 7.46 (d, $J = 1.5$ Hz, 2H; $\text{H}^{5\text{A}}$), 7.00 (d, $J = 3.5$ Hz, 2H; $\text{H}^{3\text{B}}$), 6.55 (d, $J = 3.5$ Hz, 2H; $\text{H}^{4\text{B}}$), 2.70 (s, 6H; H^{CH_3}).

2.3.1.4 Preparation of 6,6'-dimethyl-2,2'-bipyridine -4,4' dicarboxylic acid, dmdcbpy.

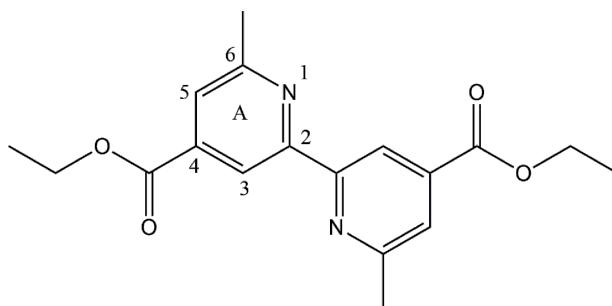


6,6'-dimethyl-2,2'-bipyridine -4,4' dicarboxylic acid

4, 4'-difuryl-6, 6'-dimethyl-2, 2'-bipyridine (18 mmol) was suspended into $\text{H}_2\text{O}/t\text{-BuOH}$ (1:3, v/v, 100 mL) mixture, and the reaction mixture was heated up to 40 °C with stirring. 8-10 equivalents of KMnO_4 powder were slowly added to the warm mixture, and the resulted brown mixture was heated to 45 °C overnight. After cooled to room temperature, the reaction mixture was filtered through Celite 454 to get rid of the non-soluble residual. The clear solution was collected and was evaporated till 1/3 of the volume. 0.1 M NaOH in water was used to adjust the pH to 2. Precipitates formed and were collected by filtration. 6,6'-dimethyl-2,2'-bipyridine -4,4' dicarboxylic acid ligand was obtained as bright yellow solid in 57% yield.

^1H NMR (MeOD , 500MHz): δ /ppm 8.70 (s, 2H; $\text{H}^{3\text{A}}$), 7.81 (s, 2H; $\text{H}^{5\text{A}}$), 2.71 (s, 6H; H^{CH_3}).

2.3.1.5 Preparation of diethyl 6,6'-dimethyl-2,2'-bipyridine -4,4' dicarboxylate, dmdebpy.

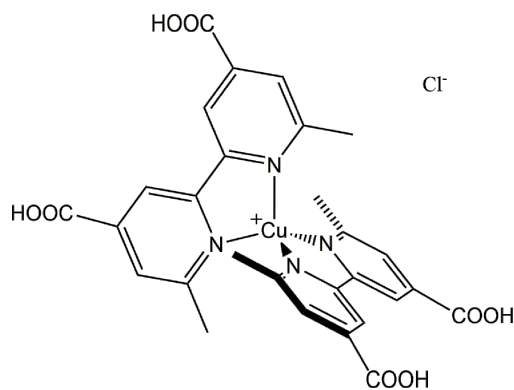


diethyl 6,6'-dimethyl-2,2'-bipyridine -4,4' dicarboxylate

50 equivalents of concentrated sulfuric acid were added into a suspension of 1 equivalent dmdebpy in 100 equivalents of ethanol (EtOH). The reaction mixture was heated to 80 °C and refluxed for 2h. After cooled to room temperature, 1 M NaOH in water was added to adjust the pH to 7. The precipitates were filtered and washed with cold EtOH and dried under vacuum overnight. Dmdebpy was obtained as a white solid.

^1H NMR (500 MHz, CDCl_3) δ /ppm 8.72 (dd, 4H, $\text{H}^{3\text{A}}$), 7.75 (dd, 4H, $\text{H}^{5\text{A}}$), 4.45 (q, 8H, $\text{H}^{\text{OCH}_2\text{CH}_3}$), 2.73 (s, 12H, $\text{H}^{\text{OCH}_2\text{CH}_3}$), 1.44 (t, 12H, H^{CH_3}).

2.3.1.6 Preparation of copper(I) bis(6,6'-dimethyl-2,2'-bipyridine-4,4'-dicarboxylic) chloride, $\text{Cu}(\text{dmdebpy})_2\text{Cl}$.¹²



copper(I) bis(6,6'-dimethyl-2,2'-bipyridine-4,4'-dicarboxylic) chloride

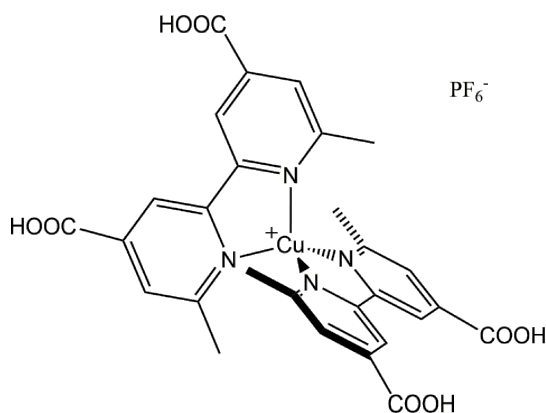
The suspension of dmdebpy (4 mmol) in water (50 mL) was heated to 70 °C. 1 M NaOH in water was added dropwise until dmdebpy got fully dissolved. 2 mmol copper sulfate pentahydrate ($\text{CuSO}_4 \cdot 5\text{H}_2\text{O}$) in water (5 mL) was added, followed by the addition of 1 M NaOH in water.

Ascorbic acid (3 mmol) was added to the reaction mixture to reduce Cu^{2+} to Cu^+ , and there was an obvious color change from brown to dark red/orange. The pH was adjusted to 2 using 1 M hydrochloric acid (HCl) in water, and red precipitates were formed. Since the precipitate was very fine powder, it was separated from the solution by centrifugation. It was washed with large amount of pH 5 HCl water solution. Finally, the dark red product was dried under vacuum overnight. The complex is stable in air.

^1H NMR (MeOD, 500MHz): δ /ppm 8.88 (s, 2H), 8.05 (s, 2H), 2.31 (s, 6H).

Anal. Calc. for: $\text{C}_{28}\text{H}_{24}\text{ClCuN}_4\text{O}_8$: C, 52.26%; H, 3.76%; N, 8.71%. Found: C, 50.87%; H, 3.73%; N, 8.39%.

2.3.1.7 Preparation of copper(I) bis(6,6'-dimethyl-2,2'-bipyridine-4,4'-dicarboxylic) hexafluorophosphate, $\text{Cu}(\text{dmdcbpy})_2\text{PF}_6$.



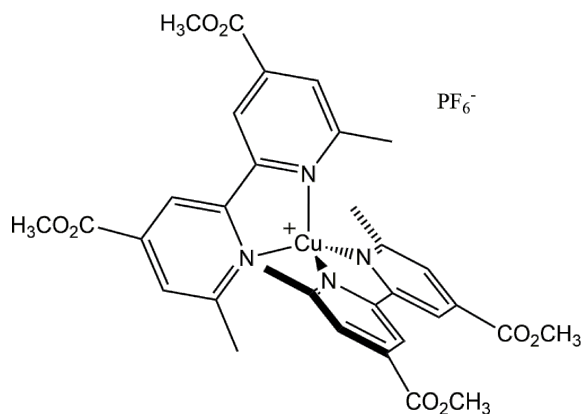
copper(I) bis(6,6'-dimethyl-2,2'-bipyridine-4,4'-dicarboxylic) hexafluorophosphate

1 equivalent of copper(I) tetrakis(acetonitrile) hexafluorophosphate (2 mmol) was added into 2.2 equivalents of dmdcbpy ligand (4.4 mmol) in THF (10 mL). The reaction mixture was stirred for 1h. Red precipitates were crashed out by adding diethyl ether to the reaction mixture. The collected powder was washed and dried under vacuum overnight. Elemental analysis was done to confirm the product. The complex is stable in air.

Anal. Calc. for: $C_{28}H_{24}CuN_4O_8PF_6$: C, 44.66%; H, 3.21%; N, 7.44%. Found: C, 44.85%; H, 3.25%; N, 7.40%

2.3.1.8 Preparation of copper(I) diethyl 6,6'-dimethyl-2,2'-bipyridine-4,4'-dicarboxylate, $Cu(dmdebpy)_2PF_6$.

1 equivalent of copper(I) tetrakis(acetonitrile) hexafluorophosphate (2 mmol) was added into 2.2



copper(I) diethyl 6,6'-dimethyl-2,2'-bipyridine-4,4'-dicarboxylate hexafluorophosphate

equivalents of dmdebpy ligand (4.4 mmol) in DCM (10 mL). The reaction mixture was stirred for 1h. Red precipitates were crashed out by hexane to the reaction mixture. The collected powder was washed and dried under vacuum overnight.

Anal. Calc. for: $C_{36}H_{40}CuN_4O_8PF_6$: C, 49.97%; H, 4.66%; N, 6.48%. Found: C, 49.92%; H, 4.50%; N, 6.46%

2.3.2 Photophysical and Electrochemical Measurement

The absorption spectra of different sensitizers were measured under room temperature. Liquid samples were prepared with dry solvents in the glovebox. A screwed-cap quartz cuvette was used for the measurement. The absorption spectra of dyes attached to nanoparticles were obtained by measuring the absorption of sensitized TiO_2 films on blank microscope slide glass (VWR). UV-

Vis data was acquired using a Lambda 35 (PerkinElmer) spectrometer. Additionally, an integrating sphere was used for solid samples.

As a comparison, ruthenium(II) cis-bis(isothiocyanato)bis(2,2'-bipyridyl-4,4'-dicarboxylato) (N3 dye) was used as the model complex for ruthenium chromophores. The cyclic voltammetry (CV) measurement of both dyes was done on tin-doped indium oxide (ITO) films. ITO films were made from synthesized ITO nanoparticle paste (by Mandal). The paste was doctor bladed onto the FTO glass (TEC 15, Hartford Glass) followed by annealing at programmed temperatures (325 °C for 5 minutes, 375 °C for 5 minutes, 450 °C for 5 minutes, and 500 °C for 15 minutes sequentially) in air. After cooled down to room temperature, the film was sensitized by the dye molecule by soaking in the dye solution overnight. The was 0.2 mM N3 dye dissolved in ethanol. Copper wire was attached to the sensitized ITO film by silver epoxy (MG Chemicals) to be used in the electrochemical measurement and clamped onto the home-made electrochemical cell. Electrolyte contained 0.1 M tetrabutylammonium hexafluorophosphate (TBAPF₆) as the supporting electrolyte in DCM. Reference electrode was a home-made Ag/AgNO₃ (0.01 M AgNO₃ in acetonitrile, see Appendix Figure 2.9). The counter electrode was a high-surface-area Pt mesh. An Autolab PGSTAT128N potentiostat was used for the measurement. While measuring, the environmental light intensity was kept low by using cloth to cover the cell. The same technique was applied for other sensitizers to obtain electrochemical information.

2.3.3 DSSC preparation and characterization

Both photoanode and counter electrode (anode and cathode) were prepared on 12 ohm/square FTO coated glass (Hartford Glass). Details are explained in the following subsections.

2.3.3.1 Preparing photoanodes

Bare FTO glass slide was cut into small pieces (2 cm by 2 cm). All the small pieces were sequentially sonicated in soap solution in water (15 min), distilled water (15 min), isopropyl alcohol (15 min), and acetone (15 min) and were air-dried. The organic residual on the glass was removed by heating at 400 °C for 30 minutes. The blocking layer of nanocrystalline TiO₂ was deposited by atomic layer deposition (ALD, 500 cycles) using titanium isopropoxide (TIPS, Aldrich) and water as precursors with a Savannah 100 instrument (Cambridge Nanotech, Inc.). The thickness of the film was calibrated by measuring the sample on silicon substrate deposited at the same time. The TiO₂ layers were grown at 225 °C and the reactant exposure times were 0.3 s and 0.015 s for TIPS and H₂O respectively. Nitrogen purge time was 5 s between exposures. A transparent TiO₂ nanoparticle layer was prepared by doctor blading a paste of TiO₂ nanoparticles (Ti-Nanoxide T/SP, Solaronix) on the FTO glass. The resulting electrodes were annealed at 325 °C for 5 minutes, 375 °C for 5 minutes, 450 °C for 5 minutes, and 500 °C for 15 minutes sequentially in air. After cooled to room temperature, the anodes were immersed in a dye solution for about 12 hours. Dye solution contained low concentrations of dye molecules (0.3 mM N3 dye dissolved in ethanol and 0.3 mM copper dye dissolved in MeOH/DCM 1:1 mixture). A color change of the transparent TiO₂ film to dark red indicated the successful adsorption of the dye molecules. The sensitized anodes were rinsed with the same solvent used for dye loading and then acetonitrile and were left air dry.

TiCl₄ post-treatment was applied when necessary to increase the surface area of the TiO₂ nanoporous film. The films were soaked in 0.5 mM aqueous solution of TiCl₄ for 30 min at 70 °C. After heating, films were taken out to be dipped into water and then isopropyl alcohol (IPA) for

rinsing, and were left air dried. Annealing the dried films at 500 °C for 30 min helped to form crystallized TiO₂.

Different dyes were loaded onto TiO₂ in different solutions. N3 dye solution was prepared freshly in ethanol. For Cu(dmdbcby)₂Cl and Cu(dmdbcby)₂PF₆, solution was prepared freshly in methanol (or a mixture of methanol and dichloromethane, 1:1 v/v). The concentration of dye was 0.3 to 0.5 mM. Chenodeoxycholic acid of 10 times of the dye concentration was added in the dye solution to prevent aggregation of the dye molecules (will be indicated in the text). Sonication may be applied to help to dissolve.

2.3.3.2 Preparing counter electrodes

Bare FTO glass slide was cut into small pieces (2 cm by 2 cm). Two holes were drilled on the small pieces of glass before cleaning. The pre-drilled FTO glass was sequentially sonicated in soap water solution, distilled water, 0.1 M HCl ethanol solution, and acetone. The organic residual was removed by heating at 400 °C for 30 minutes. A layer of Pt was deposited onto the glass by drop-casting 15 µL of 5 mM solution of chloroplatinic acid (HPtCl₆) in IPA and heating at 380 °C for 20 min.

2.3.3.3 Preparing electrolyte

Tiiodide/iodide electrolyte contained 0.6 M LiI, 0.03 M I₂ and 0.5 M 4-tert-butylpyridine (TBP). Co^{3+/2+} electrolyte contained 0.2 M Co(II) species, 0.02 M Co(III) species and 0.1 M Li salt (the detailed chemical composition will be mentioned in the result and discussion section. The solvent used was acetonitrile, propylene carbonate, or gamma-butyrolactone.

2.3.3.4 Cell assembling

25 μm thick Surlyn film (Solaronix) with a self-cut square hole was used as a spacer and was sandwiched between the photoanode and counter electrodes. By pressing on the top glass slide and heating at 145 $^{\circ}\text{C}$, Surlyn film will be heated and form the connection between electrodes. Electrical contact was achieved using silver epoxy to connect copper wire and the FTO substrate (the ALD TiO_2 blocking layer on the photoanode was gently scraped off by sandpaper). The epoxy was cured at 80 $^{\circ}\text{C}$ for 15 min. The electrolyte was filled afterward into the sandwich cell through the pre-drilled holes on the counter electrode. The holes were then covered with pre-cleaned microglass slides and Surlyn film.

As for the “Sample cells” for the light-harvesting experiment, a similar procedure was used to make sandwich cells as stated above. Transparent glass slide was used instead of FTO glass.

2.3.4 General methods for the characterization of DSSCs.

Current density to the potential change (JV) measurement was done by connecting the anode of the DSSC to the positive side of the potentiostat and the counter electrode to the negative side. This makes a two-electrode system with cathode being both the reference and counter electrode. The illumination was achieved by using a short arc lamp, and the light beam passed through the AM 1.5 filter to match the solar spectrum. The power density of the incident light was calibrated by the power meter before measuring. 1 sun condition was 100 mW/cm^2 . A 400 nm long-pass filter was used to block UV light, and a black mask on the DSSC was used to block scattered or reflected light.

Open circuit voltage decay (OCVD) measurements were done by connecting the cell as described before. The illumination time was usually 15 s during which period the measured potential can

reach a stable value. Then the incident light was blocked by the shutter, and the V_{OC} was monitored over time. The time interval of the potential measurement was 0.05 s, which is longer than the instrument response to avoid useless points.

Current transient (CT) measurement was done by measuring the J_{SC} response over time when the incident light was switched from off to on.

Incident photon to current conversion efficiency (*IPCE*) was measured under monochromatic light illumination. The light source passed through a monochromator, and the resolution achieved was 8 nm. Therefore, the wavelength interval was controlled to be 10 nm. The J_{SC} was measured at each wavelength from 2 to 7 seconds after rotating the grating. The power density of the light source was measured by the power meter with a surface area of 0.71 cm².

For light-harvesting efficiency (*LHE*) measurement, integrating sphere was used with Lambda 35 (PerkinElmer) spectrometer to collect the transmitted and reflected light by the sandwich cell. Transmittance (T%) and reflectance (R%) were measured and used to calculate the *LHE*.

The dye loading amount on the nanoporous TiO₂ film was measured by desorption. TiO₂ films were made using the same method as before. After soaking in the dye solution, loosely bonded dyes were washed off by methanol, acetone, and air dried. 0.01 M NaOH stock solution was made for the dye desorption. A calibration curve was made by dissolving dyes in 0.01 M NaOH and measuring the absorbance.

2.4 Result and discussion

2.4.1 Structure of the copper dye

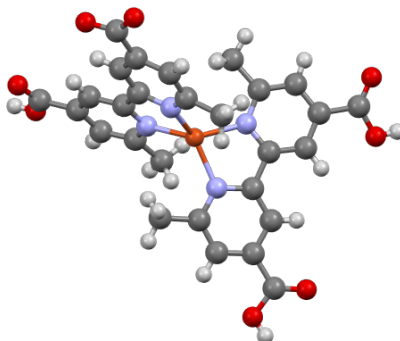


Figure 2.2 Crystal structure of $\text{Cu}(\text{dmdbcby})_2\text{Cl}$ solved by single-crystal X-ray diffraction. Oxygen (red), carbon (gray), hydrogen (white), nitrogen (blue), and copper (center red) atoms are shown (see Appendix Table 2.1-2.2 and the notes for the detailed crystallography data).

$\text{Cu}(\text{dmdbcby})_2\text{Cl}$ has a slightly flattened tetrahedral geometry with the dihedral angle between two ligand planes (N1-Cu1-N2 and N3-Cu1-N4) being 78.72° . The Cu(I) center is coordinated by two 6,6'-dimethyl-2,2'-bipyridine-4,4'-dicarboxylic acids. During the synthetic process, NaOH deprotonates the carboxylic acid on the ligand and helps to dissolve it in water. At the same time NaOH reacts with the copper precursor, CuSO_4 , to form cupric hydroxide. Upon the addition of ascorbic acid Cu^{2+} gets reduced to form the dye molecule with the deprotonated dmdbcby ligands. The solution becomes dark red and remains basic. When the pH is adjusted to 2, the protonated dye molecule is no longer soluble in water and red precipitate forms. The elemental analysis confirmed the existence of the chlorine anion in the solid structure. But no chlorine was observed in the single crystal structure. One of the carboxyl groups is deprotonated and balances the charge of Cu(I). Chlorine anion is not in the coordinating sphere and is not in the crystal structure of this complex.

Both the solid $\text{Cu}(\text{dmdbcby})_2\text{Cl}$ and the solution of it are stable in air. NMR and elemental analysis were used to confirm the structure of the complex. The solubility of $\text{Cu}(\text{dmdbcby})_2\text{Cl}$ was poor

(<0.3 mM in MeOH). A synthetic method in nonaqueous solvent was therefore developed to make the PF₆⁻ salt analog. Cu(MeCN)₄PF₆ is used as copper precursor and can react with dmcbpy in THF mixture to get Cu(dmcbpy)₂PF₆. However, the solubility of this analog is still less than 1 mM in AcN, which is necessary for electrochemical measurements like CV scan. Therefore, the ethyl ester analog of the dye, Cu(dmdebpy)₂PF₆, was made to increase the solubility it in organic solvent for electrochemical measurement.

2.4.2 Electrochemical and photophysical measurement

The redox potential of molecules can be measured in organic solutions and on ITO nanoporous film. The CV curves of Cu(dmcbpy)₂PF₆ are shown in Figure 2.3.

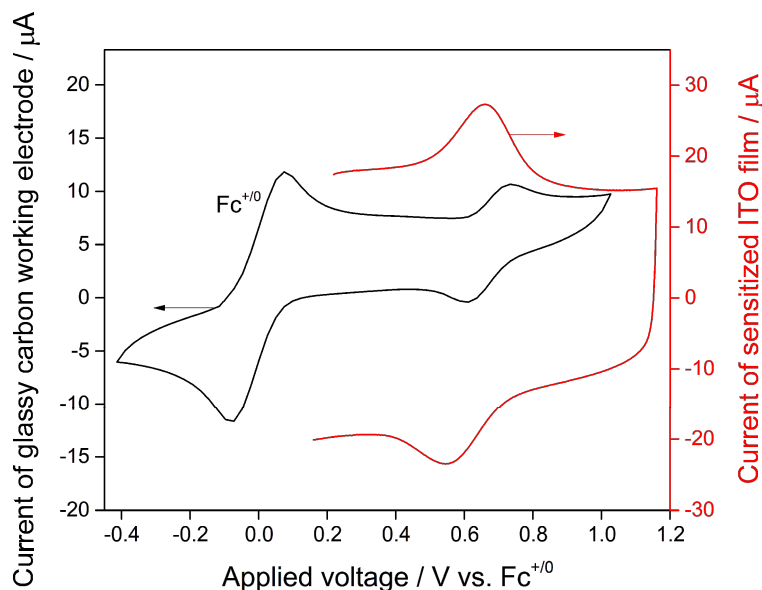


Figure 2.3 Black curve is the CV plot of Cu(dmdebpy)₂PF₆ and ferrocene in DCM on a glassy carbon working electrode. Ferrocene was used as an internal potential reference. The red curve is the CV plot of Cu(dmcbpy)₂Cl sensitized ITO film in AcN. The electrolyte has 0.1 M TBAPF₆ as supporting electrolyte. Both scans are taken under an inert atmosphere using dry solvents. The scan rate was 200 mV/s.

There are different binding modes for dyes with carboxylic functional groups to bind onto nanoporous semiconductor, but they all involved the deprotonation of the carboxylic groups.²⁴ The redox potential of Cu(dmcbpy)₂Cl attached onto ITO film in AcN is mimicking the practical

condition that the dyes bind onto the TiO_2 in DSSCs. As shown by the red curve in Figure 2.3, the sensitized ITO film shows a pair of redox waves centered at 0.60 V in AcN and 0.73 V vs. $\text{Fc}^{+/0}$ in DCM. The CV of the ethyl ester analog, $\text{Cu}(\text{dmdebpy})_2\text{PF}_6$, in DCM is shown by the black curve in Figure 2.3, with a pair of redox waves centered at 0.67 V vs. $\text{Fc}^{+/0}$ in DCM. The same method was used to measure the redox potential of N3 dye. When attached onto ITO, the redox wave of N3 was not reversible and the redox potential was estimated to be 0.80 V vs $\text{Fc}^{+/0}$ in DCM (see Appendix Figure 2.13). When dissolved in AcN, N3 shows two pairs of redox waves centered at 0.49 and 0.82 V vs. $\text{Fc}^{+/0}$ respectively (see Appendix Figure 2.11). Compared to N3 dye, the redox potential of $\text{Cu}(\text{dmcbpy})_2\text{Cl}$ on the film is 90 mV negative, and it shifts more drastically in different solvents (comparing Figure 2.3 red and Appendix Figure 2.12). The solvent dependence was explained by Scaltrito, that it is due to the addition of the solvent molecule to the coordinating sphere once the copper undergoes oxidation.²⁵

The solvent dependence was not observed on the absorption measurement (see Appendix Figure 2.14). When comparing the absorption property of N3 and $\text{Cu}(\text{dmcbpy})_2\text{Cl}$, as shown in Figure 2.4, both dyes absorb strongly in the visible region. The extinction coefficient of $\text{Cu}(\text{dmcbpy})_2\text{Cl}$ is not as high as N3 dye, but they are on the same order of magnitude due to the MLCT nature of the bands.

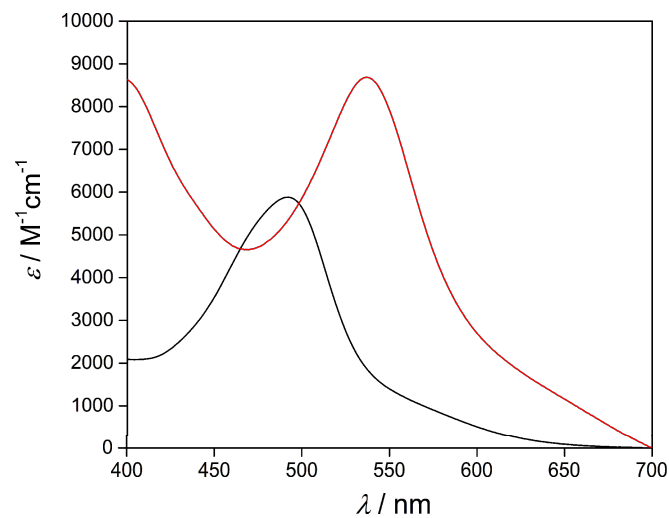


Figure 2.4 The absorption spectra of dyes in solution. The black curve is the absorption spectrum of N3 dye. The red curve is the absorption spectrum of $\text{Cu}(\text{dmdbcipy})_2\text{Cl}$. Both are measured in dry methanol under an inert atmosphere with 1 cm path length cuvette.

2.4.3 DSSCs with triiodide/iodide redox couple

DSSCs were made with $\text{Cu}(\text{dmdcbpy})_2\text{Cl}$ and N3 dye and triiodide/iodide redox couple. As shown in Figure 2.5, $\text{Cu}(\text{dmdcbpy})_2\text{Cl}$ sensitized solar cells have lower V_{OC} and J_{SC} compared to the N3 sensitized cells and thus much lower conversion efficiency. Since these two batches of DSSCs used the same material and techniques during assembling, the only different element which introduces the difference in performance should be the sensitizer. As described in Equation 2.1, the magnitude of J_{SC} is controlled by different quantum efficiencies. The electron injection efficiency (η_{inj}), dye regeneration efficiency (η_{reg}), and light-harvesting efficiency (LHE_{λ}) are all sensitizer dependent. And the charge collection efficiency (η_{cc}) mainly depends on the redox couple used in the cells.

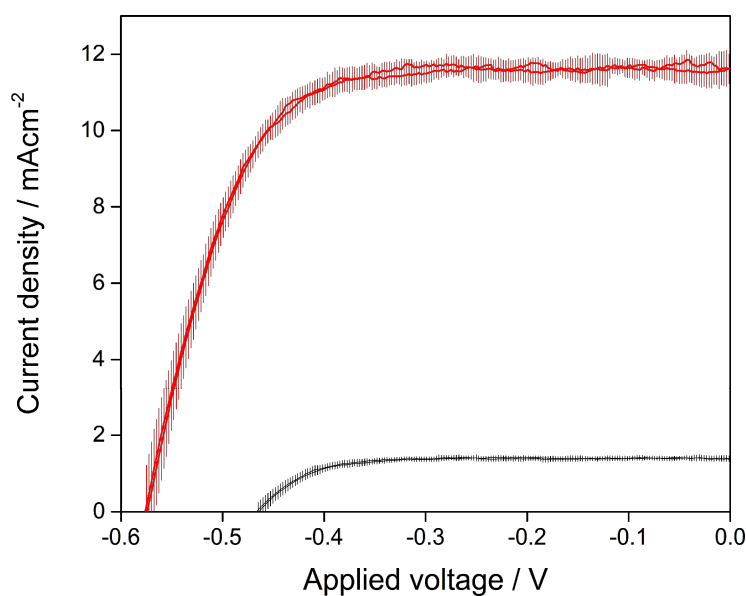


Figure 2.5 JV curves of DSSCs with different dyes. The red curve is the averaged JV curve of cells with N3 sensitizer. The black curve is the averaged JV curve of cells with $\text{Cu}(\text{dmdcbpy})_2\text{Cl}$ sensitizer. Error bars are from the standard deviation between samples (more than 3 samples for each condition). DSSCs have anodes with a $7\ \mu\text{m}$ transparent layer and $5\ \mu\text{m}$ scattering layer TiO_2 . Electrolyte contains $0.6\ \text{M LiI}$, $0.03\ \text{M I}_2$ and $0.5\ \text{M TBP}$ in acetonitrile. The counter electrode is Pt coated FTO glass. $15\ \mu\text{m}$ thick Surlyn film is used between anode and cathode as spacer. Cells were measured under 1 sun condition with AM 1.5 spectrum.

$$J_{SC} = q \left(\int_{\lambda} \Phi_{\lambda} LHE_{\lambda} d\lambda \right) \eta_{inj} \eta_{reg} \eta_{cc} \quad (2.1)$$

$$IPCE_{\lambda} = LHE_{\lambda} \eta_{inj} \eta_{reg} \eta_{cc} = LHE_{\lambda} APCE_{\lambda} \quad (2.2)$$

In the above equations, q is the elementary charge. Φ_{λ} is the incident photon flux at each wavelength. This should have the same value as the AM 1.5 solar spectrum when the incident light is used as 1 sun condition. $APCE_{\lambda}$ is the absorbed photon to current conversion efficiency. The different current response can be a result of the difference in different quantum efficiencies. $IPCE_{\lambda}$, LHE_{λ} and $APCE_{\lambda}$ of N3 and Cu(dmdcbpy)₂Cl sensitized cells are shown in Figure 2.6. The maximum of the $IPCE_{\lambda}$ curve for N3 cells is at a longer wavelength than that for copper cells which is consistent with the absorption spectra of two dyes. LHE_{λ} was calculated by using sample sandwich cells, which used highly transparent micron glass slides as substrate. The absorption by triiodide/iodide electrolyte has a larger influence on the light-harvesting of Cu(dmdcbpy)₂Cl sensitized cells and the effect has been corrected in the calculation. The correction of the absorption from FTO was corrected when calculating $APCE_{\lambda}$ (see Appendix for calculation details). At wavelength between 650 and 700 nm, the calculated $APCE$ is larger than 100%, which is resulted from the low values from both $IPCE$ and LHE at those wavelengths. Because the dyes do not absorb strongly at wavelengths longer than 650 nm, the errors accumulated during the measurements of the current output, the absorptivity of sample cells, and during the calculation of LHE at these wavelengths can be huge. The error bars introduced in Figure 2.6 is only the standard deviation of values obtained between different samples.

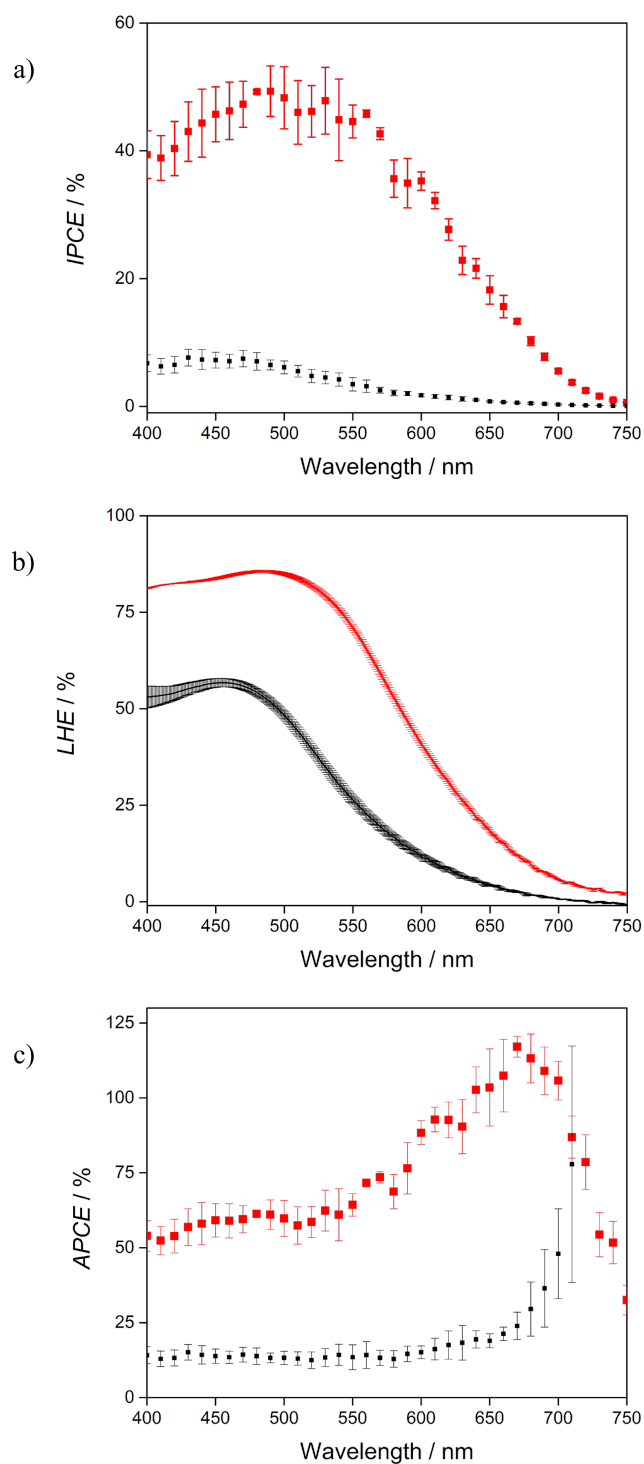


Figure 2.6 a) $IPCE_{\lambda}$ b) LHE_{λ} and c) $APCE_{\lambda}$ curves of cells. Red curves are for cells with N3 sensitizer. Black curves are for cells with $Cu(dmcbpy)_2Cl$ sensitizer. Error bars are from the standard deviation between samples. Electrolyte contains 0.6 M LiI, 0.03 M I_2 and 0.5 M TBP in acetonitrile. The counter electrode is Pt coated FTO glass. 25 μm thick Surlyn film is used between anode and cathode as a spacer.

The lower *IPCE* and *LHE* of Cu(dmdcbpy)₂Cl cells compared to N3 cells over the whole spectrum is a direct reflection of the bad photon capturing ability (absorptivity) of the photoanode. The absorptivity of the photoanode are controlled by two parameters, the absorptivity of the dye and the dye coverage on the film. It is already known from the absorption spectra of both dyes that the extinction coefficients of Cu(dmdcbpy)₂Cl are lower than N3 in all wavelength. Also we tested the dye coverage of both dyes and our result suggested that the dye coverage for both N3 and Cu(dmdcbpy)₂Cl dyes on the 8 μm thick TiO₂ nanoporous films are of the same magnitude, being 10⁻⁸ mol/cm² (see Appendix for the measurement of dye coverage).²⁶ Therefore, it is necessary to design new ligands for making copper sensitizers with higher extinction coefficients and improve the absorptivity of the photoanode.

The low light absorptivity is only one reason for the low photocurrent response, but it can not be the only reason. As shown in Figure 2.6c, the *APCE*_λ value of N3 cells is much higher than the value for Cu(dmdcbpy)₂Cl sensitized cells. Unlike *LHE*_λ, *APCE*_λ is the internal conversion efficiency of DSSCs and it is only controlled by the three quantum efficiencies as listed in Equation 2.2. Among the whole wavelength range, the *APCE* value for Cu(dmdcbpy)₂Cl DSSCs is around 1/3 of that for N3 DSSCs. This indicates that some, or all, of the three quantum yields that contribute to the value of *APCE* (η_{inj} , η_{reg} , and η_{cc}) are lower for Cu(dmdcbpy)₂Cl DSSCs than for N3 DSSCs.

The η_{cc} represents the kinetic competition between the electron transport within the porous semiconductor film toward the photoanode, and the recombination by intercepting of the electron with the electron acceptor in the electrolyte. In the electrolyte used for the cells, I₃⁻ is the electron acceptor near the photoanode. Electron diffusion distance of the electron inside the semiconductor

(L_n) is the average distance the electrons can travel before disappearing by recombination, and this can bring insights of η_{cc} . L_n can be expressed by Equation 2.3²⁷:

$$L_n = \sqrt{D_n \tau_n} \quad (2.3)$$

In this equation, D_n and τ_n are the charge diffusion coefficient and the effective electron lifetime inside the semiconductor, respectively. τ_n represents the rate of interception of electrons, and it can be measured by the open-circuit voltage decay (OCVD) based on Equation 2.4.

$$\tau_n = -\frac{k_B T}{e} \left(\frac{dV_{OC}}{dt} \right)^{-1} \quad (2.4)$$

The electron lifetimes under different applied potential of N3 and Cu(dmdcbpy)₂Cl DSSCs are calculated from the data obtained by the OCVD measurement. In both N3 and Cu(dmdcbpy)₂Cl DSSCs, the electrolyte composition was kept the same by using the same concentrations of triiodide/iodide redox couple and supporting electrolyte. Therefore, the applied voltage is referenced to the same reference potential, which is also the thermodynamic potential of the electrolyte on the counter electrode. By applying the same potential, electron densities on TiO₂ film (and the Fermi level of TiO₂) are kept the same for different DSSCs.

As shown in Figure 2.7, Cu(dmdcbpy)₂Cl DSSC has shorter electron lifetime compared to N3 DSSC under the same applied potential. Since the electron-accepting species in the electrolyte are the same for both systems, the shorter electron lifetime for Cu(dmdcbpy)₂Cl DSSCs should be introduced by the dye. If the dye⁺ is not efficiently reduced by the I⁻, the recombination can happen to the dye⁺. Since Cu(dmdcbpy)₂Cl has a less positive redox potential than N3, the driving force for regenerating the dye⁺ is smaller for Cu(dmdcbpy)₂Cl which can result in a faster recombination of the electrons to dye⁺. Additionally, if the electron-accepting species has a higher local

concentration near the photoanode, by the interaction with Cu^{2+} center, the recombination to the electrolyte can also be faster. Both factors are related to the reaction kinetics between $\text{Cu}(\text{dmdcbpy})_2\text{Cl}$ and I^- .

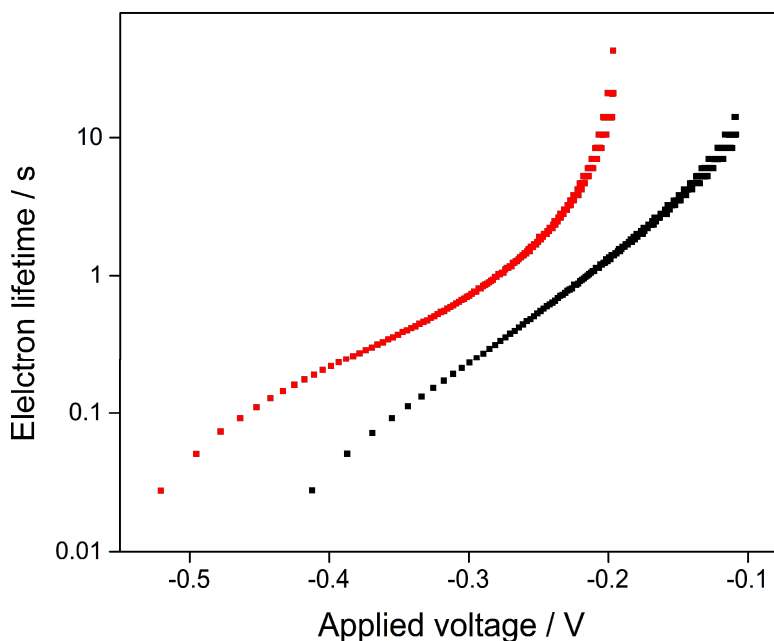


Figure 2.7 Electron lifetime plot under different applied voltage between photoanode and counter electrode of DSSCs. The red curve is the representative electron lifetime curve of DSSCs with N3 sensitizer. The black curve is the representative electron lifetime curve of DSSCs with $\text{Cu}(\text{dmdcbpy})_2\text{Cl}$ sensitizer. Electrolyte contains 0.6 M LiI, 0.03 M I_2 and 0.5 M TBP in acetonitrile. The counter electrode is Pt coated FTO glass. 25 μm thick Surlyn film is used between anode and cathode as a spacer.

So far, we don't have a detailed study about the dye regeneration kinetics of $\text{Cu}(\text{dmdcbpy})_2^{2+}$ by I^- on the surface of the photoanode, but it has been well understood that the I^\cdot radical forms after I^- transfers an electron to the dye⁺.²⁸ The radical reacts with another I^- and forms I_2^\cdot . disproportionation reaction takes place and generates I_3^- . These reactions of iodide species occur fast enough in solution, and therefore electron recombination is mainly due to the reaction with the resulted I_3^- . With $\text{Cu}(\text{dmdcbpy})_2\text{Cl}$ sensitized photoanode, however, the internal reactions between the iodide species can be interrupted. Any electron-rich group has a chance to exciplex

quenching the excited $\text{Cu}(\text{dmdcbpy})_2\text{Cl}$ or coordinate the oxidized $[\text{Cu}(\text{dmdcbpy})_2]^{2+}$.²⁹ As a result, it will build up the concentrations of different electron acceptors near the TiO_2 surface. Triiodide/iodide redox couple works well for N3 because of their fast dye regenerating and the slow recombination kinetics. But with $\text{Cu}(\text{dmdcbpy})_2\text{Cl}$, the advantages may not exist.

We also tested the reversibility of the electrochemical properties of $\text{Cu}(\text{dmdcbpy})_2\text{Cl}$ on the film with the presence of 4-tert-butylpyridine in the electrolyte. Although TBP is a neutral ligand, it has the lone pair of electrons on the pyridyl nitrogen than can coordinate to positively charged metal centers. The CV curve is shown in Figure 2.8.

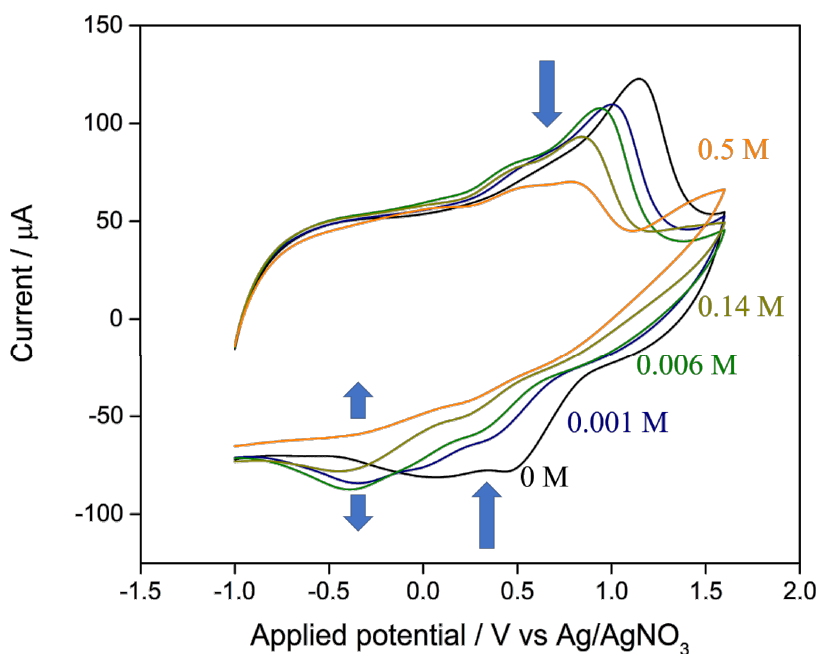


Figure 2.8 CV of $\text{Cu}(\text{dmdcbpy})_2\text{Cl}$ on ITO film measured in DCM. The concentrations of TBP in the electrolyte are indicated in the graph.

By attaching $\text{Cu}(\text{dmdcbpy})_2\text{Cl}$ on ITO film, the flexibility of the molecule is expected to be less than in solution. The addition of TBP induced some changes in the CV curve under different concentrations. But more strikingly is when TBP is at the same concentration as in the electrolyte

for DSSCs, 0.5 M, the reversibility of $\text{Cu}(\text{dmdebpy})_2\text{Cl}$ on ITO film almost disappeared. We attribute this to the coordinating behavior that TBP has on the Cu^{2+} center. Considering the electron density of the neutral TBP ligand, the coordinating ability of the negatively charged iodide species should be much higher. This supports our hypothesis that the coordinating species in the electrolyte hurts the performance of the cells with copper sensitizers

2.5 Research summary

Electrochemical and photophysical measurements all suggest that $\text{Cu}(\text{dmdebpy})_2\text{Cl}$, as a model copper centered sensitizer, should perform similarly as a ruthenium centered N3 dye in DSSCs. However, in this chapter, we have shown that with the same triiodide/iodide redox couple, DSSCs sensitized by $\text{Cu}(\text{dmdebpy})_2\text{Cl}$ showed much lower current conversion efficiency than N3. The research was performed to look for the limiting factors for lousy performance. By noticing how much the neutral TBP ligand in the electrolyte can change the electrochemical property of $\text{Cu}(\text{dmdebpy})_2\text{Cl}$ attached to the film, we propose that the triiodide/iodide electrolyte contains negatively charged species and may coordinate to Cu^{2+} center. This coordination can quench the excited state of the dye, lower the regeneration rate and induce fast recombination. Further research should be done to prove this hypothesis.

APPENDIX

APPENDIX

The home-made reference electrode has used for the electrochemical measurement. The glass tubes used for the reference electrode were cleaned and dried before assembling. Silver wire was first polished using sandpaper and dipped into concentrated nitric acid for 5 min. In the acid, the silver wire will be coated with a layer of silver nitrate. The coated silver wire was rinsed with water and dried before assembling. A piece Pt wire was melted into the clean glass tube. Fritz was connected to the second glass tube with polymer sleeve. Solution used in the reference electrode was made freshly and was changed every month or anytime necessary. As shown in Figure 2.9, a salt bridge was used to prevent the leaking of silver ion.

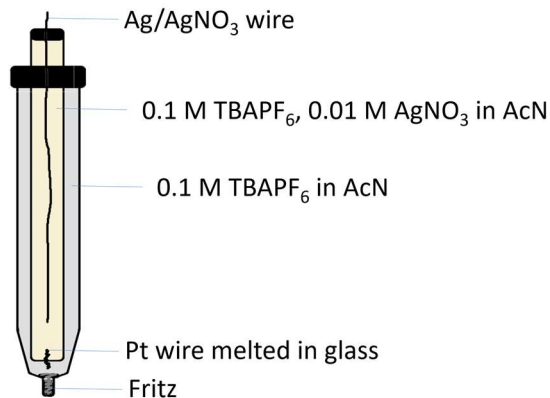


Figure 2.9 The home-made reference electrode.

Compound Cu(dmdcbpy)₂Cl

Formula C_{38.5}H_{34.5}CuN₄O₈
*D*_{calc.}/ g cm⁻³ 1.454
 μ /mm⁻¹ 0.703
 Formula Weight 744.74
 Colour yellow
 Shape needle
 Max Size/mm 0.46
 Mid Size/mm 0.05
 Min Size/mm 0.02
T/K 173(2)
 Crystal System monoclinic
 Space Group P2₁/c
a/Å 12.1764(18)
b/Å 19.523(3)
c/Å 15.325(2)
 α /° 90
 β /° 110.974(2)
 γ /° 90
V/Å³ 3401.7(9)
Z 4
Z' 1
 \mathcal{O}_{min} /° 1.764
 \mathcal{O}_{max} /° 25.379
 Measured Refl. 27285
 Independent Refl. 6247
 Reflections Used 2769
*R*_{int} 0.1668
 Parameters 423
 Restraints 0
 Largest Peak 0.707
 Deepest Hole -0.495
 GooF 0.993
*wR*₂ (all data) 0.2193
*wR*₂ 0.1622
*R*₁ (all data) 0.1917
*R*₁ 0.0759

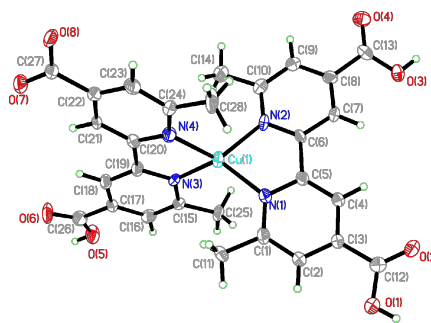


Figure 2.10 Crystal structure of Cu(dmdcbpy)₂Cl.

Table 2.1 Bond lengths in Å for Cu(dmdcbpy)₂Cl

Atom	Atom	Length/Å
Cu1	N1	2.033(5)
Cu1	N2	2.035(5)
Cu1	N3	2.020(5)
Cu1	N4	2.040(5)

Table 2.2 Bond angles in ° for Cu(dmdcbpy)₂Cl

Atom	Atom	Atom	Angle/°
N1	Cu1	N2	81.1(2)
N1	Cu1	N4	132.7(2)
N2	Cu1	N4	117.4(2)
N3	Cu1	N1	121.8(2)
N3	Cu1	N2	129.7(2)
N3	Cu1	N4	81.2(2)

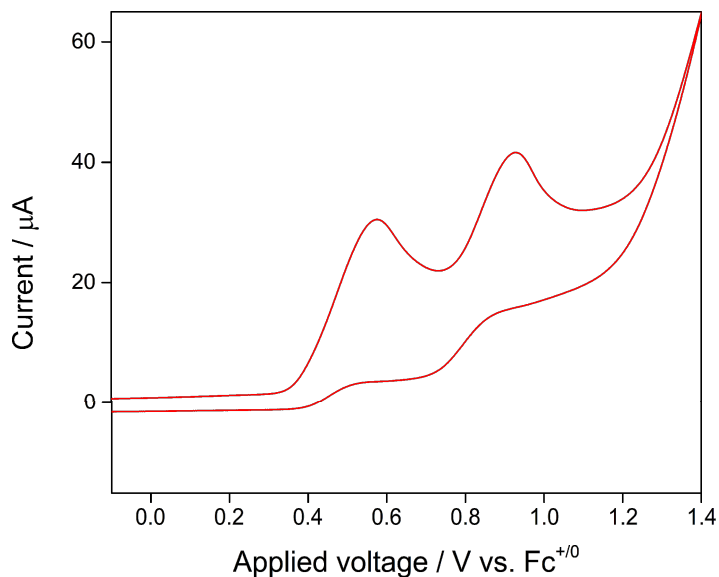


Figure 2.11 CV of 4 mM N3 dye in AcN. Working electrode was glassy carbon disk. Reference electrode was Ag/AgNO₃ (0.01 M in AcN). Counter electrode was Pt mesh. Supporting electrolyte was 0.1 M TBAPF₆. Scan rate was 0.1 V/s. $E_{1/2}$ for two pairs of waves are 0.49 and 0.81 V vs Fc⁺⁰.

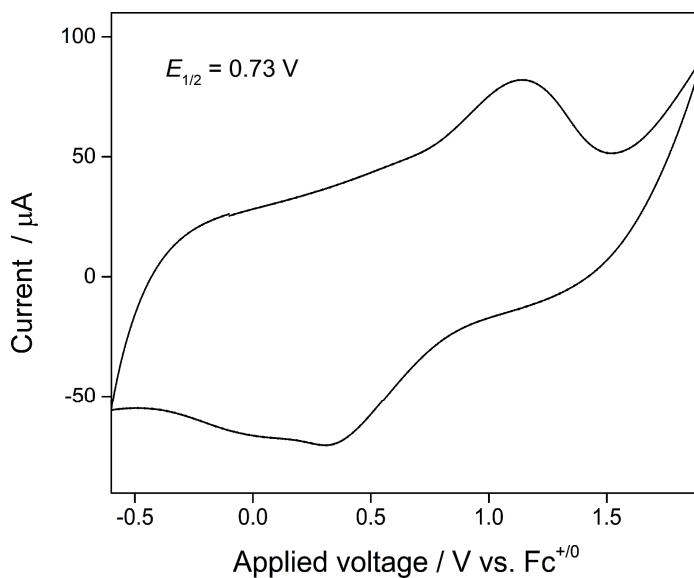


Figure 2.12 CV of Cu(dmcbpy)₂Cl on ITO film in DCM. Working electrode was Cu(dmcbpy)₂Cl sensitized ITO nanoporous film. Reference electrode was Ag/AgNO₃ (0.01 M in AcN). Counter electrode was Pt mesh. Supporting electrolyte was 0.1 M TBAPF₆. Scan rate was 0.1 V/s.

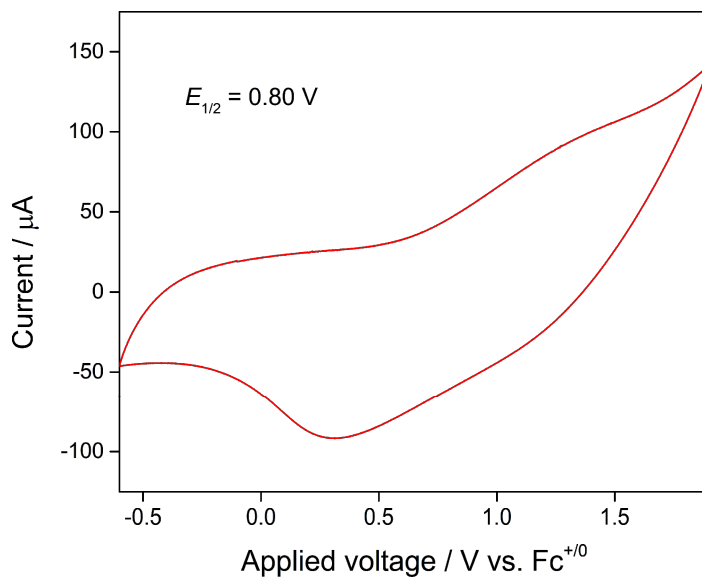


Figure 2.13 CV of N3 on ITO film in DCM. Working electrode was N3 sensitized ITO nanoporous film. Reference electrode was Ag/AgNO₃ (0.01 M in AcN). Counter electrode was Pt mesh. Supporting electrolyte was 0.1 M TBAPF₆. Scan rate was 0.1 V/s.

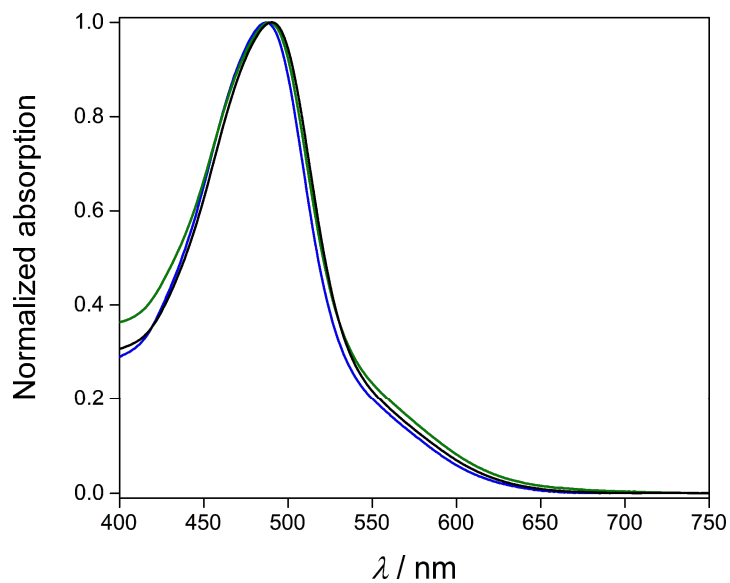


Figure 2.14 UV-vis of Cu(dmdcbpy)₂Cl in MeOH/DCM 1:1 v/v mixture (green), MeOH (blue) and water (black).

The light harvesting efficiency is calculated by a series of Equations 2.5 - 2.8.

$$\alpha_{\text{dye}} = -\frac{1}{d_{\text{TiO}_2}} \ln \left(\frac{T_{\text{comp.cell}}}{1 - R_{\text{comp.cell}}} \right) \quad (2.5)$$

$$\alpha_1 = -\frac{1}{d_1} \ln \left(\frac{T_1}{1 - R_1} \right) \quad (2.6)$$

$$d_1 = d_{\text{spacer}} - d_{\text{TiO}_2} + d_{\text{TiO}_2} \times 70\% \quad (2.7)$$

$$LHE\% = \frac{(1 - R_{\text{FTO}}) \alpha_{\text{dye}} \left(1 - e^{-(\alpha_{\text{dye}} + \alpha_1) d_{\text{TiO}_2}} \right)}{\alpha_{\text{dye}} + \alpha_1} \quad (2.8)$$

The measured parameters are the transmittance and reflectance of a complete sandwich cell ($T_{\text{comp.cell}}$ and $R_{\text{comp.cell}}$), the transmittance and reflectance of a sandwich cell without dye (T_1 and R_1), the thickness of the TiO_2 film (d_{TiO_2}) and the reflectance of FTO glass (R_{FTO}). Calculated parameters are the absorption coefficient of dye sensitized TiO_2 film (α_{dye}), the absorption coefficient of triiodide/iodide electrolyte (α_1), the thickness of the triiodide/iodide electrolyte layer (d_1) and the light harvesting efficiency (LHE). $APCE$ can be calculated by Equation 2.9.

$$APCE = \frac{IPCE}{LHE} \times 100\% \quad (2.9)$$

The dye coverage on TiO_2 surface was measured first by the desorption method. Dye sensitized TiO_2 nanoporous films were prepared by the same method as preparing the photoanode for DSSCs. Dyes used are N3, N719 and $\text{Cu}(\text{dmdcbpy})_2\text{Cl}$. The extinction coefficient of each dye dissolved in 10 mM NaOH solution in water are measured, as shown in Figure 2.15. Three of the dye sensitized TiO_2 film on glass substrate were prepared for each dye. Each piece of glass was immersed into 5 mL of 10 mM NaOH water solution and stored in the dark. After 48 hours, the absorption of each solution containing desorbed dye was measured, as shown in Figure 2.16. Three samples of each dye were prepared, and the error is from the standard deviation between samples. The number of

dye molecules desorbed from each sample are calculated. The dye coverage of N3 is 3.8×10^{-8} ($\pm 9.7 \times 10^{-10}$) mol/sample, and of $\text{Cu}(\text{dmdcbpy})_2\text{Cl}$ is 1.9×10^{-9} ($\pm 1.9 \times 10^{-10}$) mol/sample.

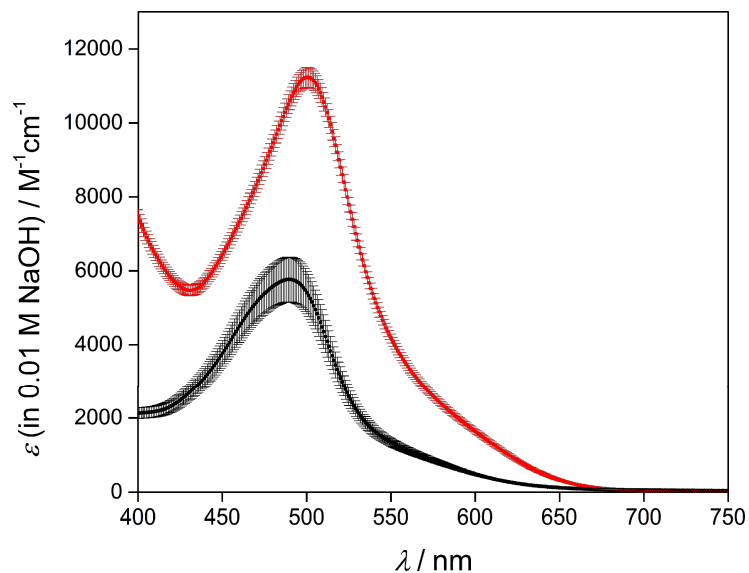


Figure 2.15 Extinction coefficient of $\text{Cu}(\text{dmdcbpy})_2\text{Cl}$ (black) and N3 (red) in 10 mM NaOH water solution. Errors are from the standard deviation between different samples of the same dye.

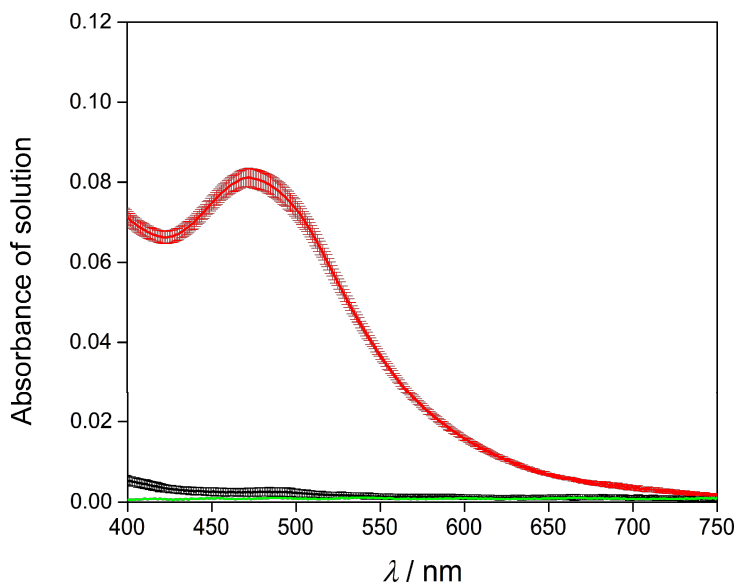


Figure 2.16 Absorption spectrum of desorbed dye in 10 mM NaOH water solution, 10 mM NaOH in water (green), $\text{Cu}(\text{dmdcbpy})_2\text{Cl}$ (black) and N3 (red). Errors are from the standard deviation between different samples of the same dye.

The relationship between *LHE* and the dye coverage on the film can be expressed by Equation 2.10.³⁰

$$LHE_{\lambda} = 1 - 10^{-\Gamma\sigma_{\lambda}} \quad (2.10)$$

$$\sigma_{\lambda} = \varepsilon_{\lambda} \times 1000 \quad (2.11)$$

In Equation 2.10, Γ is the surface coverage of dye in mol/cm² of the projected surface area. The projected area was 0.36 cm². σ_{λ} is the absorption cross section in cm²/mol. The relationship between the absorption cross section and the extinction coefficient is shown in Equation 2.11. The extinction coefficient has a unit of M⁻¹cm⁻¹ and the multiplier is 1000 cm³/L.

Using the experimental value for the dye coverage, the light harvesting efficient can be calculated. The calculated *LHE* are 91.2 (±0.55) % and 7.05 (±0.65) % for N3 and Cu(dmdcbpy)₂Cl at their absorption maximum wavelength. The calculated *LHE* value for N3 has a 4% error compared to the experimental value (Figure 2.6). However, the calculated *LHE* value for Cu(dmdcbpy)₂Cl has an 87% error compared to the experimental value. The dye coverage of Cu(dmdcbpy)₂Cl was highly underestimated when measured by the desorption method.

We then used Equation 2.10 to back calculate the dye coverage with the measured *LHE* value and the measured extinction coefficient. The calculated dye coverage for N3 and Cu(dmdcbpy)₂Cl are 11.7 (±3) × 10⁻⁸ mol/cm² and 7.6 (±1.8) × 10⁻⁸ mol/cm² respectively, on the 8 μm TiO₂ nanoporous film.

REFERENCES

REFERENCES

- (1) United Nations. *The Paris Agreement*; <https://unfccc.int/process-and-meetings/the-paris-agreement/the-paris-agreement>
- (2) Lopez, A.; Roberts, B.; Heimiller, D.; Blair, N.; Porro, G., U.S. Renewable Energy Technical Potentials: A GIS-Based Analysis, *Natl. Renew. Energy Lab. Doc.* **2012**.
- (3) O'Regan, B.; Grätzel, M. *Nature* **1991**, *353*, 737
- (4) Tang, H.; Prasad, K.; Sanjinès, R.; Schmid, P. E.; Lévy, F. *J. Appl. Phys.* **1994**, *75*, 2042
- (5) Housecroft, C. E.; Constable, E. C. *Chem. Soc. Rev.* **2015**, *44*, 8386
- (6) Bessho, T.; Constable, E. C.; Graetzel, M.; Hernandez Redondo, A.; Housecroft, C. E.; Kylberg, W.; Nazeeruddin, M. K.; Neuburger, M.; Schaffner, S. *Chem. Commun.* **2008**, *32*, 3717
- (7) Hernandez Redondo, A.; Constable, E. C.; Housecroft, C. E. **2008**, *63*, 205
- (8) Constable, E. C.; Hernandez Redondo, A.; Housecroft, C. E.; Neuburger, M.; Schaffner, S. *Dalton Trans.* **2009**, *33*, 6634
- (9) Colombo, A.; Dragonetti, C.; Fagnani, F.; Roberto, D.; Melchiorre, F.; Biagini, P. *Dalt. Trans.* **2019**, *48*, 9818
- (10) Polander, L. E.; Yella, A.; Curchod, B. F. E.; Ashari Astani, N.; Teuscher, J.; Scopelliti, R.; Gao, P.; Mathew, S.; Moser, J.-E.; Tavernelli, I.; Rothlisberger, U.; Grätzel, M.; Nazeeruddin, M. K.; Frey, J. *Angew. Chemie Int. Ed.* **2013**, *52*, 8731
- (11) Alonso-Vante, N.; Nierengarten, J.-F.; Sauvage, J.-P. *J. Chem. Soc. Dalt. Trans.* **1994**, *11*, 1649
- (12) Sakaki, S.; Kuroki, T.; Hamada, T. *J. Chem. Soc. Dalt. Trans.* **2002**, *6*, 840
- (13) Bozic-Weber, B.; Brauchli, S. Y.; Constable, E. C.; Furer, S. O.; Housecroft, C. E.; Malzner, F. J.; Wright, I. A.; Zampese, J. A. *Dalt. Trans.* **2013**, *42*, 12293
- (14) Baldenebro-Lopez, J.; Flores-Holguin, N.; Castorena-Gonzalez, J.; Glossman-Mitnik, D. *J. Photochem. Photobiol. A Chem.* **2013**, *267*, 1
- (15) Colombo, A.; Dragonetti, C.; Roberto, D.; Valore, A.; Biagini, P.; Melchiorre, F. *Inorganica Chim. Acta* **2013**, *407*, 204
- (16) Sandroni, M.; Kayanuma, M.; Planchat, A.; Szuwarski, N.; Blart, E.; Pellegrin, Y.; Daniel, C.; Boujtita, M.; Odobel, F. *Dalton Trans.* **2013**, *42*, 10818

- (17) Sandroni, M.; Favereau, L.; Planchat, A.; Akdas-Kilig, H.; Szuwarski, N.; Pellegrin, Y.; Blart, E.; Le Bozec, H.; Boujtita, M.; Odobel, F. *J. Mater. Chem. A* **2014**, *2*, 9944
- (18) McMillin, D. R.; Kirchoff, J. R.; Goodwin, K. V. *Coord. Chem. Rev.* **1985**, *64*, 83
- (19) Fürer, S. O.; Luu, L. Y. N.; Bozic-Weber, B.; Constable, E. C.; Housecroft, C. E. *Dye. Pigment.* **2016**, *132*, 72
- (20) Fürer, S. O.; Bozic-Weber, B.; Schefer, T.; Wobill, C.; Constable, E. C.; Housecroft, C. E.; Willgert, M. *J. Mater. Chem. A* **2016**, *4*, 12995
- (21) Takada, Y.; Nomura, K.; Matsubara, S. *Org. Lett.* **2010**, *12*, 5204
- (22) Allgäuer, D. S.; Mayr, H. *European J. Org. Chem.* **2013**, 6379
- (23) Mukkala, V.-M.; Kankare, J. J. *Luminescence* **1992**, *75*, 1578
- (24) Lee, K. E.; Gomez, M. A.; Elouatik, S.; Demopoulos, G. P. *Langmuir* **2010**, *26*, 9575
- (25) Scaltrito, D. V.; Thompson, D. W.; O'Callaghan, J. a; Meyer, G. J. *Coord. Chem. Rev.* **2000**, *208*, 243
- (26) Grätzel, M. *J. Photochem. Photobiol. A Chem.* **2004**, *164*, 3
- (27) Barnes, P. R. F.; Liu, L.; Li, X.; Anderson, A. Y.; Kisserwan, H.; Ghaddar, T. H.; Durrant, J. R.; O'Regan, B. C. *Nano Lett.* **2009**, *9*, 3532
- (28) Boschloo, G.; Hagfeldt, A. *Acc. Chem. Res.* **2009**, *42*, 1819
- (29) Lazorski, M. S.; Castellano, F. N. *Polyhedron* **2014**, *82*, 57
- (30) Barnes, P. R. F.; Anderson, A. Y.; Koops, S. E.; Durrant, J. R.; O'Regan, B. C. *J. Phys. Chem. C* **2009**, *113*, 1126

Chapter 3. Ligand exchange between 4-*tert*-butylpyridine and [Cu(dmbpy)₂]²⁺

3.1 Introduction

Copper coordination complexes have been used in the field of energy conversion because of their good electron transfer properties between copper(I) and copper(II). The redox potential of bipyridine and their derivatives coordinated copper complexes are relatively high (0.2 to 0.6 V vs. Fc⁺⁰), therefore they are more stable in ambient condition in their reduced copper(I) form. For the copper(I) complexes with a long-live metal-to-ligand charge transfer (MLCT) band in the visible region, they can be used as photosensitizers in dye-sensitized solar cells (DSSCs). Their fast self-exchange kinetics also makes them good candidates as redox couples in DSSCs. However as mentioned in chapter 1, copper coordination complexes intrinsically are very sensitive to other coordinating species in the surrounding. Tetrahedral is the favored geometry for bipyridyl coordinated copper(I) complexes, and due to Jahn-Teller distortion, distorted tetrahedral or square pyramidal is the favored geometry for the coordinated copper(II) complexes. No matter what role the copper complexes play in the DSSC system, the photosensitizer or the redox couple, the operation of the DSSC relies on the electron transfer of the copper center. This is mediated by the change of the oxidation state of copper center in the complexes. The structural change upon oxidation from Cu⁺ to Cu²⁺ changes the geometry of the bipyridyl copper complexes from tetrahedral to square pyramidal. According to Marcus theory for electron transfer, the reorganization energy is defined as the energy needed for the geometry of reactant to match with the geometry of the product. And the larger the reorganization energy, the slower the electron transfer rate. Therefore, under the presence of other coordinating species, unlike other outersphere redox complexes, copper bipyridyl redox couples will have an affected self-exchange rate. Due to the same reason, copper photosensitizers will have an affected excited-state lifetime.

In the electrolyte of DSSCs, the present coordinating species are not scarce. The effect of triiodide/iodide redox couple on the performance of copper sensitizers has already been studied in the previous chapter. However, the common additive in the liquid electrolyte, 4-*tert*-butylpyridine (TBP) has Lewis basic character. Pyridine derivatives can coordinate to transition metals through the lone pair of electrons on the nitrogen.¹ The high concentration of TBP in the electrolyte (0.4 to 0.6 M) makes it a potential competing ligand to ligate the Cu²⁺ centers (0.02 to 0.05 M). This potential coordination between TBP and Cu(II) center is important for DSSCs applying copper redox couples and DSSCs applying copper sensitizers. In liquid electrolyte, the Cu(II) species is part of the redox couple to mediate electron transfer between electrodes. While on the photoanode, Cu(I) center of the photosensitizer gets oxidized to Cu(II) upon the photoexcitation of its ground. Therefore, the interaction between Cu(II) centers and the attacking ligand in solution can affect both the electronic and photophysical properties of the copper complexes used in DSSCs. This can change the operating mechanism of the DSSCs and must be investigated if we want to control or improve the kinetics of such a system.

Cu(dmbpy)₂OTf is used as a model for this study since the redox pair, [Cu(dmbpy)₂]^{2+/+}, has been used as a redox couple for DSSCs and had good current and voltage output. At the same time, its analogy with -COOH being the anchoring group on the 4, 4' position of the bipyridine act as a good photosensitizer in DSSCs. In both cases, the electrolyte solution of the DSSCs contains high excess amount of TBP relative to the copper complex. It is reasonable to predict that during the electron transfer process, either photoexcitation of the dye molecule on the film or the electronic oxidation of the reduced species in the electrolyte, TBP ligand may find the vacant spot of the oxidized copper complex and coordinate to the Cu²⁺ center. If this is the case, as Marcus theory predicts, the reorganization energy for the electron transfer between copper(I) and copper(II) can

be increased by this structural change, and this harms the overall operational efficiency of the DSSCs.

To understand the chemistry between TBP and the copper complex a solution-based titration method was applied. The result can help us understand the regeneration process of copper dye and the electron transfer through the copper redox couple in the DSSC operation system.

3.2 Experimental methods

3.2.1 Synthetic methods

3.2.1.1 Preparation of Copper(I) bis(6,6-dimethyl-2,2'-bipyridine) triflate, $[Cu(dmbpy)_2]OTf$.

$[Cu(dmbpy)_2]OTf$ was made using a previously published method with modifications.² Under inert atmosphere, 1 equivalent (2.7 mmol) of tetrakisacetonitrile copper(I) triflate (sensitive to moisture and oxygen), $[Cu(MeCN)_4]OTf$, was dissolved in 5 mL of dry acetonitrile. 2.1 equivalents (5.7 mmol) of 6,6'-dimethyl-2,2'-bipyridine, dmbpy, was dissolved in 3 mL of dry dichloromethane. The $[Cu(MeCN)_4]OTf$ solution in acetonitrile was added into dmbpy solution in dichloromethane drop wisely. The transparent solution became dark red upon mixing. The reaction mixture was stirred for half an hour. Since the red product is stable in air, the recrystallization and filtration can be done in air. Diethyl ether was added into the reaction mixture slowly (diethyl ether is not necessary to be dry). Red powders started to crash out when the amount of the added diethyl ether was larger than 15 mL. The precipitates were collected by filtration. The volume of the filtrate can be reduced to 1/5 by the rotary evaporator. Again, diethyl ether was added, and more product was collected. Further purification can be achieved by recrystallize the product in acetonitrile with the addition of diethyl ether.

^1H NMR (500 MHz, Acetonitrile- d_3): δ 8.26 (d, $J = 7.9$ Hz, 4H), 8.02 (t, $J = 7.9$ Hz, 4H), 7.50 (d, $J = 7.7$ Hz, 4H), 2.23 (s, 12H).

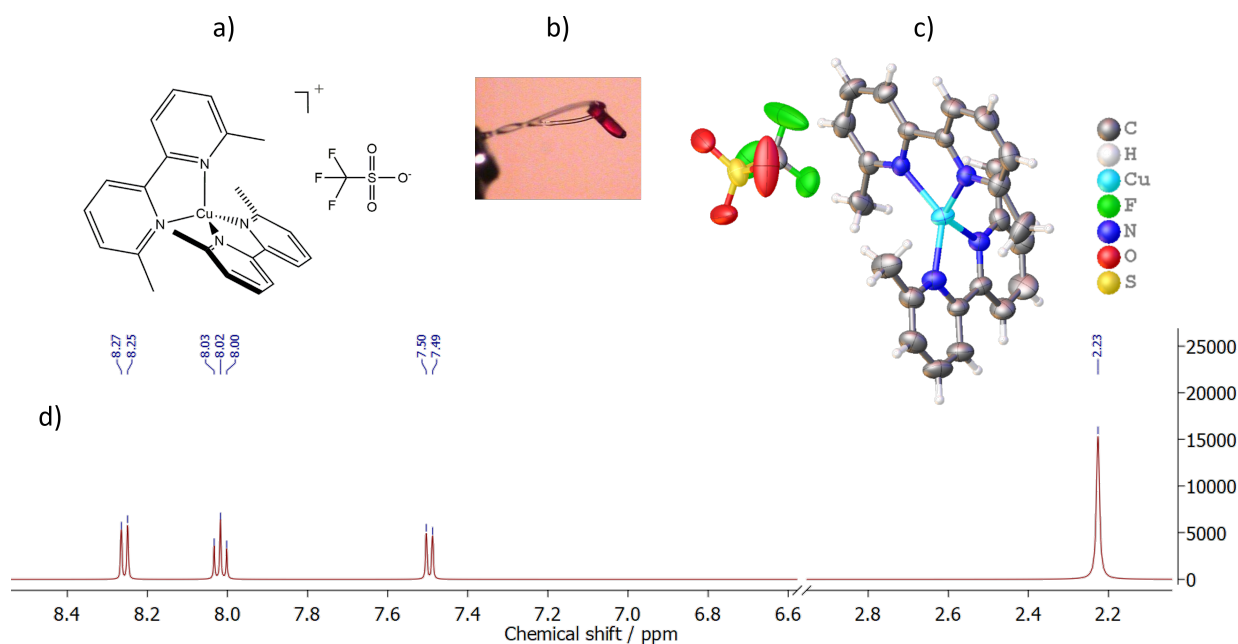


Figure 3.1 **a)** Molecular drawing of $[\text{Cu}(\text{dmbpy})_2]\text{OTf}$. **b)** Red crystal of $[\text{Cu}(\text{dmbpy})_2]\text{OTf}$, formed by diethyl ether diffusion method into acetonitrile. **c)** The molecular structure measured by single-crystal XRD (see Appendix for more detailed crystallography information). **d)** ^1H NMR spectrum of $[\text{Cu}(\text{dmbpy})_2]\text{OTf}$ in CD_3CN .

3.2.1.2 Preparation of Copper(II) aqua bis(6,6-dimethyl-2,2-bipyridine) triflate, $[\text{Cu}(\text{dmbpy})_2\text{H}_2\text{O}]\text{OTf}_2$.

$[\text{Cu}(\text{dmbpy})_2\text{H}_2\text{O}]\text{OTf}_2$ was made with similar method as $[\text{Cu}(\text{dmbpy})_2]\text{OTf}$. Under an inert atmosphere, 1 equivalent (2.8 mmol) of copper(II) triflate, CuOTf_2 , was dissolved in 5 mL of dry acetonitrile. This copper precursor is sensitive to moisture and oxygen. 2.1 equivalents (5.9 mmol) of dmbpy were dissolved in 3 mL of dry dichloromethane. The CuOTf_2 solution in acetonitrile was added into dmbpy solution in dichloromethane drop wisely. The solution became dark brown upon mixing. The reaction mixture was stirred for half an hour. Two methods were adapted to collect the product from the reaction mixture. Method one is to collect the product under inert atmosphere by adding dry diethyl ether. To perform method one, 20 mL dry diethyl ether was added into the reaction mixture slowly. Brown oily layer would form at the bottom of the solution.

The clear upper solution was decanted. The remaining brown oily product was washed several times with dry diethyl ether and dry dichloromethane mixture. The reaction flask was transferred to Schlenk line and left under vacuum overnight to dry the product. The dried product was brown powder, and it turned into bright green when exposed to air. Method two is to collect the product outside the box by adding diethyl ether (diethyl ether is not necessary to be dry). The reaction mixture was brought out of the glovebox. 20 mL diethyl ether (not dry) was added into the reaction mixture slowly. The reaction mixture was left stirring for 30 min in air and was sonicated every 5 minutes to help the formation of the precipitates. The dark oily product would become dark brown powders and can be collected by filtration. During the filtration process, the product will change its color from dark brown to bright green. The green product is stable at solid form in air. The filtrate is dark red/brown in color, indicating some residual product was still dissolved in the solution but was partially reduced in air. A small amount of ascorbic acid can be added into the filtrate. Then this filtrate was treated as described in the synthetic method for $[\text{Cu}(\text{dmbpy})_2]\text{OTf}$. Further purification of $[\text{Cu}(\text{dmbpy})_2\text{H}_2\text{O}]\text{OTf}_2$ can be achieved by re-dissolve the product into acetonitrile and recrystallize by adding diethyl ether under an inert atmosphere.

^1H NMR (500 MHz, Acetonitrile- d_3): δ 13.4 (s, broad peak, 4H), 2.6 (s, broad peak), -6.5 (s, broad peak, 12H). The water residual peak is also broadened, and the chemical shift is shifted depending on the concentration of sample, 2.63 (s, broad peak).

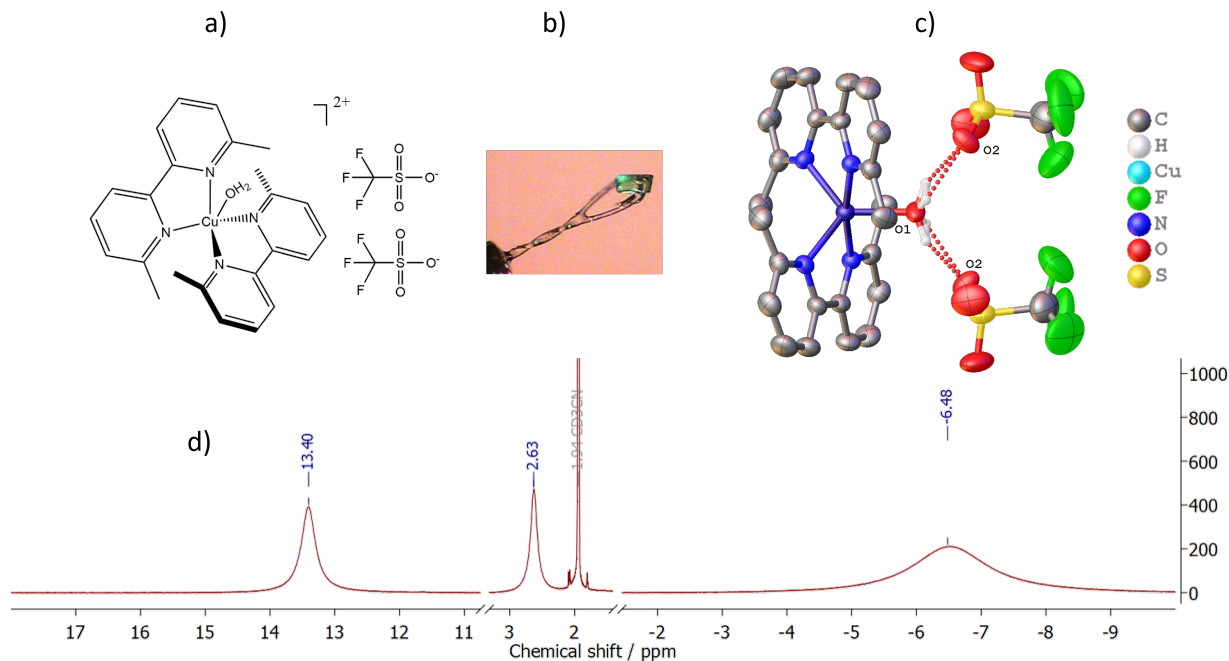


Figure 3.2 **a)** Molecular drawing of $[\text{Cu}(\text{dmbpy})_2\text{H}_2\text{O}]\text{OTf}_2$. **b)** Green crystal of $[\text{Cu}(\text{dmbpy})_2\text{H}_2\text{O}]\text{OTf}_2$, formed by diethyl ether diffusion method into dichloromethane. **c)** The molecular structure measured by single-crystal XRD. (see Appendix for more detailed crystallography information) **d)** ^1H NMR spectrum of $[\text{Cu}(\text{dmbpy})_2\text{H}_2\text{O}]\text{OTf}_2$ in CD_3CN .

3.2.1.3 Preparation of Copper(II) tetra(4-tert-butylpyridine) triflate, $[\text{Cu}(\text{TBP})_4]\text{OTf}_2$.

$[\text{Cu}(\text{TBP})_4]\text{OTf}_2$ was made with similar method as $[\text{Cu}(\text{dmbpy})_2]\text{OTf}$. Under an inert atmosphere, 1 equivalent (2.8 mmol) of CuOTf_2 was dissolved in 5 mL of dry acetonitrile. 7 equivalents (19.6 mmol) of TBP was added into the solution. The solution became blue/purple upon mixing. The reaction mixture was stirred for half an hour. Then the reaction flask was brought out of the glovebox. Diethyl ether was added into the reaction mixture slowly. Purple powder and the purple oily layer started to form upon the addition of diethyl ether. The mixture was sonicated to help the forming of the precipitates. The upper clear solution was decanted. The oily layer and precipitates were washed at least three times with diethyl ether. The resulted product was left under vacuum to dry and to remove the residual TBP. The final product was blue/purple powder and can be further purified by recrystallization in acetonitrile with diethyl ether.

^1H NMR (500 MHz, Acetonitrile- d_3): δ 0.82 (s, broad peak, 36H). The water residual peak is also broadened, and the chemical shift is shifted depending on the concentration of sample, 2.19 (s, broad peak).

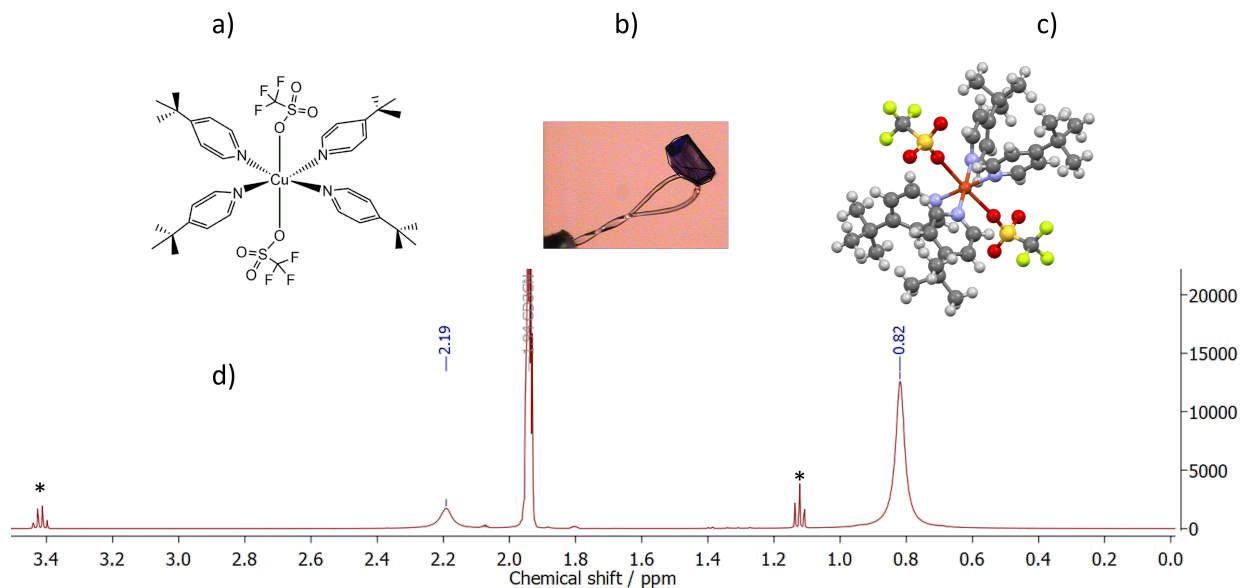


Figure 3.3 a) Molecular drawing of $[\text{Cu}(\text{TBP})_4]\text{OTf}_2$. b) Purple crystal of $[\text{Cu}(\text{TBP})_4]\text{OTf}_2$, formed by diethyl ether diffusion method into acetonitrile. c) The molecular structure measured by single-crystal XRD. (see Appendix for more detailed crystallography information) d) ^1H NMR spectrum of $\text{Cu}(\text{TBP})_4\text{OTf}_2$ in CD_3CN . Peaks with stars are from diethyl ether.

3.2.2 Electrochemical methods

All the electrochemical measurements were performed by using $\mu\text{AutoLabII}$ potentiostat or Autolab PGSTAT128N in a home-made electrochemical cell under N_2 atmosphere (see Appendix Figure 3.16 and notes). Copper complexes were dissolved in dry acetonitrile (concentration will be specified in the result and discussion section). Together dissolved was 0.1 M supporting electrolyte (will be specified in the main text).

For the cyclic voltammetry (CV) and differential pulse voltammetry (DPV) measurements, glassy carbon disk was used as the working electrode. The reference electrode was a home-made Ag/AgNO_3 reference electrode. A salt bridge was used to prevent the leakage of the silver containing electrolyte in the reference electrode. The CV of ferrocene was measured in the same

solvent before measuring the sample. The redox potential of ferrocene/ferrocenium was used to correct the potential of the home-made reference electrode. The counter electrode for CV measurement was a platinum mesh. Scan rate was varied and will be specified in the main text. For the titration measurement, different concentrations of TBP were added into the solution containing copper complexes and supporting electrolyte. The solution was stirred and then stabilized before measuring. The shape change of the CV peaks with different amount of TBP was monitored. DPV was used to measure the redox potential of the species in solution, and at the same time to detect the produced redox active species in solution when TBP was added.

For the bulk electrolysis of the solution containing copper complexes, a platinum mesh was used as the working electrode. The same home-made Ag/AgNO₃ was used as a reference electrode. The counter electrode was also home-made which contained a sacrificial redox couple. A platinum wire was also used as a second working electrode. CV measurement was done on the platinum wire to monitor if the bulk electrolysis was complete. The solution was kept stirring at high speed during the bulk electrolysis and was kept steady during the CV measurement. (see Appendix Figure 3.17-18 and notes for more details).

3.2.3 Other spectroscopic methods

The absorption spectra were measured with Lambda 35 (PerkinElmer) spectrometer. Solutions containing copper complexes were prepared in the glovebox under an inert atmosphere with dry acetonitrile. Screw-cap quartz cuvette with 1 cm path length was used for all the absorption measurements in solution. Blank acetonitrile was used as the reference for the absorption. For the titration measurement, a stock solution (usually 20 mL) containing a constant concentration of copper complex was prepared in the glove box. Each sample contains 2 mL of the stock solution and different amount of TBP. The absorption spectra of different samples were measured.

Proton NMR of copper complexes were measured using a J-Young NMR tube under an inert atmosphere with Agilent DDR2 500 MHz NMR spectrometer at room temperature. For the titration measurement, 0.6 mL solution containing a constant concentration of copper complex was prepared in the glove box with deuterated acetonitrile (CD_3CN). Dichloromethane was used as a non-coordinating reference proton source to calibrate the proton peak area. After running NMR of the pure copper complex, the tube was brought back into the glove box and some additional TBP was continued added into the same sample. For each run, the parameters (number of scans, temperature, decay time and scan range) used for the NMR measurement were kept the same.

Stopped-flow measurement was done with the Olis stopped-flow instrument with RSM-1000 operation control interface from Professor Robert Hausinger's group at MSU. The instrument uses a Xenon short-arc lamp as the light source.

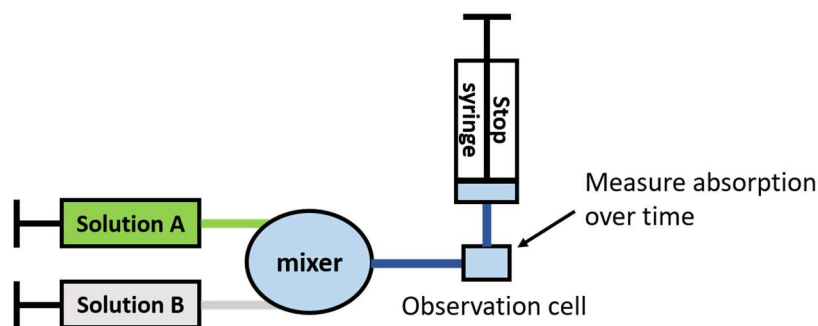


Figure 3.4 A simplified diagram of stopped-flow instrument. Solution A was $[\text{Cu}(\text{dmbpy})_2]^{2+}$ and solution B was TBP, in acetonitrile. 0.1 M LiOTf was used as supporting electrolyte and to control the ionic strength. Stop syringe was set to 0.35 mL.

Upon mixing of two solution (Part A and B) from the instrument-controlled injecting syringe, the absorption change of the observation cell overtime was measured with a scan speed as fast as 1000 scan per second. Solutions were prepared in the glove box with dry acetonitrile (0.1 M LiOTf was dissolved to maintain the ionic strength for samples with concentrations low concentrations). Part A was a stock solution contained a constant concentration of copper complex in 20 mL acetonitrile (enough for 5 - 7 samples). After dissolving the complex, the solution was put into the gas tight

syringe (total volume 25 mL). Different samples were prepared for Part B. Each sample contained a certain concentration of TBP in 3 mL of acetonitrile. After dissolving TBP, the solution of each sample was put into a gas tight disposable syringe (total volume 3 mL). Blank runs were prepared with solvents in syringes for Part B. Needles were kept for the syringes and each of them was injected into a 4 mL screw-cap vial with a silicone septum (see Appendix Figure 3.19) to help transfer between labs without exposing the solutions to air. This technique helped to gain kinetic information about the ligand exchange reaction between copper complex and TBP. Before running, the instrument was rinsed more than three times with DI water, acetonitrile, dry acetonitrile and dry acetonitrile with 0.1 M LiOTf in acetonitrile. Solution containing syringes were quickly removed from the needles and be connected to Part A and Part B lines on the instrument. After changing the sample, the system was rinsed with each sample solution for three times before collecting data. For each sample, at three sets of data were collected.

The self-exchange rate constant for $[\text{Cu}(\text{dmbpy})_2]^{2+/+}$ pair was measured by NMR.⁴ Stock solution of 15 mM of $[\text{Cu}(\text{dmbpy})_2]^{2+}$ and $[\text{Cu}(\text{dmbpy})_2]^+$ were prepared in dry CD_3CN (dried by 3A molecular sieves for more than 24 hours) separately. Each sample contained different ratios of $[\text{Cu}(\text{dmbpy})_2]^{2+}$ and $[\text{Cu}(\text{dmbpy})_2]^+$ and the total volume was kept the same, as shown in Table 3.1. The induced broadening of methyl proton signals of the $[\text{Cu}(\text{dmbpy})_2]^+$ by introducing the paramagnetic $[\text{Cu}(\text{dmbpy})_2]^{2+}$ was used to calculate the electron transfer rate constant, k_{ex} , between $[\text{Cu}(\text{dmbpy})_2]^{2+}$ and $[\text{Cu}(\text{dmbpy})_2]^+$. The measurement was done under room temperature.

Table 3.1 The detailed sample information for the kinetic study by NMR.

Sample #	1	2	3	4	5	6
Volume of stock solution of [Cu(dmbpy)₂]⁺ / mL^a	0.12	0.18	0.3	0.42	0.48	0.6
Volume of stock solution of [Cu(dmbpy)₂]²⁺ / mL^a	0.48	0.42	0.3	0.18	0.12	0
Total volume / mL	0.6					

a. The volume was measured by autopipette (± 0.05 mL / 1 mL).

3.3 Result and discussion

3.3.1 The structural difference between $[\text{Cu}(\text{dmbpy})_2]\text{OTf}$ and $[\text{Cu}(\text{dmbpy})_2\text{H}_2\text{O}]\text{OTf}_2$

By doing single-crystal XRD, the chemical structure of $[\text{Cu}(\text{dmbpy})_2]\text{OTf}$ and $[\text{Cu}(\text{dmbpy})_2\text{H}_2\text{O}]\text{OTf}_2$ are fully resolved. Not surprisingly, the geometries of these complexes are different when the oxidation state of copper is different. As expected, $[\text{Cu}(\text{dmbpy})_2]\text{OTf}$ has a nearly tetrahedral geometry with the dihedral angle between N-Cu-N planes (formed by each bipyridine and copper center) being closer to 90° . And the $[\text{Cu}(\text{dmbpy})_2\text{H}_2\text{O}]\text{OTf}_2$ has a flattened tetrahedral structure formed by two dmbpy ligands. There is also a water molecule in the crystal. Unlike other outer-sphere coordination complexes, this difference in geometry is much bigger for copper complexes. This makes the self-exchange electron transfer reaction of $[\text{Cu}(\text{dmbpy})_2]^{2+/+}$ more complicated.

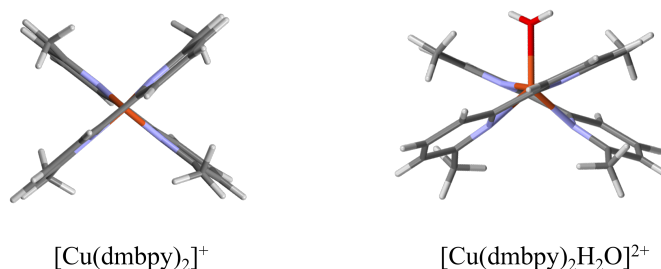


Figure 3.5 The geometry difference between $[\text{Cu}(\text{dmbpy})_2]\text{OTf}$ and $[\text{Cu}(\text{dmbpy})_2\text{H}_2\text{O}]\text{OTf}_2$. The dihedral angles are 83.2° and 71.7° , respectively (counter ions are not shown because they are not in the coordination sphere).

During the synthetic process of $[\text{Cu}(\text{dmbpy})_2]\text{OTf}$, it has been noticed that this complex is very stable in air, in both solid-state and when dissolved in solution. On the contrary, the oxidized form of this complex, $[\text{Cu}(\text{dmbpy})_2]\text{OTf}_2$, can be synthesized under strictly controlled inert and dry condition (method one as stated in the experimental section). The product is brown powder, but the color of the powder can be changed to bright green by sitting in the air. This is explained by the coordination of Cu^{2+} center by a water molecule under ambient condition and $[\text{Cu}(\text{dmbpy})_2]\text{OTf}_2$ will be converted into $[\text{Cu}(\text{dmbpy})_2\text{H}_2\text{O}]\text{OTf}_2$. This water coordination process

is reversible. The bright green complex can be dried under vacuum and become brown again by removing the coordinated water. However, if the synthesized by the second method in the experimental section, which allows the water coordination to occur in the reaction mixture before crystallization. And the green color stays even under vacuum. In both cases, the resulted green powder, $[\text{Cu}(\text{dmbpy})_2\text{H}_2\text{O}]\text{OTf}_2$, is stable under the ambient condition in the solid form but can be reduced to $[\text{Cu}(\text{dmbpy})_2]\text{OTf}$ when dissolved in solution. The structure of $[\text{Cu}(\text{dmbpy})_2]\text{OTf}_2$ and $[\text{Cu}(\text{dmbpy})_2\text{H}_2\text{O}]\text{OTf}_2$ are resolved by single-crystal X-ray diffraction. But the brown powder forms crystal only when the additional water molecule exists, so structural information was collected for the brown powder.

3.3.2 The electrochemical properties of $[\text{Cu}(\text{dmbpy})_2]\text{OTf}$ and $[\text{Cu}(\text{dmbpy})_2\text{H}_2\text{O}]\text{OTf}_2$ and the effect of TBP

Cyclic voltammetry (CV) was used to measure the redox property of both $[\text{Cu}(\text{dmbpy})_2]\text{OTf}$ and $[\text{Cu}(\text{dmbpy})_2\text{H}_2\text{O}]\text{OTf}_2$ in acetonitrile. As shown in Figure 3.6, both complexes have identical $E_{1/2}$ and peak shape in acetonitrile. The redox potential of $[\text{Cu}(\text{dmbpy})_2]\text{OTf}/[\text{Cu}(\text{dmbpy})_2\text{H}_2\text{O}]\text{OTf}_2$ is 0.33 V (vs. $\text{Fc}^{+/0}$). By changing the scan rate, the peak separation is only slightly increased, indicating the self exchange rate of this redox pair is moderate, and this is a reversible, one-electron redox process. The shape of the CV curves of $[\text{Cu}(\text{dmbpy})_2]\text{OTf}$ and $[\text{Cu}(\text{dmbpy})_2\text{H}_2\text{O}]\text{OTf}_2$ are identical in Figure 3.6a and b. This indicates that the coordinated water molecule in $[\text{Cu}(\text{dmbpy})_2\text{H}_2\text{O}]\text{OTf}_2$ may be replaced by the solvent molecule when dissolved in solution. And this makes it undistinguishable between different method synthesized copper complex. Therefore, the easier synthetic method was adapted in the later study and $[\text{Cu}(\text{dmbpy})_2\text{H}_2\text{O}]\text{OTf}_2$ was used. The redox couple $[\text{Cu}(\text{dmbpy})_2]\text{OTf}_2/[\text{Cu}(\text{dmbpy})_2\text{H}_2\text{O}]\text{OTf}_2$ is abbreviated as $[\text{Cu}(\text{dmbpy})_2]^{2+/+}$ in the text.

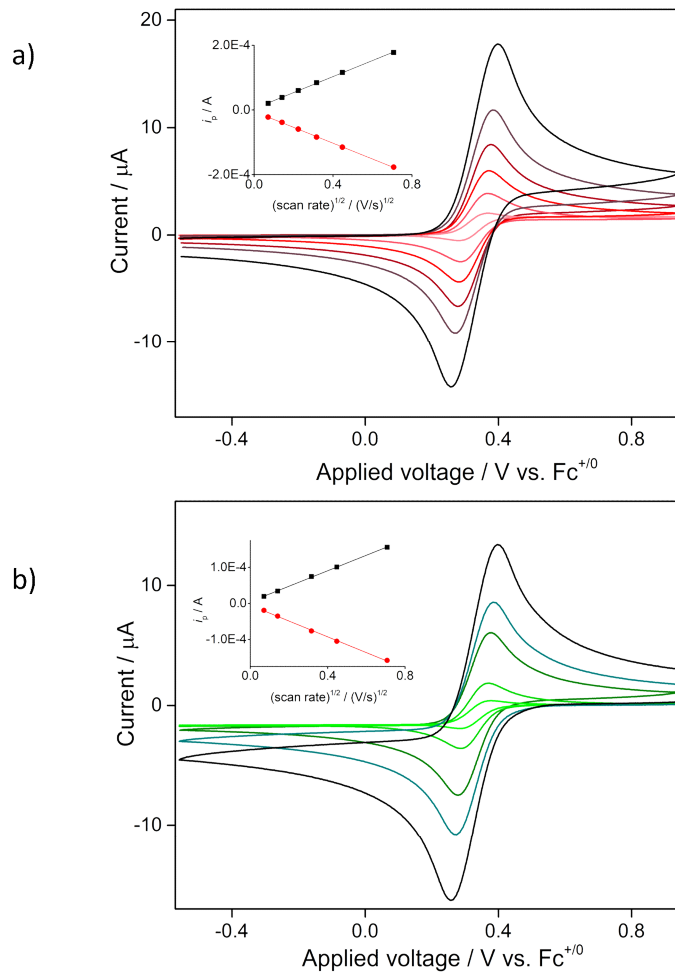
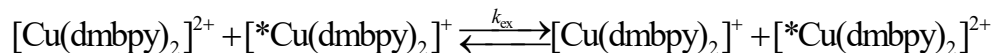


Figure 3.6 CV scans of 4mM **a)** [Cu(dmbpy)₂]⁺ and **b)** [Cu(dmbpy)₂]²⁺ in acetonitrile. Colors from light to dark represent scan rates from 0.005 to 0.5 V/s. A peak current versus square root of scan rate (*i_p* vs. $v^{1/2}$) is plotted in the insert. The linear behavior and the ratio between the cathodic and anodic peak current indicates the good electrochemical reversibility of the redox couple.

The self-exchange rate constant, k_{ex} , of $[\text{Cu}(\text{dmbpy})_2]^{2+/+}$ was measured by NMR.



The broadening of the methyl peak in ^1H NMR of $[\text{Cu}(\text{dmbpy})_2]^+$ was observed when different amounts of $[\text{Cu}(\text{dmbpy})_2]^{2+}$ were introduced in the solution, without an obvious change in its chemical shift as shown in Figure 3.7a. The intrinsic linewidth of solvent peak is independent of the concentration of $[\text{Cu}(\text{dmbpy})_2]^{2+}$ (see Appendix Table 3.7). The peak width was measured, and the relationship can be expressed in Equation 3.1⁴:

$$k_{\text{obs}} = \pi(\nu_{\text{obs}} - \nu_0) = k_{\text{ex}} \left[[\text{Cu}(\text{dmbpy})_2]^{2+} \right] \quad (3.1)$$

In the equation, ν_{obs} is the line width at the half signal maximum of the methyl proton peak when $[\text{Cu}(\text{dmbpy})_2]^{2+}$ was introduced into the solution of 15 mM $[\text{Cu}(\text{dmbpy})_2]^+$, while ν_0 is the intrinsic linewidth at the half signal maximum of the methyl proton peak when only $[\text{Cu}(\text{dmbpy})_2]^+$ was present in the solution. The dependence of the k_{obs} on the concentration of $[\text{Cu}(\text{dmbpy})_2]^{2+}$ is shown in Figure 3.7b. The estimated self-exchange electron transfer rate at room temperature is $9.97 \times 10^3 \text{ M}^{-1}\text{s}^{-1}$ (± 745 , $R^2 = 0.973$). (This uncertainty is from the linear fitting of data in Figure 3.7b. In the measurement, error from the autopipette was estimated to be 5%, and in the calculation, the error of the line width was estimated to be 5%. Both errors are reflected on the plotted data.) There are a lot of debate about the self exchange rate of copper redox couples. And our value obtained was consistent with Doine's report for $\text{Cu}(\text{dmp})_2^{2+/+}$ (dmp=2,9-dimethyl-1,10-phenanthroline) which was $4.8 \times 10^3 \text{ M}^{-1}\text{s}^{-1}$ (± 300) in acetonitrile.⁵ The condition of our measurement was at room temperature in acetonitrile. This is the same condition as in the solar cell electrolyte. The concentrations of copper species (both Cu^+ and Cu^{2+}) used in our measurement (total 0.015 M)

were lower than the concentrations used in the solar cell electrolyte, and thus the ionic strength. It has been reported by the Doine that the ionic strength (I) has an influence on the self-exchange rate constant of copper redox couple in acetonitrile (an increase of ionic strength by 6 times introduced a decreased of self-exchange rate constant by 12%). Therefore, the expected self-exchange rate in the higher concentrated electrolyte ($I = 0.32$ M) can be smaller.

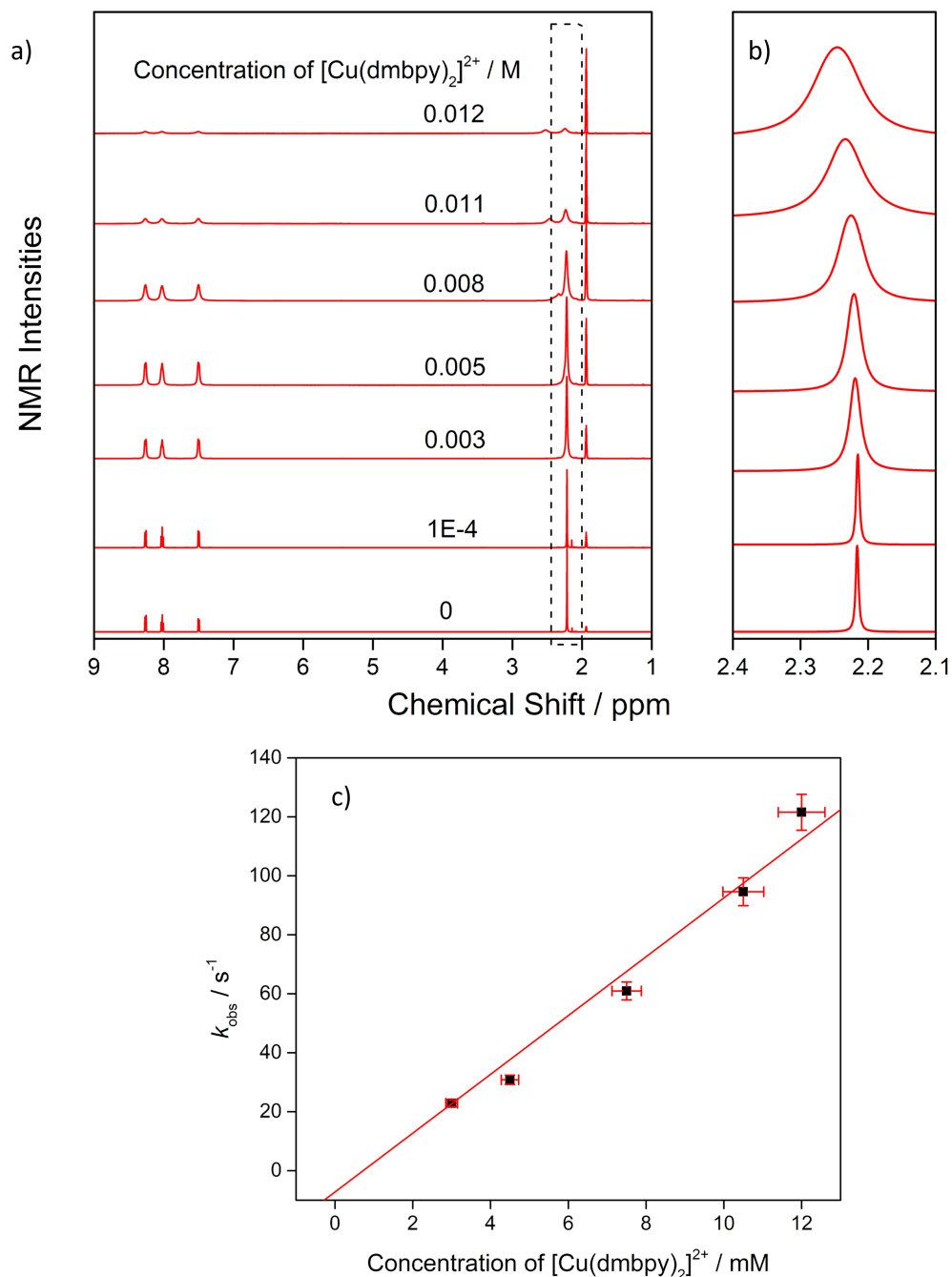


Figure 3.7 **a)** Proton NMR spectrums measured by 500 MHz NMR spectrometer (Max T. Rogers NMR Facility of MSU) in deuterated acetonitrile (purchased from Sigma Aldrich) under room temperature. Solutions contained different concentrations of $[\text{Cu}(\text{dmbpy})_2]^{2+}$. The dashed rectangular indicates the methyl proton peaks of the dmbpy ligand in $[\text{Cu}(\text{dmbpy})_2]^{2+}$. **b)** Fitted peaks around 2.2 ppm, indicated by the dashed rectangular in a). All the fittings were done by Mnova software, and the FWHM of each peak was calculated. **c)** Dependence of k_{obs} on the concentration of $[\text{Cu}(\text{dmbpy})_2]^{2+}$. Samples were prepared under N_2 atmosphere with dry solvents. The measurements were done under air-free condition and room temperature.

Different amounts of TBP was added into the solution to test the effect of TBP on the electrochemical property of $\text{Cu}(\text{dmbpy})_2\text{OTf}_2$, and the CV plots are shown in Figure 3.8. When TBP is included in the electrolyte, the cathodic wave is dramatically distorted, with only a minor change observed from the anodic peak.

The slight decrease of the anodic peak current can be due to the increased viscosity with TBP in the solution and decreased diffusion coefficient of the redox species. Kavan et al. have reported that the addition of TBP will slow down the diffusion of the $[\text{Cu}(\text{dmp})_2]^{2+/+}$ couple by measuring the finite-length Warburg diffusion impedance in a symmetrical dummy cell.⁶ While increased viscosity can account for the diminished anodic peak, it cannot account for the transformation of the cathodic wave.

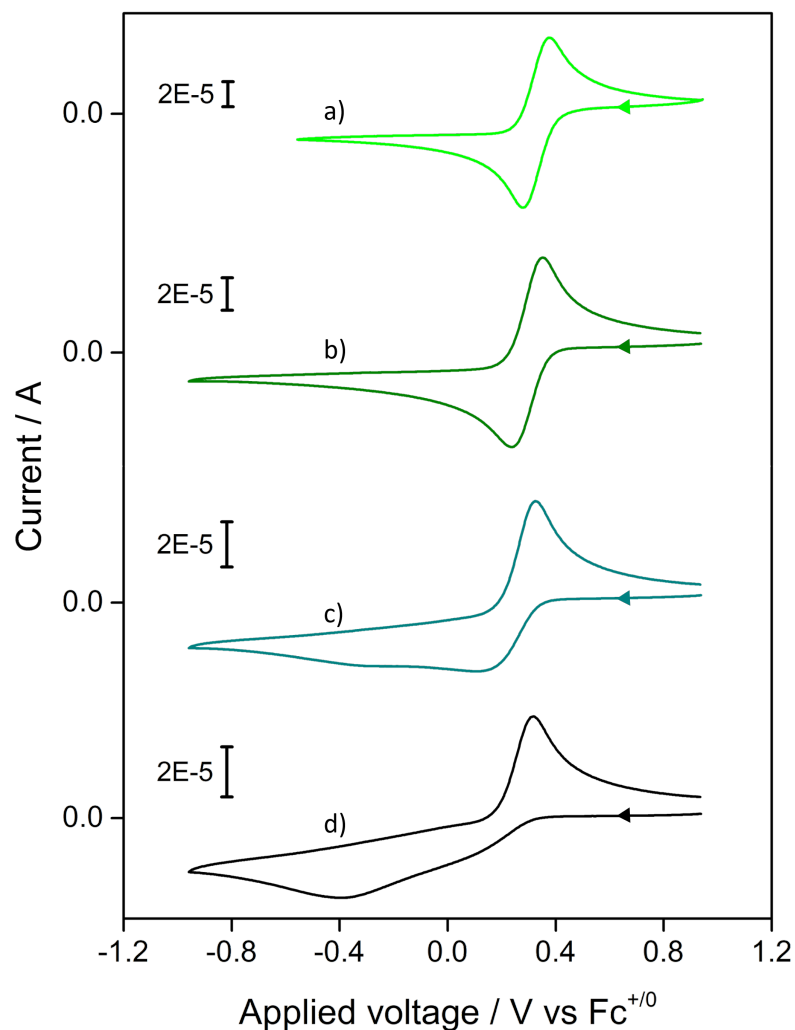


Figure 3.8 Electrochemical behavior of $[\text{Cu}(\text{dmbpy})_2]^{2+}$ in acetonitrile with the presence of TBP. 4 mM $[\text{Cu}(\text{dmbpy})_2]^{2+}$ with the addition of 0, 3, 13 and 25 equivalents of TBP to the copper complex (**a** to **d**). The scan rate was 0.1 V/s. Glassy carbon disk was used as a working electrode, and the same peak shape was also observed on a Pt disk electrode.

Hupp et al. showed that TBP is not innocent in the redox behavior of the $[\text{Cu}(\text{PDTO})]^{2+/+}$ (PDTO = 1,8-bis(2'-pyridyl)-3,6-dithiaoctane) redox couple. TBP displaces the tetradentate PDTO ligand on the Cu^{2+} center while PDTO displaces TBP on the Cu^+ center.³ This displacement occurs because the tetradentate PDTO ligand is rigid and it is hard for it to maintain the distorted tetrahedral structure when Cu^+ is oxidized to Cu^{2+} .

In order to determine if a similar effect is occurring for the $[\text{Cu}(\text{dmbpy})_2]^{2+/+}$ redox couple, TBP was titrated into the solution of $[\text{Cu}(\text{dmbpy})_2]^{2+}$ in acetonitrile. After 10 equivalents of TBP were introduced to the electrolyte, the cathodic peak decreased, and another peak around -0.4 V appeared. When 25 equivalents of TBP were present, even at high scan rates (ca. 3 V/s) the cathodic peak is dominated by the peak at -0.4 V. This behavior is consistent with the hypothesis that TBP readily displaces the dmbpy ligand once $[\text{Cu}(\text{dmbpy})_2]^+$ is oxidized. The same titration was also done with $[\text{Cu}(\text{dmbpy})_2]^+$ in acetonitrile, and the consistent result was observed (see Appendix Figure 3.21).

One thing worth noticing was the color change of the solution when adding TBP. The green solution of $[\text{Cu}(\text{dmbpy})_2]^{2+}$ changes to blue and the red solution of $[\text{Cu}(\text{dmbpy})_2]^+$ stays the same. This is an evidence of the formation of a new complex when an excess amount of TBP is present in the solution of $[\text{Cu}(\text{dmbpy})_2]^{2+}$, but the reaction is unlikely to perform in the solution of $[\text{Cu}(\text{dmbpy})_2]^+$. The color change of the solution also indicates that this reaction can be monitored by spectroscopic method.

3.3.3 Monitoring the ligand exchange of dmbpy by TBP

In order to test this idea, we independently synthesized the $\text{Cu}(\text{TBP})_4(\text{OTf})_2$ complex. Figure 3.9a shows the absorption spectra of $[\text{Cu}(\text{dmbpy})_2]^+$, $[\text{Cu}(\text{dmbpy})_2]^{2+}$ and $[\text{Cu}(\text{TBP})_4]^{2+}$ complexes dissolved in acetonitrile. The $[\text{Cu}(\text{TBP})_4]^{2+}$ complex exhibits a weak absorption peak at 580 nm, whereas the $[\text{Cu}(\text{dmbpy})_2]^{2+}$ complex has weak absorption maxima at 724 nm and 1038 nm. Titration of the $[\text{Cu}(\text{dmbpy})_2]^{2+}$ solution with aliquots TBP results in the disappearance of the peak at 1038 nm and an apparent shift of the lower wavelength peak. No isosbestic point is seen, which we attribute to the likely presence of multiple species in solution upon the addition of moderate concentrations of TBP. When 25 or more equivalents of TBP was added, the solution exhibits a

nominally identical spectrum as the $[\text{Cu}(\text{TBP})_4]^{2+}$ solution. This result strongly suggests the TBP ligand exchanges with one dmbpy ligand at the Cu^{2+} center at low to intermediate concentrations, and fully displaces it at larger concentrations.

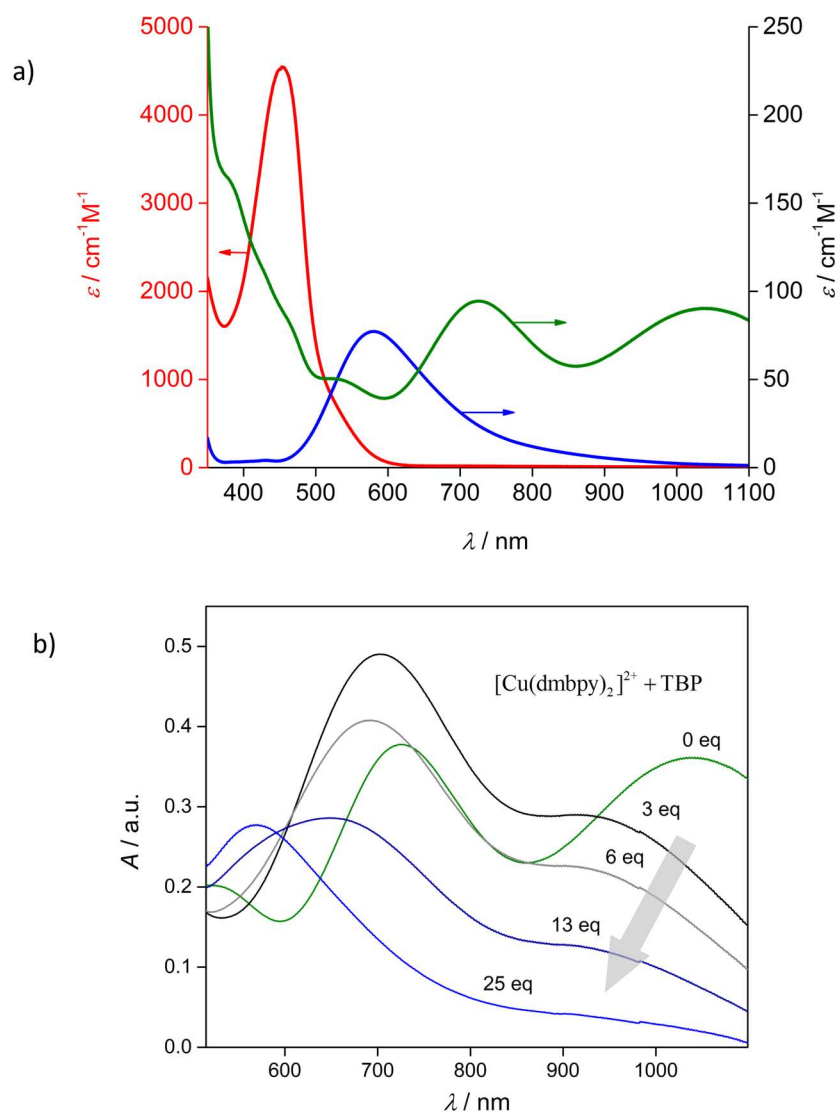


Figure 3.9 **a)** Plots of the absorption spectra of $[\text{Cu}(\text{dmbpy})_2]^{2+}$ (red), $[\text{Cu}(\text{dmbpy})_2]^{2+}$ (green) and $[\text{Cu}(\text{TBP})_4]^{2+}$ (blue) in acetonitrile. **b)** Absorption spectra corresponding to the titration of $[\text{Cu}(\text{dmbpy})_2]^{2+}$ with aliquots of TBP in acetonitrile. The concentration of $[\text{Cu}(\text{dmbpy})_2]^{2+}$ was 4 mM, with 0, 3, 6, 13 and 25 equivalents TBP introduced to the solution.

Titration of the $[\text{Cu}(\text{TBP})_4]^{2+}$ solution with aliquots of dmbpy (up to 13 equivalents) does not show a complete transformation to $[\text{Cu}(\text{dmbpy})_2]^{2+}$ as indicated by the absorption spectra in Figure 3.10. But this titration shows the evidence for the existence of the intermediate in the reaction. There is no difference between adding 4 to 6.5 eq of dmbpy, which indicates the solution reaches an intermediate equilibrium. An intermediate complex with a higher extinction coefficient ($\sim 180 \text{ M}^{-1} \text{ cm}^{-1}$) than the starting $[\text{Cu}(\text{TBP})_2]^{2+}$ was observed. When more equivalents of dmbpy was added (up to 13 equivalents), the absorption maximum of the mixture starts to shift to longer wavelength. The spectrum feature of the observed intermediate (black curve in Figure 3.10) is consistent with that of the observed intermediate (black curve in Figure 3.9b). Their absorption peak maximums are at 707 nm and 950 nm. Therefore, the reaction between $[\text{Cu}(\text{dmbpy})_2]^{2+}$ and TBP is believed to involve at least one intermediate that can be observed by UV-vis.

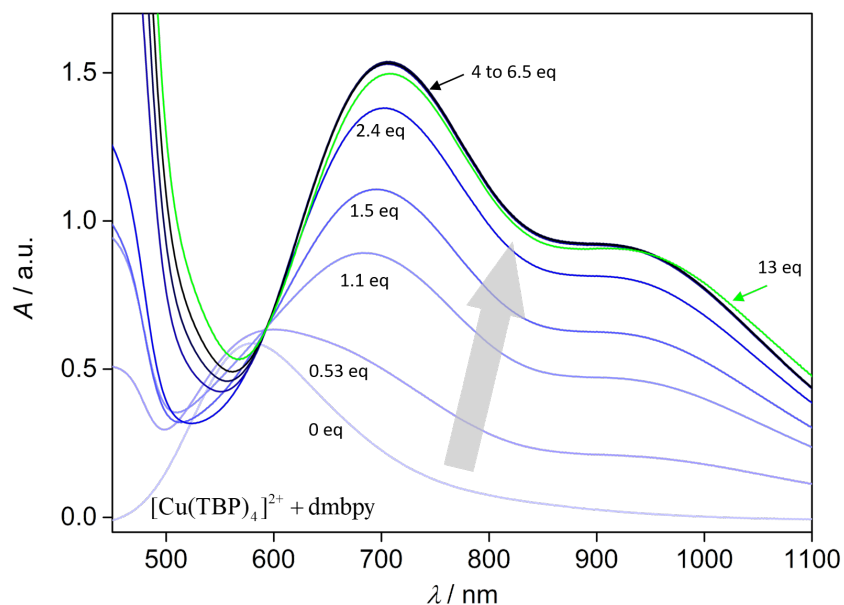


Figure 3.10 Absorption spectra corresponding to the titration of $[\text{Cu}(\text{TBP})_4]^{2+}$ with aliquots of dmbpy in acetonitrile. The concentration of $[\text{Cu}(\text{TBP})_4]^{2+}$ was 8 mM, with 0, 0.53, 1.1, 1.5, 2.4, 4.0, 5.2, 6.5 and 13 equivalents of dmbpy (from bottom to top) introduced to the solution.

From the observations during the UV-vis titration, there are at least two steps involved in the ligand exchange reaction between TBP and $[\text{Cu}(\text{dmbpy})_2]^{2+}$. From the forward titration (adding TBP into $[\text{Cu}(\text{dmbpy})_2]^{2+}$), the intermediate showed up at low TBP concentrations. The intermediate state can be reached at 3:1 ratio between TBP and $[\text{Cu}(\text{dmbpy})_2]^{2+}$. This is also a 3:2 ratio between TBP and dmbpy. From the backward titration (adding dmbpy into $[\text{Cu}(\text{TBP})_4]^{2+}$), the same intermediate state showed up at 4:1 ratio between dmbpy and $[\text{Cu}(\text{TBP})_4]^{2+}$. This is a 4:4 ratio between TBP and dmbpy. Because the ligand exchange is a competition between TBP and dmbpy to bind to Cu^{2+} center, the formation of the intermediate state the extent of the reaction should be controlled by the ratio between TBP and dmbpy.

To unambiguously and quantitatively determine the extent of the displacement of dmbpy by TBP, proton NMR spectra were taken of $[\text{Cu}(\text{dmbpy})_2]^{2+}$ in deuterated acetonitrile without and with the addition of TBP. Because $[\text{Cu}(\text{dmbpy})_2]^{2+}$ is paramagnetic, the proton signals of the dmbpy ligands coordinated to the Cu^{2+} center show very different chemical shifts than free dmbpy ligands in the solution. In Figure 3.11, proton signal “a” represents one of the aromatic proton peaks in dmbpy ligand that is coordinated to the paramagnetic Cu^{2+} center. Proton signal “group b” represents all three aromatic proton peaks in dmbpy ligand that is free in solution. “group b” signals match with the proton signals of pure dmbpy ligand (see Appendix Figure 3.24). These distinguishable peaks allowed the determination of the concentrations of free, i.e., displaced, dmbpy ligands. The aromatic protons in free dmbpy ligand and in $[\text{Cu}(\text{dmbpy})_2]^{2+}$ complex show different chemical shifts in NMR as in Figure 3.11. Therefore, the increase of the “group b” signals is clearly an indication of the increase of the free dmbpy in solution.

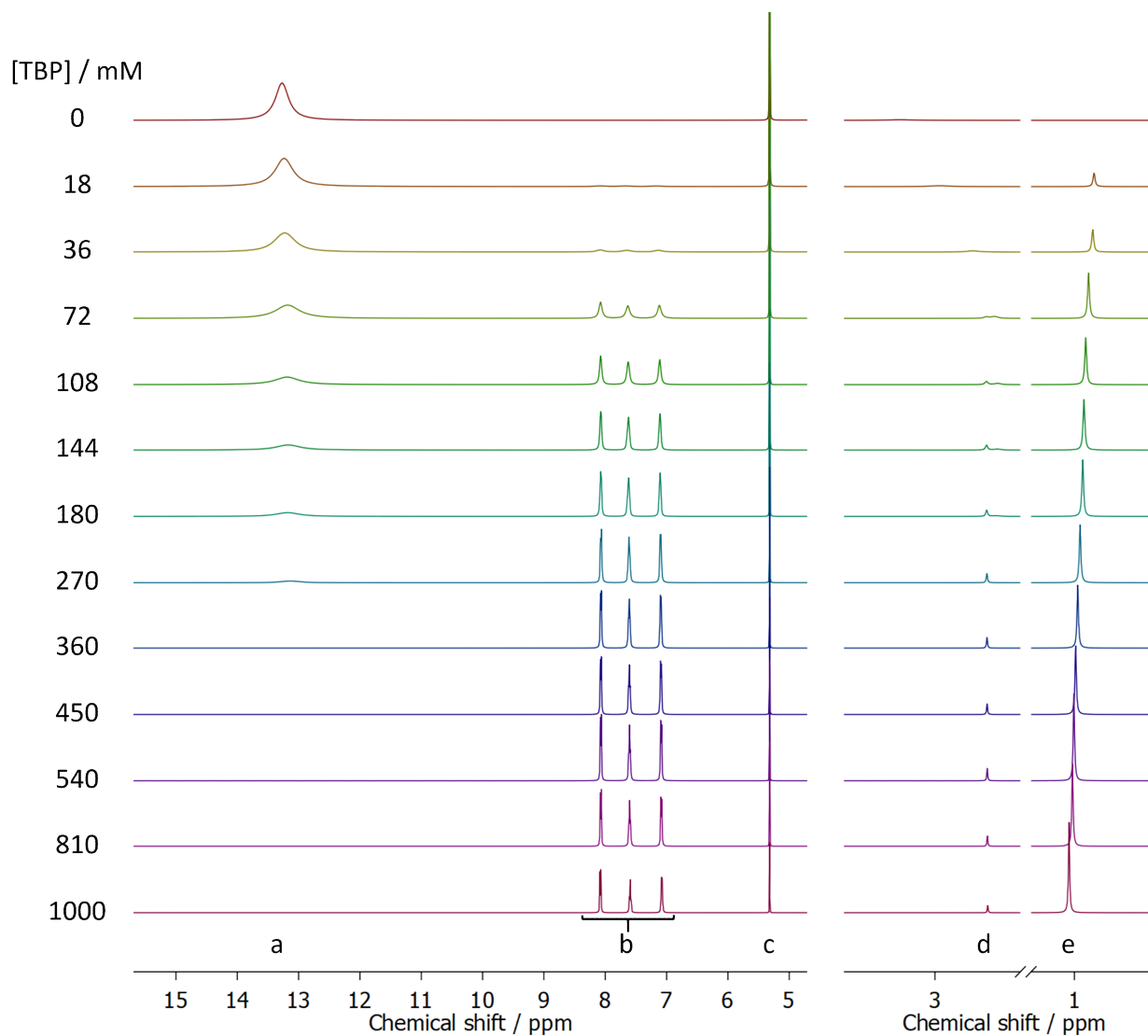


Figure 3.11 Partial ^1H NMR titration spectra of $[\text{Cu}(\text{dmbpy})_2]^{2+}$ with TBP in AcN-d_3 at room temperature. The concentration of $[\text{Cu}(\text{dmbpy})_2]^{2+}$ was 39 mM. The concentration of TBP added is listed on the left of the figure. The internal standard was dichloromethane which is non-coordinating. The concentration of dichloromethane was 26 mM. The signal of the proton in dichloromethane was integrated and used to calibrate the concentration of other protons. Signals of **a**) aromatic protons in dmbpy in $[\text{Cu}(\text{dmbpy})_2]^{2+}$ complex, **b**) aromatic protons in free dmbpy ligand, **c**) protons in dichloromethane, **d**) methyl protons in free dmbpy ligand and **e**) methyl protons in TBP. The samples were prepared with dry solvent under the air-free condition and measured under air-free condition using J. Young NMR tube.

The singlet peak at 5.32 ppm shown on the full ^1H NMR spectrum corresponds to the proton signal of DCM, which is used as an internal standard to calibrate the concentration of other protons. The broadened peaks at 13.2, 2.6 and -6.67 ppm (shown in Figure 3.2d) are attributed to the dmbpy

ligand coordinated to the paramagnetic Cu^{2+} center. Peaks at around 1 ppm can be seen upon the introduction of TBP to the solution. The absence of distinct chemical shifts for complexed and free TBP on the spectrum can be attributed to the fast ligand exchange rate between TBP and Cu^{2+} centered complex.⁷

There are three sharp peaks between 7 to 8.5 ppm, which correspond to the aromatic proton signals of the free dmbpy ligand. By integrating the proton signals at 8.07, 7.62 and 7.10 ppm and comparing this to the integrated DCM standard peak area at 5.32 ppm, a ratio of the free ligand to the total Cu^{2+} concentration can be calculated. An increased ratio between free dmbpy and Cu^{2+} was observed during titration. When more than 15 eq. of TBP was added into the solution, the ratio reaches a plateau at a value of 2, which indicates complete replacement of the dmbpy ligand by TBP. Titrations of $[\text{Cu}(\text{dmbpy})_2]^+$ with TBP were also performed and monitored with UV-Vis and NMR, which showed no evidence of ligand exchange. (see Appendix Figure 3.25 and 3.26)

In Figure 3.12, the more TBP added into the $[\text{Cu}(\text{dmbpy})_2]^{2+}$, the more displaced dmbpy can be observed in the solution. The displacement of dmbpy starts to occur at the very beginning of the titration curve, at less than 1 equilibrium of TBP. This shows the equilibrium favors the intermediate state for the first step of the reaction. When TBP is close to 3 equilibrium, there is not a plateau in Figure 3.12. This shows the system is not stabilized at this intermediate state and start to perform the second step. Although we observed this strong absorbing (higher extinction coefficient) intermediate in the UV-vis titration, we can not isolate this species easily. Finally, at more than 15 equivalents TBP, the curve in Figure 3.12 reaches a plateau with the released dmbpy being twice of the original concentration of $[\text{Cu}(\text{dmbpy})_2]^{2+}$. This figure shows that finally all the dmbpy that were coordinated to Cu^{2+} centers are dissociated by the addition of TBP.

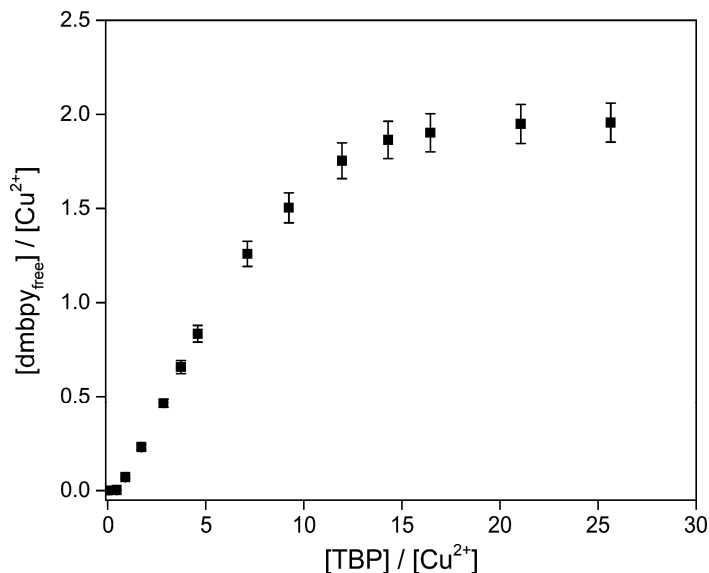


Figure 3.12 Titration results obtained by NMR. The ratio between the detected free dmbpy ligand and the total Cu^{2+} species is plotted versus the aliquots of TBP in the solution. The concentration of dmbpy was determined based on the integration of aromatic proton peaks. A controlled amount of DCM was added as an internal standard for the quantitative calculation.

Unfortunately, equilibrium constants could not be derived by NMR. The concentration of free TBP in solution could not be accurately determined because the coordinated and free TBP exchange too quickly at room temperature on the NMR time scale to be isolated. Only one set of proton signals are shown for the coordinated and non-coordinated TBP and their chemical shifts vary with the amount of free TBP in solution (see Appendix Figure 3.28 for the titration of TBP in to $[\text{Cu}(\text{TBP})_4]^{2+}$).

3.3.4 Reversibility, kinetics and equilibrium of the ligand exchange reaction

All the titration results above have shown that ligand exchange reaction happens between TBP and $[\text{Cu}(\text{dmbpy})_2]^{2+}$ in acetonitrile. This result in a dissociation of dmbpy. On the contrary, ligand exchange reaction does not happen between TBP and $[\text{Cu}(\text{dmbpy})_2]^+$. To test the reversibility of this ligand exchange when copper changes its oxidation state, we used bulk electrolysis together with spectroscopic method. Bulk electrolysis can cleanly reduce the copper complex,

$[\text{Cu}(\text{TBP})_4]^{2+}$, without introducing any additional chemical species. UV-vis was used to determine the composition of the electrolyte. As shown in the series of CV and UV-vis spectra in Figure 3.13, when the $[\text{Cu}(\text{TBP})_4]^{2+}$ in the electrolyte was fully reduced, TBP will dissociate from the copper center. At the same time, dmbpy can coordinate back to the copper which results in the formation of $[\text{Cu}(\text{dmbpy})_2]^+$. $[\text{Cu}(\text{dmbpy})_2]^+$ complex is strongly favored over a $[\text{Cu}(\text{TBP})_4]^+$ complex which we attribute to the chelate effect, when the geometry constrain is not serious.

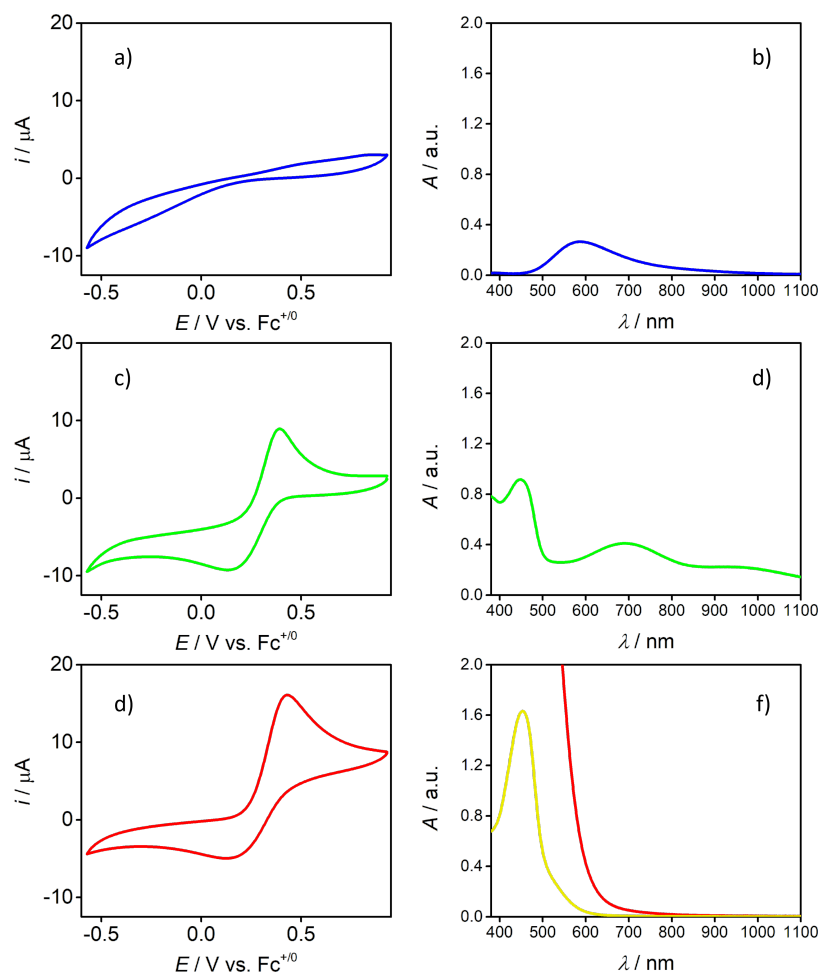


Figure 3.13 Plots of CV spectra (left) and absorption spectra (right) for solutions containing: a, b) 4 mM $[\text{Cu}(\text{TBP})_4]^{2+}$ and 0.1 M LiOTf (blue lines) in acetonitrile; c, d) 4 mM $[\text{Cu}(\text{TBP})_4]^{2+}$, 0.1 M LiOTf and 8 mM dmbpy in acetonitrile (green lines); e, f) 4 mM $[\text{Cu}(\text{TBP})_4]^{2+}$ 0.1 M LiOTf and 8 mM dmbpy in acetonitrile after bulk electrolysis at -0.37 V vs. $\text{Fc}^{+/0}$ which resulted in passing 1.7 C of charge cathodically (red lines). The absorption spectrum of the 10-fold diluted spectrum is shown in yellow line of plot f). The working electrode was a Pt disk, and the scan rate was 0.1 V/s.

Stopped-flow was used to study the kinetics of the ligand exchange reaction. The pseudo-first-order condition was met by keeping the TBP concentration more than 20 times higher than the $[\text{Cu}(\text{dmbpy})_2]^{2+}$ concentration. Therefore, the ligand exchange is complete under the high excess amount of TBP. According to the absorption measurement, the product $[\text{Cu}(\text{TBP})_4]^{2+}$ has a lower extinction coefficient at 730 nm compare to the reactant $[\text{Cu}(\text{dmbpy})_2]^{2+}$. Therefore, the decay of the solution absorption at 730 nm was measured over time. The absorption decay curves were fitted with a single exponential. Figure 3.14a is one example of the fitting of the kinetic trace at 730 nm with a single exponential function (see Appendix Figure 3.20 for the complete data set). k_{obs} can be extrapolated from each fitted curve. Figure 3.14b is the plot of k_{obs} versus different concentrations of TBP. The rate constant for the reaction, k_{tot} , is obtained by the slope on the k_{obs} vs [TBP] plot. The slope in Figure 3.14b shows the value of k_{tot} being $43 \text{ M}^{-1}\text{s}^{-1}$. The time scale for the ligand exchange with 0.02 M $[\text{Cu}(\text{dmbpy})_2]^{2+}$ and 0.6 M TBP can be evaluated. Since TBP is in large excess compare to $[\text{Cu}(\text{dmbpy})_2]^{2+}$, the reaction can be pseudo-first order with a $k_{\text{obs}} = k_{\text{tot}} \times [\text{TBP}] = 25.8 \text{ s}^{-1}$. The time constant of this pseudo-first order is therefore estimated to be 39 ms.⁸ If the concentration of $[\text{Cu}(\text{dmbpy})_2]^{2+}$ is higher, the time scale of the ligand exchange can be smaller.

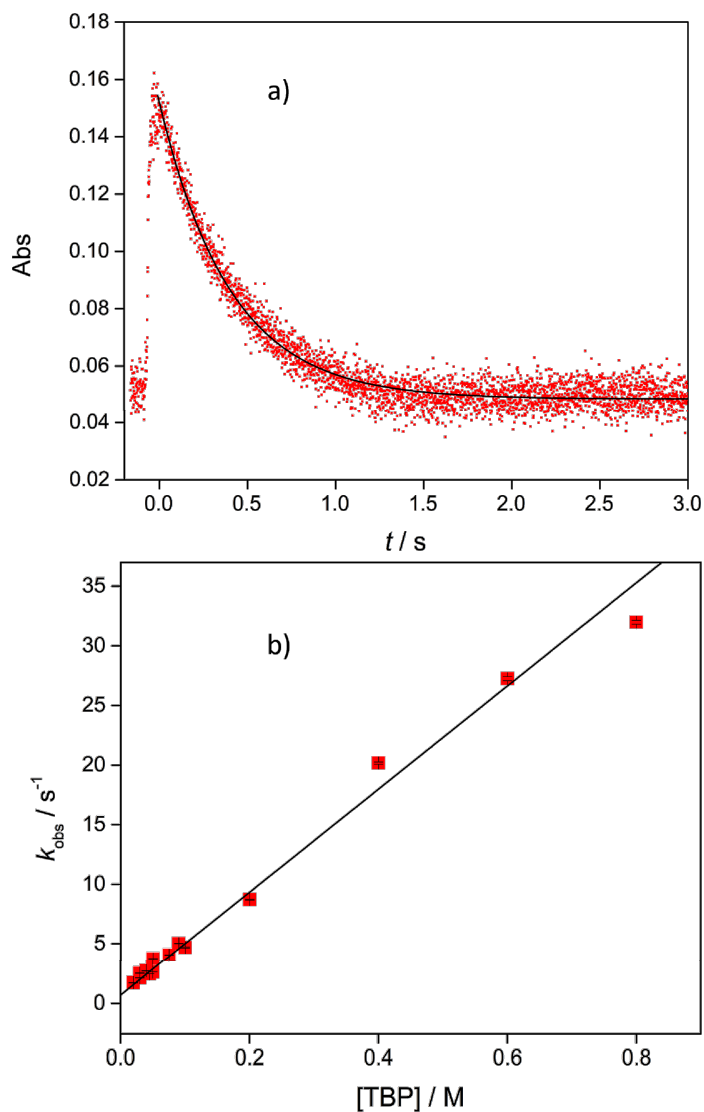


Figure 3.14 a) Plot of absorbance at 730 nm vs. time, corresponding to decay of the $[\text{Cu}(\text{dmbpy})_2]^{2+}$ species (red dot) and the resulting fit (black line) for the ligand displacement of $[\text{Cu}(\text{dmbpy})_2]^{2+}$ by TBP. The resulted $[\text{Cu}(\text{TBP})_4]^{2+}$ absorbs less under this wavelength. **b)** The resulting observed pseudo-first-order rate constants, k_{obs} , versus the excess concentration of reactant for the reactions between $[\text{Cu}(\text{dmbpy})_2]^{2+}$ and TBP. The measurement was done under room temperature with dry solvent. Efforts were made to get the data under air-free condition by using a dry and air-free solvent to rinse the instrument before measuring. But there should still be residual water and oxygen. 0.1 M of LiOTf was added to maintain the ionic strength for the samples with concentration lower than 0.1 M.

Since UV-vis and NMR are not able to provide a clear detection of both $[\text{Cu}(\text{dmbpy})_2]^{2+}$ and $[\text{Cu}(\text{TBP})_4]^{2+}$ at the same time, EPR was used to obtain the equilibrium constant of the ligand exchange reaction. At room temperature, the EPR spectrum of $[\text{Cu}(\text{dmbpy})_2]^{2+}$ shows a broad peak (as shown in Figure 3.15a Samp1) without the resolved ESR patterns as normal Cu(II) complexes. Similar behavior of EPR was observed in some square planar Cu(II) complexes, and it was attributed to the structural exchange between square pyramidal and square planar.⁹ Surprisingly $[\text{Cu}(\text{TBP})_4]^{2+}$ shows very well resolved EPR line shapes and even for the nitrogen hyperfine coupling from the ligand under room temperature (as shown in Figure 3.15a Samp3). The EPR line shape of $[\text{Cu}(\text{TBP})_4]^{2+}$ is the normal type for Cu(II) complex with a elongated octahedron, square pyramid or square planar geometry.¹⁰ From the previous UV-vis titration, we observed the intermediate in a mixture of dmbpy and $[\text{Cu}(\text{TBP})_4]^{2+}$, and the ratio between these two species is 6:1. Thus this ratio was also measured in EPR and the spectrum of it was assumed to be the intermediate, which is shown as Samp2 in Figure 3.15a. These three EPR spectra were fitted in MATLAB with EasySpin script.¹¹ The fitting results are Spec1, Spec2 and Spec3 for Samp1, Samp2 and Samp3 respectively. The parameters used to generate Spec1, Spec2 and Spec3 are listed in Appendix.

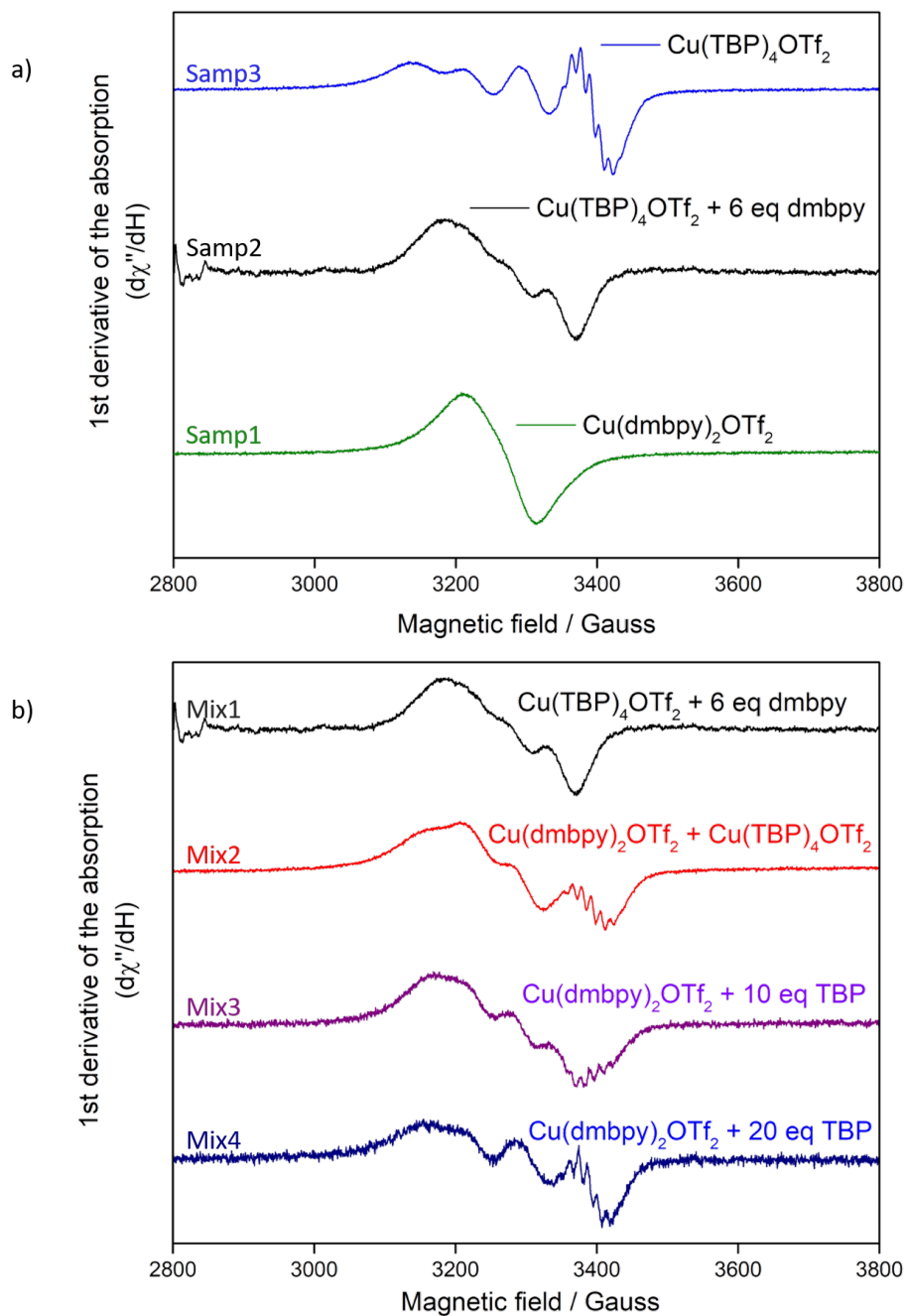
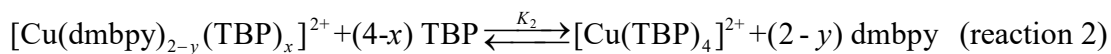
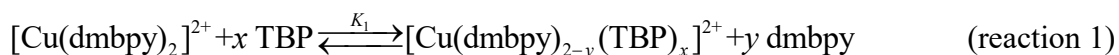


Figure 3.15 EPR spectra of different copper complexes in solution. **a)** Spectra that are fitted and used to generate other spectra. **b)** Steady state spectra of mixing different complexes which are used to calculate K_2 . All samples were prepared in the gloved box with dry acetonitrile. Measurements were done at room temperature.

The weighted average of these three spectra were used to generate other spectra in Figure 3.15b. For spectrum that is labeled as Mix1, 1 mM $[\text{Cu}(\text{dmbpy})_2]^{2+}$ was mixed with 1 mM $[\text{Cu}(\text{TBP})_4]^{2+}$. This curve can not be well fitted using Spec1 and Spec3 (which are the spectra of $[\text{Cu}(\text{dmbpy})_2]^{2+}$ and $[\text{Cu}(\text{TBP})_4]^{2+}$), but instead can be better fitted with the contribution from the Spec2. This is surprising because it shows that the ligand environment of $[\text{Cu}(\text{dmbpy})_2]^{2+}$ and $[\text{Cu}(\text{TBP})_4]^{2+}$ at 1:1 ratio in solution may rearrange to form a more stable state. Mix2, Mix3 and Mix4 are spectra of $[\text{Cu}(\text{dmbpy})_2]^{2+}$ with different equivalents (>10) of TBP. Under these TBP concentrations, the system already past the first step (reaction 1) of the ligand exchange. The majority species in these solutions are the intermediate and $[\text{Cu}(\text{TBP})_4]^{2+}$. Therefore, the equilibrium we can established is K_2 in reaction 2.



Different fitting results are shown in Table 3.8 in the Appendix. As expected, these spectra are fitted better with Spec2 and Spec3, but without Spec1. The fitting method is described in the Appendix. The calculated equilibrium constants show a high dependent on the reaction order of TBP ($4-x$ value in reaction 2). Only when $x=3$, the calculated K_2 value has a consistent result for all three Mix spectra, which is 0.086 (± 0.003). Although the number of samples that were measured is limited, this result is consistent with the stopped-flow data. Both the stopped-flow and EPR result suggest that in reaction 2, the reaction order of TBP is 1.

3.4 Conclusion

From the results presented in this chapter, we conclude that in solution, the dmbpy ligands that are in the coordination sphere of $[\text{Cu}(\text{dmbpy})_2]^{2+}$ can be replaced by the TBP ligand at large excess amount and produces $[\text{Cu}(\text{TBP})_4]^{2+}$. This ligand exchange reaction is reversible. When $[\text{Cu}(\text{TBP})_4]^{2+}$ is being reduced, with the presence of as low as only 2 equivalent of dmbpy ligand, the reduced product is $[\text{Cu}(\text{dmbpy})_4]^+$. This phenomenon can be explained by the difference in the favored geometry of Cu(I) and Cu(II) centers.

$[\text{Cu}(\text{dmbpy})_2]^{2+/+}$ is a redox pair whose redox potential is 0.33 V vs $\text{Fc}^{+/0}$, and it has good electrochemical reversibility. The self-exchange rate constant of this redox pair is around $9 \times 10^3 \text{ M}^{-1}\text{s}^{-1}$, which makes it a moderate rate self-exchanger. However, due to the difference in the geometry between $[\text{Cu}(\text{dmbpy})_2]^{2+}$ and $[\text{Cu}(\text{dmbpy})_2]^+$, the $[\text{Cu}(\text{dmbpy})_2]^{2+}$ species is sensitive to the chemical environment in solution. Coordinating ligand like TBP can readily coordinate to the Cu^{2+} center and replace the dmbpy at around 20 times excess amount. This ligand replacement produces a new species in solution, $[\text{Cu}(\text{TBP})_4]^{2+}$ which doesn't show as good redox reversibility as $[\text{Cu}(\text{dmbpy})_2]^{2+}$ and can only be reduced at a more negative potential. Different from $[\text{Cu}(\text{dmbpy})_2]^{2+}$, $[\text{Cu}(\text{dmbpy})_2]^+$ very good stability in solution at the presence of TBP. The dmbpy and TBP ligands are inter-exchangeable during the redox reaction between Cu(I) and Cu(II). Therefore, the redox scheme can be established.

The discovery of this ligand exchange phenomenon between $[\text{Cu}(\text{dmbpy})_2]^{2+/+}$ redox pair and TBP has practical meaning in the field of DSSC research. As mentioned at the beginning of this chapter, dye cells using this redox couple has shown good photocurrent and voltage response at the presence of a high excess amount of TBP. Now since we are sure that this ligand exchange reaction happens in the operating system of the DSSCs, further study can be done to understand how this

in-situ ligand exchange affects the dye cell performance and whether we need to prevent or utilize it to improve the efficiency of the DSSCs.

APPENDIX

APPENDIX

Crystallography data for [Cu(dmbpy)₂]OTf, [Cu(dmbpy)₂H₂O]OTf₂ and Cu(TBP)₄OTf₂:

Compound [Cu(dmbpy)₂]OTf

Formula	C ₂₅ H ₂₄ CuF ₃ N ₄ O ₃ S
<i>D</i> _{calc.} / g cm ⁻³	1.462
μ /mm ⁻¹	0.962
Formula Weight	581.08
Colour	red
Shape	needle
Size/mm ³	0.37×0.11×0.08
<i>T</i> /K	173(2)
Crystal System	orthorhombic
Flack Parameter	0.003(11)
Hooft Parameter	0.014(11)
Space Group	<i>P</i> 2 ₁ 2 ₁ 2 ₁
<i>a</i> /Å	11.9051(9)
<i>b</i> /Å	13.7921(10)
<i>c</i> /Å	16.0754(12)
α /°	90
β /°	90
γ /°	90
<i>V</i> /Å ³	2639.5(3)
<i>Z</i>	4
<i>Z'</i>	1
Wavelength/Å	0.710730
Radiation type	MoK α
θ _{min} /°	1.946
θ _{max} /°	25.370
Measured Refl.	16649
Independent Refl.	4731
Reflections Used	3745
<i>R</i> _{int}	0.0450
Parameters	338
Restraints	0
Largest Peak	0.607
Deepest Hole	-0.347
GooF	1.083
<i>wR</i> ₂ (all data)	0.1275
<i>wR</i> ₂	0.1174
<i>R</i> ₁ (all data)	0.0641
<i>R</i> ₁	0.0484

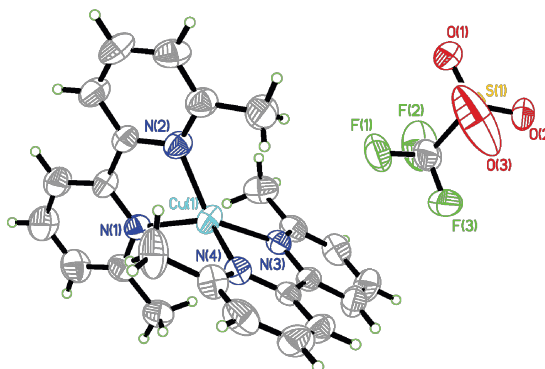


Table 3.2 Bond lengths in Å for [Cu(dmbpy)₂]OTf.

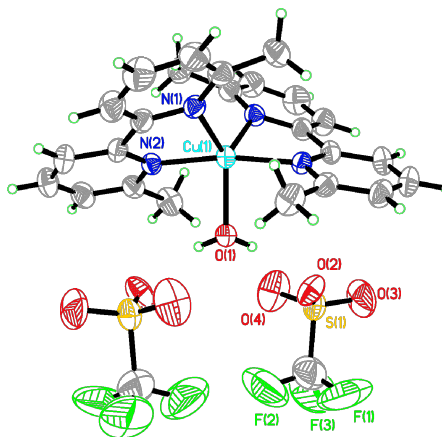
Atom	Atom	Length/Å
Cu1	N1	2.022(5)
Cu1	N2	2.008(5)
Cu1	N3	2.008(5)
Cu1	N4	2.028(5)

Table 3.3 Bond angles in ° for [Cu(dmbpy)₂]OTf.

Atom	Atom	Atom	Angle/°
N1	Cu1	N4	124.5(2)
N2	Cu1	N1	81.8(2)
N2	Cu1	N3	132.8(2)
N2	Cu1	N4	119.0(2)
N3	Cu1	N1	123.8(2)
N3	Cu1	N4	81.0(2)

Compound [Cu(dmbpy)₂H₂O]OTf₂

Formula	C ₂₆ H ₂₆ CuF ₆ N ₄ O ₇ S ₂
<i>D</i> _{calc.} / g cm ⁻³	1.557
<i>μ</i> /mm ⁻¹	0.899
Formula Weight	748.17
Colour	green
Shape	plate
Size/mm ³	0.29×0.16×0.03
<i>T</i> /K	173(2)
Crystal System	monoclinic
Space Group	<i>C</i> 2/ <i>c</i>
<i>a</i> /Å	21.678(4)
<i>b</i> /Å	10.9980(19)
<i>c</i> /Å	15.194(3)
<i>α</i> /°	90
<i>β</i> /°	118.217(2)
<i>γ</i> /°	90
<i>V</i> /Å ³	3191.9(9)
<i>Z</i>	4
<i>Z</i> '	0.5
Wavelength/Å	0.710730
Radiation type	MoK _α
<i>θ</i> _{min} /°	2.132
<i>θ</i> _{max} /°	25.398
Measured Refl.	9966
Independent Refl.	2906
Reflections Used	2233
<i>R</i> _{int}	0.0399
Parameters	212
Restraints	0
Largest Peak	0.557
Deepest Hole	-0.382
Goof	1.057
<i>wR</i> ₂ (all data)	0.1298
<i>wR</i> ₂	0.1184
<i>R</i> ₁ (all data)	0.0640
<i>R</i> ₁	0.0481

**Table 3.4** Bond lengths in Å for [Cu(dmbpy)₂H₂O]OTf₂.

Atom	Atom	Length/Å
Cu1	O1	2.021(3)
Cu1	N1	2.112(3)
Cu1	N1 ¹	2.112(3)
Cu1	N2	1.978(3)
Cu1	N2 ¹	1.978(3)

Table 3.5 Bond angles in ° for [Cu(dmbpy)₂H₂O]OTf₂.

Atom	Atom	Atom	Angle/°
O1	Cu1	N1	123.89(7)
O1	Cu1	N1 ¹	123.89(7)
N1 ¹	Cu1	N1	112.22(15)
N2	Cu1	O1	85.09(7)
N2 ¹	Cu1	O1	85.09(7)
N2 ¹	Cu1	N1	104.91(10)
N2	Cu1	N1 ¹	104.91(10)
N2 ¹	Cu1	N1 ¹	80.68(10)
N2	Cu1	N1	80.68(10)
N2 ¹	Cu1	N2	170.18(14)

Table 3.6 Hydrogen bond information for [Cu(dmbpy)₂H₂O]OTf₂.

D	H	A	d(D-H)/Å	d(H-A)/Å	d(D-A)/Å	D-H-A/deg
O1	H1A	O2	0.88	1.92	2.675(3)	143.7
O1	H1B	O2 ¹	0.88	2.08	2.675(3)	124.9

¹1-x, +y, 1/2-z

For $\text{Cu}(\text{TBP})_4\text{OTf}_2$, a crystal was chosen, and the data were collected using a Bruker CCD (charge coupled device) based diffractometer equipped with an Oxford Cryostream low-temperature apparatus operating at 173 K. Although the unit cell [$a=20.24$ $b=38.07$ $c=11.94$ $\beta=94.20$ $\text{Vol}=91193(1)$] matched that of the known compound, CCDC 1484482, REFCODE: IPEWAD tetrakis(4-*t*-Butylpyridine)-bis(trifluoromethanesulfonato)-copper hydrate reported (At 100K) by Hupp, a partial data set was collected (63%) which confirmed the structure was the same as that reported in the literature.³ Complete data set was not collected.

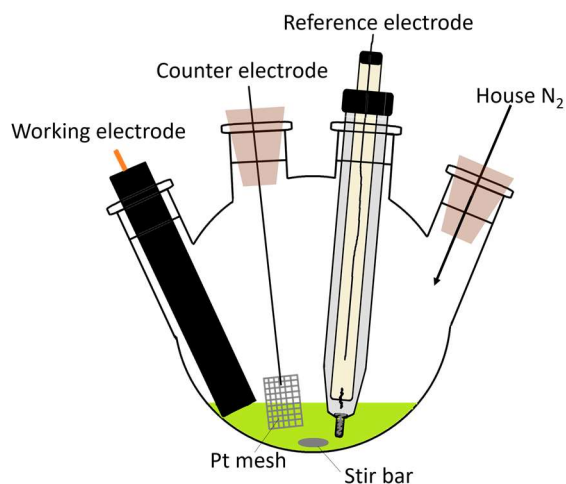


Figure 3.16 The electrochemical cell configuration used for CV measurement.

Counter electrode for the bulk electrolysis was made with solution containing sacrificial redox couple. As shown in Figure 3.17, the Pt wire was melted into a glass tube. A small stir bar was kept in the tube. High surface area silver wire polished with sandpaper and then dried before assembling. The solution used was prepared freshly and was changed every month or anytime necessary. Solution contains 0.1 M LiOTf and the concentration of AgOTf is determined by the amount of reactant in the bulk electrolysis solution. The AgOTf was more than 5 times the concentration of the reactant that need to be oxidized or reduced in the bulk electrolysis cell. The long silver wire was immersed in the electrolyte on one end and used as a connection on the other end.

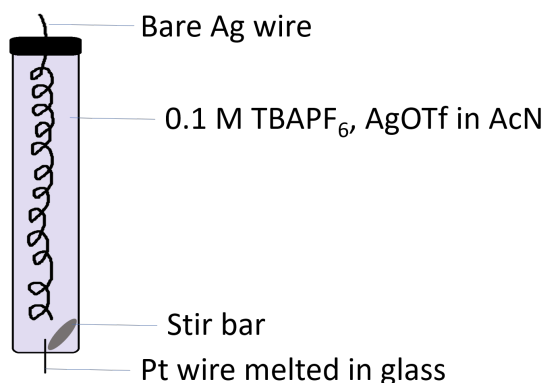


Figure 3.17 The home-made counter electrode for bulk electrolysis.

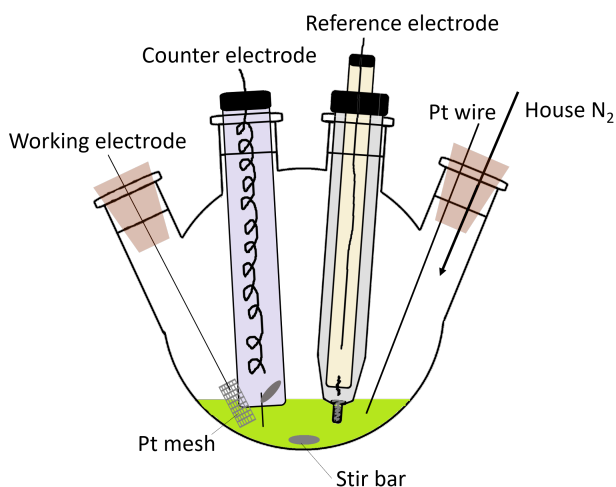


Figure 3.18 The electrochemical cell configuration used for bulk electrolysis.



Figure 3.19 The method used for transferring stopped-flow air sensitive samples.

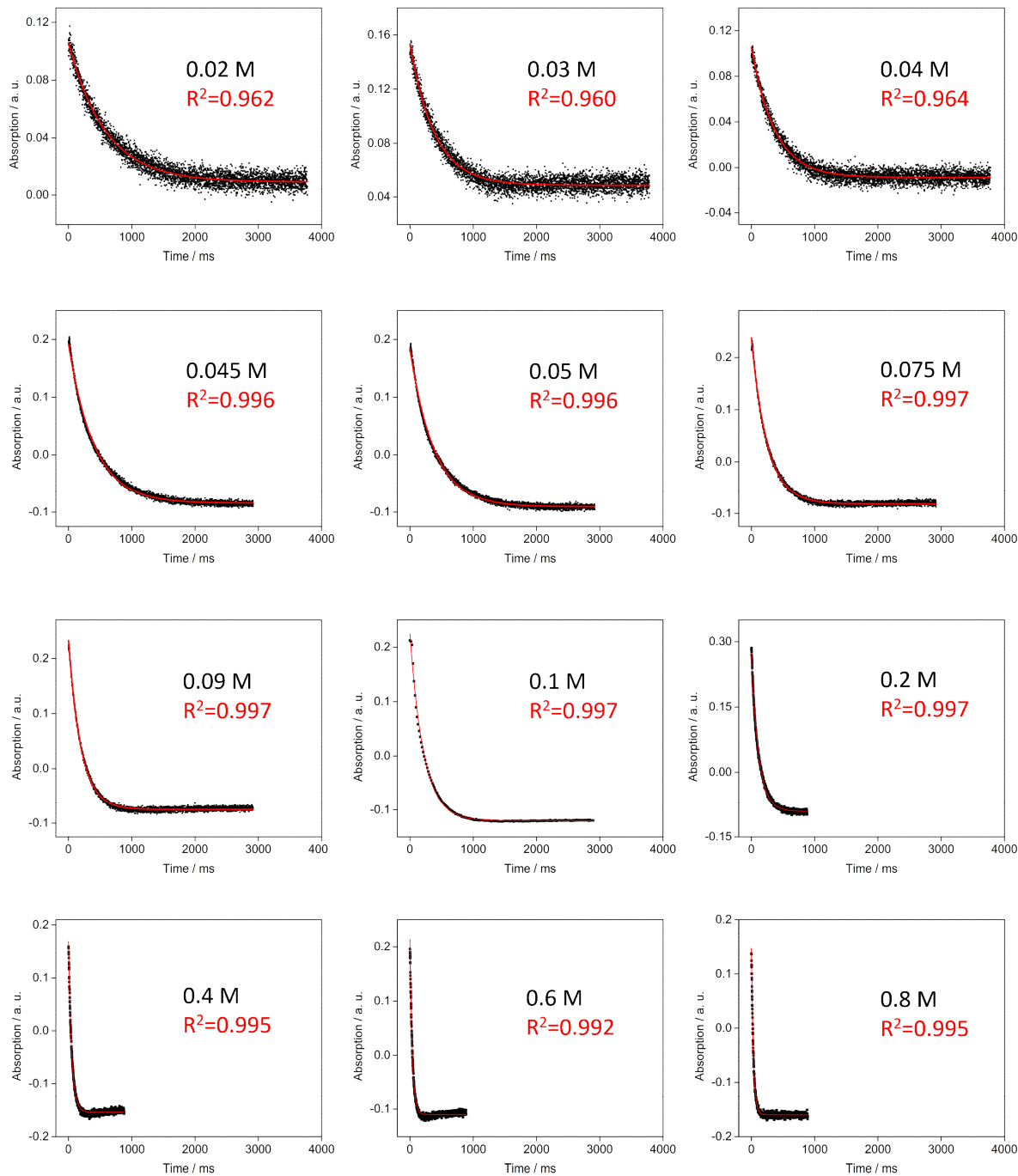


Figure 3.20 The stopped-flow raw data. Black are the raw data and red are the fitted curve. Concentrations of TBP and the R^2 of the fitting are shown in each plot.

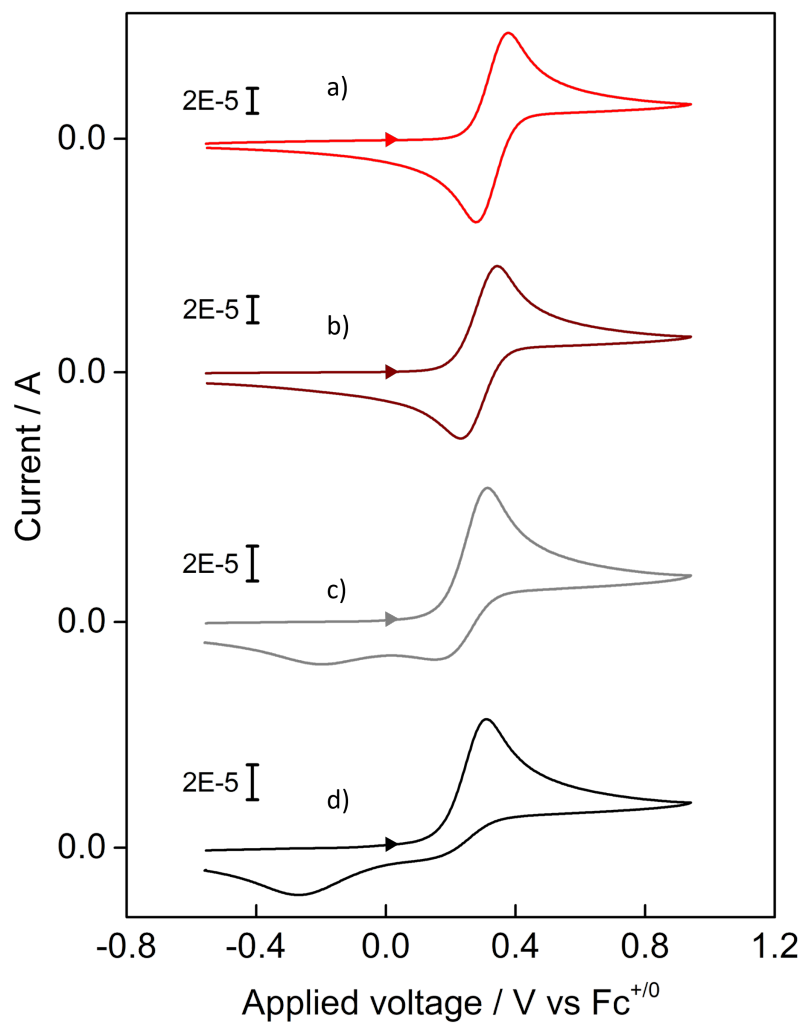


Figure 3.21 Electrochemical behavior of $[\text{Cu}(\text{dmbpy})_2]^+$ in acetonitrile with the presence of TBP. 4 mM $[\text{Cu}(\text{dmbpy})_2]^+$ with the addition of 0, 3, 13 and 25 equivalents of TBP to the copper complex (**a** to **d**). The scan rate was 0.1 V/s. Glassy carbon disk was used as a working electrode, and the same peak shape was also observed on a Pt disk electrode.

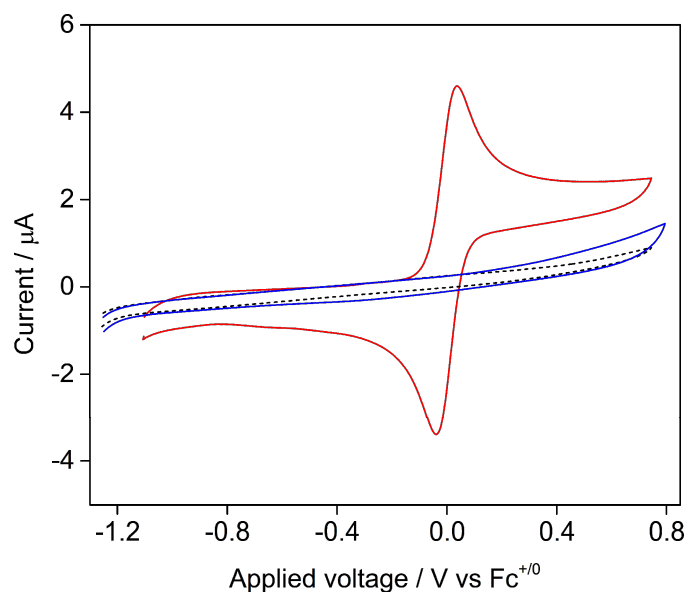


Figure 3.22 CV scans of 1 mM ferrocene (red) and 0.5 M TBP (blue) in acetonitrile on glassy carbon working electrode. Supporting electrolyte was 0.1 M TBAPF₆. Scan rate was 0.1 V/s. Black dashed curve is the blank scan.

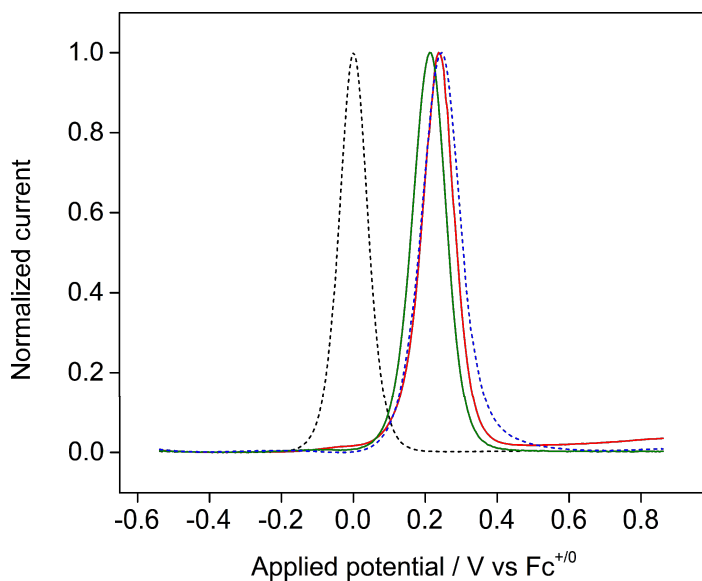


Figure 3.23 Differential pulse voltammogram of different redox solutions in acetonitrile on glassy carbon working electrode. 0.5 mM ferrocene (black dashed); 1 mM [Cu(dmbpy)₂]⁺ and 2.5 mM TBP (red); 1 mM [Cu(dmbpy)₂]⁺, 0.1 mM [Cu(dmbpy)₂]²⁺ and 2.5 mM TBP (green); 1 mM [Cu(dmbpy)₂]⁺, 0.1 mM [Cu(TBP)₄]²⁺ and 2.5 mM TBP (blue dashed).

Table 3.7 The linewidths of solvent peak at 1.94 ppm at different $[\text{Cu}(\text{dmbpy})_2]^{2+}$ concentrations.

Sample #	1	2	3	4	5	6
Concentration of $[\text{Cu}(\text{dmbpy})_2]^{2+}$ / mM	12	10.5	7.5	4.5	3	0
Linewidth of solvent peak (acetonitrile) / Hz	1.13	2.00	3.31	1.69	2.09	1.11

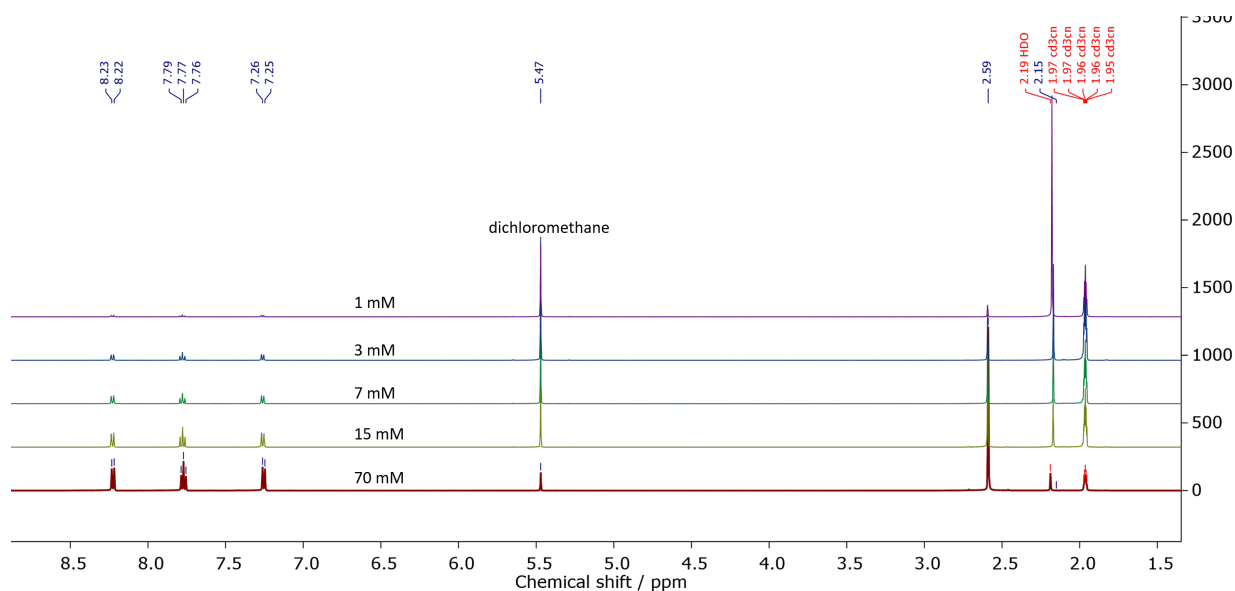


Figure 3.24 ^1H NMR of dmbpy ligand from 1 mM to 70 mM. 20 mM DCM was used as a standard.

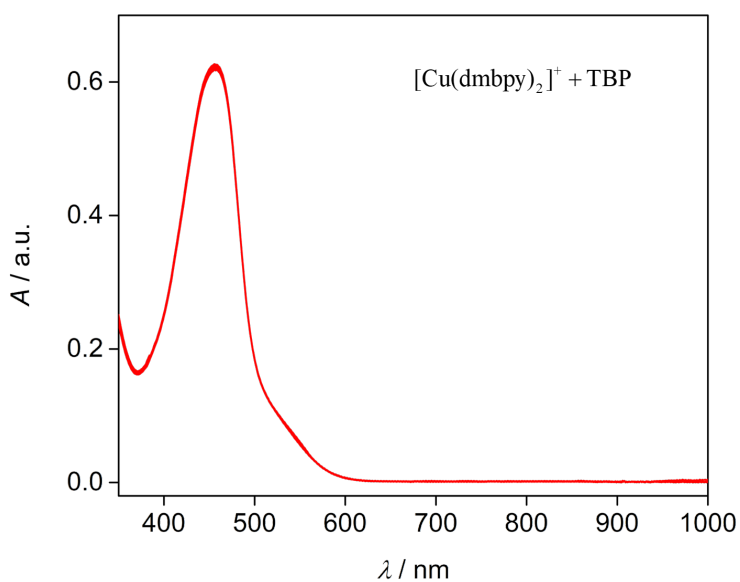


Figure 3.25 The absorption spectra of 0.014 mM $[\text{Cu}(\text{dmbpy})_2]^+$ adding 4, 8, 12, 16, 20, 24, 28, 32, 36 and 40 equivalents TBP in DCM.

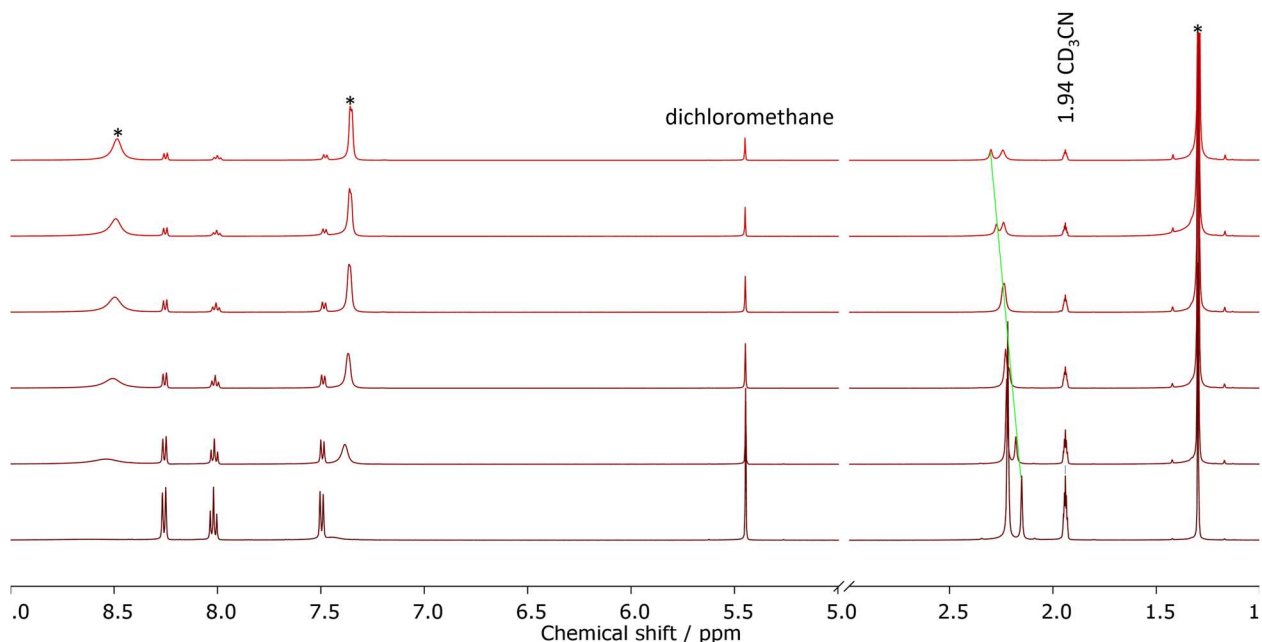


Figure 3.26 ^1H NMR spectra of $[\text{Cu}(\text{dmbpy})_2]\text{OTf}$ with the addition of TBP measured under room temperature in CD_3CN with dichloromethane as the internal standard. Spectra of 12.5 mM $[\text{Cu}(\text{dmbpy})_2]\text{OTf}$ and different concentrations of TBP (from bottom to top, 12.5 to 320 mM) are shown. The * labeled peaks are from TBP. The green line labeled peaks are from water.

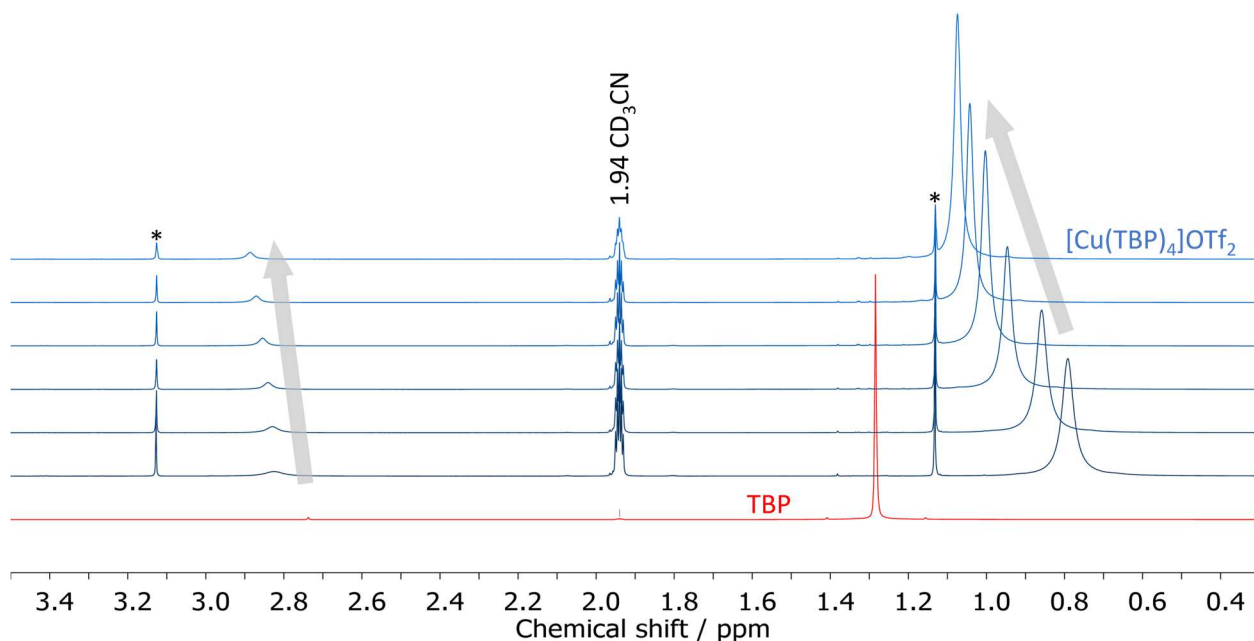


Figure 3.27 ^1H NMR spectra of $[\text{Cu}(\text{TBP})_4]\text{OTf}_2$ with the addition of TBP measured under room temperature in CD_3CN . The * labeled peaks are from the internal standard, 20 mM MTBE. Pure TBP spectrum is shown in red. Spectra of 16.7 mM $[\text{Cu}(\text{TBP})_4]\text{OTf}_2$ with different concentrations of TBP (from bottom to top, 0 to 80 mM) are shown in blue.

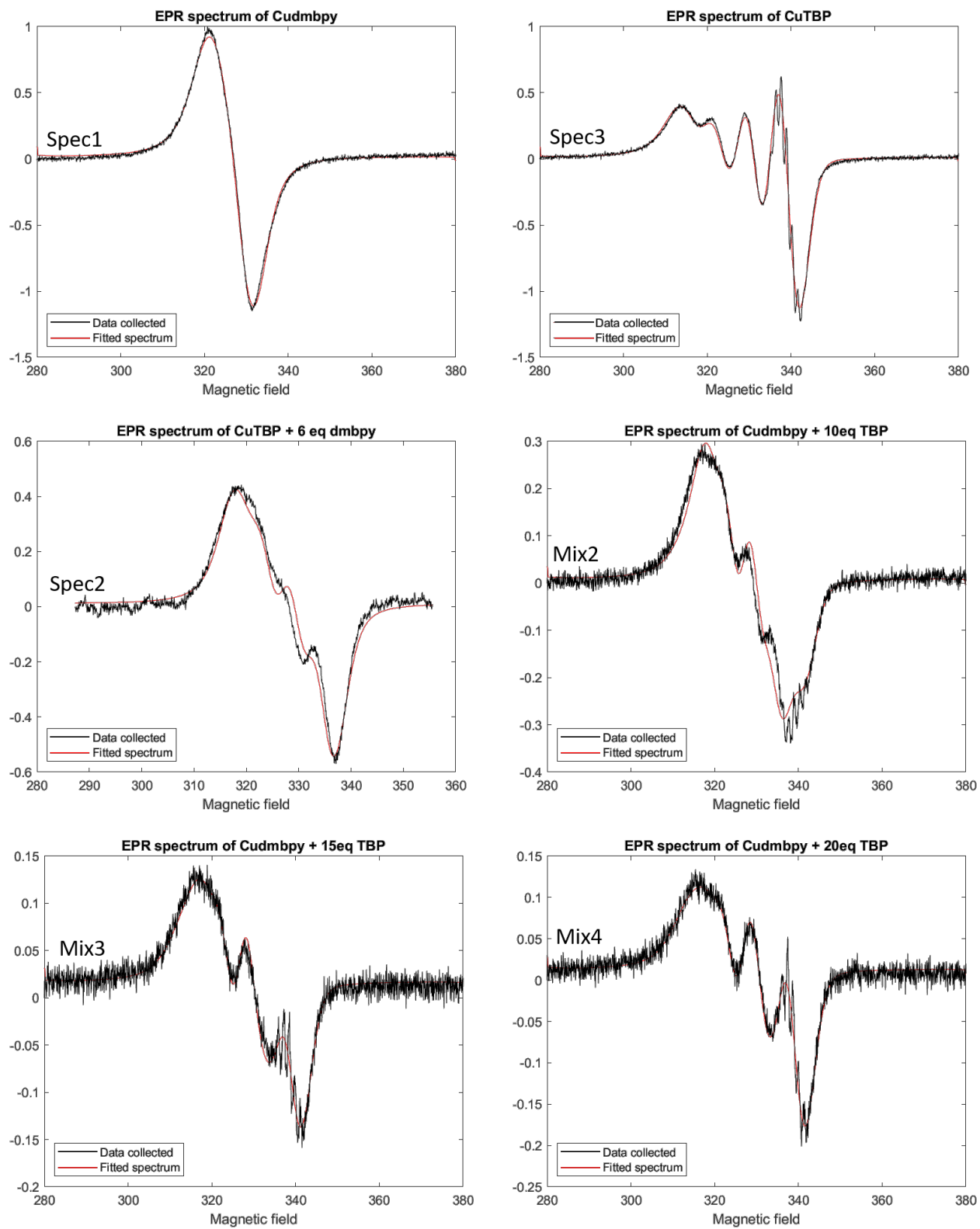


Figure 3.28 The fitted spectra: Spec1, Spec2, Spec3, Mix2, Mix3, Mix4.

MATLAB script used in EasySpin for the fitting of the Spec1, Spec2 and Spec3.

1) For Spec1, $[\text{Cu}(\text{dmbpy})_2]^{2+}$

```

Sys = struct('S',1/2,'g',[2.3145,2.0567,2.0567]);
Sys.lwpp=4.805;
Sys.Nucs='Cu';
Sys.A=[129.8357,47.6302,47.6302];
Sys.tcorr=0.1193*1e-9;

```

2) For Spec2, intermediate

```

Sys = struct('S',1/2,'g',[2.15,2.12,2.12]);
Sys.lwpp=4.66;
Sys.Nucs='Cu';
Sys.A=[505,-47,-47];
Sys.tcorr=0.10*1e-9;

```

3) For Spec3, $[\text{Cu}(\text{TBP})_4]^{2+}$

```

Sys = struct('S',1/2,'g',[2.2217,2.0774,2.0774]);
Sys.lwpp=5.6689;
Sys.Nucs='Cu';
Sys.A=[527,59,59];
Sys.tcorr=0.0908*1e-9;

```

Table 3.8 Fitting results for EPR spectra Mix1, Mix2, Mix3.

	Amp1	Amp2	Amp3	Fitting residual
	0.0048	0.0144	0.0089	12.5526
Mix1	0	0.0162	0.0077	14.7021
	0.4070	0	0.5972	24.7705
	0.2311	0.7569	0	42.5977
Mix2	-0.0338	0.6339	0.2408	0.9984
	0	0.6909	0.2747	1.0406
Mix3	-0.0207	0.2532	0.2640	0.2098
	0	0.2390	0.2690	0.2204
Mix4	-0.0437	0.3553	0.6189	0.2293
	0	0.2379	0.4670	0.2442

The Mix spectra are fitted by $Mix(n) = Amp1 \times Spec1 + Amp2 \times Spec2 + Amp3 \times Spec3$. The residual is calculated by sum of the square of the difference between fitted spectrum and measured spectrum. The assumptions made for the equilibrium: reaction 1 is complete at these TBP concentrations; there is one intermediate state that is generated by the dissociation of one dmbpy.

$$K_2 = \frac{[Cu(TBP)_4^{2+}][dmbpy]}{[Cu(dmbpy)TBP_{4-x}^{2+}][TBP]^{4-x}} \quad (3.2)$$

$$= \frac{[Cu(TBP)_4^{2+}] \times (2 \times [Cu(TBP)_4^{2+}] + [Cu(dmbpy)(TBP)_x^{2+}])}{[Cu(dmbpy)(TBP)_x^{2+}] \times ([TBP]_0 - 4 \times [Cu(TBP)_4^{2+}] - x [Cu(dmbpy)(TBP)_x^{2+}])^{4-x}}$$

Table 3.9 Concentrations of species in the Mix samples for EPR measurement.

	$[Cu(dmbpy)(TBP)_x^{2+}] / \text{mM}$	$[Cu(TBP)_4^{2+}] / \text{mM}$	$[TBP] / \text{mM}$
Mix2	0.76	0.30	10
Mix3	0.38	0.42	18
Mix4	0.23	0.44	26.7

The value of x can influence the value of K_2 . When $x=1$, K_2 are calculated to be 0.0010, 0.0003 and 0.0014 mM^{-2} . When $x=2$, K_2 are calculated to be 0.0101, 0.0055 and 0.0035 mM^{-1} . When $x=3$, K_2 are calculated to be 0.0823, 0.0888 and 0.0876.

REFERENCES

REFERENCES

- (1) Pal, S. *Pyridine: A Useful Ligand in Transition Metal Complexes*; InTech, **2018**
- (2) Williams, R. M.; Cola, L. De; Hartl, F.; Lagref, J.-J.; Planeix, J.-M.; Cian, A. De; Hosseini, M. W. *Coord. Chem. Rev.* **2002**, *230*, 253
- (3) Hoffeditz, W. L.; Katz, M. J.; Deria, P.; Cutsail III, G. E.; Pellin, M. J.; Farha, O. K.; Hupp, J. T. *J. Phys. Chem. C* **2016**, *120*, 3731
- (4) Koshino, Nobuyoshi; Kuchiyama, Yoshio; Funahashi, Shigenobu; Takagi, H. D. *Can. J. Chem.* **1999**, *77*, 1498
- (5) Doine, H.; Yano, Y.; Swaddle, T. W. *Inorg. Chem.* **1989**, *28*, 2319
- (6) Kavan, L.; Saygili, Y.; Freitag, M.; Zakeeruddin, S. M.; Hagfeldt, A.; Grätzel, M. *Electrochim. Acta* **2017**, *227*, 194
- (7) Forsberg, J. H.; Dolter, T. J.; Carter, A. M.; Singh, D.; Aubuchon, S. A.; Timperman, A. T.; Ziaee, A. *Inorg. Chem.* **1992**, *31*, 5555
- (8) Bisquert, J.; Fabregat-Santiago, F.; Mora-Seró, I.; Garcia-Belmonte, G.; Giménez, S. *J. Phys. Chem. C* **2009**, *113*, 17278
- (9) Lee, H. W.; Sengottuvelan, N.; Seo, H.-J.; Choi, J. S.; Kang, S. K.; Kim, Y.-I. *Bull. Korean Chem. Soc.* **2008**, *29*, 1711
- (10) Garribba, E.; Micera, G. *J. Chem. Educ.* **2006**, *83*, 1229
- (11) Stoll, S.; Schweiger, A. *J. Magn. Reson.* **2006**, *178*, 42

Chapter 4 The effect of the *in-situ* ligand exchange reaction between [Cu(dmbpy)]^{2+/+} redox couple and TBP, on the DSSC performance

4.1 Introduction

In the years following Grätzel's breakthrough report of a 10% efficient dye-sensitized solar cell, DSSC, efforts to further improve the efficiency were stymied by the reliance on the triiodide/iodide (I³⁻/I⁻) redox shuttle.¹ The major limitation of utilizing I³⁻/I⁻ stems from the high driving force necessary for efficient dye regeneration.² Over the past decade, use of outer-sphere redox shuttles has allowed systems to be designed which are capable of reducing this driving force and improving the performance.^{3, 4} Cobalt-based redox shuttles have received the most attention, and DSSCs employing the [Co(bpy)₃]^{3+/2+} (bpy = 2,2'-bipyridine) redox mediator produced a reported efficiency of over 12%.⁵

DSSCs employing copper-based redox shuttles have been the subject of increasing interest. Copper-based redox shuttles have been investigated in DSSCs as early as 2005.⁶ In that first report, the [Cu(dmp)₂]^{2+/+} (dmp = 2,9-dimethyl-1,10-phenanthroline) redox shuttle showed relatively poor performance due to poor regeneration of N719 which was attributed to the considerable reorganization energy associated with a distortion of the pseudo-tetrahedral [Cu(dmp)₂]⁺ complex upon oxidation. Interestingly, use of the structurally very similar [Cu(dmbpy)₂]^{2+/+} (dmbpy = 6,6'-dimethyl-2,2'-bipyridine) redox shuttle was recently shown to produce near-unity dye regeneration efficiency with only a 0.11 V overpotential when paired with the Y123 dye.^{7, 8} Such systems have recently shown very exciting efficiencies of over 13% for liquid electrolytes, 32% under ambient lighting, as well as solid-state systems over 11%.⁹

The energy diagram of DSSCs applying $[\text{Cu}(\text{dmbpy})_2]^{2+/+}$ as the redox couple is shown in Figure 4.1. Conventionally, the energy difference between the Fermi level (E_F) of the TiO_2 and the redox potential ($E_{1/2}$) of the redox couple determines the optimum open-circuit voltage (V_{OC}) of the solar cell. By far, the best performing DSSCs with $[\text{Cu}(\text{dmbpy})_2]^{2+/+}$ generates 1.0 V V_{OC} , which is smaller than the predicted value from the thermodynamics. Therefore, we believe this energy mismatch of the system should be studied because there can still be room for improvement.

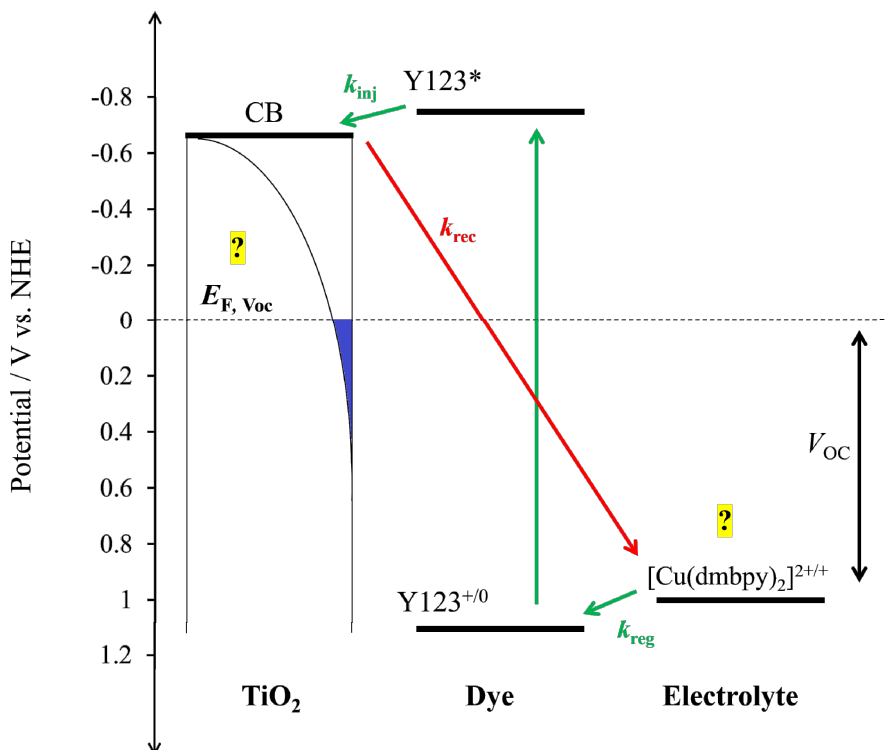


Figure 4.1 Energy diagram of a DSSC showing the relevant kinetic processes involving $[\text{Cu}(\text{dmbpy})_2]^{2+/+}$ redox couple. In the diagram, dye regeneration by the redox couple, electron recombination to the $\text{Cu}(\text{II})$ species in the electrolyte, and electron injection to the conduction band of TiO_2 are shown by k_{reg} , k_{rec} , and k_{inj} respectively.

Historically, 4-*tert*-butylpyridine (TBP) was first used to increase the photovoltage of DSSC.¹ Later studies have also shown that the adsorbed TBP on the TiO_2 surface can shift the energy level of the conduction band of TiO_2 .^{10, 11, 12} It is also believed that TBP can bind onto the active site on the TiO_2 surface and to suppress the electron recombination at the semiconductor electrolyte interface.^{12, 13} Therefore, TBP has been used as a common additive in the electrolyte of DSSCs to

improve power conversion efficiency. The same was done for the DSSCs using $[\text{Cu}(\text{dmbpy})_2]^{2+/+}$ as the redox couple. The DSSC electrolytes used to produce the highest efficiency with $[\text{Cu}(\text{dmbpy})_2]^{2+/+}$ are prepared by mixing 0.2 M $[\text{Cu}(\text{dmbpy})_2]^+$, 0.04 M $[\text{Cu}(\text{dmbpy})_2]^{2+}$ and 0.6 M TBP in acetonitrile with a supporting electrolyte.⁸ Thus, approximately 15 equivalents of TBP, with respect to the Cu^{2+} complex, are present. From the previous chapter, we have shown that under this high excess amount of the TBP, the bidentate dmbpy ligand should be displaced, and the reaction generates the $[\text{Cu}(\text{TBP})_4]^{2+}$ complex in the solution. The composition of the relevant redox-active species actually consists of 0.2 M $[\text{Cu}(\text{dmbpy})_2]^+$ and 0.04 M $[\text{Cu}(\text{TBP})_4]^{2+}$, with additional free dmbpy and TBP in solution.

By adding TBP in the electrolyte, the E_{CB} is reported to be negatively shifted compared to the bare surface, and so is the E_{F} .¹² On the energy diagram, $E_{\text{F}, \text{voc}}$ was calculated by the known redox potential of $[\text{Cu}(\text{dmbpy})_2]^{2+/+}$ and the best V_{OC} reported for the DSSC ($E_{\text{F}, \text{voc}} = E_{1/2} - V_{\text{OC}}$), but the value is questionable. These two values (E_{F} and $E_{\text{F}, \text{voc}}$) are off by around 500 mV. There are two possible explanations for this energy mismatch. 1) The electron recombination is fast, which lowers the E_{F} . And the domain pathways for the recombination may be from some other traps states in a lower energy level. This can be true when the reorganization energy for the electron recombination to the $[\text{Cu}(\text{dmbpy})_2]^{2+}$ be less than the driving force of the recombination, so the lower-energy traps state recombination is in the Marcus theory inverted region.¹⁴ 2) The assignment of the energy level of the redox couple ($E_{1/2}$) is not accurate and should be reconsidered based by including the effect of the *in-situ* ligand exchange.

In this chapter, further investigations are done using electrochemical methods, such as impedance spectroscopy, on real DSSCs. Measurements on solutions mimicking the functional electrolyte

were performed to study the effect of the *in-situ* ligand exchange on the performance of the DSSCs and to understand the origin of the energy mismatch in the system.

4.2 Experimental methods

4.2.1 Solar cell assembly

Photoelectrodes were prepared on $12 \Omega/\text{cm}^2$ FTO-coated glass (cut into 2 cm by 2cm squares, TEC 15 Hartford Glass) cleaned by sonicating in soap water solution, deionized water, isopropanol, and acetone, and then heated to 450 °C for 30 min. The blocking layer of TiO_2 was deposited on the precleaned FTO glass using atomic layer deposition (ALD). 500 cycles deposition of TiO_2 was performed using titanium isopropoxide (TIPS, Aldrich) and water as precursors with a Savannah 200 instrument (Cambridge Nanotech, Inc.). TiO_2 layer was grown at 225 °C using reactant exposure times of 0.3 s and 0.015 s for TIPS and H_2O , respectively, and nitrogen purge time of 5 s between exposures. The thickness of the TiO_2 blocking layer was determined to be ~ 10 nm by ellipsometry performed on Si samples coated concurrently. A transparent nanoporous TiO_2 layer (electrode area 0.36 cm^2) was prepared by doctor blading a paste of TiO_2 nanoparticles (Ti-Nanoxide HT/SP, Solaronix) on the FTO. The resulting electrodes were annealed after drying at 325 °C for 5 min, 375 °C for 5 min, 450 °C for 5 min, and 500 °C for 15 min in air. The nanoporous TiO_2 film thickness, d , was measured using a Dektak3 Surface Profiler to be $\sim 8 \mu\text{m}$. TiCl_4 post-treatment was done by immersing the electrodes in 40 mM TiCl_4 water solution at 80 °C for 30 min, followed by annealing at 500 °C for 30 min.

The anodes were immersed in dye solution (0.2 mM solution of 3-{6-{4-[bis(2',4'-dibutyloxybiphenyl-4-yl)amino-]phenyl}-4,4-dihexyl-cyclopenta-[2,1-b:3,4-b']dithiophene-2-yl}-2-cyanoacrylic acid, D35cpdt, in 1:1 acetonitrile and t-butyl alcohol). Chenodeoxylic acid was

used in the dye solution as a co-absorber to prevent dye aggregation. After 20-24 hours, the films were picked up from the solution and rinsed with acetonitrile.

Counter electrodes were the same size as the photoanode. Two holes were drilled on each piece of glass. There are two different types of counter electrode used in this chapter. 1) The platinum-coated counter electrode was made by drop-casting 15 μL of 5 mM H_2PtCl_4 and followed by annealing under 380 $^\circ\text{C}$ for 30 min in air. 2) PEDOT electrode was made following the reported electrochemical deposition method.¹⁵ Two pieces of FTO glass with the same surface area were used as working and counter electrodes. The electrolyte was made of 0.1 M sodium dodecyl sulfate (SDS) and 0.01 M 3,4-ethylenedioxythiophene (EDOT) in water. The electrodeposition was done with $\mu\text{AutoLabII}$ potentiostat or Autolab PGSTAT128N by applying a fixed current between two electrodes (0.16 mA/cm^2) for 600 s. The thickness of the PEDOT layer on FTO was estimated to be 100 nm by ellipsometry.

A $\sim 25 \mu\text{m}$ thick Surlyn film (Solaronix) was sandwiched between the anode and the counter electrode. Pressure was applied at 150 $^\circ\text{C}$ to seal the cells. The electrolyte was filled by capillary force through the two pre-drilled holes on the platinum counter electrode and sealed with micro glass and Surlyn film.

The electrolyte used in DSSCs were prepared by the addition of 0.2 M $[\text{Cu}(\text{dmbpy})_2]\text{OTf}$, 0.02 M $[\text{Cu}(\text{dmbpy})_2\text{H}_2\text{O}]\text{OTf}_2$, 0.1 M LiOTf and different concentrations (0.1, 0.2, 0.3, 0.4, 0.5 M) of TBP in acetonitrile.

Symmetrical cells were made by using two identical electrodes (Pt or PEDOT coated FTO glass) as working and counter electrodes. One of the electrodes was drilled for electrolyte filling, and the other was a whole piece.

4.2.2 Cell characterization methods

Photoelectrochemical measurements were performed with Autolab PGSTAT128N interfaced with a Xe Arc Lamp. An AM 1.5 solar filter was used to simulate sunlight at 100 mW/cm^2 . A 400 nm long-pass filter was used to prevent direct excitation of the TiO_2 in all light measurements. A Horiba Jobin Yvon MicroHR was used for monochromatic light for IPCE measurements. The scan rate for current-voltage measurements under illumination and in dark condition was 0.01 V/s . Other DSSC characterization methods are described in chapter 2.

All electrochemical impedance (EIS) measurements were performed in the dark with Autolab PGSTAT128N interfaced FRA2 module and controlled by NOVA software. The impedance spectra were recorded at applied voltages from -0.4 to -1.2 V , stepped in 25 mV increments, with a 10-mV alternating potential superimposed on the direct bias. Each impedance measurement consisted of frequency sweeps from 0.05 to 10^5 Hz in equally spaced logarithmic steps. The equivalent circuit for fitting the EIS data is shown in Figure 4.2.

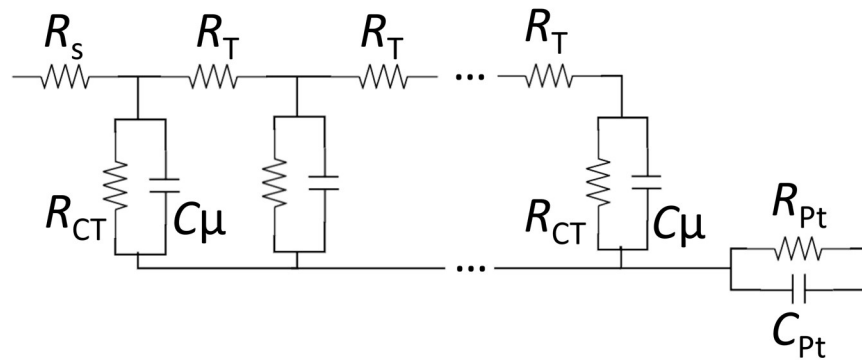


Figure 4.2 Equivalent circuit used to fit the EIS data measured for sandwich cells under dark condition. R_s is the series resistance of the cell. R_T is the charge transport resistance inside TiO_2 nanoporous structure. R_{CT} is the charge transfer resistance between TiO_2 and liquid electrolyte interface. C_μ is the chemical capacitance of TiO_2 . R_{Pt} and C_{Pt} are the resistance and capacitance on the counter electrode/electrolyte interface.¹⁶ (Figure 4.8 in the Appendix shows the elements used in Zview software for this equivalent circuit.)

The solution potential of the electrolyte was measured by dipping the working and reference electrode in the electrolyte with constant stirring of the solution using a magnetic stir bar and read the open circuit potential versus the reference electrode. Different electrodes were used to measure the equilibrium potential of the electrolyte on different interfaces.

4.2.3 Three-electrode setup

The working electrode was prepared the same way as in the DSSCs, but the dye soaking step was eliminated. It was clamped over an opening in the cell and sealed with a Viton O-ring. A home-made reference electrode (0.01 M Ag/AgNO₃ in acetonitrile) was used for all three-electrode measurements, of which the potential was corrected by measuring the CV of ferrocene. The counter electrode consisted of a high surface area platinum mesh. All the three-electrode measurement were done under the constant stirring condition to reduce the effect of the diffusion.

The EIS of the three-electrode setup was done in the dark, under different applied potential, the impedance was measured using the same method as for DSSCs. Dark JV and OCVD measurements were also performed for the three-electrode setup. The dark OCVD was done by applying a constant potential to the working electrode, then switch the cell to open circuit by setting the cell to be “off”. The chronoamperometry method was used to monitor the voltage decay between the working and reference electrodes. Electron lifetime can be calculated based on the OCVD data.

4.3 Result and discussion

4.3.1 The effect of the addition TBP on the solution potential of the electrolyte

The DSSC electrolytes used to produce the highest efficiencies are generated by mixing 0.2 M [Cu(dmbpy)₂]⁺, 0.04 M [Cu(dmbpy)₂]²⁺ and 0.6 M TBP in acetonitrile with an additional

supporting electrolyte. Thus, approximately 15 equivalents of TBP with respect to the Cu^{2+} complex are present. From the previous chapter, the in-situ ligand exchange is proved to happen in the electrolyte. The composition of the relevant redox-active species actually consists of 0.2 M $[\text{Cu}(\text{dmbpy})_2]^+$ and 0.04 M $[\text{Cu}(\text{TBP})_4]^{2+}$, with additional free dmbpy and TBP in solution. There are many consequences to this ligand exchange. For one, the formal potential of the $[\text{Cu}(\text{dmbpy})_2]^{2+/+}$ redox couple is not a reasonable estimate of the solution potential when TBP is present in the electrolyte, even accounting for the ~ 40 mV shift due to concentration differences in accord with the Nernst equation. Due to the in-situ ligand exchange, there is an additional electrochemical active species produced, $[\text{Cu}(\text{TBP})_4]\text{OTf}_2$. This new species has a more negative redox potential and is less electrochemically reversible. Since the V_{OC} of the solar cell is determined by the difference between the Fermi level of the TiO_2 and the equilibrium solution potential on the counter electrode, any change of the solution potential will introduce a change in the determination of the V_{OC} . Attempts to measure the $[\text{Cu}(\text{TBP})_4]^{2+/+}$ redox potential were thwarted as the complex does not exhibit a reversible wave. We, therefore, measured the solution potential as a function of the electrolyte composition. Note that this corresponds roughly to the reference potential in a DSSC is a 2-electrode sandwich cell configuration. In the electrolyte of DSSCs applying $[\text{Cu}(\text{dmbpy})_2]^{2+/+}$ as redox couple, the amount of TBP was varied, and the solution potential (E_{sol}) of the electrolyte was measured on different working electrode. The result is shown in Table 4.1.

Table 4.1 Solution potentials of the electrolyte with different concentrations of TBP. The solution potential was measured on Pt, glassy carbon and PEDOT electrodes, versus Ag/AgNO₃ (Fc⁺⁰ is 0.09 V vs Ag/AgNO₃). Electrolyte contains 0.2 M [Cu(dmbpy)₂]OTf, 0.02 M [Cu(dmbpy)₂H₂O]OTf₂, 0.1 M LiOTf and different concentrations TBP in acetonitrile.

Concentration of TBP / M	$E_{\text{sol}} / \text{V vs. Fc}^{+/0}$
0	0.25
0.1	0.16
0.2	0.10
0.3	0.05
0.4	0.01
0.5	-0.02

As shown in the table, the addition of TBP changed the solution potential dramatically due to the in-situ ligand exchange. As a comparison, the effect of TBP on the solution potential for [Co(bpy)₃]^{3+/2+} was also measured, and it showed negligible change. Addition of TBP to the electrolyte induced a negative shift of the solution potential by 270 mV. This negative shift of the solution potential with the addition of TBP represents a loss of voltage of the cell and thus efficiency. We note that a similar effect was shown by Hupp et al. upon addition of TBP to solutions of [Cu(PDTCO)]^{2+/+}.¹⁷

4.3.2 The effect of TBP on solar cell performance

Given this loss in reference potential, it is striking that such large open-circuit photovoltages, V_{OC} , have been reported for DSSCs employing [Cu(dmbpy)₂]^{2+/+}. Cells were prepared using the same electrolyte compositions discussed above. Photocurrent density vs. applied voltage (J - V) was measured and shown in Figure 4.3. It is interesting to note that the short circuit photocurrent density, J_{SC} , increases significantly upon the introduction of TBP to the electrolyte. Since the

addition of TBP should not increase the light-harvesting, injection or regeneration processes, we attribute the increased J_{SC} to an improved charge collection efficiency from reduced recombination. This is consistent with the concomitant ~ 200 mV larger V_{OC} observed in the presence of TBP.

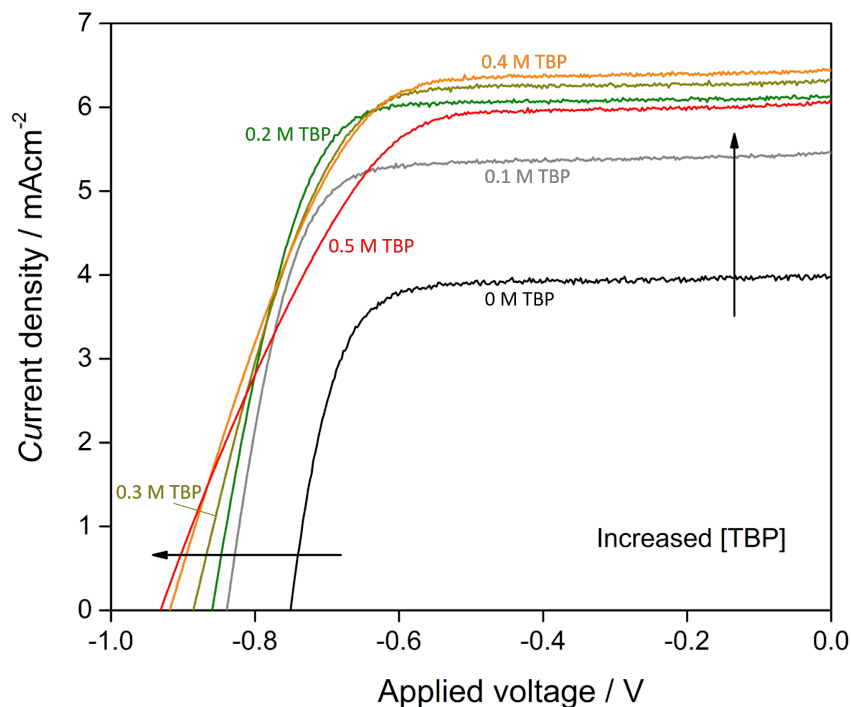


Figure 4.3 Plots of J-V curves for DSSCs employing different concentrations of TBP to the electrolyte. Plots are color-coded according to concentrations of TBP in the electrolyte: 0 M (black), 0.1 M (gray), 0.2 M (green), 0.3 M (dark yellow), 0.4 M (orange) and 0.5 M (red).

Since the V_{oc} is the difference in solution potential and Fermi level (E_F) in TiO_2 , and the V_{oc} and the solution potential have shifted ~ 200 mV and 270 mV respectively with the addition of TBP, the E_F is shifted by ~ 470 mV negatively upon the addition of TBP. The E_F is determined by the conduction band edge and recombination kinetics; thus, there is either a negative shift of conduction band edge, reduced recombination kinetics, or both, upon the introduction of TBP. It is well known that TBP shifts the conduction band edge to more negative values by more than 200 mV.^{18, 19, 20}

4.3.3 Reduced recombination by the in-situ ligand exchange

To isolate the effect of TBP on the energetics of the semiconductor. The recombination process was measured by electrochemical impedance spectroscopy (EIS) under dark conditions. As a comparison, the effect of the introduction of TBP on the chemical capacitance of cells employing the chemically inert $[\text{Co}(\text{bpy})_3]^{3+/2+}$ redox shuttle was measured. The resulted spectra were fitted using the equivalent circuit displayed in Figure 4.2, and the fitting result is shown in Figure 4.4.

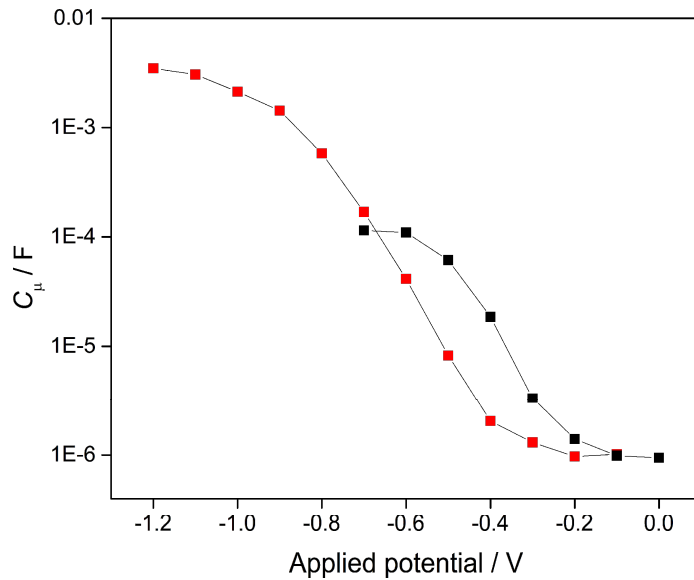


Figure 4.4 Chemical capacitance measured (C_{μ}) by EIS of DSSCs applying $[\text{Co}(\text{bpy})_3]^{3+/2+}$ electrolyte. Black: 0.2 M $[\text{Co}(\text{bpy})_3]^{2+}$ and 0.02 M $[\text{Co}(\text{bpy})_3]^{3+}$, 0.1 M LiOTf. Red: 0.2 M $[\text{Co}(\text{bpy})_3]^{2+}$ and 0.02 M $[\text{Co}(\text{bpy})_3]^{3+}$, 0.1 M LiOTf and 0.5 M TBP.

The chemical capacitance versus applied voltage shows a distribution of trap states on TiO_2 . The negatively change by roughly 200 mV upon the addition of TBP reflects a conduction band shift to a more negative potential and it is in agreement with reports using I^{3-}/I^- .²¹ Thus, as much as a ~270 mV increase in E_F should be due to reduced recombination.

EIS was then done on the DSSCs employing $[\text{Cu}(\text{dmbpy})_2]^{2+/+}$ redox couple. The charge transfer resistance (R_{CT}) is plotted versus the chemical capacitance (C_{μ}) in Figure 4.5. Since the density and distribution of trap states is constant upon surface modification, C_{μ} can be used as an internal standard of the electrochemical potential of electrons in TiO_2 and used to compare relative rate constants of recombination reflected in R_{CT} .²²

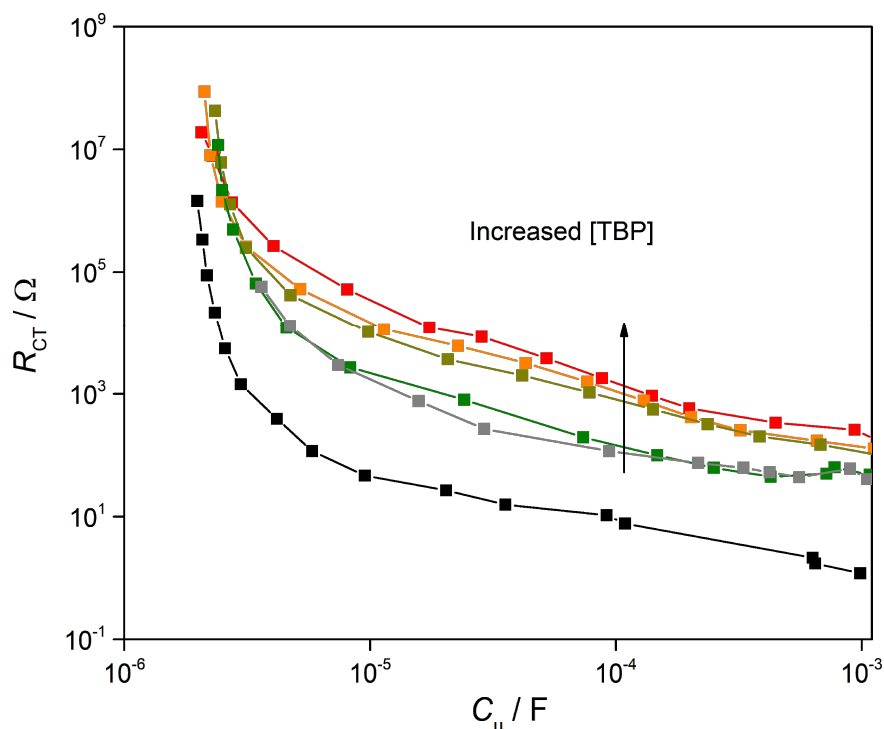


Figure 4.5 EIS measurement on DSSCs with $[\text{Cu}(\text{dmbpy})_2]^{2+/+}$ redox couple. Plots of the charge transfer resistance (R_{CT}) vs the chemical capacitance (C_{μ}) of DSSCs to show the effect of TBP on recombination kinetics. Plots are color-coded according to concentrations of TBP in the electrolyte: 0 M (black), 0.1 M (gray), 0.2 M (green), 0.3 M (dark yellow), 0.4 M (orange) and 0.5 M (red).

Upon the addition of TBP to the electrolyte, R_{CT} increases by a factor of ~ 500 under the same electrochemical potential of electrons (C_{μ}). The slower rate of electron recombination agrees with our proposed ligand exchange reaction in the electrolyte when TBP is present. In other words, the addition of TBP replaces the fast electron acceptor $[\text{Cu}(\text{dmbpy})_2]^{2+}$ with the worse electron acceptor $[\text{Cu}(\text{TBP})_4]^{2+}$ that manifests in slower recombination (higher R_{CT}). The ~ 500 times slower

recombination is consistent with a 270 mV higher E_F , as well as the larger open-circuit photovoltages and charge collection efficiencies.

4.3.4 Reorganization energy of electron recombination reaction to $[\text{Cu}(\text{dmbpy})_2]^{2+}$

Under the condition of the electrolyte without the presence of TBP, the kinetics of electron recombination has been analyzed. In accordance with the self-exchange electron transfer rate constant of $[\text{Cu}(\text{dmbpy})_2]^{2+/+}$ in acetonitrile, the total reorganization energy of the self-exchange reaction can be estimated using Equation 4.1.

$$k_{\text{se}} = \nu_n e^{-\lambda_{\text{tot}}/4k_{\text{B}}T} \quad (4.1)$$

k_{se} is the self-exchange electron transfer rate constant, ν_n is the frequency factor, k_{B} is the Boltzmann constant, and T is the temperature. The value for the vibrational frequency term can range from 10^{11} to 10^{13} Hz depending on the changes attributed to the outer-sphere (solvent) or inner-sphere (bond length changes) reaction coordinate during electron transfer. A value of 10^{13} Hz was used as the frequency factor for $[\text{Cu}(\text{dmbpy})_2]^{2+/+}$ due to the larger inner-sphere contribution to the total reorganization energy (as shown in the large structural change between crystals under different oxidation states). The total reorganization energies, λ_{tot} , is the sum of both the outer-sphere, λ_o , and inner-sphere reorganization energies, λ_i . The outer-sphere self-exchange reorganization energy can be obtained from the dielectric continuum theory in Equation 4.2.²³

$$\lambda_o = \frac{(\Delta z q)^2}{4\pi\epsilon_0} \left(\frac{1}{a} - \frac{1}{R_e} \right) \left(\frac{1}{n_{\text{sol}}^2} - \frac{1}{\epsilon_{\text{sol}}} \right) \quad (4.2)$$

Δz is the change in charge of the copper complex after electron transfer, q is the charge of an electron, ϵ_0 is the permittivity of free space, ϵ_{sol} is the static dielectric constant of acetonitrile (36)²⁴,

n_{sol} is the refractive index of acetonitrile (1.3442)²⁵, a is the radii of the reactant, and R is the reactant center-to-center separation distance ($R = 2a$). The radii of $[\text{Cu}(\text{dmbpy})_2]^{2+/+}$ is estimated from the solid-state crystal structure, 5.7 Å. The inner-sphere reorganization energy can be determined using the total reorganization energy (from Equation 4.1) and the outer-sphere reorganization energy (from Equation 4.2).

For the electron recombination reaction, electrons from the TiO_2 reacts with the electron acceptor in the electrolyte. The inner sphere reorganization energy of the recombination reaction is half of the redox couple's λ_{in} , and the outer sphere reorganization energy can be calculated using Equation 4.3. This is the revised dielectric continuum theory to include the property of the anatase TiO_2 .²⁶

$$\lambda_{\text{o,TiO}_2} = \frac{(\Delta zq)^2}{8\pi\epsilon_0} \left[\frac{1}{a} \left(\frac{1}{n_{\text{sol}}^2} - \frac{1}{\epsilon_{\text{sol}}} \right) - \frac{1}{2R_e} \times \left(\frac{1}{n_{\text{sol}}^2} \left(\frac{n_{\text{TiO}_2}^2 - n_{\text{sol}}^2}{n_{\text{TiO}_2}^2 + n_{\text{sol}}^2} \right) - \frac{1}{\epsilon_{\text{sol}}} \left(\frac{\epsilon_{\text{TiO}_2} - \epsilon_{\text{sol}}}{\epsilon_{\text{TiO}_2} + \epsilon_{\text{sol}}} \right) \right) \right] \quad (4.3)$$

In the equation, n_{TiO_2} is the refractive index of TiO_2 (2.54)²⁵, ϵ_{TiO_2} is the static dielectric of TiO_2 (114)^{27, 28}, R_e is the distance from the electron acceptor to the electrode (5.7 Å). By using both Equation 4.2 and 4.3, the total reorganization energy of the electron transfer from the electrons on the TiO_2 can be calculated by $\lambda_{\text{rec}} = \lambda_{\text{o,TiO}_2} + \frac{1}{2}\lambda_{\text{i}}$, and results are summarized in Table 4.2.

Table 4.2 Summary of the reorganization energies and the electron transfer rate constants calculated for $[\text{Cu}(\text{dmbpy})_2]^{2+/+}$ redox couple in acetonitrile. $-\Delta G$ is the free energy change of the electron recombination from the conduction band of TiO_2 to $[\text{Cu}(\text{dmbpy})_2]^{2+}$ in the electrolyte.

k_{se}	$1.0 \times 10^4 \text{ M}^{-1}\text{s}^{-1}$
λ_{tot}	2.13 eV
λ_{o}	0.66 eV
λ_{i}	1.47 eV
$\lambda_{\text{o, TiO}_2}$	0.47 eV
λ_{rec}	1.22 eV
$-\Delta G$	1.56 eV

From the calculated results, the free energy change of the electron recombination reaction is larger than the reorganization energy. This results in the kinetic of the recombination lie in the Marcus inverted region. The fastest recombination happens when $-\Delta G = \lambda_{\text{rec}}$, which is expressed as k_{max} .

$$k_{\text{rec}} = k_{\text{max}} e^{-(\Delta G + \lambda_{\text{rec}})^2 / 4\lambda_{\text{rec}}k_{\text{B}}T} \quad (4.4)$$

By substituting the $-\Delta G = 1.56 \text{ eV}$ for the recombination of electrons in the conduction band of TiO_2 , and the value for the reorganization energy from above, the exponential in Equation 4.4 has a value of 0.02. This indicates that the rate constant for electrons from the conduction band recombining with the electron acceptor, $[\text{Cu}(\text{dmbpy})_2]^{2+}$, is much smaller than the recombination rate constant for the electrons from the k_{max} energy level. However, the rate of the electron

recombination also depends on the concentration of electrons, and a complete recombination kinetic model can be established with more care.

4.3.5 The discussion about the origin of the electron recombination

Knowing that the recombination of the electrons from the conduction band is in the Marcus inverted region, it is reasonable to question if the recombination dominates by the electrons from the surface states.¹⁴ The electron lifetime is a measurable parameter that reflects the electron recombination kinetics. It is the average lifetime of an electron on the TiO₂ before it reacts with the electron acceptor in the electrolyte. The electron lifetime has an exponential dependence on potential.²⁹ This exponential dependence holds true when recombination is occurring primarily from the conduction band. If the recombination is mainly mediated by surface states, the electron lifetime will show a parabolic component as a deviation of log-linear behavior observed for conduction band recombination.³⁰ Also the inverted region recombination has been modeled before, and the parabolic component was well resolved experimentally. To better understand if the DSSCs applying [Cu(dmbpy)₂]^{2+/+} redox couple suffers from surface states recombination, electron lifetime was studied.

Since the in-situ ligand exchange induced a negative shift in the solution potential of the electrolyte of DSSCs as shown previously, the two-electrode sandwich cell configuration is not anymore an excellent way to compare the electron lifetime due to the lack of recognition of the actual electronic potential. Three-electrode setup was applied to correct this potential change of the counter electrode in the two-electrode system. A new scan of TiO₂ film in contact with electrolyte without [Cu(dmbpy)₂]^{2+/+} is shown in Figure 4.6.

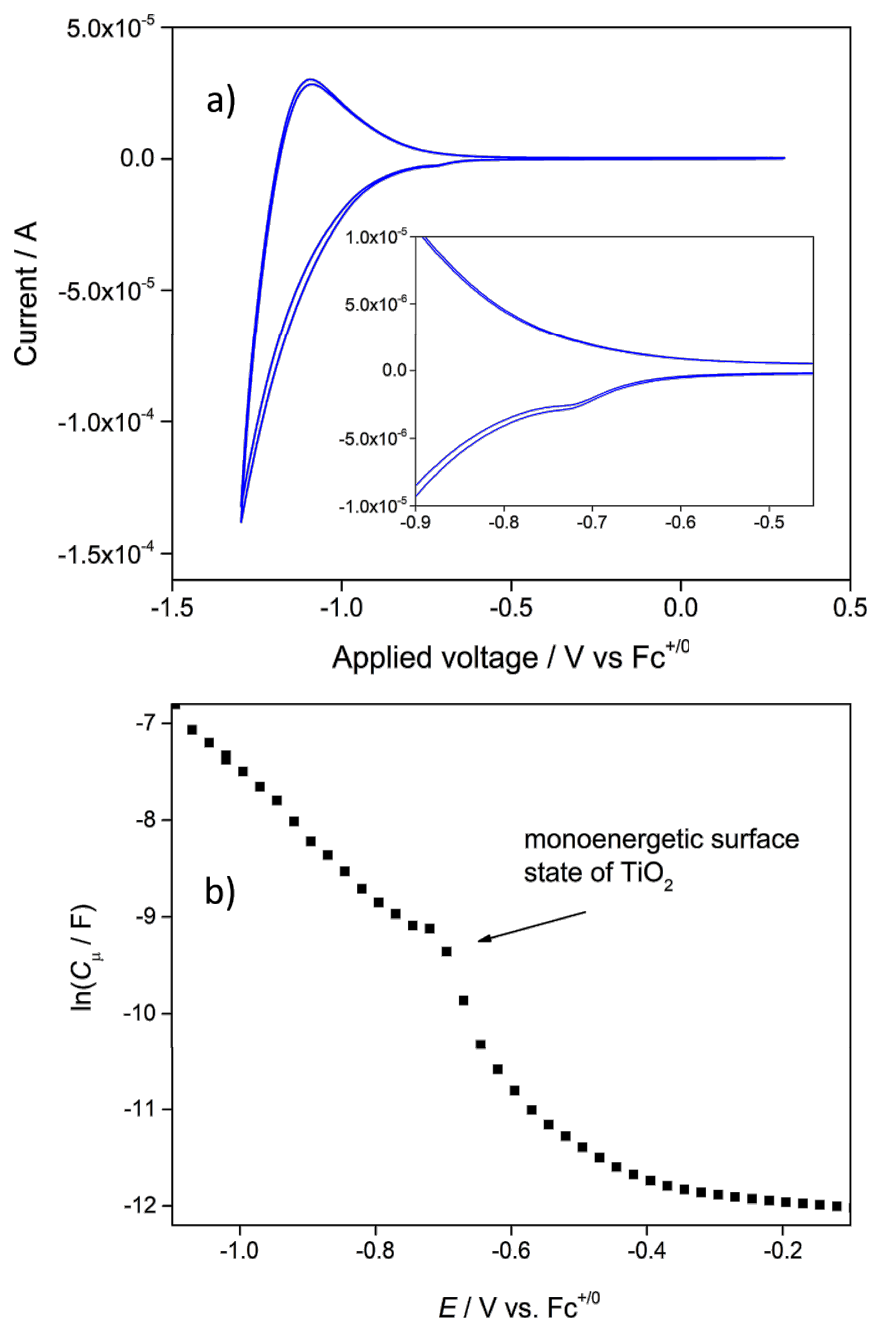


Figure 4.6 a) Cyclic voltammogram done in a three-electrode cell setup for a TiO_2 nanoporous electrode in contact with electrolyte by 0.1 V/s scan rate. The electrolyte composed of 0.1 M LiOTf in acetonitrile. **b)** Chemical capacitance, C_{μ} , measured by EIS using the same setup, plotted on the \ln scale versus the potential energy. The electrolyte composed of 0.1 M LiOTf, 0.5 M TBP, 0.02 M $[\text{Cu}(\text{dmbpy})_2]^{2+}$ in acetonitrile.

The small peak at a potential -0.72 vs. $\text{Fc}^{+/0}$ on the CV curve shows the existence of the monoenergetic surface state on TiO_2 . Plotting the chemical capacitance obtained from EIS measurement resolved the same feature of this monoenergetic surface state, even with the presence of TBP. The energy of this surface state matches with the reported value for the same material. Therefore the $-\Delta G$ for the recombination of electrons from this monoenergetic surface state to the electron acceptor $[\text{Cu}(\text{dmbpy})_2]^{2+}$ should be 1.05 eV, which is smaller but close to the reorganization energy of recombination, 1.21 eV. Figure 4.7 shows the difference between electron lifetimes with and without TBP in the electrolyte:

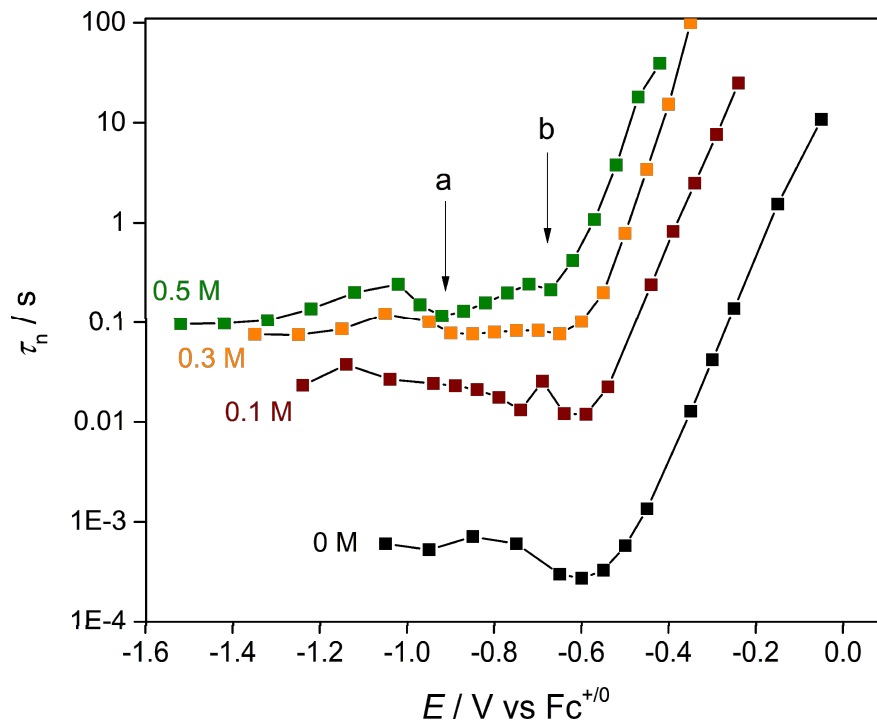


Figure 4.7 Electron lifetime of DSSCs measured in the dark with different amounts of TBP (concentration labeled in the plot). The electrolyte contains 0.2 M $[\text{Cu}(\text{dmbpy})_2]^+$, 0.02 M $[\text{Cu}(\text{dmbpy})_2]^{2+}$, 0.1 M LiOTf and TBP. Arrow a and b indicate two local minimums on the lifetime curve, indicates the different recombination pathways. The applied voltage on the two-electrode DSSCs is converted to the energy of the electrons by applying a correction for the equilibrium potential on the counter electrode use values in Table 4.1.

At least two local minimums show up in the lifetime curves. The local minimum b is around -0.6 to 0.65 eV versus $\text{Fc}^{+/0}$. Therefore, it can be attributed to the recombination from the monoenergetic surface state. This minimum in lifetime is near the energetic center of the monoenergetic state (-0.72 eV versus $\text{Fc}^{+/0}$) but shifts slightly to negative. It also shows a less prominent feature when the TBP concentration increases which we attribute to the passivating effect of the surface states from the TBP. Besides the recombination from the monoenergetic surface state, there is still electron recombination from the exponential distributed surface states. The local minimum occurs where the driving force, $-\Delta G$, equals the reorganization energy, λ . The k_{rec} in this energy reaches its maximum. With more of TBP, this local minimum does not disappear, but the overall electron lifetime increases. Comparing four curves in Figure 4.7, although the addition of TBP increased the electron lifetime, the pattern of the lifetime curve is not changed. The same recombination pathways exist when the *in-situ* ligand exchange takes place. The produced electron acceptor, $[\text{Cu}(\text{TBP})_4]^{2+}$ is not responsible for the recombination, and the reduced concentration of $[\text{Cu}(\text{dmbpy})_2]^{2+}$ explained the increased electron lifetime.

4.4 Conclusion

The results presented above explained the excellent performance of the recently reported DSSCs employing $[\text{Cu}(\text{dmbpy})_2]^{2+/+}$ electrolytes and the critical role of TBP. We showed that the addition of TBP to $[\text{Cu}(\text{dmbpy})_2]^{2+/+}$ electrolytes results in a rapid ligand substitution reaction to form the $[\text{Cu}(\text{TBP})_4]^{2+}/[\text{Cu}(\text{dmbpy})_2]^+$ redox species in solution. The $[\text{Cu}(\text{dmbpy})_2]^+$ species has previously been shown to quantitatively regenerate dyes with minimal driving force (ca. 0.1 V), which is critical in achieving high efficiencies. The consequence of the substitution reaction is that recombination is reduced, which further improves both the V_{OC} and J_{SC} . The reorganization energy of the electron recombination to $[\text{Cu}(\text{dmbpy})_2]^{2+}$ is 1.22 eV, which is smaller than the driving force

for the recombination from the energy of the conduction band of TiO₂. The kinetic of conduction band electron recombination, therefore, lies in the Marcus theory inverted region, but the recombination of the electrons from the monoenergetic surface states is in the normal region. All these contribute to multiple local minimums in the electron lifetime curve. Reduced recombination is a result of the reduced [Cu(dmbpy)₂]²⁺ concentration in the electrolyte once TBP is added. The ligand exchange reaction also induces a negative shift of the solution potential, which results in a ~270 mV loss in V_{OC} . Thus, optimization of the ligand substitution product solution potential offers a path to further improve the photovoltage by over 200 mV without concomitant loss in photocurrent.

APPENDIX

APPENDIX

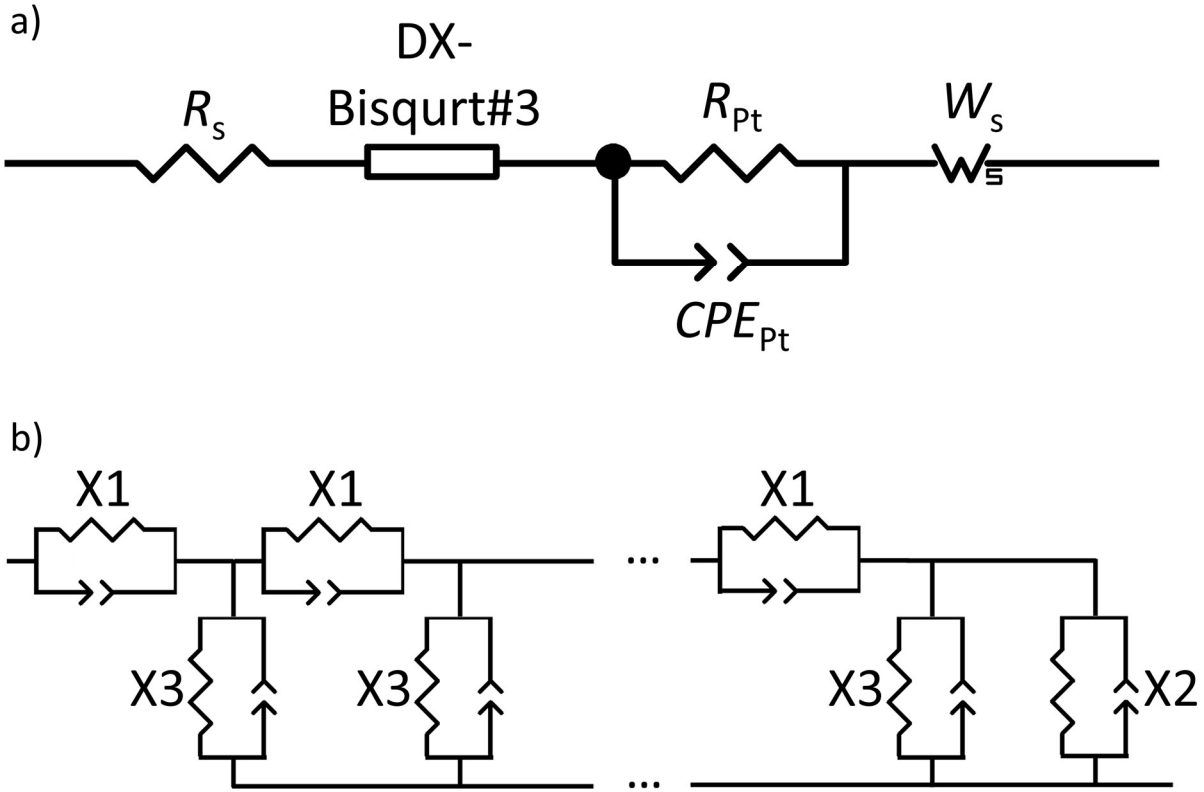


Figure 4.8 Equivalent circuit in Z-view software. **a)** The circuit built by using the elements provided in Z-view. R is resistance, CPE is constant phase element, DX is a complex module and W is the Warburg element. **b)** The equivalent circuit of DX module used in a). $X1$, $X2$, $X3$ are each a parallel resistor and constant phase element combination.

Table 4.3 The parameters in the DX-Bisqurt#3 model.

Parameters in Z-view	Physical meaning
DX-R (X1)	R_T
DX-T (X1)	unused
DX-P (X1)	unused
DX-U (X2)	unused
DX-A (X2)	unused
DX-B (X2)	unused
DX-C (X3)	R_{CT}
DX-D (X3)	C_μ
DX-E (X3)	Fitted (0-1), the closer to 1 the more ideal the capacitor behavior.
DX-F (Length)	Fixed (1)

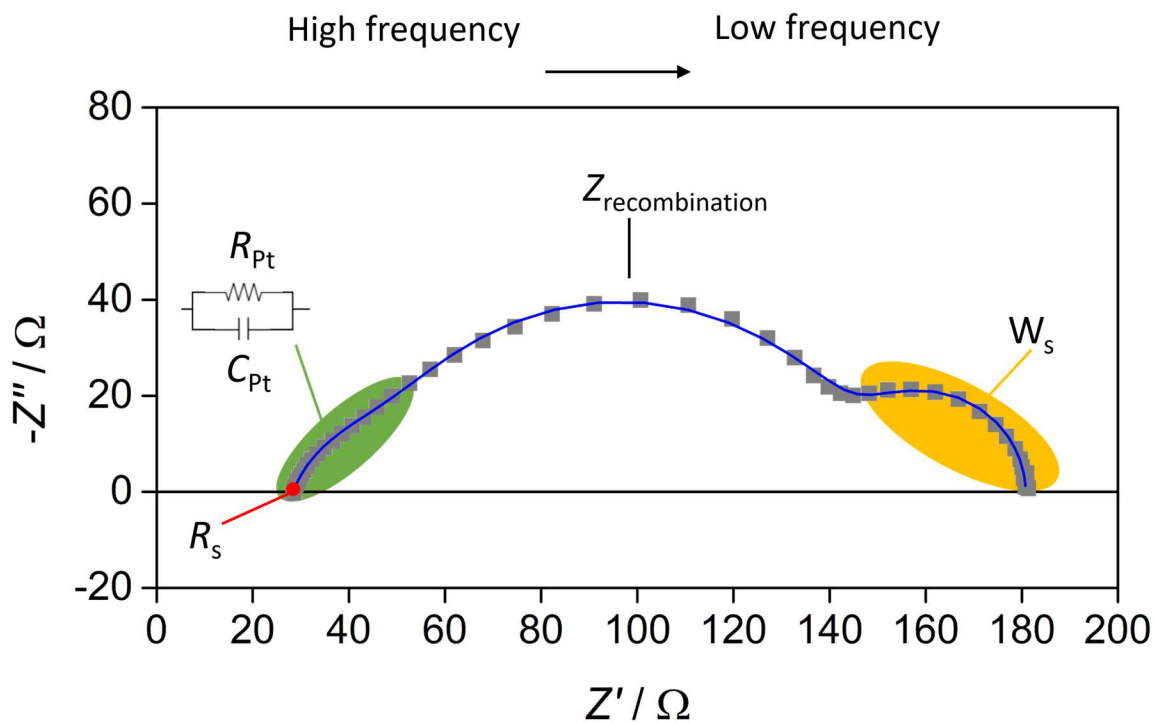


Figure 4.9 Nyquist plot of a DSSC at a fixed applied potential and the information that can be extracted from it. Each raw data point is collected with a different frequency of the potential perturbation which follows a sine wave. From high to low frequency region, the main information that can be obtained from the plot are charge transfer on the counter electrode, charge transfer on the anode/electrolyte interface and the diffusion of charge carrier in the electrolyte.

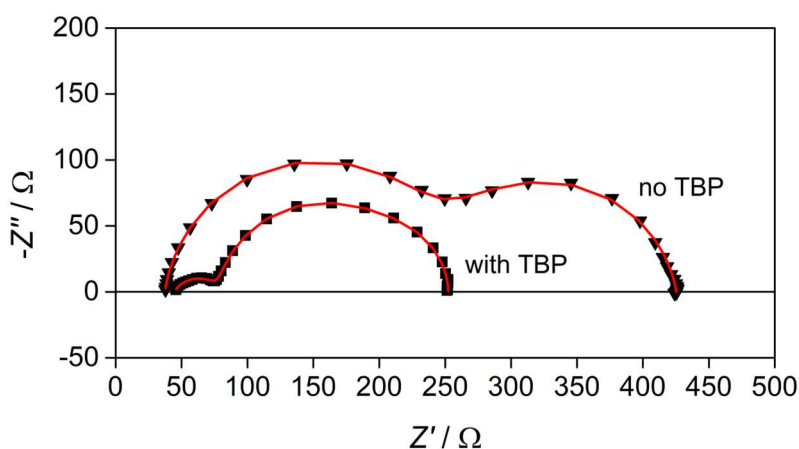


Figure 4.10 Nyquist plots of DSSCs with Y123 dye. Electrolyte contains 0.1 M LiOTf, 0.2 M $[\text{Co}(\text{bpy})_3]^{2+}$, 0.02 M $[\text{Co}(\text{bpy})_3]^{3+}$ and 0 M TBP (no TBP) or 0.5 M TBP (with TBP). The EIS was done in the dark. The plots shown are at the V_{OC} of each cell (-0.5 V for “no TBP” and -0.8 V for “with TBP”). Scattered plots are raw EIS data. Red curves are the fitted curves.

Table 4.4 Parameters extracted from fitting dark EIS data of cobalt DSSC with Y123 dye. Electrolyte contains 0.1 M LiOTf, 0.2 M [Co(bpy)₃]³⁺, 0.02 M [Co(bpy)₃]²⁺ and 0.5 M TBP.

Applied potential V / vs. CE	R_s / Ω	R_{CT} / Ω	C_{μ} / F	R_T / Ω	R_{Pt} / Ω	C_{Pt} / F
0	41.46	3.199E+2	1.0042E-6	-	-	-
-0.1	43.57	4.562E+1	1.0524E-6	-	-	-
-0.2	45	1.000E+2	1.0561E-6	-	-	-
-0.25	45.38	9.961E+1	1.1401E-6	-	-	-
-0.3	44.25	3.4857E7	1.3235E-6	-	-	-
-0.4	44.12	2.8708E6	2.5584E-6	-	17033	5.338E-6
-0.5	42.38	184140	8.3112E-6	-	1335	9.2523E-6
-0.6	42.06	10157	4.13E-5	207.9	50.46	2.0941E-6
-0.7	44.27	774.9	0.000141	41.39	34.62	1.0042E-5
-0.8	44.36	177	0.000489	12.91	27.98	4.2417E-5
-0.9	45.7	48.68	0.001200	3.022	20.23	4.143E-5
-1	46.27	55.28	0.003150	2.905	15.06	2.1189E-5
-1.1	45.94	36.22	0.003710	2.492	13.27	1.5116E-5
-1.2	45.52	23.75	0.003421	1.451	12.2	1.7178E-5

Table 4.5 Parameters extracted from fitting dark EIS data of cobalt DSSC with Y123 dye. Electrolyte contains 0.1 M LiOTf, 0.2 M $[\text{Co}(\text{bpy})_3]^{3+}$ and 0.02 M $[\text{Co}(\text{bpy})_3]^{2+}$.

Applied potential V / vs. CE	R_s / Ω	R_{CT} / Ω	C_{μ} / F	R_T / Ω	R_{Pt} / Ω	C_{Pt} / F
0	37.77	5.741E7	9.4825E-7	-	-	-
-0.1	37.81	1.7715E7	1.031E-6	-	-	-
-0.2	37.22	171200	3.4202E-6	-	1.0652E6	1.9201E-6
-0.3	36.17	45947	3.7214E-6	-	4735	4.5875E-6
-0.4	36.58	1443	1.8429E-5	-	426.8	3.2811E-6
-0.5	36.87	158.4	5.0308E-5	-	227.2	2.6007E-6
-0.6	37.48	48.07	0.0002064	-	128.6	1.9893E-6
-0.7	37.75	25.62	0.00012138	-	63.46	1.7806E-6
-0.8	37.74	16.83	0.00028692	-	35.01	1.8612E-6
-0.9	37.46	6.3	0.00076761	22.19	21.58	1.6593E-6
-1	37.51	6.155	0.0023655	17.05	15.17	1.5315E-6

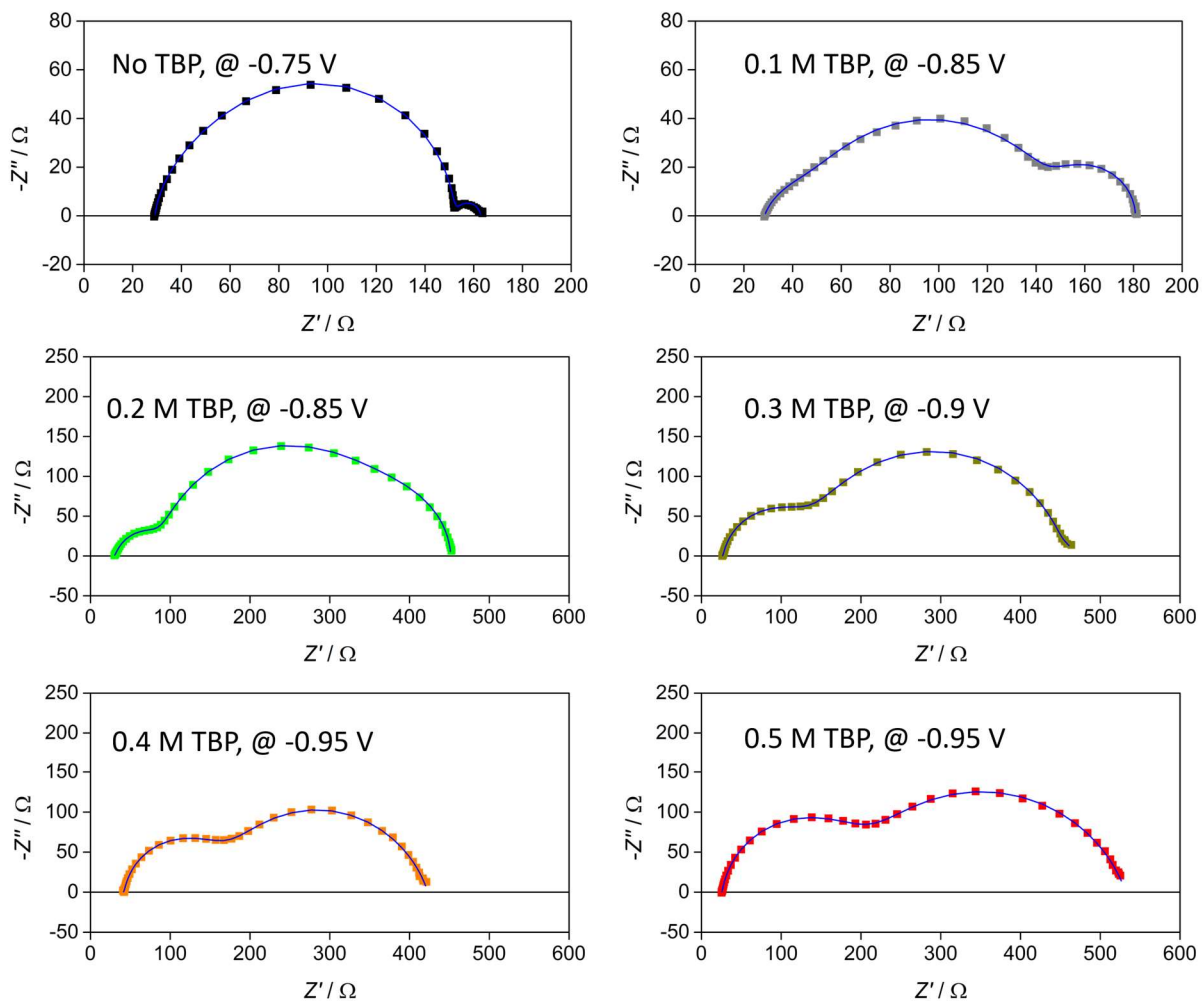


Figure 4.11 Nyquist plots of DSSCs with Y123 dye. Electrolyte contains 0.1 M LiOTf, 0.2 M $[\text{Cu}(\text{dmbpy})_2]^+$, 0.02 M $[\text{Cu}(\text{dmbpy})_2]^{2+}$ and different concentrations of TBP. The EIS was done in the dark. The plots shown are at the V_{OC} of each cell. Scattered plots are raw EIS data. Blue curves are the fitted curves.

Table 4.6 Parameters extracted from fitting dark EIS data of copper DSSC with Y123 dye. Electrolyte contains 0.1 M LiOTf, 0.2 M [Cu(dmbpy)₂]⁺ and 0.02 M [Cu(dmbpy)₂]²⁺.

Applied potential V / vs. CE	R_s / Ω	R_{CT} / Ω	C_{μ} / F	R_T / Ω	R_{Pt} / Ω	C_{Pt} / F	W_{S-R}	W_{S-T}
-0.4	26.02	1.471E6	2.0128E-6	-	-	-	-	-
-0.45	26.18	340500	2.1239E-6	9.414	-	-	-	-
-0.5	29.56	88706	2.2408E-6	-	-	-	-	-
-0.55	27.24	21929	2.4595E-6	6.931	-	-	-	-
-0.6	27.15	5637	2.8123E-6	7.032	-	-	-	-
-0.65	29.13	1408	2.7586E-6	-	32.66	3.0161E-5	-	-
-0.7	28.99	340.9	3.6538E-6	-	50.28	2.3307E-5	-	-
-0.75	29.11	107.3	5.9676E-6	-	16.28	1.5801E-5	10.7	0.4639
-0.8	29.17	47.23	1.1243E-5	-	6.01	9.6129E-6	17.18	0.32951
-0.85	29.06	28.49	3.035E-5	-	3.188	8.4146E-6	21.12	0.27115
-0.9	29.15	16.11	4.3218E-5	-	3.707	6.9598E-6	12.84	0.25018
-0.95	29.59	9.491	6.9212E-5	-	3.565	1.3452E-5	6.384	0.15283
-1	29.22	6.571	8.0472E-5	-	3.351	2.3201E-5	4.638	0.14756
-1.1	27.8	4.391	0.0001796	7.37	3.073	2.7766E-5	2.741	0.15063
-1.2	27.82	3.136	0.0002629	5.765	2.514	8.5256E-6	2.33	0.13619
-1.3	27.61	2.583	0.0004403	4.752	2.029	4.3384E-6	2.14	0.14152

Table 4.7 Parameters extracted from fitting dark EIS data of copper DSSC with Y123 dye. Electrolyte contains 0.1 M LiOTf, 0.2 M [Cu(dmbpy)₂]⁺, 0.02 M [Cu(dmbpy)₂]²⁺ and 0.1 M TBP.

Applied potential V / vs. CE	R_s / Ω	R_{CT} / Ω	C_{μ} / F	R_T / Ω	R_{Pt} / Ω	C_{Pt} / F	W_{S-R}	W_{S-T}
-0.6	28.34	55074	3.0874E-6	-	108	3.8672E-5	-	-
-0.65	28.26	12631	3.8077E-6	-	87.26	4.2942E-5	-	-
-0.7	28.44	2831	5.6237E-6	-	53.19	2.865E-5	-	-
-0.75	28.21	682.3	1.0543E-5	-	44.14	3.1725E-5	-	-
-0.8	28.25	209.3	2.4626E-5	-	29.22	3.1381E-5	40.47	0.32153
-0.85	28.42	92.56	6.7924E-5	-	19.49	3.8091E-5	40.37	0.24596
-0.9	28.07	48.67	0.0001171	5.07	16.87	8.3629E-5	33.63	0.17362
-0.95	28.61	42.19	0.0002043	-	8.549	4.348E-5	31.06	0.15199
-1	28.75	34.75	0.0002805	-	4.778	1.4389E-5	29.06	0.1462
-1.05	28.68	27.81	0.0003630	-	3.337	1.1193E-5	25.03	0.14582
-1.1	28.52	22.37	0.0006280	-	3.593	3.7832E-5	47.78	0.1518
-1.15	28.41	18.16	0.0006877	-	2.548	7.9438E-6	28.18	0.13861
-1.2	28.29	14.15	0.0007949	-	2.126	8.2924E-6	21.7	0.12613
-1.25	28.26	11.6	0.0009324	-	1.812	9.1855E-6	17.96	0.11988
-1.3	28.08	9.556	0.0011001	-	1.661	1.0481E-5	15.77	0.11874

Table 4.8 Parameters extracted from fitting dark EIS data of copper DSSC with Y123 dye. Electrolyte contains 0.1 M LiOTf, 0.2 M [Cu(dmbpy)₂]⁺, 0.02 M [Cu(dmbpy)₂]²⁺ and 0.2 M TBP.

Applied potential V / vs. CE	R_s / Ω	R_{CT} / Ω	C_μ / F	R_T / Ω	R_{Pt} / Ω	C_{Pt} / F	W_{S-R}	W_{S-T}
-0.4	28.92	6.2709E7	2.265E-6	-	169.3	1.5589E-5	-	-
-0.45	28.94	2.6122E7	2.4168E-6	-	135.6	1.4633E-5	-	-
-0.5	28.9	2.4708E6	2.5389E-6	-	139.4	1.5286E-5	-	-
-0.55	28.84	464420	2.7323E-6	-	150.9	1.6197E-5	-	-
-0.6	30.09	60062	3.2544E-6	-	165	1.3983E-5	-	-
-0.65	30.02	11792	4.3259E-6	-	164.8	1.4085E-5	-	-
-0.7	30	2600	7.9143E-6	-	169.4	1.2044E-5	-	-
-0.75	29.85	729.9	2.543E-5	-	166.6	1.5842E-5	-	-
-0.8	29.96	309.1	5.6095E-5	-	125.5	2.3216E-5	64.63	0.2637
-0.85	29.54	272	0.0001027	19.53	47.07	1.3847E-5	96.07	0.3073
-0.9	30.22	183.9	0.0001584	2.7521	30.51	1.5003E-5	109.3	0.3223
-0.95	30.24	114.1	0.0002381	1.309	20.27	1.4153E-5	88.99	0.3269
-1	30.25	68.63	0.0003389	-	14.82	1.5092E-5	66.49	0.3065
-1.05	30.15	40.92	0.0004601	-	10.99	1.2598E-5	53.6	0.2784
-1.1	30.02	26.81	0.0006689	-	8.336	1.176E-5	44.63	0.2493
-1.15	29.92	18.61	0.0009810	-	6.375	8.7524E-6	37.7	0.2118
-1.2	29.84	13.15	0.0012473	-	5.21	8.7959E-6	31.9	0.1820
-1.25	29.73	12.2	0.0026958	-	5.954	1.2633E-5	30.71	0.1716
-1.3	29.67	14.14	0.0036515	-	4.482	1.0936E-5	20.34	0.1688

Table 4.9 Parameters extracted from fitting dark EIS data of copper DSSC with Y123 dye. Electrolyte contains 0.1 M LiOTf, 0.2 M [Cu(dmbpy)₂]⁺, 0.02 M [Cu(dmbpy)₂]²⁺ and 0.3 M TBP.

Applied potential V / vs. CE	R_s / Ω	R_{CT} / Ω	C_{μ} / F	R_T / Ω	R_{Pt} / Ω	C_{Pt} / F	W_{S-R}	W_{S-T}
-0.4	25.35	3.622E7	2.3426E-6	-	521.7	1.312E-5	-	-
-0.45	25.23	5.9762E6	2.4757E-6	-	518.7	1.3592E-5	-	-
-0.5	25.22	1.2565E6	2.692E-6	-	511.1	1.4009E-5	-	-
-0.55	25.26	249460	3.122E-6	-	452.2	1.4049E-5	-	-
-0.6	25.89	41362	4.6699E-6	-	645.4	1.213E-5	-	-
-0.65	25.65	9430	1.0024E-5	-	1327	9.1455E-6	-	-
-0.7	25.61	3452	2.1775E-5	-	809.3	1.4075E-5	-	-
-0.75	25.29	1908	4.2129E-5	13.76	414.1	2.2467E-5	-	-
-0.8	25.85	1048	7.7848E-5	17.18	245.8	2.0521E-5	-	-
-0.85	26.13	563.6	0.0001325	8.302	164.5	1.873E-5	-	-
-0.9	26.14	325.4	0.0002132	4.318	105.7	1.7464E-5	-	-
-0.95	26.54	183.8	0.0002929	-	72.4	1.8854E-5	-	-
-1	26.1	120.4	0.0010221	-	40.79	1.4425E-5	30.68	0.035
-1.1	26.01	59.98	0.0017825	-	22.21	1.3447E-5	48.97	0.294
-1.2	25.91	31.09	0.003212	-	14.27	1.4282E-5	37.38	0.189
-1.3	25.81	10.91	0.0018695	-	8.204	1.1313E-5	32.33	0.178
-1.4	25.69	10.44	0.0024134	3.002	5.561	1.247E-5	22.19	0.182

Table 4.10 Parameters extracted from fitting dark EIS data of copper DSSC with Y123 dye. Electrolyte contains 0.1 M LiOTf, 0.2 M [Cu(dmbpy)₂]⁺, 0.02 M [Cu(dmbpy)₂]²⁺ and 0.4 M TBP.

Applied potential V / vs. CE	R_s / Ω	R_{CT} / Ω	C_{μ} / F	R_T / Ω	R_{Pt} / Ω	C_{Pt} / F	W_{S-R}	W_{S-T}
-0.4	40.08	4.3476E7	2.1144E-6	-	905.7	1.6841E-5	-	-
-0.45	40.03	7.4265E6	2.2384E-6	-	795.2	1.7465E-5	-	-
-0.5	40.04	1.3926E6	2.492E-6	-	706.7	1.8832E-5	-	-
-0.55	39.98	257010	3.1108E-6	-	632.8	2.0985E-5	-	-
-0.6	39.8	50990	5.0856E-6	-	1135	1.3525E-5	-	-
-0.65	39.59	10642	1.2493E-5	-	2249	9.144E-6	-	-
-0.7	41.22	5649	2.4158E-5	-	1235	1.8742E-5	-	-
-0.75	40.49	2995	4.4633E-5	46.37	679	2.2035E-5	-	-
-0.8	40.85	1199	0.0001103	3.665	373.6	1.8367E-5	413.8	0.182
-0.85	41.28	650.9	0.0001613	4.463	272.5	1.7053E-5	167.7	0.169
-0.9	41.32	369.1	0.0002315	3.511	183.7	1.685E-5	67.67	0.122
-0.95	41.07	220.3	0.0003957	2.605	115.6	1.6592E-5	44.1	0.087
-1	40.81	161.7	0.0007460	1.86	76.52	1.7184E-5	29.23	0.053
-1.1	40.47	78.21	0.0020254	1.996	38.8	1.6993E-5	64.27	0.307
-1.2	39.74	35.3	0.0045979	11.86	21.89	1.8622E-5	49.79	0.200
-1.3	39.71	26.14	0.0027496	3.195	16.02	3.2341E-5	24.88	0.198
-1.4	39.22	19.51	0.0031483	1.659	11.2	4.2609E-5	15.66	0.170
-1.5	38.5	13.63	0.0036988	1.02	8.509	5.1492E-5	12.01	0.157

Table 4.11 Parameters extracted from fitting dark EIS data of copper DSSC with Y123 dye. Electrolyte contains 0.1 M LiOTf, 0.2 M [Cu(dmbpy)₂]⁺, 0.02 M [Cu(dmbpy)₂]²⁺ and 0.5 M TBP.

Applied potential V / vs. CE	R_s / Ω	R_{CT} / Ω	C_{μ} / F	R_T / Ω	R_{Pt} / Ω	C_{Pt} / F	W_{S-R}	W_{S-T}
-0.4	25.22	1.8029E7	2.1842E-6	-	2161	1.1925E-5	-	-
-0.5	25.25	975400	2.8302E-6	-	1226	1.4811E-5	-	-
-0.55	24.98	223330	4.0565E-6	-	2644	1.0795E-5	-	-
-0.6	24.82	60063	7.7982E-6	-	4725	7.0884E-6	-	-
-0.65	24.6	20657	1.5023E-5	-	2532	1.0157E-5	-	-
-0.7	24.77	7236	3.0898E-5	-	1992	2.1147E-5	-	-
-0.75	24.77	2989	5.5823E-5	27.47	1303	1.8516E-5	-	-
-0.8	25.21	1483	8.9573E-5	16.02	790	8.9573E-5	-	-
-0.85	25.54	730.9	0.0001345	5.123	483.8	1.5635E-5	77.25	0.858
-0.9	25.52	447.9	0.0001894	2.739	296.1	1.5152E-5	34.38	1.004
-0.95	25.46	270	0.0002889	0.931	180.7	1.5002E-5	50.44	0.765
-1	25.4	176.2	0.0005141	-	111.8	1.4689E-5	73.65	0.652
-1.05	25.18	130.8	0.0010818	-	72.8	1.4319E-5	80.34	0.481
-1.1	24.73	91.4	0.001845	138.7	46.89	1.2781E-5	27.99	0.153
-1.15	24.82	55.35	0.0026787	78.74	33.85	1.3511E-5	35.73	0.160
-1.2	24.93	34.04	0.0035999	51.32	24.17	1.3908E-5	31	0.133
-1.3	24.99	11.57	0.0018249	7.673	13.46	1.3797E-5	34.09	0.196
-1.4	24.97	9.381	0.0021143	5.418	8.289	1.2871E-5	22.66	0.185
-1.5	24.96	9.269	0.0035939	-	6.505	1.7546E-5	16	0.171

Table 4.12 Parameters extracted from fitting dark EIS data of three electrode cell system. Electrolyte contains 0.1 M LiOTf, 0.2 M [Cu(dmbpy)₂]⁺, 0.02 M [Cu(dmbpy)₂]²⁺ and 0.5 M TBP. Working electrode was Y123 dye sensitized TiO₂ nanoparticle film on FTO. Counter electrode was Pt mesh. Reference was Ag/AgNO₃. The solution was stirred during the measurement.

Applied potential V / vs. CE	R_s / Ω	R_{CT} / Ω	C_μ / F	R_T / Ω
-0.1	567.5	4.4309E6	1.2033E-5	171.3
-0.125	570	1.5372E6	1.136E-5	169.6
-0.15	569.3	795780	1.0717E-5	173.2
-0.175	570.8	463200	1.0069E-5	178.1
-0.2	569.8	277160	9.987E-6	172.3
-0.225	570.5	156320	1.0274E-5	173.6
-0.25	571.1	87802	1.126E-5	164.8
-0.275	570.7	131110	7.5813E-6	177.1
-0.3	571.1	94350	8.0796E-6	176.5
-0.325	570.4	69693	8.6747E-6	175.6
-0.35	572.1	50722	9.5985E-6	173.2
-0.375	571.2	34842	1.064E-5	171.3
-0.4	575.9	23271	1.1254E-5	93.18
-0.425	574.8	14412	1.2572E-5	74.95
-0.45	574.8	8811	1.4061E-5	65.4
-0.475	577.8	5130	1.6621E-5	46.37
-0.5	574.2	3115	1.9907E-5	77.09
-0.525	574.9	1958	2.3955E-5	117.7
-0.55	576.1	1212	3.1307E-5	129.9
-0.575	573.5	848.8	5.2297E-5	188.6
-0.6	573.2	622.8	8.5349E-5	525
-0.625	582.8	536.8	0.00010187	456.7
-0.65	591.8	474.3	0.00011359	283.5
-0.675	589.8	423.3	0.00012996	179
-0.7	602.6	388.7	0.000135349	135.4

Table 4.12 (cont'd)

Applied potential V / vs. CE	R_s / Ω	R_{CT} / Ω	C_μ / F	R_T / Ω
-0.725	578.9	369.7	0.0001598	58.04
-0.75	578.5	337	0.00018844	77.96
-0.775	572.3	317.1	0.00022503	66.27
-0.8	570.1	296.8	0.00025806	65.86
-0.825	577	286.4	0.00031382	28.59
-0.85	572.9	291.2	0.00039331	49.98
-0.875	574.2	282.2	0.00045147	49.36
-0.9	573.8	261.1	0.00049953	63.59
-0.925	576	280.1	0.00057513	38.35
-0.95	570.2	291.3	0.00067121	44.94
-0.975	568	269.6	0.00071577	48.48
-1	563.3	271.9	0.00090553	69.46
-1.025	567.1	290.1	0.0010103	49.31
-1.05	564.3	295.5	0.0011962	41.56
-1.075	560	354.8	0.0015092	52.21
-1.1	563.5	275.8	0.0013818	45.5
-1.125	563	255	0.0013844	29.91
-1.15	558	252.2	0.0016285	38.83
-1.175	558.2	150.7	0.0015271	127.6
-1.2	560.9	222.7	0.0018225	23.56

REFERENCES

REFERENCES

- (1) Nazeeruddin, M. K.; Kay, A.; Rodicio, I.; Humphry-Baker, R.; Mueller, E.; Liska, P.; Vlachopoulos, N.; Graetzel, M. *J. Am. Chem. Soc.* **1993**, *115*, 6382
- (2) Boschloo, G.; Hagfeldt, A. *Acc. Chem. Res.* **2009**, *42*, 1819
- (3) Aghazada, S.; Gao, P.; Yella, A.; Marotta, G.; Moehl, T.; Teuscher, J.; Moser, J. E.; De Angelis, F.; Grätzel, M.; Nazeeruddin, M. K. *Inorg. Chem.* **2016**, *55*, 6653
- (4) Saygili, Y.; Stojanovic, M.; Flores-Díaz, N.; Zakeeruddin, S. M.; Vlachopoulos, N.; Grätzel, M.; Hagfeldt, A. *Inorganics.* **2019**, *7*, 30
- (5) Yella, A.; Lee, H.-W.; Tsao, H. N.; Yi, C.; Chandiran, A. K.; Nazeeruddin, M. K.; Diau, E. W.-G.; Yeh, C.-Y.; Zakeeruddin, S. M.; Gratzel, M. *Science.* **2011**, *334*, 629
- (6) Hattori, S.; Wada, Y.; Yanagida, S.; Fukuzumi, S. *J. Am. Chem. Soc.* **2005**, *127*, 9648
- (7) Li, J.; Yang, X.; Yu, Z.; Gurzadyan, G. G.; Cheng, M.; Zhang, F.; Cong, J.; Wang, W.; Wang, H.; Li, X.; Kloo, L.; Wang, M.; Sun, L. *RSC Adv.* **2017**, *7*, 4611
- (8) Saygili, Y.; Söderberg, M.; Pellet, N.; Giordano, F.; Cao, Y.; Muñoz-García, A. B.; Zakeeruddin, S. M.; Vlachopoulos, N.; Pavone, M.; Boschloo, G.; Kavan, L.; Moser, J.-E.; Grätzel, M.; Hagfeldt, A.; Freitag, M. *J. Am. Chem. Soc.* **2016**, *138*, 15087
- (9) Cao, Y.; Liu, Y.; Zakeeruddin, S. M.; Hagfeldt, A.; Grätzel, M. *Joule* **2018**, *2*, 1108
- (10) Schlichthörl, G.; Huang, S. Y.; Sprague, J.; Frank, A. J. *J. Phys. Chem. B* **1997**, *101*, 8141
- (11) Nakade, S.; Kanzaki, T.; Kubo, W.; Kitamura, T.; Wada, Y.; Yanagida, S. *J. Phys. Chem. B* **2005**, *109*, 3480
- (12) Boschloo, G.; Häggman, L.; Hagfeldt, A. *J. Phys. Chem. B* **2006**, *110*, 13144
- (13) Shi, C.; Dai, S.; Wang, K.; Pan, X.; Kong, F.; Hu, L. *Vib. Spectrosc.* **2005**, *39*, 99
- (14) Ondersma, J. W.; Hamann, T. W. *J. Am. Chem. Soc.* **2011**, *133*, 8264
- (15) Ellis, H.; Vlachopoulos, N.; Häggman, L.; Perruchot, C.; Jouini, M.; Boschloo, G.; Hagfeldt, A. *Electrochim. Acta* **2013**, *107*, 45
- (16) Bisquert, J. *Phys. Chem. Chem. Phys.* **2000**, *2*, 4185
- (17) Hoffeditz, W. L.; Katz, M. J.; Deria, P.; Cutsail III, G. E.; Pellin, M. J.; Farha, O. K.; Hupp, J. T. *J. Phys. Chem. C* **2016**, *120*, 3731
- (18) Haque, S. a.; Palomares, E.; Cho, B. M.; Green, A. N. M.; Hirata, N.; Klug, D. R.; Durrant,

- J. R. *J. Am. Chem. Soc.* **2005**, *127*, 3456
- (19) Haque, S. A.; Tachibana, Y.; Willis, R. L.; Moser, J. E.; Grätzel, M.; Klug, D. R.; Durrant, J. R. *J. Phys. Chem. B* **2000**, *104*, 538
- (20) Boschloo, G.; Häggman, L.; Hagfeldt, A. *J. Phys. Chem. B* **2006**, *110*, 13144
- (21) Yin, X.; Zhao, H.; Chen, L.; Tan, W.; Zhang, J.; Weng, Y.; Shuai, Z.; Xiao, X.; Zhou, X.; Li, X.; Lin, Y. *Surf. Interface Anal.* **2007**, *39*, 809
- (22) Fabregat-Santiago, F.; Garcia-Belmonte, G.; Mora-Seró, I.; Bisquert, J. *Phys. Chem. Chem. Phys.* **2011**, *13*, 9083
- (23) Marcus, R. A.; Sutin, N. *Biochim. Biophys. Acta - Rev. Bioenerg.* **1985**, *811*, 265
- (24) Orbakh, D. *Non-aqueous Electrochemistry*; New York : Marcel Dekker, ©1999., **1999**.
- (25) *J. Am. Chem. Soc.* **2000**, *122*, 12614
- (26) Xie, Y.; Baillargeon, J.; Hamann, T. W. *J. Phys. Chem. C* **2015**, *119*, 28155
- (27) Enright, B.; Fitzmaurice, D. *J. Phys. Chem.* **1996**, *100*, 1027
- (28) Rothenberger, G.; Fitzmaurice, D.; Graetzel, M. *J. Phys. Chem.* **1992**, *96*, 5983
- (29) Zaban, A.; Greenshtein, M.; Bisquert, J. *ChemPhysChem* **2003**, *4*, 859
- (30) Bisquert, J.; Fabregat-Santiago, F.; Mora-Seró, I.; Garcia-Belmonte, G.; Giménez, S. *J. Phys. Chem. C* **2009**, *113*, 17278

Chapter 5 Searching for bases other than TBP to be used as an additive in copper DSSCs

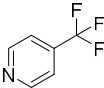
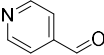
5.1 Introduction

From the previous chapters, we understand that in-situ ligand exchange happens to copper(II) aqua bis(6,6-dimethyl-2,2-bipyridine) triflate, $[\text{Cu}(\text{dmbpy})_2\text{H}_2\text{O}]\text{OTf}_2$, in solution when 4-*tert*-butylpyridine, TBP, exists at a large excess amount. $[\text{Cu}(\text{dmbpy})_2]^{2+}$ will be used in the text to represent the cation in the solution (the reason was explained in Chapter 3). Multiple TBP ligands replace the dmbpy ligands around Cu^{2+} centers. Therefore, it reduces the concentration of $[\text{Cu}(\text{dmbpy})_2]^{2+}$ and increases the concentration $[\text{Cu}(\text{TBP})_4]^{2+}$ in the electrolyte. The benefit of this in-situ ligand exchange is the reduced electron recombination rate, which explained the improved photovoltage and photocurrent of DSSCs. But the problems introduced by the in-situ ligand exchange include the negatively shifted solution potential, the increased overpotential on the counter electrode, and the reduced mass transport of the copper(II) species. All of these contribute to energy losses in DSSCs. The use of TBP in the electrolyte is a standard method to improve cell efficiency and it also helped to make the best performing DSSC with copper redox couple in the past. But it may not be the best base to add for cells with copper redox couples. A study by Ferdowsi had shown the base-specific electrochemical properties for the copper redox couple when different types of base added into the electrolyte.¹ In this chapter, by using the same model molecule, $[\text{Cu}(\text{dmbpy})_2]^{2+}$, the effect of different bases on the DSSC performance has been explored, and efforts were made to seek for a better basic additive for $[\text{Cu}(\text{dmbpy})_2]^{2+/+}$ redox couple.

Pyridine ring can be substituted by different functional groups, and the electronic effects of the functional groups and the position of the substitution can affect the pKa of the pyridine derivatives. Electron donating groups like methyl and butyl groups increase the basicity of the pyridine;

electron withdrawing groups like halogen reduce the basicity of the pyridine one the 2 and 4 positions. Imidazole and the derivatives have similar sizes to the pyridine family and also have been used as additives in electrolyte for batteries and DSSCs. In order to have a distribution of basicities, seven different bases were selected, as shown in Table 5.1.

Table 5.1 A list of bases used in this chapter and their pKa value in water.

Chemical name	Symbol	Structure	pKa ⁱ
4-Trifluoromethyl pyridine	TFMP		2
4-carboxaldehyde pyridine	CAP		4.77
pyridine	py		5.23
4- <i>tert</i> -butyl pyridine	TBP		5.99
imidazole	Im		6.95
1-methyl benzimidazole	MBIm		7.4
4-dimethylamino pyridine	DMAP		10.14
1-methyl imidazole	MeIm		12.46

i. pKa in water.²

5.2 Experimental methods

Cyclic voltammetry (CV) was performed by using μ AutoLabII potentiostat or Autolab PGSTAT128N using a home-made electrochemical cell under N₂ atmosphere. The change of the

shape of the reversible CV curve of copper complex, $[\text{Cu}(\text{dmbpy})_2]^{2+}$, was monitored in solution when the different amount of each base was added. Acetonitrile is the solvent of the electrolyte for all the measurements. The working electrode was a glassy carbon disk; reference electrode was a home-made Ag/AgNO_3 reference electrode (0.01 M AgNO_3 in acetonitrile) and the counter electrode was a high surface area Pt mesh.

Similar experimental methods, such as UV-vis and NMR, were applied as described in chapter 3. Instead of TBP, different bases were used to titrate the solution containing $\text{Cu}(\text{dmbpy})_2\text{OTf}_2$.

DSSCs were made by the same methods described in chapter 4. Photoanode was TiO_2 nanoporous (need to have the brand of the paste) layer of 8 μm ; counter electrode was electrodeposited PEDOT film on FTO. Instead of TBP, different bases were used as an additive in the electrolyte. Other than the additive, the electrolyte consists of $\text{Cu}(\text{dmbpy})_2\text{OTf}$, $\text{Cu}(\text{dmbpy})_2\text{OTf}_2$, and LiOTf in acetonitrile.

The performance of the DSSCs was characterized using the same methods described in chapters 2 and 4. Photocurrent response (JV), open-circuit voltage decay (OCVD) and current transient (CT) were done under 1 sun condition (AM 1.5, 100 mW/cm^2). Incident photon to current conversion efficiency (IPCE) was done under monochromatic light. Electrochemical impedance spectroscopy (EIS) of DSSCs was measured under dark, and the obtained result was fitted with the DX12 model in Z-View. The equivalent circuit was described in Chapter 4.

Symmetrical cells using two Pt or PEDOT electrodes were made with different additives in the electrolyte. The CV of the symmetrical cells was measured using μ AutoLabII potentiostat or Autolab PGSTAT128N. A scan rate of 5-10 mV/s was applied to compare mass transport properties between different electrolyte compositions. EIS was also done with the symmetrical cells under the dark condition. Although there were no dye molecules in the symmetrical cells, dark condition was applied to avoid any photoexcitation of the $[\text{Cu}(\text{dmbpy})_2]^+$ in the liquid electrolyte. The impedance data were fitted with the equivalent circuits in Figure 5.1.

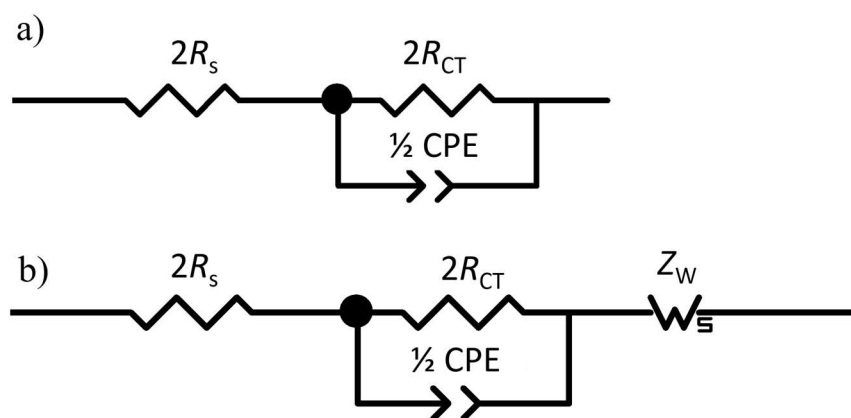


Figure 5.1 Equivalent circuit to fit the impedance data of the symmetric cells a) with only one semicircle and b) with two semicircles. R_s is the series resistance. R_{CT} is the charge transfer resistance of reduction of Cu(II) species on the PEDOT electrode. Z_W is the Warburg impedance. The constant phase element (CPE) represents the chemical capacitance of the electron transfer reaction on the PEDOT electrode. Since the PEDOT is a rough surface, the capacitance is not an ideal model, CPE has the correction factor to account for the imperfection.

When the impedance data shows the diffusion feature peak in the low-frequency region, the finite-length Warburg element was used as in Figure 5.1b. The expression of the finite length Warburg impedance-short circuit terminus (Z_w) is in Equation 5.1.³

$$Z_w = R_w \frac{\tanh \sqrt{i T_w \omega}}{\sqrt{i T_w \omega}} \quad (5.1)$$

In Z-view software, the resistance (R_w) is fitted by “Ws-R” and the frequency factor is fitted by “Ws-T”. Usually, only for DSSCs with large cell thickness or electrolytes with low diffusion coefficients, the diffusion peak can be well distinguished on the Nyquist plot.⁴ The diffusion coefficients of electrolytes, $D_{\text{electrolyte}}$, were estimated using Equation 5.2.¹

$$D_{\text{electrolyte}} = \frac{\delta^2}{T_w} \quad (5.2)$$

δ is the diffusion length of the electrolytes, which is half of the thickness of the electrolyte film (25 μm).⁵

5.3 Results and discussion

5.3.1 Ligand exchange of $[\text{Cu}(\text{dmbpy})_2]^{2+}$ in solution with different bases

From chapter 3 of this dissertation, we learned that the ligand exchange could be easily observed by UV-vis spectroscopy if the product shows a different absorption peak compare to $[\text{Cu}(\text{dmbpy})_2]^{2+}$ in solution. Different bases were titrated into the solution of $[\text{Cu}(\text{dmbpy})_2]^{2+}$ in acetonitrile and change of the absorption spectra is recorded in Figure 5.2.

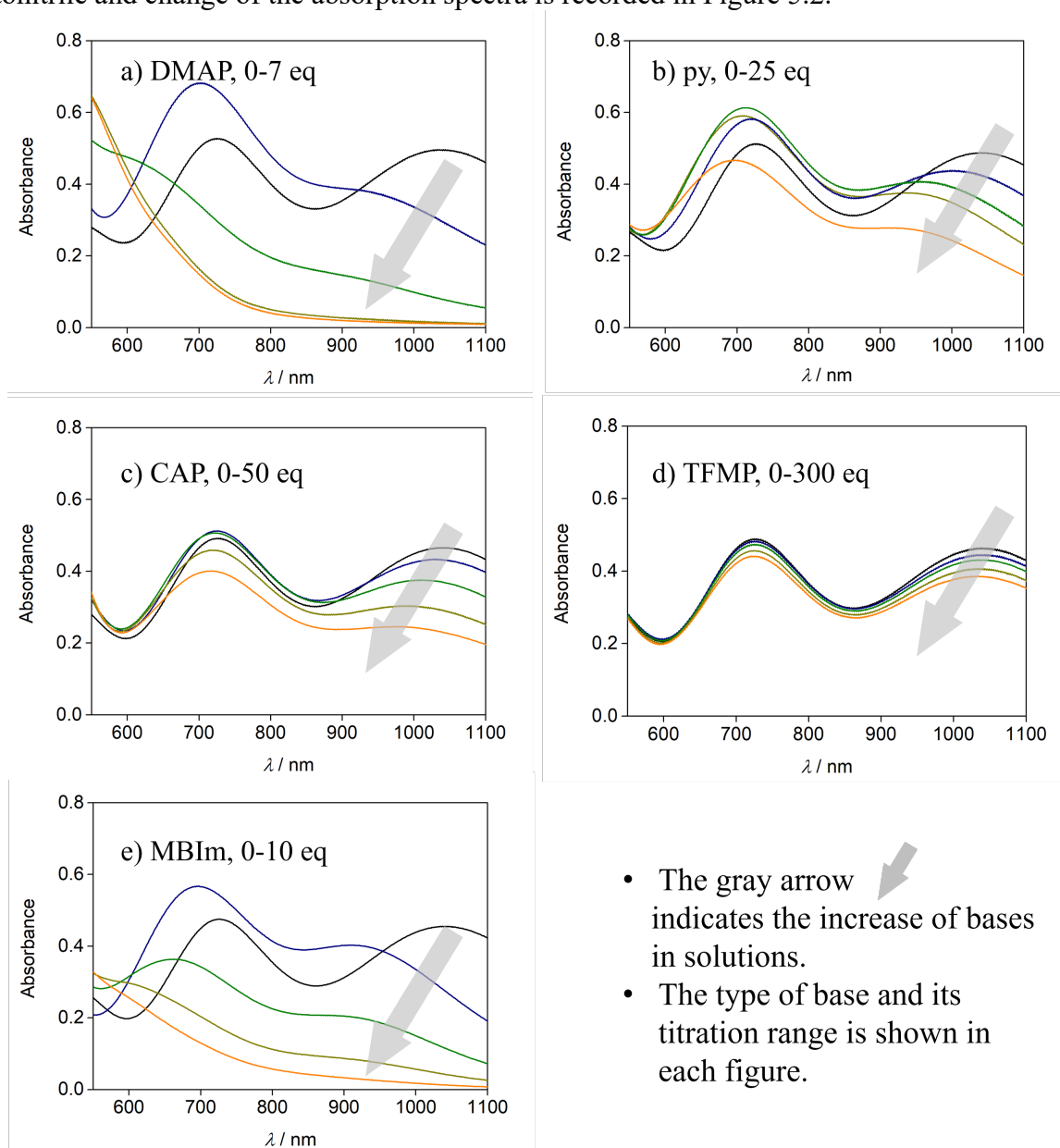


Figure 5.2 a) to e) Absorption spectra corresponding to the titration of 4 mM $[\text{Cu}(\text{dmbpy})_2]^{2+}$ with aliquots of different bases in acetonitrile. The experiment was done under an inert atmosphere.

The absorption spectrum of $[\text{Cu}(\text{dmbpy})_2]^{2+}$ in acetonitrile changed upon the addition of all the bases we have tested. Few general trends are established: 1) the increased amount of the base induced a decrease of the absorption at 1150 nm; 2) the peak around 730 nm first increased and then decreased, indicating there are multiple steps in the reaction; 3) for all the para-substituted pyridines, the larger the pKa of the base, the more significant change was observed on the spectrum with the same equivalents of the base added. The concentration of $[\text{Cu}(\text{dmbpy})_2]^{2+}$ in solution was kept constant at 4 mM for all the titration experiments. Therefore, the absorption peak we observed in the visible range is weak, with the extinction coefficient being around $100 \text{ M}^{-1}\text{cm}^{-1}$. These bands can be d-d transition bands. Their low extinction because d-d transition is forbidden by the Laporte rule. The electron-donating ability of the pyridine nitrogen of the bases is of the order, $\text{DMAP} > \text{TBP} > \text{py} > \text{CAP} > \text{TFMP}$. With the higher the electron density on the pyridine nitrogen, stronger interaction forms between the ligand to the metal center. The absorption band of the DMAP titrated solution is the highest in energy, while the absorption band of TFMP titrated solution is the lowest in energy. Assuming the pyridine derivatives form a square planar geometry with Cu(II), the base with larger pKa tends to induce a larger d orbital splitting energy on the metal center, which is reflected in the peak position.

We estimate that dmbpy should have a pKa slightly larger than that of 2,2'-bipyridine (pKa = 4.33), due to the inductive effect of the substituted methyl groups on the 6,6'-position. Interestingly, even by adding the acidic TFMP, there is an observable change in the absorption spectrum. This tells us the basicity difference is not the only reason that drives the ligand exchange reaction. During all the titration processes, a stronger absorbing intermediate was observed. This is a strong indication of the reducing symmetry geometry of the $[\text{Cu}(\text{dmbpy})_2]^{2+}$ by replacing the binding sites from dmbpy with the incoming ligands. Multiple d-d transition bands exist for

$[\text{Cu}(\text{dmbpy})_2]^{2+}$. It has been shown in Chapter 3 that $[\text{Cu}(\text{dmbpy})_2]^{2+}$ undergoes flattening distortion and forms a C_{2v} symmetry. The multiple peaks result from the splitting of the d orbitals which was described in Hoffmann's work.⁶ The reducing contribution from the peak at 1150 nm makes the resulted spectrum more toward a single d-d transition band. The smaller peak intensity of the final product compared to the intermediate species also suggests an increased symmetry of the product when the titration is closer to the ending point. (This qualitative analysis is based on the overall absorption of the reaction mixture. Deconvolution of the spectrum is needed before making any qualitative analysis.) From here, we propose that the driving force for the ligand exchange can come from two aspects: the stronger electron-donating ability of the incoming ligand compared to dmbpy; and the better flexibility of the incoming monodentate ligand, than the bidentate dmbpy, to fulfill the favored geometry for Cu(II) center. Further, the stabilization of the Cu(II) state achieved by the ligand exchange, therefore, lowers the reduction potential of it.

Besides the observations from the titrations with all the para-substituted pyridines, the difference is also found between the imidazole family and the pyridine family. According to the pKa values, one should expect to see similar ligand exchange behavior of MBIIm and TBP. However, having a much smaller pKa value compared to DMAP, MBIIm shows similar reactivity and spectroscopic feature with DMAP. The electronic contribution for the ligand exchange could not explain this phenomenon, so we attribute it to the better geometric fulfillment that can be achieved by the smaller MBIIm. Comparing to the bulkiness TBP and DMAP may have when forming a square planar molecule as shown in Figure 5.3, MBIIm ligands can have a better-compacted structure by aligning the benzyl rings. Therefore, the ligand exchange between MBIIm happened more readily than expected.

The stability of the Cu(I) species were tested by adding DMAP into the solution and monitoring its absorption spectrum. Considering the ratio between the concentrations of Cu^+ and additive in the electrolyte, 0 to 8 equivalents of DMAP were used. A 10 % decrease in the intensity of the MLCT band was observed as shown in Figure 5.3.

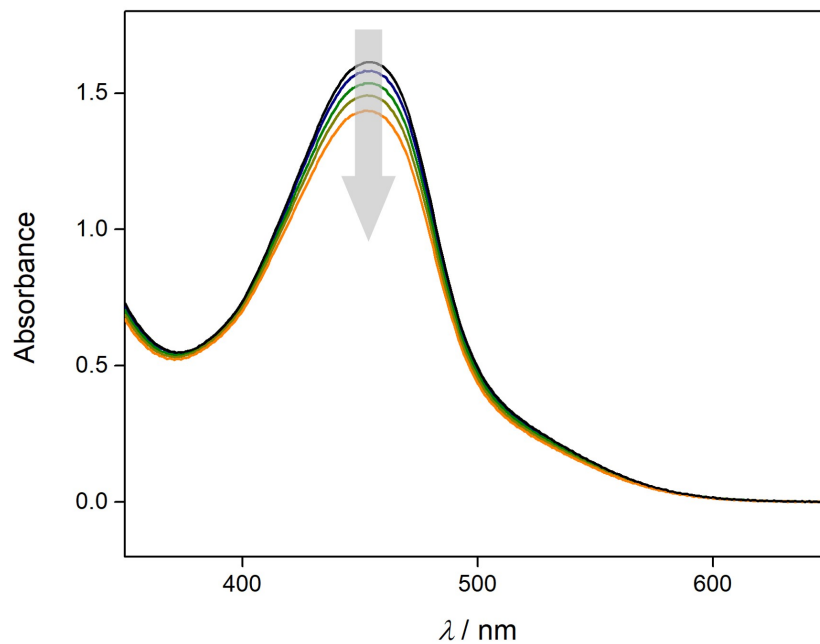


Figure 5.3 Absorption spectra of 0.3 mM $[\text{Cu}(\text{dmbpy})_2]^+$ in acetonitrile with DMAP. From top to bottom, the added amount of DMAP is 0 to 8 equivalents.

Qualitative analysis of ligand exchange was done by titrating $[\text{Cu}(\text{dmbpy})_2]^{2+}$ with a different base and monitor the proton NMR change as described in Chapter 3. Some of the results are shown in Figure 5.4. Among the three para-substituted pyridine derivatives that were tested, the equilibrium follows the same general trend with the pKa.

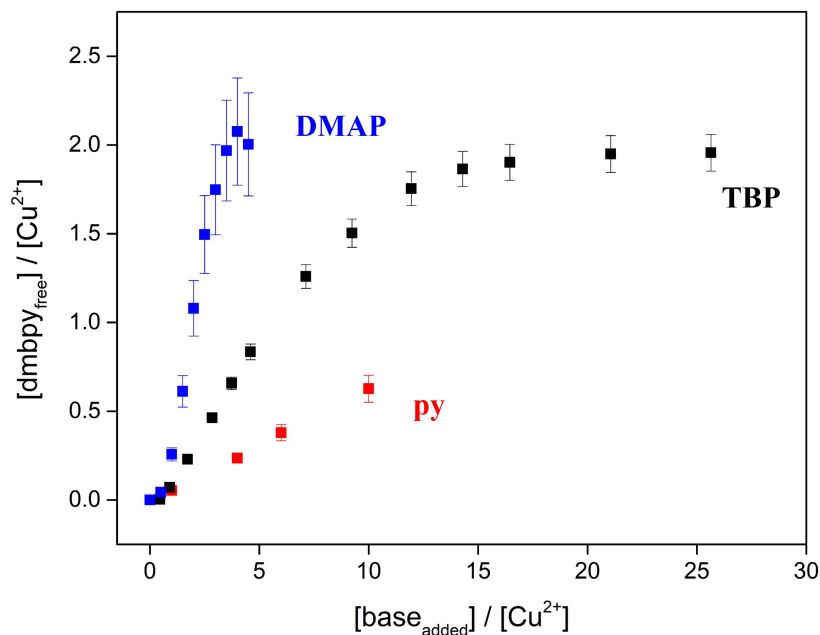


Figure 5.4 Titration results obtained by NMR. The ratio between the detected free dmbpy ligand and the total Cu^{2+} species is plotted versus the aliquots of bases in the solution. The concentration of dmbpy was determined based on the integration of aromatic proton peaks. A controlled amount of DCM was added as an internal standard for the quantitative calculation. The curve for TBP has been shown in Chapter 3, and here it's shown for comparison.

5.3.2 Ligand exchange induced electrochemical changes of the redox species with different bases

The electrochemical property of $[\text{Cu}(\text{dmbpy})_2]^{2+}$ can be affected by the ligand exchange. The CV was measured when aliquots of different bases were added into the solutions of $[\text{Cu}(\text{dmbpy})_2]^+$ and $[\text{Cu}(\text{dmbpy})_2]^{2+}$ in acetonitrile. Some of the titration results are shown in Figure 5.5.

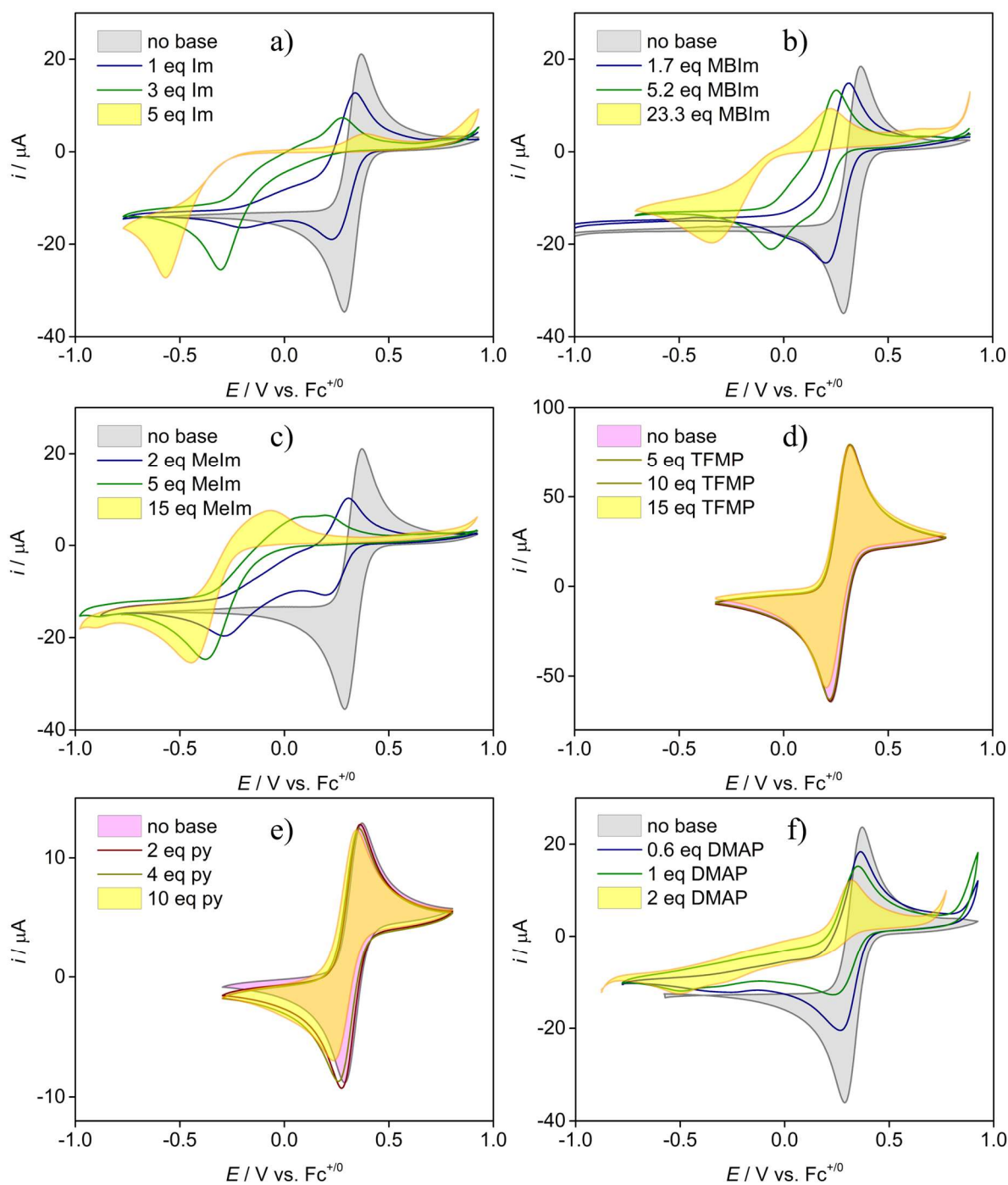


Figure 5.5 Cyclic voltammetry scans of $[\text{Cu}(\text{dmbpy})_2]^+$ (d and e) and $[\text{Cu}(\text{dmbpy})_2]^{2+}$ (a-c and f) in acetonitrile with different amount of bases added. The initial scan without any base is shaded purple for $[\text{Cu}(\text{dmbpy})_2]^+$, and gray for $[\text{Cu}(\text{dmbpy})_2]^{2+}$. The shade is to help observe the changes in the shape.

Although the base will not displace the ligands around Cu^+ , the cathodic wave of the CV scan should still reflect a distortion in shape. This is due to the reaction between the electrochemically generated $[\text{Cu}(\text{dmbpy})_2]^{2+}$ near the electrode and the base. But this distortion, compared to the CV of the solution containing a bulk concentration of $[\text{Cu}(\text{dmbpy})_2]^{2+}$, should have a more significant dependence on the scan rate. Generally, all the bases we have tested shift the cathodic wave to more negative. Pyridine family reduces the cathodic peak intensity and generates a very broadened peak, while imidazole family reduces the original cathodic peak and generates a sharp peak at a more negative potential. According to this, the imidazole derivatives coordinated Cu(II) complexes is electrochemically more reversible than pyridine derivatives coordinated Cu(II).

5.3.3 The effect of different bases on overpotentials and charge transfer kinetics at the counter electrode

In DSSCs, we, therefore, predict that by adding imidazole derivatives, a lower overpotential should be needed on the counter electrode. Symmetrical cells were made by using two PEDOT electrodes as anode and cathode, and the concentration of the basic additives are shown in Table 5.2. A low scan-rate CV was performed on these two-electrode cells. As shown in Figure 5.6, with the addition of basic additives, the overpotential required to maintain the same current flow through the cell has been increased.

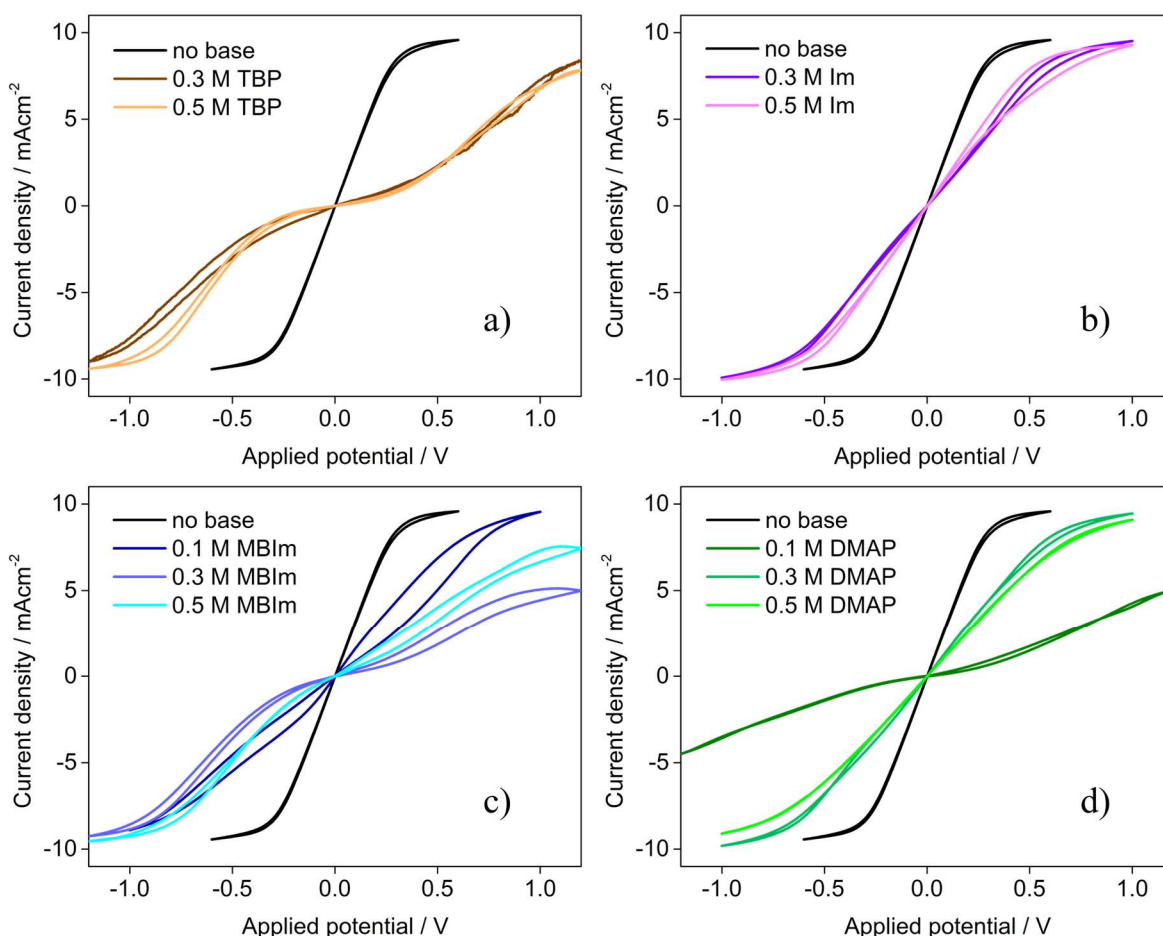


Figure 5.6 CV curves of symmetrical cells with PEDOT electrodes. Different bases are added to the electrolyte. Other than the basic additive, the electrolyte contains: 0.1 M LiOTf, 0.2 M $[\text{Cu}(\text{dmbpy})_2]^+$ 0.04 M $[\text{Cu}(\text{dmbpy})_2]^{2+}$ in acetonitrile. Measurement was done in the dark. The scan rate was 0.01 V/s.

The asymmetric shape of the CV curves can be due to different surface areas of the PEDOT electrodes because, on one of the PEDOT electrodes, holes were made to help to inject the electrolyte. But clearly from Figure 5.6, we observed that Im and DMAP reduced the large overpotential comparing to the cells with TBP. This phenomenon is consistent with the prediction from Figure 5.5a.

The slope of the CV curve at open circuit (applied potential equals zero) reflects the electron transfer kinetics on the surface of PEDOT electrode. Without any basic additive, the slope of the

curve is the highest, indicating a fast electron transfer rate. The addition of the bases lowered the electron transfer rate. Also, by measuring the impedance of the symmetric cells, a charge transfer resistance, R_{CT} , can be obtained. The results are listed in Table 5.2, and these numbers are consistent with the trend of the slopes on the CV curve.

Table 5.2 Electrolyte composition^a and the corresponding charge transfer resistance, R_{CT} , on the counter electrode.

Base additive	Base concentration / M	Equivalents to $[Cu^{2+}]$	$R_{CT}^b / \Omega cm^2$ (error)	D from EIS data / $10^{-5} cm^2 s^{-2}$
no	-	-	0.05 (0.004)	3.36 (0.00)
TBP	0.3	15	47.66 (1.39)	0.27 (0.11)
	0.5	25	89.51 (0.69)	0.19 (0.06)
Im	0.3	15	7.95 (0.15)	1.42 (0.01)
	0.5	25	2.31 (0.10)	3.30 (0.00)
MBlm	0.1	5	9.91 (0.50)	2.66 (0.01)
	0.3	15	31.64 (1.19)	3.37 (0.19)
	0.5	25	15.50 (0.96)	2.22 (0.01)
DMAP	0.1	5	81.09 (0.83)	3.07 (0.01)
	0.3	15	6.40 (0.09)	2.31 (0.00)
	0.5	25	1.83 (0.12)	3.51 (0.00)

a. All the electrolyte contains 0.1 M LiOTf, 0.2 M $Cu(dmbpy)_2OTf$ and 0.04 M $Cu(dmbpy)_2OTf_2$ in acetonitrile.

b. The R_{CT} is obtained by fitting the impedance data of symmetric cells with PEDOT electrodes and multiplied by the active area of the electrode.

5.3.4 The effect of different bases on mass transport in electrolyte

Comparing the titration results of DMAP and TBP, we found that DMAP replaces the dmbpy ligand more readily. Similar electrochemical behavior was found under a much lower base concentration. Therefore, less DMAP can be used in the solar cell electrolyte to prevent the mass transport issue created by the addition of substantial equivalents of TBP. By fitting the EIS data of symmetrical cells with the equivalent circuit shown in Figure 5.1b, the diffusion coefficient of the charge carriers in the electrolyte can be calculated. The results are shown in Table 5.2. Im, MBI_m, and DMAP did not slow down the diffusion of the charge carriers in the electrolyte as much as TBP, which agrees with the CV scan of the symmetrical cells. This can be due to a more significant increase in the viscosity induced by the addition of TBP but not other bases.

5.3.5 The effect of different bases on the charge recombination

DSSCs were made with different basic additives in the electrolyte. The performance of the DSSCs was measured under the same condition. From chapter 4, we know that the improvement of the DSSC is induced by the ligand exchange and the reduced electron recombination. Here, some of the *JV* curves and the corresponding electron lifetimes measured by OCVD are shown in Figure 5.7. Generally, all the bases additive improves the cell performance by increasing the charge transfer resistance of the recombination reaction. The “ R_{CT} vs $C\mu$ ” for TBP system has been shown in chapter 4, Figure 4.4. Here, similar plots are shown for different base systems as a parallel comparison. All the base-facilitated systems show an increased R_{CT} , which can be attributed to both the passivating effect and the ligand exchange effect. A control experiment is needed to separate these two effects before drawing a conclusion. For example, by using $\text{Cu}(\text{TBP})_4\text{OTf}_2$ as the oxidized species in the electrolyte, the ligand exchange effect can be eliminated, and the

passivating effect can be solely evaluated. For different bases, different oxidized species can be used, such as $\text{Cu}(\text{Im})_4\text{OTf}_2$, $\text{Cu}(\text{DMAP})_2\text{OTf}_2$.

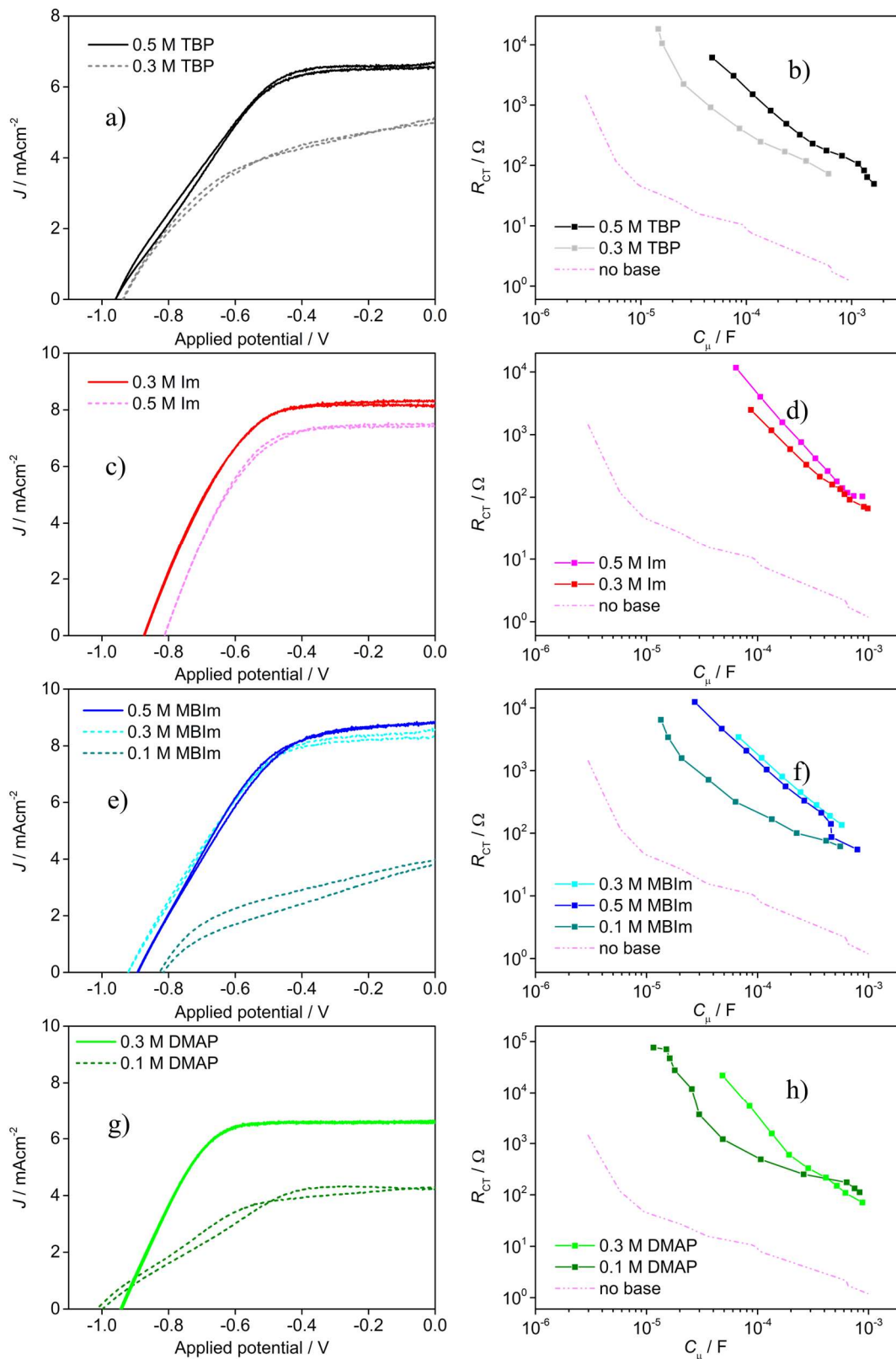


Figure 5.7 JV plots and R_{CT} vs. C_{μ} plots for DSSCs with different bases. JV curves were measured under 1 sun condition. R_{CT} and C_{μ} were obtained from EIS data measured in the dark.

5.4 Conclusion and remaining questions

In this chapter, some pyridine and imidazole derivatives have been used to study the ligand exchange between bases and $\text{Cu}(\text{dmbpy})_2\text{OTf}_2$. Different bases have shown the ability to displace dmbpy ligand from the Cu^{2+} center. The driving force of this ligand exchange results from two significant contributions, the geometric preference, and the electronic preference. The goal of this study is to explore the ability of different bases toward the ligand exchange with $\text{Cu}(\text{dmbpy})_2\text{OTf}_2$ and further to search for a base that can replace TBP as the additive in DSSCs with copper redox couples. This “better additive” should still facilitate the ligand exchange in order to reduce the charge recombination. And at the same time, should help reduce the massive energy loss from the negative shift of the solution potential and the large overpotential on the counter electrode.

So far, different bases all showed the ligand exchanging ability and different effects on the electrochemical property of the electrolyte. Especially, DSSCs with Im showed better photocurrent response, and there is a high possibility that we can find a better base additive than TBP, which can help DSSCs with copper redox couples achieving higher conversion efficiency.

APPENDIX

APPENDIX

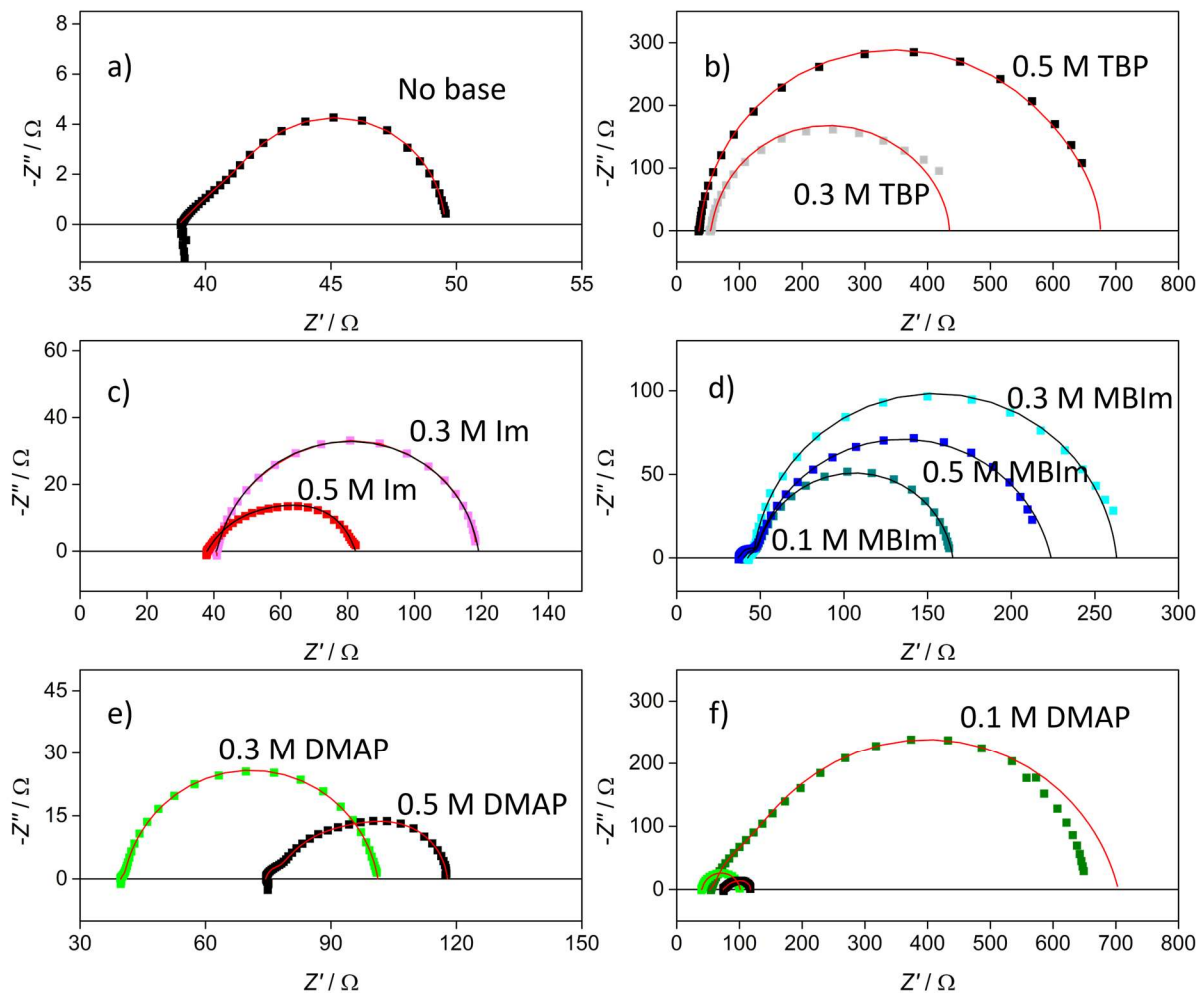


Figure 5.8 Nyquist plots of symmetrical cells with PEDOT electrodes, measured at 0 V applied potential. Electrolyte contains 0.1 M LiOTf, 0.2 M $[\text{Cu}(\text{dmbpy})_2]^+$, 0.04 M $[\text{Cu}(\text{dmbpy})_2]^{2+}$ and different concentrations of base additives. **a)** cells with no base. **b)** cells with TBP. **c)** cells with Im. **d)** cells with MBIm. **e/f)** cells with DMAP. The EIS was done in the dark. Scattered plots are raw EIS data. Red/black lines are the fitted curves.

Table 5.3 Parameters extracted from fitting dark EIS data of symmetrical PEDOT cells at 0 V applied potential. Electrolyte contains 0.1 M LiOTf, 0.2 M [Cu(dmbpy)₂]⁺ and 0.04 M [Cu(dmbpy)₂]²⁺ and different basic additives. The active area of the cell was 0.36 cm².

Basic additive	Base concentration / M	$2R_s / \Omega$	$2R_{CT} / \Omega$	$1/2C_\mu / F$	$W_s\text{-R}$	$W_s\text{-T}$
no	-	38.93	0.94433	0.12063	9.698	0.18648
TBP	0.3	53.85	341.5	0.0011025	39.56	2.887
	0.5	35.39	586.5	0.00080738	53.66	5.704
Im	0.3	40.7	70.23	0.0015612	8.168	0.35542
	0.5	37.94	31.28	0.0022062	13.13	0.21498
MBIm	0.1	40.11	117.4	0.0013574	7.536	0.0021582
	0.3	42.4	217.1	0.00090932	3.477	0.0015261
	0.5	36.6	177.1	0.0013927	10.1	0.0016266
DMAP	0.1	53.37	643	0.0011621	74.14	1.575
	0.3	39.73	41.26	0.0011361	19.6	0.28278
	0.5	74.46	21.52	0.0020257	19.73	0.22577

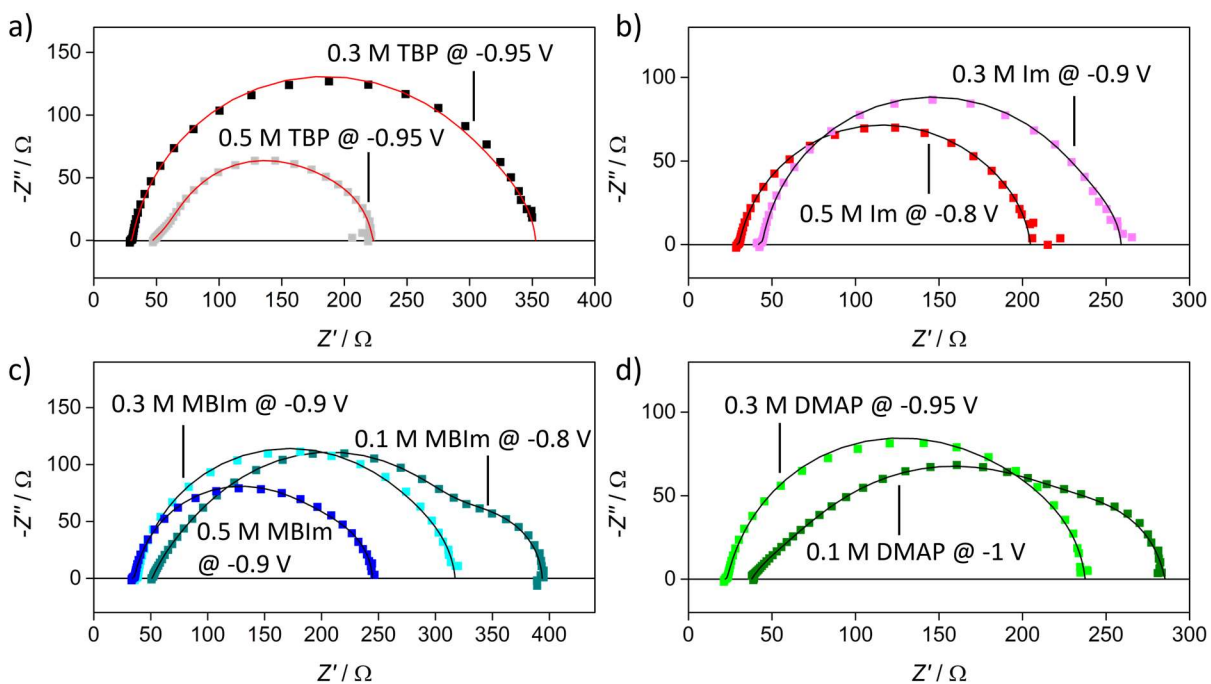


Figure 5.9 Nyquist plots of DSSCs with Y123 dye. Electrolyte contains 0.1 M LiOTf, 0.2 M $[\text{Cu}(\text{dmbpy})_2]^+$, 0.04 M $[\text{Cu}(\text{dmbpy})_2]^{2+}$ and different concentrations of base additives. **a)** DSSCs with TBP. **b)** DSSCs with Im. **c)** DSSCs with MBIm. **d)** DSSCs with DMAP. The EIS was done in the dark. The plots shown are at the V_{OC} of each cell. Scattered plots are raw EIS data. Red/black lines are the fitted curves.

Table 5.4 Parameters extracted from fitting dark EIS data of copper DSSC with Y123 dye. Electrolyte contains 0.1 M LiOTf, 0.2 M [Cu(dmbpy)₂]⁺, 0.04 M [Cu(dmbpy)₂]²⁺ and 0.3 M TBP.

Applied potential V / vs. CE	R_s / Ω	R_{CT} / Ω	C_μ / F
-0.6	47.19	15623	1.6422E-5
-0.65	47.04	5207	2.7013E-5
-0.75	47.51	1727	2.9334E-5
-0.8	47.45	616	5.3359E-5
-0.85	47.25	199.3	0.00010112
-0.9	47.38	126.8	0.00012002
-0.95	47.53	100.5	0.0001622
-1	47.72	71.54	0.00022013
-1.05	48.06	44.26	0.00041707

Table 5.5 Parameters extracted from fitting dark EIS data of copper DSSC with Y123 dye. Electrolyte contains 0.1 M LiOTf, 0.2 M [Cu(dmbpy)₂]⁺, 0.04 M [Cu(dmbpy)₂]²⁺ and 0.5 M TBP

Applied potential V / vs. CE	R_s / Ω	R_{CT} / Ω	C_μ / F
-0.7	28.56	5936	5.0199E-5
-0.75	28.1	3007	7.58E-5
-0.8	27.99	1392	0.00012062
-0.85	29.15	769.9	0.00015971
-0.9	29.57	458.3	0.00021661
-0.95	29.6	294.2	0.00027873
-1.0	29.68	192.9	0.000342
-1.05	29.39	128.3	0.00041142
-1.1	29.15	83.99	0.00049239
-1.15	29	52.65	0.00060025
-1.2	28.93	38.31	0.00080648
-1.25	28.83	23.11	0.0009137
-1.3	28.89	16.71	0.0011733

Table 5.6 Parameters extracted from fitting dark EIS data of copper DSSC with Y123 dye. Electrolyte contains 0.1 M LiOTf, 0.2 M [Cu(dmbpy)₂]⁺, 0.04 M [Cu(dmbpy)₂]²⁺ and 0.3 M Im

Applied potential V / vs. CE	R_s / Ω	R_{CT} / Ω	C_μ / F
-0.6	28.05	11262	6.5371E-5
-0.65	28.72	3951	0.00010557
-0.7	28.9	1383	0.0001636
-0.75	29.29	699.9	0.00023282
-0.8	29.31	387.5	0.00030955
-0.85	29.22	246.5	0.00039749
-0.9	29.18	157.7	0.00047479
-0.95	29.14	115.2	0.00053142
-1	29.31	75.09	0.00054275
-1.05	29.26	62.97	0.00060095
-1.1	29.02	46.39	0.00066726

Table 5.7 Parameters extracted from fitting dark EIS data of copper DSSC with Y123 dye. Electrolyte contains 0.1 M LiOTf, 0.2 M [Cu(dmbpy)₂]⁺, 0.04 M [Cu(dmbpy)₂]²⁺ and 0.5 M Im

Applied potential V / vs. CE	R_s / Ω	R_{CT} / Ω	C_μ / F
-0.6	39.75	2511	8.9899E-5
-0.65	41.84	1180	0.00013616
-0.7	41.34	566.5	0.0001921
-0.75	41.84	312.4	0.00025534
-0.8	41.86	196	0.00032578
-0.85	41.81	142	0.00040224
-0.9	41.77	112.4	0.00044862
-0.95	41.67	88.81	0.00047875
-1	41.58	71.08	0.00052587
-1.05	41.51	46.64	0.0006447
-1.1	41.41	42.89	0.00068405

Table 5.8 Parameters extracted from fitting dark EIS data of copper DSSC with Y123 dye. Electrolyte contains 0.1 M LiOTf, 0.2 M [Cu(dmbpy)₂]⁺, 0.04 M [Cu(dmbpy)₂]²⁺ and 0.1 M MBIm

Applied potential V / vs. CE	R_s / Ω	R_{CT} / Ω	C_μ / F
-0.6	49.68	6120	1.5103E-5
-0.65	49.93	3126	1.7242E-5
-0.7	50.7	1399	1.9569E-5
-0.75	50.86	537.4	2.4977E-5
-0.8	50.97	208.2	4.2455E-5
-0.85	50.83	101.2	7.103E-5
-0.9	51.08	55.97	0.00012018
-0.95	51.16	31.74	0.00018505
-1	51.12	25.12	0.00021032

Table 5.9 Parameters extracted from fitting dark EIS data of copper DSSC with Y123 dye. Electrolyte contains 0.1 M LiOTf, 0.2 M [Cu(dmbpy)₂]⁺, 0.04 M [Cu(dmbpy)₂]²⁺ and 0.3 M MBIm

Applied potential V / vs. CE	R_s / Ω	R_{CT} / Ω	C_μ / F
-0.7	33.26	2672	9.6586E-5
-0.75	35.13	1432	0.00011671
-0.8	36.25	753.6	0.00015762
-0.85	36.59	419.4	0.00022265
-0.9	36.59	248	0.00029767
-0.95	36.52	152.3	0.00037429
-1	36.46	97.39	0.00044577

Table 5.10 Parameters extracted from fitting dark EIS data of copper DSSC with Y123 dye. Electrolyte contains 0.1 M LiOTf, 0.2 M $[\text{Cu}(\text{dmbpy})_2]^+$, 0.04 M $[\text{Cu}(\text{dmbpy})_2]^{2+}$ and 0.5 M MBIm.

Applied potential V / vs. CE	R_s / Ω	R_{CT} / Ω	C_μ / F
-0.6	34.64	8479	4.4784E-5
-0.65	33.99	4383	5.2017E-5
-0.7	33.73	1975	7.8076E-5
-0.75	33.86	947.1	0.00011362
-0.8	33.49	492.8	0.00016142
-0.85	33.86	271.4	0.00021494
-0.9	33.88	155	0.00026981
-0.95	33.87	94.74	0.00032502
-1	33.82	61.78	0.00038039
-1.1	33.78	35.04	0.000594

Table 5.11 Parameters extracted from fitting dark EIS data of copper DSSC with Y123 dye. Electrolyte contains 0.1 M LiOTf, 0.2 M $[\text{Cu}(\text{dmbpy})_2]^+$, 0.04 M $[\text{Cu}(\text{dmbpy})_2]^{2+}$ and 0.1 M DMAP.

Applied potential V / vs. CE	R_s / Ω	R_{CT} / Ω	C_μ / F
-0.6	35.84	80155	1.2081E-5
-0.65	36.58	68413	1.4873E-5
-0.7	36.62	46870	1.6452E-5
-0.75	36.08	26225	1.8659E-5
-0.8	36.32	10646	2.3669E-5
-0.85	36.46	3492	3.2029E-5
-0.9	37.19	1171	4.9766E-5
-0.95	37.56	349	8.8737E-5
-1	37.52	173.9	0.00017875
-1.05	37.13	79.66	0.00036378
-1.1	37.31	54.04	0.00045179
-1.15	37.54	29.72	0.00044367

Table 5.12 Parameters extracted from fitting dark EIS data of copper DSSC with Y123 dye. Electrolyte contains 0.1 M LiOTf, 0.2 M [Cu(dmbpy)₂]⁺, 0.04 M [Cu(dmbpy)₂]²⁺ and 0.3 M DMAP.

Applied potential V / vs. CE	R_s / Ω	R_{CT} / Ω	C_μ / F
-0.7	20.83	20788	5.092E-5
-0.75	20.76	5348	8.5262E-5
-0.8	21.05	1053	0.00013999
-0.85	21.64	539	0.00019704
-0.9	21.89	322.9	0.00028067
-0.95	22	182.7	0.0003653
-1	21.96	108.5	0.00041701
-1.05	21.9	72.8	0.00045768
-1.1	23.33	40.87	0.00056051

REFERENCES

REFERENCES

- (1) Ferdowsi, P.; Saygili, Y.; Zakeeruddin, S. M.; Mokhtari, J.; Grätzel, M.; Hagfeldt, A.; Kavan, L. *Electrochim. Acta* **2018**, *265*, 194
- (2) pKa Data Compiled by R. Williams
https://www.chem.wisc.edu/areas/reich/pkatable/pKa_compilation-1-Williams.pdf
- (3) Kavan, L.; Saygili, Y.; Freitag, M.; Zakeeruddin, S. M.; Hagfeldt, A.; Grätzel, M. *Electrochim. Acta* **2017**, *227*, 194
- (4) Sarker, S.; Ahammad, A. J. S.; Seo, H. W.; Kim, D. M. *Int. J. Photoenergy* **2014**, *2014*, 1
- (5) Kern, R.; Sastrawan, R.; Ferber, J.; Stangl, R.; Luther, J. *Electrochim. Acta* **2002**, *47*, 4213
- (6) Hoffmann, S. K.; Goslar, J. *J. Solid State Chem.* **1982**, *44*, 343

Chapter 6 Future directions for copper redox couples for DSSCs

6.1 Summary of results

Copper II/I redox center plays a wide variety of roles in nature that involve reactions like electron transfer (ET). Research in the field of bioinorganic chemistry has developed a detailed understanding of the intrinsic nature of the copper active site in enzymes. The unique redox activity of it exists only through the combination of the copper ion with each amino acid held in specific orientations by the protein conformation. It is also because of the unique geometric requirement, the inorganic coordinating complexes of copper are hard to be used as an exact model for the copper active site. The electrochemical and photophysical properties of the copper center are susceptible to their coordinating environment. The origin of this unique feature of copper is its electronic structure. Being a first-row transition metal, copper has nine d-electrons in the plus two oxidation states and ten d-electrons in the plus one oxidation state. Unlike the classic outer-sphere electron transfer species, the electron exchange between copper(I) and copper(II) complexes is more complicated, because it will be accompanied by changes in coordination number of copper and the geometry of the complex. Ligand exchange, therefore, happens to some copper complexes when new electron-donating species present. For some labile species, the changes in the coordinating sphere may be rapid and not kinetically separable from electron transfer.

Because of the positive redox potential and desired absorptivity of copper polypyridyl complexes, they can act as photosensitizers in dye-sensitized solar cells (DSSCs). With the larger earth abundance than the ruthenium metal, they are believed to be able to replace the widely used ruthenium polypyridyl complexes.¹ Due to the intrinsic electronic feature, the electrochemical and photophysical properties of copper coordination complexes are susceptible to the geometry that's held by the ligand binding to the copper center.^{2, 3} But on the other hand, this flexibility gives

copper sensitizers the chance to be tuned and meet different energetic and kinetic requirements. Most widely studied is 2,2'-bipyridine has been modified by changing the functional group on its 6,6'- position to bring more geometric hindrance to the copper(I) complex, and therefore the complex can be more rigid and forms a distorted tetrahedron. During photoexcitation or the electrochemical oxidation, the rigidity of the structure reduced the extent of the intrinsic structural change from copper(I) to copper(II). A longer excited-state lifetime and faster electron transfer rate can be achieved this way.^{4, 5} However, when the complex acts as a sensitizer in a DSSC, it needs to make contact with the electrolyte solution, which contains solvent molecules, supporting electrolyte, the redox mediator, and conventional additives. All these components are at a significant excess to the sensitizer that's bind on the semiconductor surface. In chapter 2 of this dissertation, by using a model sensitizer, copper(I) bis(6,6'-dimethyl-2,2'-bipyridine-4,4'-dicarboxylic) hexafluorophosphate, $[\text{Cu}(\text{dmdcbpy})_2]\text{PF}_6$, the effects of different components in the electrolyte to this sensitizer and the cell performance have been revealed. Unlike ruthenium sensitizers, $[\text{Cu}(\text{dmdcbpy})_2]\text{PF}_6$ has low performance when paired with triiodide/iodide redox couple. The negatively charged small ions of iodide in the electrolyte can potentially bind to the copper(II) centers and facilitate fast electron recombination, by increasing the local concentration of the electron acceptor. Outersphere redox couples like cobalt(III/II) tri(2,2'-bipyridine), $[\text{Co}(\text{bpy})_3]^{3+/2+}$, and derivatives can regenerate the copper sensitizer without changing its coordination sphere, but the electron transfer rate suffers from the lowing kinetics of cobalt complexes. The common additive 4-tert-butylpyridine, TBP, makes the redox reaction of the sensitizer less reversible, even when the sensitizer is attached to the film. Having an electron-donor in the structure (pyridyl nitrogen), TBP is an excellent ligand that can find its way to be close to the copper(II) center and help it maintain the preferred tetragonal geometry. Once the copper center

is oxidized to copper(II) during the photoexcitation, the incoming TBP lowers the energy of the oxidized sensitizer and stabilizes $[\text{Cu}(\text{dmdcbpy})_2]^{2+}$, therefore reduces the rate of the dye regeneration. As a result, the interaction between copper complex and other species in solution needs to be studied.

Because of the difficulty of studying the sensitizer on the semiconductor surface directly, and the low solubility of $[\text{Cu}(\text{dmdcbpy})_2]^+$ in solution, a similar molecule with better solubility has been used for molecular study. The copper(I/II) bis(6,6'-dimethyl-2,2'-bipyridine) triflate, $\text{Cu}(\text{dmbpy})_2(\text{OTf})$, and $\text{Cu}(\text{dmbpy})_2(\text{OTf})_2$ and can be used to study the effect of TBP. Besides, $[\text{Cu}(\text{dmbpy})_2]^{2+/+}$ is a good redox couple for DSSCs, and the use of this redox couple produced V_{OC} larger than 1 V. In chapter 3 of this dissertation, we found the ligand exchange happens between $[\text{Cu}(\text{dmbpy})_2]^{2+}$ and TBP in acetonitrile, at an excess amount of TBP. The product of the ligand exchange is a tetracoordinate copper(II) bis(4-tert-butylpyridine) ion, $[\text{Cu}(\text{TBP})_4]^{2+}$ (with acetonitrile or triflate anion being in the coordination sphere to maintain the favored geometry). $[\text{Cu}(\text{dmbpy})_2]^+$ is stable under the same condition. The ligand exchange happens at least in two steps; the rate-limiting step has a rate constant of $43 \text{ M}^{-1}\text{s}^{-1}$. Under the working condition, where TBP concentration is 15 to 25 eq to $[\text{Cu}(\text{dmbpy})_2]^{2+}$, the ligand exchange goes close to complete. With electrochemical methods, we proved that the TBP ligands would fall off once the $[\text{Cu}(\text{TBP})_4]^{2+}$ gets reduced to copper(I), and then $\text{Cu}(\text{dmbpy})_2^+$ forms. Comparing to $[\text{Cu}(\text{dmbpy})_2]^{2+}$, the ligand exchange product, $[\text{Cu}(\text{TBP})_4]^{2+}$, is more stabilized due to its geometry. Therefore, the reduction of $[\text{Cu}(\text{TBP})_4]^{2+}$ happens in a more negative potential.

This ligand exchange brings us to consider the real electrolyte composition of the DSSCs applying the same complex as the redox couple. In chapter 4, we looked at the effect of this ligand exchange on the performance of DSSCs. With the presence of a large amount of TBP, it should be identified

as $[\text{Cu}(\text{dmbpy})_2]^+ / [\text{Cu}(\text{TBP})_4]^{2+}$ pair. The equilibrium solution potential of the electrolyte, therefore, does not follow the prediction by the Nernst equation. The measured value is 270 mV negatively shifted with the addition of TBP. But surprisingly, we noticed the V_{OC} didn't reduce because of this energy shift but increased by 200 mV. We found that the in-situ ligand exchange increases the electron lifetime by reducing the recombination, and this is also why the J_{SC} and V_{OC} both increased when TBP presents.

TBP is commonly used as an additive only because it helps to make the best performing DSSCs with triiodide/iodide redox couple. Since we already understand the importance of the in-situ ligand exchange and how this dynamic equilibrium improves the DSSCs with $[\text{Cu}(\text{dmbpy})_2]^{2+/+}$, we believe there may be a better base that can be used in the electrolyte and reduce the energy loss but still help boost the performance of DSSCs applying $[\text{Cu}(\text{dmbpy})_2]^{2+/+}$ redox couple. So finally, in chapter 5, different bases with nitrogen donors are explored, and all of them are able to replace the dmbpy ligand. The equilibrium depends both on the pH of the base and the type of the N donor (pyridine or imidazole). With limited types of bases that we have tested, imidazole improved the performance of the DSSCs.

Overall, this dissertation builds a basic chemical understanding of using copper redox couples as redox couples in liquid DSSCs. Copper redox couples have been mostly applied in the past 3 years and helped DSSCs achieving high power conversion efficiency.⁶ The ligand exchange phenomenon is essential in the field because we could not avoid TBP or other basic additives by far in DSSCs. But as we have shown, TBP is not innocent to the copper complexes, although it facilitates to build a good performing cell. Only after we can fully understand the mechanisms of the interaction between the copper complexes and any basic additive, we can conclude if we need to avoid or use this ligand exchange to further improve the cell performance.

6.2 Future directions

6.2.1 Studying the kinetics and equilibrium of the ligand exchange between $[\text{Cu}(\text{dmbpy})_2]^{2+}$ and TBP

The kinetics of the rate-limiting step in the ligand exchange reaction, between $[\text{Cu}(\text{dmbpy})_2]^{2+}$ and TBP, has been studied by stopped-flow under room temperature. Steady-state spectroscopic methods, like EPR and UV-vis, have proved the existence of at least one intermediate in the reaction. But due to instrumental limitation, minimal information was collected for the very first step of the reaction (the faster step). Either kinetic EPR or low-temperature stopped-flow can be considered to help build a complete understanding of this reaction. Together with the equilibrium knowledge, we can calculate the exact concentration of each species in the electrolyte.

Based on the knowledge of the complete kinetics, a time constant for the ligand exchange can be deduced and be compared with the electron lifetime on the semiconductor. With the mechanism for the ligand exchange being interpreted, the electron-accepting species responsible for the electron recombination can be clearly identified. And the effect of the ligand exchange on the performance of the cells can be quantitatively evaluated.

6.2.2 The effect of halogens in the coordinating sphere of copper complexes

By different synthetic methods, $[\text{Cu}(\text{dmbpy})_2\text{X}]^+$ (X is halogen) can be synthesized by using different cupric halogen precursor. The halogen binds to the Cu(II) center and is in the coordination sphere of the complex. Dissolving the complex won't remove the halogen from its inner-sphere; instead, the halogen creates another pair of redox waves in the CV curve of the complex, as shown in Figure 6.1. Unexpectedly, better performance was achieved by using $[\text{Cu}(\text{dmbpy})_2]^{2+}/[\text{Cu}(\text{dmbpy})_2\text{X}]^+$ redox pair in our preliminary test. Thus the effect of halogen can be considered in two ways.

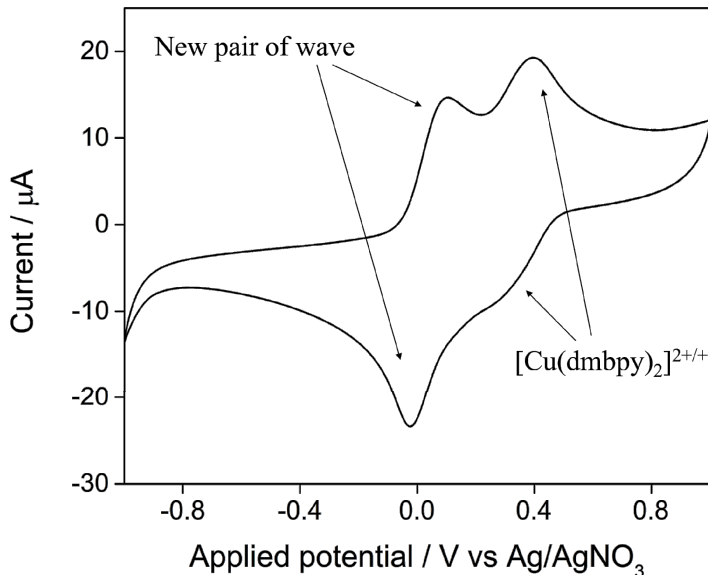


Figure 6.1 The CV curve of 4 mM $[\text{Cu}(\text{dmbpy})_2\text{Cl}]^+$ on glassy carbon measured in acetonitrile. The scan rate was 0.1 V/s.

- 1) The halogen helps to maintain a tetragonal geometry of Cu(II) complexes. It can lower the reorganization energy between Cu(I) and Cu(II).
- 2) The halogen can bridge the electron transfer to the copper center.

Both effects may lower the overpotential on the counter electrode of DSSCs but may increase the electron recombination at the same time.

A similar study should be performed as in chapter 3 of this dissertation to understand if TBP replaces the dmbpy ligand even with the presence of the halogen in the complex's coordination sphere. With a detailed understanding of the kinetics and equilibrium of the ligand exchange between TBP and $[\text{Cu}(\text{dmbpy})_2\text{X}]^+$, a comparison between $[\text{Cu}(\text{dmbpy})_2]^+ / [\text{Cu}(\text{dmbpy})_2\text{X}]^+$ and $[\text{Cu}(\text{dmbpy})_2]^+ / [\text{Cu}(\text{dmbpy})_2]^{2+}$ should be made to clear few thoughts:

- 1) Do we want to have the in-situ ligand exchange for helping reduce the recombination rate, or do we want to avoid this dynamic process to increase the charge transfer on the counter electrode?

- 2) Do we want to have labile ligands around copper to maintain an interchangeable geometry between Cu(I) and Cu(II), or do we want to have halogen or any other rigid structure to lower the reorganization between Cu(I) and Cu(II)?
- 3) What are the actual electrolyte components in the best performing DSSCs using $[\text{Cu}(\text{dmbpy})_2]^{2+/+}$?

6.2.3 Constructing a “single component” copper DSSC

Copper complexes are also intensively used as photocatalysts. There are copper complexes with very long excited-state lifetime. This was achieved by making the structure of the complex rigid enough to prevent any distortion after photoexcitation. Without the distortion, the energy of the excited state will not be lowered to facilitate the relaxation. A single-component copper DSSC can be achieved by using this long excited-state lifetime copper complex as both dye and redox couple in a traditional DSSC. Although not being attached to any surface, the long excited-state lifetime can ensure enough amount of electrons being injected to any high surface area semiconductor. The small size of the complex will ensure the fast diffusion of it from photoanode to the counter electrode. The ligand exchange between any basic additive and the complex can ensure the reduced recombination near the anode. And the ligand modification can help find the complex with the desired absorptivity and electrochemical property. Preliminary results have been collected using $\text{Cu}(\text{dsbtmp})_2\text{PF}_6$. Although very low photocurrent was produced, it proved the achievability of this idea.

6.2.4 Solid-state DSSCs with copper redox couples

The solid-state DSSC was made successfully by drying the liquid electrolyte of a normal DSSC. The performance of the solid-state cell was higher by comparing to its parent liquid-state cell. Instead of trying different electrolyte compositions and making “dried out” cells, it is wiser to

study the fundamental change of each component in the electrolyte when the solvent molecule is removed. We already have preliminary data (see Appendix) showing that during the process of drying, the dmbpy ligand around Cu(II) centers are readily replaced by TBP. Therefore, with the understanding of the ligand exchange in solution, better performed solid-state copper DSSCs can be designed.

APPENDIX

APPENDIX

Electrolyte for DSSCs was evaporated naturally in a 2 mL vial. The concentration ratio between $[\text{Cu}(\text{dmbpy})_2]^+$, $[\text{Cu}(\text{dmbpy})_2]^{2+}$ and TBP are 4:1:10. After 4000 minutes, the formed solid was checked under the microscope as shown in Figure 6.2. Blue crystal was measured by single crystal XRD. Results are presented in Figure 6.3 and Table 6.1, 6.2.

Compound	Blue crystal
CCDC	1945517
Formula	C ₅₀ H ₆₄ CuF ₆ N ₆ O ₆ S ₂
<i>D</i> _{calc.} / g cm ⁻³	1.323
<i>μ</i> /mm ⁻¹	1.891
Formula Weight	1086.73
Color	blue
Shape	needle
Size/mm ³	0.21×0.13×0.04
<i>T</i> /K	173(2)
Crystal System	monoclinic
Space Group	<i>C</i> 2/ <i>c</i>
<i>a</i> /Å	30.6079(6)
<i>b</i> /Å	14.9810(3)
<i>c</i> /Å	23.8099(4)
<i>α</i> /°	90
<i>β</i> /°	91.8650(10)
<i>γ</i> /°	90
<i>V</i> /Å ³	10911.9(4)
<i>Z</i>	8
<i>Z</i> '	1
Wavelength/Å	1.541838
Radiation type	CuK _α
<i>θ</i> _{min} /°	2.889
<i>θ</i> _{max} /°	70.163
Measured Refl.	9970
Independent Refl.	9970
Reflections with <i>I</i> > 2(<i>I</i>)	5386
<i>R</i> _{int}	.
Parameters	654
Restraints	0
Largest Peak	0.354
Deepest Hole	-0.303
Goof	0.963
<i>wR</i> ₂ (all data)	0.1643
<i>wR</i> ₂	0.1398
<i>R</i> ₁ (all data)	0.1432
<i>R</i> ₁	0.0686

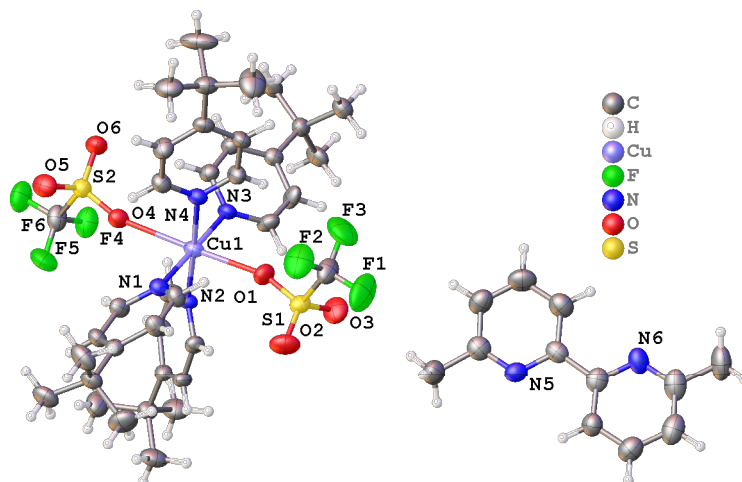


Figure 6.2 The picture of solid electrolyte under microscope.



Figure 6.3 Crystal structure of blue crystal.

Table 6.1 Bond length in Å for blue crystal.

Atom	Atom	Length/Å
Cu1	O1	2.340(3)
Cu1	N1	2.024(4)
Cu1	N2	2.032(3)
Cu1	N3	2.023(3)
Cu1	N4	2.024(4)

Table 6.2 Bond angles in ° for blue crystal.

Atom	Atom	Atom	Angle/°
N1	Cu1	O1	91.92(13)
N1	Cu1	N2	88.39(14)
N2	Cu1	O1	94.01(12)
N3	Cu1	O1	89.44(13)
N3	Cu1	N1	178.18(15)
N3	Cu1	N2	90.31(14)
N3	Cu1	N4	90.47(14)
N4	Cu1	O1	87.92(13)
N4	Cu1	N1	90.79(14)
N4	Cu1	N2	177.92(14)

Compound	Cu(DMAP)₂OTf₂
CCDC	1902791
Formula	C ₃₀ H ₄₀ CuF ₆ N ₈ O ₆ S ₂
<i>D</i> _{calc.} / g cm ⁻³	1.510
<i>μ</i> /mm ⁻¹	2.602
Formula Weight	850.36
Color	purple
Shape	block
Size/mm ³	0.46×0.27×0.16
<i>T</i> /K	173(2)
Crystal System	monoclinic
Space Group	<i>C</i> 2/ <i>c</i>
<i>a</i> /Å	20.1738(4)
<i>b</i> /Å	10.8839(2)
<i>c</i> /Å	18.2957(3)
<i>α</i> /°	90
<i>β</i> /°	111.3840(10)
<i>γ</i> /°	90
<i>V</i> /Å ³	3740.63(12)
<i>Z</i>	4
<i>Z</i> '	0.5
Wavelength/Å	1.541838
Radiation type	CuK _α
<i>θ</i> _{min} /°	4.695
<i>θ</i> _{max} /°	70.030
Measured Refl.	24244
Independent Refl.	3552
Reflections with <i>I</i> > 2(<i>I</i>)	3389
<i>R</i> _{int}	0.0332
Parameters	245
Restraints	0
Largest Peak	0.265
Deepest Hole	-0.377
Goof	1.037
<i>wR</i> ₂ (all data)	0.0841
<i>wR</i> ₂	0.0832
<i>R</i> ₁ (all data)	0.0318
<i>R</i> ₁	0.0306

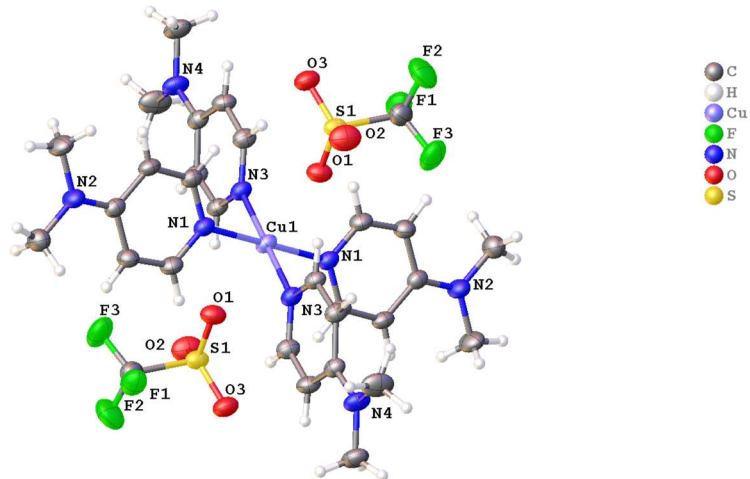


Figure 6.4 Crystal structure of Cu(DMAP)₂OTf₂.

Table 6.3 Bond length in Å for Cu(DMAP)₂OTf₂.

Atom	Atom	Length/Å
Cu1	N1 ¹	2.0225(14)
Cu1	N1	2.0226(14)
Cu1	N3	2.0437(13)
Cu1	N3 ¹	2.0437(13)
Cu1	O1	2.5130(13)

Table 6.4 Bond angles in ° for Cu(DMAP)₂OTf₂.

Atom	Atom	Atom	Angle/°
N1 ¹	Cu1	N1	180.00(7)
N1	Cu1	N3	89.21(6)
N1 ¹	Cu1	N3 ¹	89.21(6)
N1	Cu1	N3 ¹	90.79(5)
N1 ¹	Cu1	N3	90.79(5)
N1 ¹	Cu1	O1	90.84(5)
N1	Cu1	O1	89.16(5)
N3 ¹	Cu1	N3	180.0
N3 ¹	Cu1	O1	90.65(5)
N3	Cu1	O1	89.35(5)

Compound	Cu(tmbpy)₂TFSI₂
CCDC	1970926
Formula	C ₃₂ H ₃₂ CuF ₁₂ N ₄ O ₁₀ S ₄
<i>D</i> _{calc.} / g cm ⁻³	1.629
<i>μ</i> /mm ⁻¹	3.538
Formula Weight	1052.39
Colour	purple
Shape	chunk
Size/mm ³	0.32×0.20×0.17
<i>T</i> /K	173(1)
Crystal System	orthorhombic
Space Group	<i>Pbca</i>
<i>a</i> /Å	14.15500(9)
<i>b</i> /Å	17.78500(12)
<i>c</i> /Å	34.0899(3)
<i>α</i> /°	90
<i>β</i> /°	90
<i>γ</i> /°	90
<i>V</i> /Å ³	8582.02(10)
<i>Z</i>	8
<i>Z'</i>	1
Wavelength/Å	1.54184
Radiation type	Cu K _α
<i>θ</i> _{min} /°	2.592
<i>θ</i> _{max} /°	68.251
Measured Refl's.	76215
Ind't Refl's	7864
Refl's with <i>I</i> > 2(<i>I</i>)	6210
<i>R</i> _{int}	0.0609
Parameters	621
Restraints	3
Largest Peak	3.370
Deepest Hole	-1.196
Goof	1.030
<i>wR</i> ₂ (all data)	0.2066
<i>wR</i> ₂	0.1843
<i>R</i> ₁ (all data)	0.0855
<i>R</i> ₁	0.0681

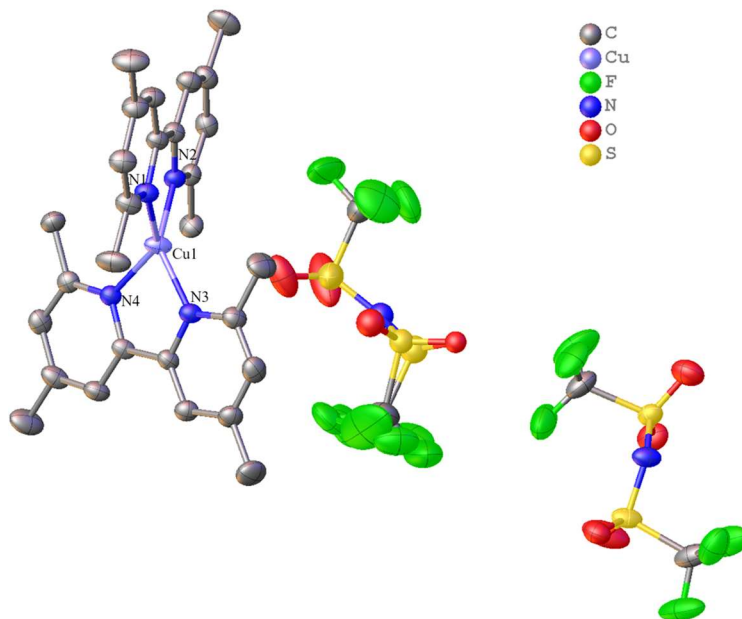


Figure 6.5 Crystal structure of Cu(tmbpy)₂TFSI₂.

Table 6.5 Bond length in Å for Cu(tmbpy)₂TFSI₂.

Atom	Atom	Length/Å
Cu1	N1	1.973(3)
Cu1	N2	1.962(3)
Cu1	N3	1.972(3)
Cu1	N4	1.985(3)

Table 6.6 Bond angles in ° for Cu(tmbpy)₂TFSI₂.

Atom	Atom	Atom	Angle/°
N1	Cu1	N4	135.02(15)
N2	Cu1	N1	83.72(14)
N2	Cu1	N3	142.94(15)
N2	Cu1	N4	109.97(14)
N3	Cu1	N1	110.76(14)
N3	Cu1	N4	84.23(14)

REFERENCES

REFERENCES

- (1) Housecroft, C. E.; Constable, E. C. *Chem. Soc. Rev.* **2015**, *44*, 8386
- (2) Shaw, G. B.; Grant, C. D.; Shirota, H.; Castner, E. W.; Meyer, G. J.; Chen, L. X. *J. Am. Chem. Soc.* **2007**, *129*, 2147
- (3) Cañon-Mancisidor, W.; Spodine, E.; Venegas-Yazigi, D.; Rojas, D.; Manzur, J.; Alvarez, S. *Inorg. Chem.* **2008**, *47*, 3687
- (4) Chen, L. X.; Shaw, G. B.; Novozhilova, I.; Liu, T.; Jennings, G.; Attenkofer, K.; Meyer, G. J.; Coppens, P. *J. Am. Chem. Soc.* **2003**, *125*, 7022
- (5) Mara, M. W.; Jackson, N. E.; Huang, J.; Stickrath, A. B.; Zhang, X.; Gothard, N. a.; Ratner, M. a.; Chen, L. X. *J. Phys. Chem. B* **2013**, *117*, 1921
- (6) Saygili, Y.; Söderberg, M.; Pellet, N.; Giordano, F.; Cao, Y.; Muñoz-García, A. B.; Zakeeruddin, S. M.; Vlachopoulos, N.; Pavone, M.; Boschloo, G.; Kavan, L.; Moser, J.-E.; Grätzel, M.; Hagfeldt, A.; Freitag, M. *J. Am. Chem. Soc.* **2016**, *138*, 15087